The Interplay between Stellar Feedback and Galactic Environment in Molecular Clouds

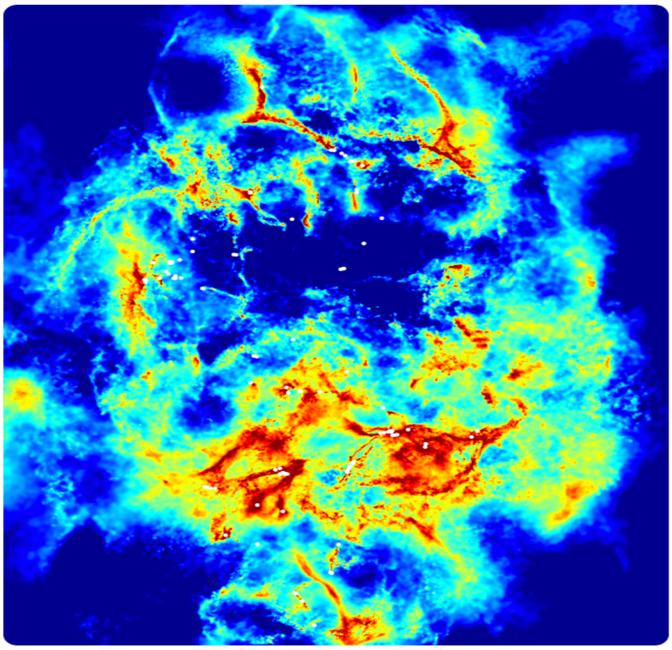

Ramón Rey Raposo

Submitted by Mr Ramón Rey Raposo to the University of Exeter as a thesis for the degree of Doctor of Philosophy in Physics, October, 2015.

I certify that all material in this thesis which is not my own work has been identified and that no material has previously been submitted and approved for the award of a degree by this or any other University.

Signed: ....

Mr Ramón Rey Raposo

Date: ....

Abstract

In this thesis we address the problem of understanding the star formation process in giant molecular clouds in a galactic context. Most simulations of molecular clouds to date use an oversimplified set of initial conditions (turbulent spheres/boxes or colliding flows). Full galactic scale models are able to generate molecular clouds with complex morphologies and velocity fields but they fail to reproduce in detail the effects that occur at sub-pc scales (e.g. stellar feedback). Our goal is to build the bridge between these two scenarios, and to model the star formation process in molecular clouds produced in a galactic context.

We extract our molecular clouds from full-scale galactic simulations, hence we need to increase the resolution by two orders of magnitude. We introduce the details of the program used to simulate molecular clouds in Chapter 2, and describe in detail the method we follow to increase the resolution of the galactic clouds.

In Chapter 3 we compare our simulated galactic clouds with the more conventional approach of using turbulent spheres. We create turbulent spheres to match the virial state of three galactic clouds. We perform isothermal simulations and find that the velocity field inherited from the full-scale galactic simulations plays an important role in the star formation process. Clouds affected by strong galactic shear produce less stars compared with clouds that are compressed. We define (and test) a set of parameters to characterise the dynamical state of our clouds.

To include stellar feedback in our simulations we need to introduce a cooling/heating algorithm. In Chapter 4 we analyse how the different velocity fields of our clouds change the temperature distribution even in the absence of feedback. To study the formation of molecules we need to model the chemistry of H_2 in our clouds. We also add CO chemistry, and produce synthetic observations of our clouds.

The effect of feedback from winds and supernovae in galactic clouds is studied in Chapter 5. We analyse the effect of winds in clouds with very different velocity fields. We find that the effect of winds is stronger in highly virialised, high star forming clouds, with clouds with weak galactic shear, compared to unbound shear-dominated clouds. The steady and continuous action of the winds appears to have a greater effect than the supernovae.

In summary, the inherited properties from the galaxy have an impact on many relevant pro-

cesses in star formation, influencing gravitational collapse, the formation of filamentary structures, the temperature field of the cloud, and have a considerable effect on the impact of feedback in the clouds.

Acknowledgements

Becoming a doctor has been the greatest project in my life, and the result of sum of joined efforts and help from colleagues, friends and family. First I have to thank Clare, not because it is customary, but because I am really grateful to the effort, hours and dedication she has committed to this project. She has been there for me every step of the way, and I have felt encouraged, protected and supported by her knowledge, patience and why not, her contagious laughter. I want to thank her specially for giving me the freedom to pursue other lines of work and investigation, allowing me to become AFHEA and to create my videolog.

My family is the pillar I lean on. So, I want to thank my mother for inculcating the values of science and skepticism since I was a little child and for being always there worrying about me. My father for teaching me the importance of order and commitment: *Let the North of your life be the fulfilment of your duty*, probably the most important lesson that I have learnt in life. I want also to thank my grandmother for encouraging me to pursue my dreams, and my brother who was the only one that never doubted that I would become a doctor.

While writing this thesis I have had in my mind, three persons that are no longer here. The first one is Araceli Rico, my high school Physics teacher. She is responsible of my vocation, and that every physical quantity in this document is written with its units. The second person is my grandfather who always believed in me and whose advice still guides my life. And the last is my good friend Tomás who dragged me to study in the library in so many occasions.

I want to give a special thanks to the Exeter Astro department, because it is an incredible place to spend 3 years working. I would like to thank everyone from the direction to the administrative staff and faculty. From the very beginning I felt surrounded by great professionals, really smart minds that you can easily approach and learn from them. Specially, although not all of them in Exeter now, I want to thank Alex, Emily, Miriam, Tom, David, Paul, Felix, Pablo and many more that I am probably forgetting. I want to give a very warm thank you to my co-host Hannah, for sharing with me hours of fun making the 36 episodes of HMAvl.

As an electrical engineer, I worked as a system admin. and I know how hard it can be. The simulations included in this thesis were performed in Zen, the University supercomputer. So, I want to give a special thanks to Dave, for being such an incredible person and for taking care of such a fantastic tool.

I have been blessed with very good friends, and to all of them I am very grateful for their support during these years. Thank you Pedro, Juan, Gonzi, Terol and Miki for being always there. Jennifer, I do not forget your help during the first stages of this journey. I am especially grateful to Susana for her advice, encouragement, and words full of wisdom during these three difficult and exciting years.

I want to thank my examiners Paul and Tim for their insightful comments that have substantially improved this Thesis, and for making my viva as interesting, exciting and educational as they possibly could.

Lastly, I want to say thank you to the most important person in my life, my partner in this journey, Quique. Thank you for supporting me from the beginning, for believing in me when no one did, and for leaving all behind so that we could share this adventure together. I could not have done this without you.

Muchísimas gracias a todos.

Ramón Rey Raposo
Exeter, U.K.
19th October 2015

Contents

List of Figures

List of Tables

Declaration

This thesis contains work published or pending publication as papers. The work in Chapters 3 form the basis of the work the paper Rey-Raposo et al. (2015). Chapter 4 and 5 form a separate paper; Rey-Raposo et al. 2016, which has been presented to MNRAS in February 2016. I am first author in both of these works, and performed the majority of the work myself with insights, advice and code development aid from my co-authors; C. Dobbs, A. Duarte-Cabral, O. Agertz and C. Alig. Part of this work is also included in the conference proceedings *The Kinematics of Star Formation: Theory and Observation in the Gaia Era* which have been published in A&G.

For this thesis we have used a modified version of GADGET2, originally created by V. Springel and adapted by P. Clark to include sink particles. Many of the figures included in this thesis were created using the program SPLASH by D. Price (Price 2007).

1

Introduction

"Y así, del poco dormir y del mucho leer, se le secó el cerebro..."
– Don Quijote de la Mancha

1.1 Motivation

Molecular clouds are the birthplace of stars. Understanding star formation begins with comprehending how molecular clouds are created, how they evolve and how they are eventually dispersed. In the last 20 years there has been a huge effort from both theoretical and observational sides to understand the evolution of the clouds in our Galaxy, and in other nearby galaxies.

The long time scales of molecular clouds (of the order of 10^7 yr) make it impossible to observe the full evolution of a single cloud through its life. Each observation corresponds to a snapshot of a cloud at a particular moment of its evolution, and its past and future has to be inferred by the conditions at the time the cloud is observed. To provide a theoretical frame to understand the evolution of molecular clouds and star formation within them, a wide variety of different numerical simulations have been produced, modelling the different effects and processes that shape the clouds. Examples of simulations at molecular cloud scales include Bate (2009); Vázquez-Semadeni et al. (2011); Clark et al. (2012b); Dale et al. (2014).

Most simulations to date share a major limitation, regardless the code used, the resolution chosen, or the different physical effects considered: Their initial conditions are very restrictive. The three usual methods of generating initial conditions to simulate molecular clouds are turbulent spheres (where a spherical mass of turbulent gas evolves to form stars), turbulent boxes (with

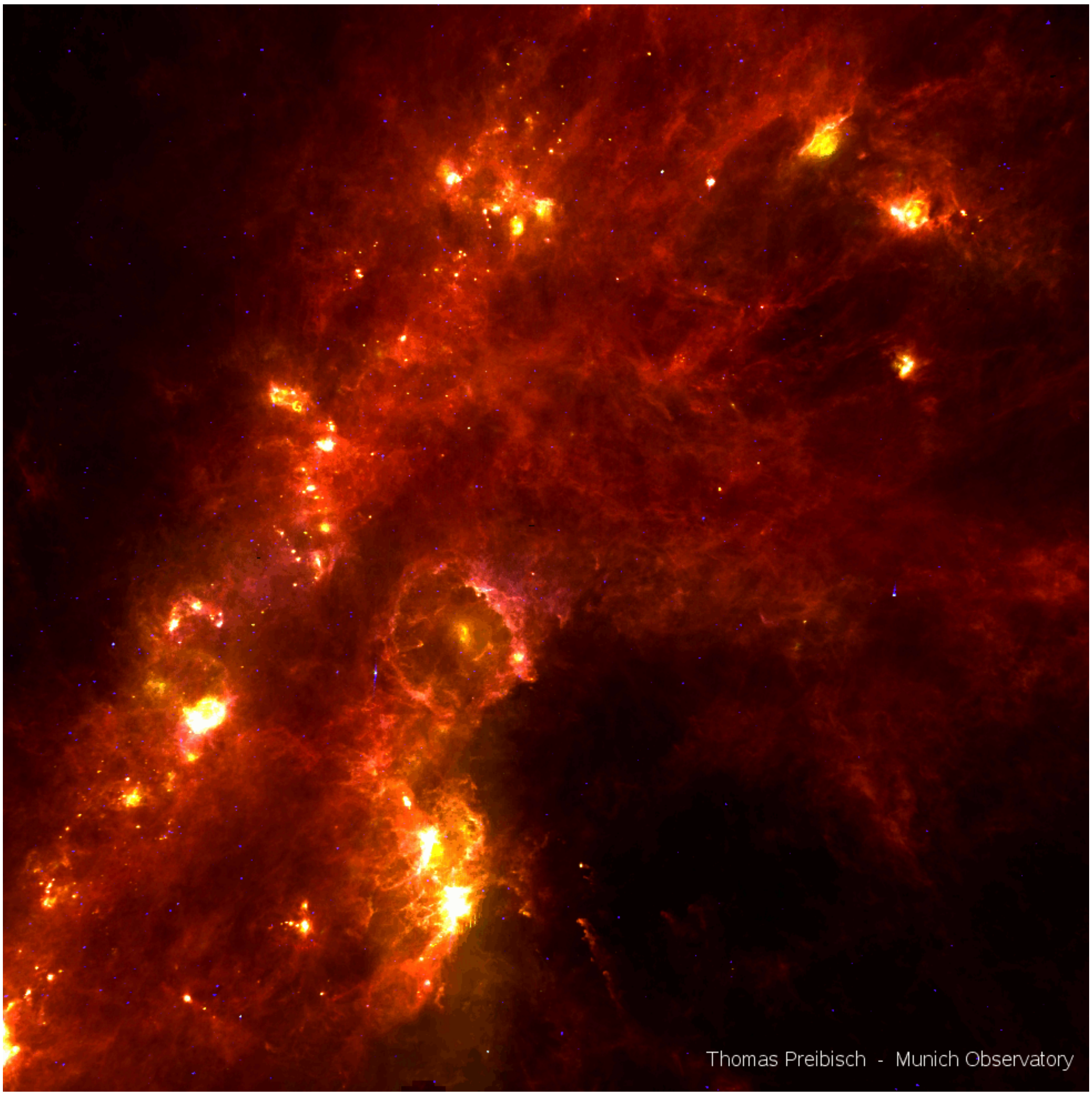

Figure 1.1: IRAS image of the Taurus - Perseus - Orion region. Blue represents 12 μm radiation, 60 μm is green and 100 μm is red. Credit: Thomas Preibisch.

periodic boundary conditions), and colliding flows (where two flows of gas collide to produce overdensities at their interface). Any of these three methods represent a very idealistic set of structures and velocity distributions, with a limited phase space. We do not observe spheres, or cylindrical masses of gas moving in the Galaxy. The observed molecular clouds present morphologies and velocity fields distinct from these typical initial conditions. In Fig. 1.1 we show an IRAS image of several molecular cloud complexes, with Taurus-Auriga in the upper left, Perseus in the upper right, and the Orion cloud in the lower centre. The diversity of morphologies and structures present in this image is wide. We observe very dense areas with strong emission in yellow with a very intricate filament network, and diffuse gas in the outer parts of the complexes. The effect of stellar feedback is clear in a spherical shell in the Orion area. Winds and radiation from massive stars have created a quasi-spherical cavity there.

I believe that we can improve upon those simulations which use simple initial conditions to better model such complicated entities. Recent galactic scale simulations (Dobbs et al. 2008; Hopkins et al. 2011; Agertz & Kravtsov 2015) provide molecular clouds with morphologies and structures more similar to the ones observed in our Galaxy and in nearby galaxies. However, the resolution of a single molecular cloud from these simulations is not high enough to study the star formation process at sub-pc scales. Recently, different groups have tried a hybrid approach (Bonnell et al. 2013; Smith et al. 2014; Dobbs 2015). They select areas in their full-scale galactic models and increase the resolution of their clouds, to resimulate them. For this thesis we will follow a similar approach. We will use galactic clouds including gravity, ISM cooling and heating, chemistry of H_2 and CO, and stellar feedback from winds and supernovae. We will increase the resolution of molecular clouds, and resimulate them in detail, trying to understand the interplay between stellar feedback, morphology and the global velocity field in the star formation process.

This Introduction is structured as it follows. First we describe the Interstellar Medium (ISM) and its main characteristics. After that we will explain the main properties of molecular clouds. In the last section of this introduction we briefly discuss the star formation process.

1.2 The ISM

The ISM is a fluid that permeates the Galaxy, consisting of interstellar gas and dust. The gas is mainly H and He which were produced during the Big Bang. These 2 species constitute 99% of the total baryonic mass of the Galaxy (Draine 2011). Compared to primordial values, the concentration of hydrogen has been reduced and the He and other metals increased due to stellar evolution. The heavier elements are present in smaller concentrations ($\leq 10^{-4}$ parts per H atom), and all components of the ISM interact in a very complicated chemical network.

The ISM has different mechanisms for cooling through emission lines, or collisions between the different components (see Chapter 4 for more details). These mechanisms allow the formation of cold and dense areas where molecules are created (Solomon et al. 1987). There is also a diffuse component with gas at temperatures of $T \sim 10^4$ K (Jenkins & Meloy 1974; Burstein et al. 1977). To explain the existence of the diffuse component Field et al. (1969) proposed that cosmic rays might heat up the ISM. Subsequent works (Draine 1978; Wolfire et al. 2003) proposed that photoeletrical heating by dust is a more probable cause for temperatures of 10^4 K. Above 10^4 K hydrogen cooling becomes very effective and thus, in the absence of stellar feedback gas does not reach higher temperatures. However, in regions affected by supernova explosions, the temperatures may reach 10^6 K (McKee & Ostriker 1977) as the hot supersonic ejecta of these events heat up the ISM.

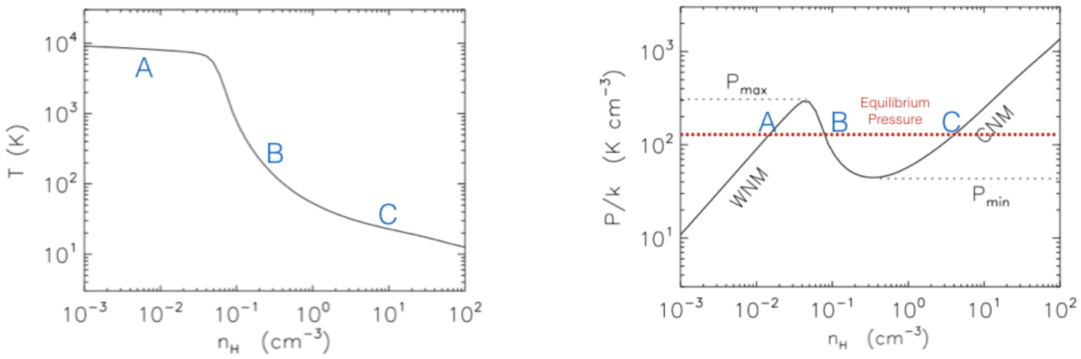

Figure 1.2: Thermodynamical properties of the ISM adapted from Sternberg et al. (2002). The left panel (a) represents the temperature profile of the ISM without stellar feedback. In the right panel (b) we show the pressure vs. density diagram.

1.2.1 Phases of the ISM

If we consider the ISM in pressure equilibrium (not expanding or contracting) the empirical value for the equilibrium pressure is $P/k_{\rm B} \sim 100$ K cm^{-3} (Sternberg et al. 2002). In Fig. 1.2 we show a scheme of the actual thermodynamical properties of the ISM (based on Sternberg et al. 2002). In the right panel we illustrate the pressure-density diagram. We select three points A, B, C that are at the equilibrium pressure. In the left panel of the figure we show a temperature-density diagram where we also highlight those three points. The three points coexist at the same pressure, but they have very different temperatures. The gas represented by the point C is cold dense gas, whereas the gas in A, is warm and diffuse. Both points represent stable regimes, in the sense that if the gas experiences a small perturbation it will return to its initial state. The gas in point B is in a different equilibrium state. In this regime the cooling and heating make the gas very unstable, and a small perturbation might cause the gas to become cold and dense (moving towards C), or warm and diffuse and move towards point A.

Field et al. (1969) considered only a two-phase ISM. However as more physical processes in the ISM were studied, the number of phases with different temperatures, chemical states, or both, increased accordingly. Nowadays it is typical to speak of a multiphase ISM. When simulating our molecular clouds, we will consider the following phases (or components) for the ISM (adapted from Draine (2011)):

1. *Hot Ionised H_{II}*: gas that has been shocked to high temperatures ($T \sim 10^6$ K) mainly by stellar feedback. It is very diffuse gas that occupies a great volume of the Galactic disk, and often referred as HIM (Hot Ionised Medium).
2. *Warm HI*: Or WNM (Warm Neutral Medium), this component consists of neutral hydrogen at lower temperatures than the ionising energy. The density of this component is small but it constitutes almost 40% of the volume of the Galactic disk. About 60% of the HI by mass

is in WNM (Heiles & Troland 2003). The temperatures in the WNM are of the order of thousands of K.

3. *Cold HI*: Atomic gas at temperatures around 100 K that constitutes only a small fraction of volume of the disk, and often referred to as the CNM (Cold Neutral Medium).
4. *Molecular Medium*: Dense and cold molecular clouds of gas with high densities of H_2. They are normally opaque clouds with high extinctions. We will refer to this phase as CMM (Cold Molecular Medium). The molecular medium is very cold with temperatures in the range 10 - 25 K.

1.2.2 Dust

Dust constitutes 1% of the total mass of the ISM. It is made of small solid particles with variable sizes from $\sim 0.1\mu$m - 10μm (Draine 2011). Dust is formed by iron or magnesium silicates, or carbon in many different forms (e.g. graphite, Polycyclic Aromatic Hydrocarbons (PAH), etc. (Ehrenfreund & Foing 2010)). The dust grains may also be covered by ice.

The origin of dust is in the cool atmospheres of red giants, where the temperatures are low and large aggregates of atoms and molecules can be created. Dust is responsible for the high extinction in molecular clouds that protects them from UV radiation. It also acts as a catalyst in the formation of H_2, and intervenes in the cooling (and heating) of the ISM through collisions (Hollenbach & McKee 1989) becoming important at number densities $n \sim 100$ cm^{-3}, and the photoelectric heating responsible of the diffuse phase of the ISM.

We do not consider the mixture of dust and gas in our simulations (though see Loren-Aguilar & Bate 2014; Laibe & Price 2014), although we include implicitly the effect of dust in our chemistry, cooling and heating model (via shielding). As the dust is in the backbone of so many different processes in the ISM, it may be interesting to consider dust explicitly in future works.

1.2.3 Processes in the ISM

The different components of the ISM are in a state of dynamical equilibrium, with several processes affecting them. Gravity affects the ISM, most obviously on the scales of cores, but may also contribute to GMC formation on larger scales (Section 1.3.3). Some authors suppose that gravity and turbulence dominate on molecular cloud scales (Klessen 2003), whereas some suppose structure is turbulence driven (Padoan & Nordlund 2011). For the rest of this section we will describe turbulence and magnetic fields leaving stellar feedback to the star formation section (1.4).

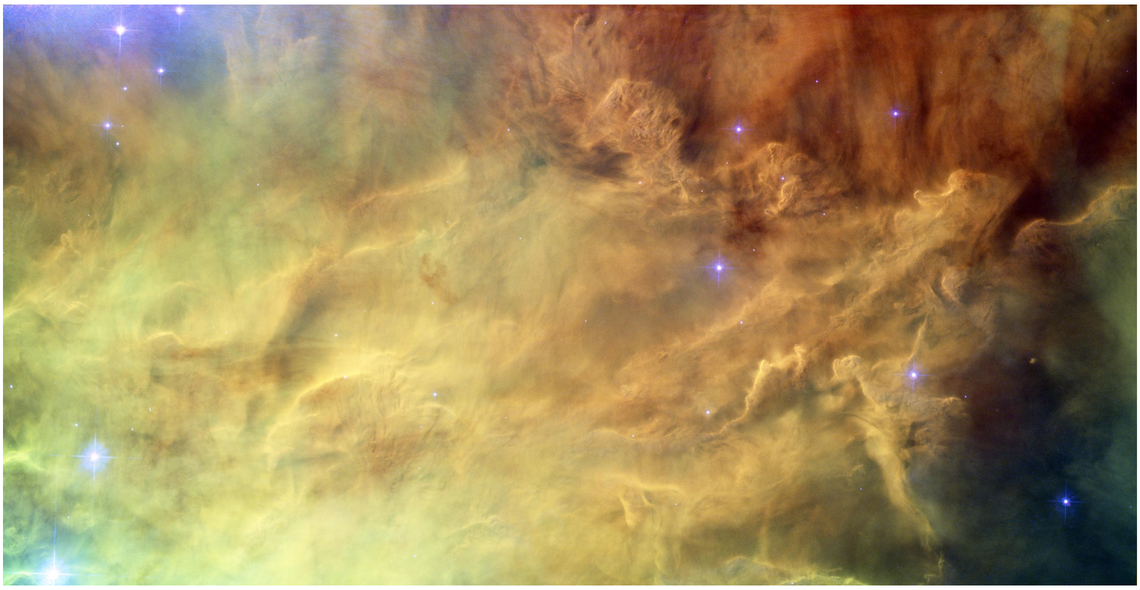

Figure 1.3: Lagoon Nebula captured the Advance Camera for Surveys (ACS) of the Hubble Space Telescope (UV - Optical). Credit NASA.

Turbulence

The ISM is highly compressible with Mach numbers ranging from $M \sim 1$ in the warm diffuse ISM ($T \sim 10^4$ K) to $M \sim 50$ in the cold and dense molecular clouds (Mac Low & Klessen 2004). In Fig. 1.3 we present a picture of the Lagoon Nebula taken by the Hubble Space Telescope. The image captures a region (almost 1 pc wide) where structures resemblant of turbulent flows are present. The gas is heated up by the UV radiation from newborn massive stars on the left. Hot gas pushes the dense material in the eastern region of the figure creating turbulent structures.

Kolmogorov (1941) considered the turbulence formed by eddies of different diameter. Eddies of different size carry different amounts of energy. This naturally leads to the concept of a turbulent velocity spectrum. Kolmogorov thought that large eddies tend to transform into smaller eddies, so the energy travels from larger scales to smaller scales (this is referred to as a turbulent cascade). At the low energy end of the cascade viscosity dissipates the energy of the smaller eddies. However, energy has to be injected at larger scales to maintain the turbulent flow through the cascade (see Fig. 1.4). The turbulent velocity spectrum is defined as (see e.g. Roman-Duval et al. (2011)):

$$E(\vec{k}) = 4\pi k^2 |\tilde{\vec{u}}(\vec{k})|^2, \tag{1.1}$$

where $\tilde{\vec{u}}(\vec{k})$ is the Fourier transform of the velocity field $\vec{u}(\vec{r})$ and $\vec{k}$ is the wavevector. This energy spectrum follows a power law, $E(\vec{k}) \propto k^{\beta}$. The exponent of this power law depends on the type of turbulence considered. If we consider an incompressible velocity field ($\nabla \cdot \vec{u} = 0$), the spectrum will have an exponent β = -5/3 (Kolmogorov turbulence). For pressureless and highly compressive turbulence the exponent is β = -2. This regime is called Burgers turbulence.

Mac Low & Klessen (2004) propose the following methods for driving turbulence: Mag-

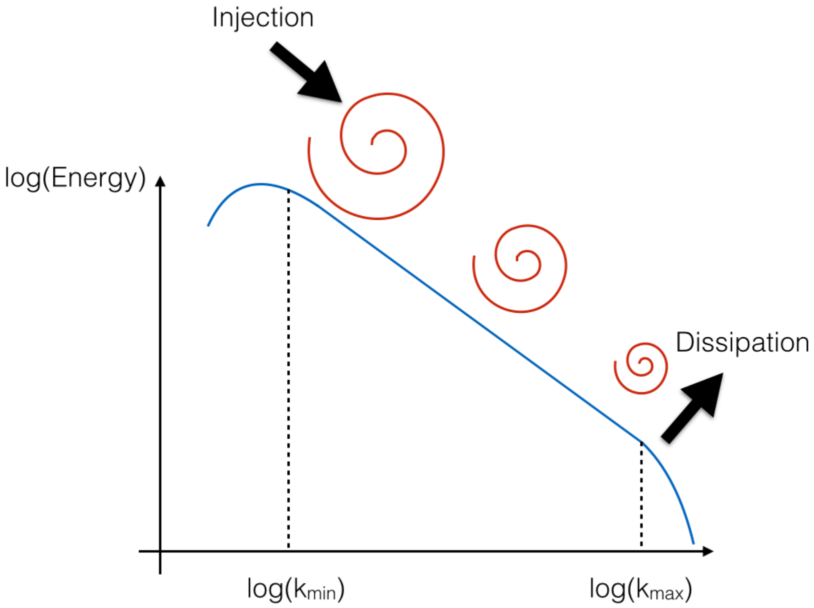

Figure 1.4: Turbulent Cascade. The energy is injected at large scales and descends towards smaller scales where it is dissipated by viscosity.

netorotational or gravitational instabilities, protostellar outflows or feedback from massive stars. Mac Low & Klessen (2004) claim that stellar feedback is the main driver of turbulence, and in particular, SNe alone can release enough energy to sustain turbulence.

There is still some debate about the role played by turbulence in star formation. Bonazzola et al. (1992) calculate that turbulence may support the ISM against gravitational collapse at small and large scales (not in the intermediate), provided that the turbulent power spectrum is steeper than β = -3. However, there is also evidence that turbulence can enhance the star formation process, as turbulent motions may create overdensities (Krumholz & Mckee 2005; Glover & Mac Low 2006; Federrath et al. 2011; Hopkins 2012). For instance, it might cause the formation of filaments (Moeckel & Burkert 2015) (at pc scales) or it may create GMCs, if considered on galactic scales (Dobbs et al. 2006; Hopkins et al. 2011; Agertz & Kravtsov 2015).

In two different works Federrath & Klessen (2012, 2013) model molecular clouds with turbulent fields, and they find that at large scales the turbulence is compatible with a Burgers turbulence (highly compressible and supersonic), whereas at lower scales the energy spectrum of the molecular clouds behaves following a Kolmogorov regime. Federrath & Klessen (2012) perform simulations of turbulent molecular clouds, with turbulent fields with different characteristics varying the composition of the turbulence between compressive and solenoidal modes. Their results also suggest that the presence of a highly compressive component increases the star formation rate in the clouds. This was also found in galactic scale simulations by Renaud et al. (2014).

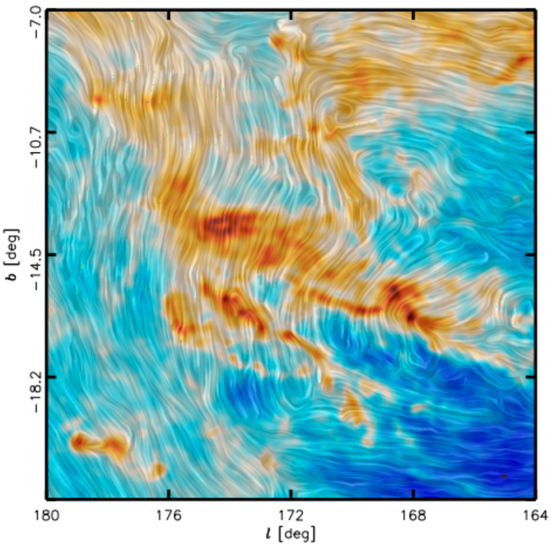

Figure 1.5: Magnetic field and column density measured by Planck towards the Taurus MC (from Planck Collaboration et al. 2015).

Magnetic Fields

The influence of magnetic fields in the star formation process is a source of controversy as there is not a clear consensus on the extent to which they are important in the star formation process. Magnetic fields behave like an extra source of pressure that therefore supports the clouds and may even decrease the star formation rate (Price & Bate 2009). Federrath & Klessen (2012) suggest that magnetic fields constitute the second most important process in star formation after turbulence.

From an observational point of view, new instruments have also improved our measurements of magnetic fields in our Galaxy. The Planck satellite has provided us with observations of magnetic fields in Galactic molecular clouds (Planck Collaboration et al. 2015). In Fig.1.5 we can observe the column density of the Taurus molecular cloud, with the magnetic field superposed (calculated measuring the intensity and polarization of dust emission). The relative orientation of the magnetic field changes with the column density ($N(H)$) from perpendicular to the densest structures in the cloud, to parallel (or no specific direction) in the diffuse areas. The space observatory Herschel has also studied the effects in molecular clouds. Palmeirim et al. (2013) study the filamentary structure of a cloud in Taurus region finding that the polarization of the magnetic fields is perpendicular to the direction of the filaments in the clouds. These two results suggest that combined with turbulence, magnetic fields may contribute to the creation of well defined filaments that eventually create stars.

Ideally magnetic fields should be considered in future works, to study their effects both at galactic scales and at sub-pc scales, but they are difficult to model in hydrodynamical simulations (see e.g. Price et al. (2011)). The galaxies from which we extract our molecular clouds do not

Figure 1.6: Colour image of M51 by the Hubble Space Telescope. Superimposed in blue is the CO (1 → 0) radiation as measured by the PAWS study using IRAM. Credit: PAWS Team/IRAM/NASA HST/T. A. Rector (University of Alaska Anchorage)

include them, and we do not consider them here.

1.3 Molecular Clouds

Molecular clouds are often referred to as stellar nurseries. They are regions in galaxies where stars are born. To give us an idea of the distribution of clouds in a galaxy, in Fig. 1.6 we present the CO (1 → 0) emission of M51 (Schinnerer et al. 2013), superposed on an image from the Hubble Space Telescope. Molecular clouds mainly trace the spiral structure of the galaxy, but some of them lie also in the space between arms. This work notes the importance of the galactic context, e.g. the presence of spiral arms, for the distribution of molecular gas and star formation. Meidt et al. (2015) also suggest that shear is the main mechanism for disrupting clouds in the centre of M51, whereas at large radii, feedback dominates.

1.3.1 Formation of H_2

The principal component of molecular clouds is H_2. The hydrogen molecule is symmetric, and therefore it lacks a permanent electrical dipole (dipole emission is highly improbable). For the molecule to emit via the quadrupole moment, electrons have to be in high energy states. However, that requires temperatures of the gas high enough for dissociation.

Creating H_2 via the collision of two hydrogen atoms is highly improbable, as at low temper-

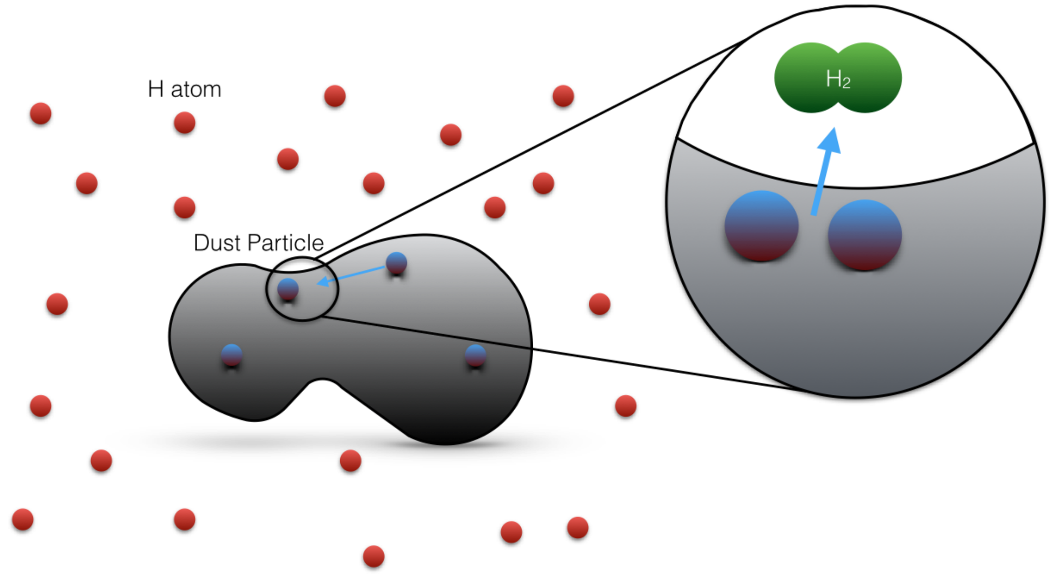

Figure 1.7: Formation of H_2 on dust grains. We show a scheme of a dust particle (in grey) surrounded by free H atoms (in red) that may get attached to the dust and form a molecule of H_2 (in green).

atures the resulting molecule is unable to emit the excess of energy via the emission of a photon. The interaction of three atoms of hydrogen is possible, as the free atom remaining is able to carry the extra energy from the system. However, even in the most dense clouds, the probability of the collision of three atoms is again too small. The only possible way to produce H_2 in the gas phase is via the formation of H^- via radiative association followed by associative detachment (Le Teuff et al. 2000). The formation of H^- is slow compared to its destruction (Draine 2011), and therefore it is difficult to explain the galactic abundances of molecular hydrogen considering only this process.

Gould & Salpeter (1963) suggested another method for the creation of H_2: the formation on dust grains. In Fig. 1.7 we show a scheme of the process of formation on the surface of a dust grain. The dust particle has an irregular shape and its size ($\sim \mu$m) is some orders of magnitude larger than the hydrogen atoms. At any time a hydrogen atom may collide with the dust grain and get trapped on the surface by partially sharing its electron with the electronic network of the grain. The strength of this bond is enough to maintain the atom on the surface for a suitable period of time. The atom may move around on the surface, ending up in a position corresponding to a minimum of energy. As the dust grain travels through the cloud, it collides with more hydrogen atoms, trapping some of them. The new atoms may fall close enough to others, or travel on the surface to form a molecule of H_2. The energy released when two hydrogen atoms form a molecule in the ground state is $\Delta E = 4.5$ eV, enough to release the molecule from the dust grain, and any excess of energy or momentum can be absorbed by the grain.

1.3.2 Observations of Molecular Hydrogen: the X-factor

Molecular hydrogen is difficult to observe, as it lacks a permanent electric dipole, and it is challenging to find observable lines of H_2. On the other hand CO has a permanent dipole, and its spectral lines can be found in the mm range. CO has been widely used as a tracer of H_2. The creation process for these two molecules is different: H_2 is formed mainly on the surface of grains whereas the CO is formed in the gaseous phase. Both molecules can be destroyed by UV radiation, but H_2 is able to protect itself by shelf shielding even at very low concentrations (Draine & Bertoldi 1996). There is reasonable evidence to suggest that CO is a good tracer of H_2 (Dame et al. 2001), and the emission of CO is widely used to trace molecular clouds.

The relationship between the observed integrated ^{12}CO (J = 1 → 0) intensity ($W_{\rm CO}$), and the H_2 column density ($N(H_2)$) is called the X-factor. The X-factor is typically used for calculating column densities of H_2 in the ISM. For this thesis we consider the value from Dame et al. (2001).

$$X_{\rm CO} = \frac{N(H_2)}{W_{\rm CO}} = (1.8 \pm 0.3) \times 10^{20}\ {\rm cm^{-2}\ K^{-1}\ km^{-1}\ s}. \tag{1.2}$$

Recent works (Pineda et al. 2008; Ripple et al. 2013) also study the abundances of other isotopes of CO, like ^{13}CO, although we only include ^{12}CO in our simulations. Other methods for calculating H_2 column densities include using other molecules (such as HCN) and estimating the absorption of dust (considering that the concentration of dust is related to the concentration of H_2). In Chapter 4 we explain in detail how we compute the formation of H_2 and CO, as well as how we create synthetic CO maps of our simulated molecular clouds.

1.3.3 Formation of Molecular Clouds

The main mechanisms that form molecular clouds are a cause of debate. Dobbs et al. (2014a) cite five possible mechanisms: Converging flows, spiral-arm induced collisions, gravitational instabilities, magneto-gravitational instabilities, and Parker instabilities. They do not consider thermal instabilities (Field 1965) because the scale of the gravity-bound structures is of the size of ~ pc, and therefore highly exposed to photodissociation of molecular gas (as the column densities are not high enough to shield the molecules). The other process not considered by Dobbs et al. (2014a) is the magnetorotational instability (Balbus & Hawley 1991) because it may not lead to a compressive velocity field.

In general, all of these processes result in a compressive velocity field ($\nabla \cdot \vec{u} < 0$, where $\vec{u}$ is the velocity field), creating converging flows and inducing gravitational collapse. We do not consider magnetic fields in our simulations, therefore the first 3 processes suggested by Dobbs et al. (2014a) are the most relevant.

1. **Converging Flows**:

Stellar feedback and turbulence may cause complex velocity fields at scales of the order of ~ 100 pc, that may produce converging flows. When two masses of gas collide, they form a highly turbulent and dense area at the interface. ISM cooling becomes effective as the density increases, and molecular clouds are created (see e.g. Vázquez-Semadeni et al. (2007); Clark et al. (2012b)).

2. **Gravitational Instability**:
   Perturbations in the Galactic disk may create overdensities that are gravitationally unstable leading to the formation of molecular clouds (see e.g. Goldreich & Lynden-Bell (1965) and (Julian & Toomre 1966)). Spiral arm regions are more susceptible to the creation of instabilities as they are denser than the inter-arm areas. In simulations with a grand design pattern, the gas travelling through the spiral arms is shocked and compressed, leading to gravitational collapse and formation of molecular clouds (Kim & Ostriker 2002, 2006). However Dobbs et al. (2008) argue that ISM compression caused by spiral shocks and orbit crowding may be sufficient to create molecular clouds in the absence of high gas surface densities.

3. **Spiral-Arms**:
   Spiral arms are density waves that travel around the galactic disk. The gas entering the spiral arm is compressed and able to cool down to form H_2 and molecular clouds that eventually will leave the spiral arm (Dobbs et al. 2006; Agertz & Kravtsov 2015).

1.3.4 Taxonomy

There are various ways of characterising molecular gas into different features (e.g. Draine 2011; Stahler & Palla 2008). In this thesis we will use the following classification.

1. *Star Forming Clump*: Dense self gravitating structure in a molecular cloud where protostars are formed (~ 0.2 pc).

2. *Molecular Cloud (MC)*: Small dense mass of molecular gas (~ 10 pc).

3. *Giant Molecular Cloud (GMC)*: Large dense molecular cloud, that may consist of different smaller molecular clouds (~ 100 pc).

4. *Giant Molecular Association (GMA)*: Group of different GMCs (≥ 100 pc).

For this thesis we will simulate GMCs extracted from galactic scale simulations. These GMCs evolve forming MCs with clumps in their interior. In our simulations the sink particles have the size of a typical clump, and therefore they constitute our resolution limit.

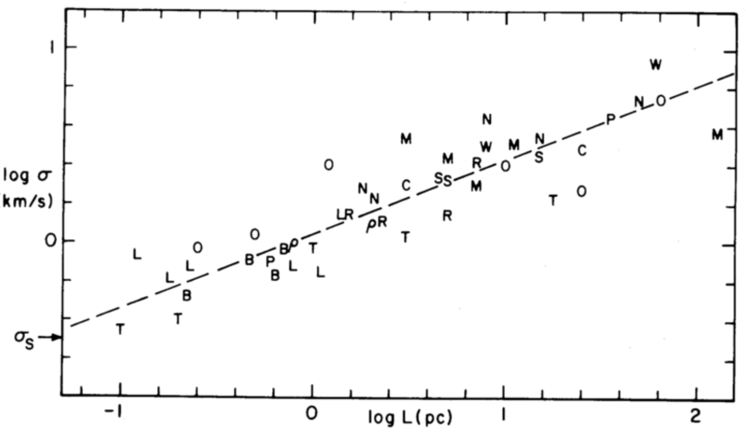

Figure 1.8: Velocity dispersion plot versus size of several molecular clouds, from Larson (1981).

1.3.5 Properties

Larson (1981) discovered correlations between the velocity dispersion and other properties of molecular clouds, defining three scaling relationships (Heyer et al. 2009).

1. The velocity dispersion (σ_v) of the cloud and its size (L) are related: $\sigma_v \propto L^{0.38}$.
2. The gravitational state of the cloud is close to equilibrium: $2\sigma_v L^2/GM \sim 1$.
3. An inverse relationship between the average density (n) and the size of the cloud: $n \propto L^{-1.1}$.

These relationships indicate that the physical properties of the clouds like the velocity dispersion, density or gravitational state depend on the size of the cloud. The first one indicates that turbulence is important when forming molecular clouds, as Larson (1981) claims that the exponent of the relation is comparable with Kolmogorov turbulence. In Fig. 1.8 we present the original plot included in Larson (1981) where the velocity dispersion of a set of molecular clouds is shown versus their observed sizes. The velocity dispersion grows with the size of the cloud, and the letters determine the cloud complex (O for Orion, T for Taurus etc.). The second relationship, implies the mass of a molecular cloud is related also with the velocity dispersion. From this relations Larson (1981) claims that molecular clouds are gravitationally bound. The last relationship comes as a consequence of the first two, if for a given velocity dispersion we have a value for the size and the mass of the cloud, then we also have a value for the density. These empirical relationships were later confirmed by other works such as Solomon et al. (1987). Another consequence of these relationships is that the clouds will have a constant surface density independent of their size (Heyer et al. 2009). This implies that the density is inversely proportional to the size of the cloud, making smaller clouds denser than the large GMCs.

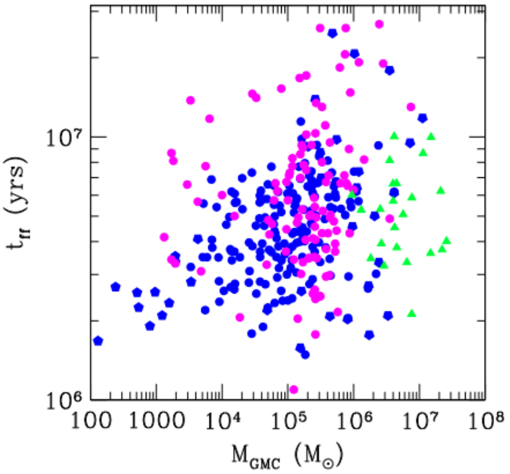

Figure 1.9: Free fall time from different GMCs (Agertz & Kravtsov 2015). The blue circles are GMCs from Heyer et al. (2009), and the blue pentagons are from Murray (2011). The magenta circles are GMCs from nearby galaxies (including the Milky Way) from Bolatto et al. (2008). Lastly the green triangles are GMCs in M64 from Rosolowsky & Blitz (2005).

1.3.6 Lifetime of Clouds

There is a substantial debate about the age of molecular clouds. If clouds are assumed to collapse under their own gravity, then they would be expected to last a free fall time (See Section 1.4). Some authors consider that this is the case (Hartmann et al. 2001; Elmegreen 2007). For a GMC with an average density $n_{\rm H} \sim 100$ cm^{-3} the free fall time (defined later in this chapter) is approximately $t_{\rm ff} \sim 5$ Myr. In Fig. 1.9 from Agertz & Kravtsov (2015) we show the different $t_{\rm ff}$ of clouds with different masses from our Galaxy and others. Most GMCs included in the figure have free fall times smaller than 10 Myr, even the large GMCs (with masses over 10^6 M$_\odot$).

In a scenario where molecular clouds survive much longer than 2 - 3 t$_{\rm ff}$, we need to find some extra force to support them e.g. magnetic fields or turbulence. Many GMCs present CO linewidths that indicate a turbulent state able to support the clouds (Murray 2011). However, this turbulence will dissipate in a dynamical time (Mac Low 1999; Ostriker et al. 2001). The dynamical time of the cloud can be approximated by its crossing time $t_{\rm cross} = L_{\rm cl} / \Delta v$, where $L_{\rm cl}$ is the size of the cloud and Δv the velocity dispersion. For the typical values of a GMC $t_{\rm cross} \sim t_{\rm ff}$, hence the turbulence will dissipate quickly, unless the turbulence is continuously driven. Bot et al. (2007) study GMCs in the Small Magellanic Cloud, and claim that the turbulence of those GMCs is not enough to support them and a magnetic field of ~ 15 μG is the extra source of support. According to Elmegreen (2000) star formation occurs quickly ($\sim$ 1 - 2 $t_{\rm cross}$) although Murray (2011) argues that stellar feedback disrupts the clouds injecting extra energy, and may be enough to explain clouds with ages greater than 2 - 3 $t_{\rm ff}$. In a recent study surveying molecular clouds in the interarm regions of M51, Meidt et al. (2015) find they have short lives (20 - 30 Myr). This is in accordance with the simulated clouds in Dobbs et al. (2014a). In Fig. 1.10 we show the evolution over 40 Myr of a GMC in a simulated galaxy from its creation in a spiral arm, until it is dispersed.

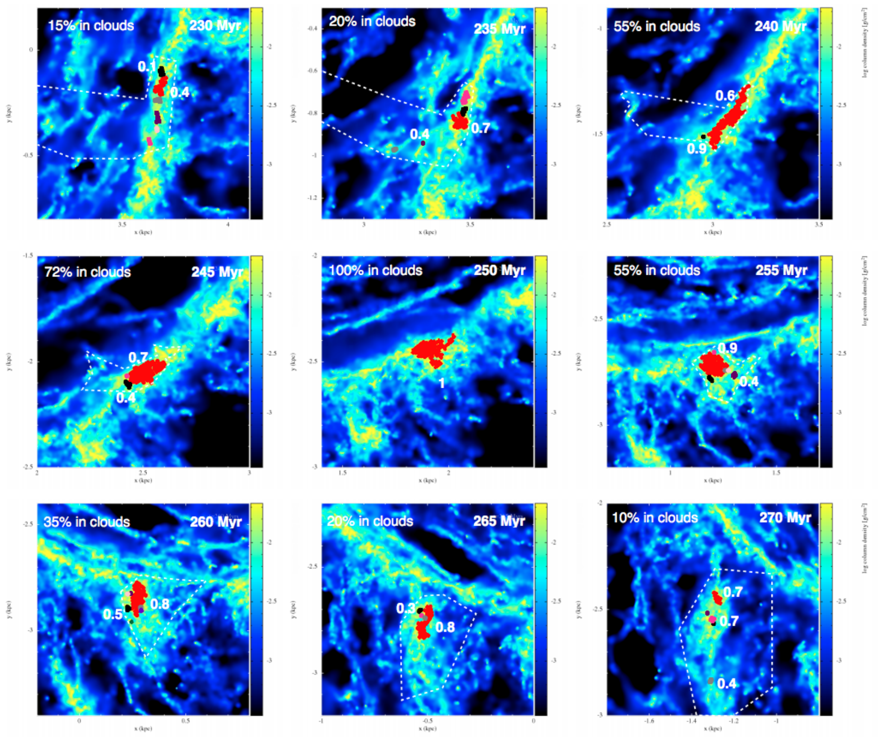

Figure 1.10: Column density evolution of a galactic molecular cloud (from Dobbs & Pringle 2013).

However, as we can observe from the sequence of images, it is difficult to define the exact moment when the cloud is created and dispersed.

1.3.7 Galactic Influence

Molecular clouds are not isolated entities. They are born in a galaxy, they evolve, produce stars and eventually die by being dispersed, they collide with other clouds or are absorbed by a spiral arm (Dobbs et al. 2014b). The idealised picture of a star-forming molecular cloud is an isolated turbulent mass of gas that collapses because it is Jeans unstable. However, galactic simulations have shown that molecular clouds are transient beings that evolve and have complex histories (e.g. Dobbs et al. 2006; Hopkins et al. 2011; Agertz & Kravtsov 2015), where it is difficult to elucidate the exact moment when a cloud is born or dispersed (Dobbs & Pringle 2013), or even the boundaries and structure of a given cloud.

In Fig. 1.10 (from Dobbs & Pringle 2013) we show the column density evolution of a molecular cloud that is created in a spiral arm and detaches from the arm at later times. On each tile, the fraction of the gas that forms the cloud at that time compared to the cloud at 250 Myr is also shown. From this figure we observe that it is not easy to strictly define the spatial and temporal boundaries of the cloud. Collisions between clouds seem to be frequent (Dobbs et al. 2014b), so during its lifetime a cloud may interact with others, different from the idealised picture of an isolated cloud.

The evolution of molecular clouds may also depend on the position of the cloud in the galaxy. The Galactic Centre is a hostile environment with strong tidal forces from Sgr. A (Kruijssen et al. 2014). Galaxies are not isolated objects either, they have a dark matter halo that may also affect the star formation process (Renaud & Gieles 2015) or they may interact with other galaxies via tidal forces or mergers (Renaud et al. 2014; Hopkins et al. 2013).

The main problem with modelling the large-scale effects on the star formation process is resolution. The final stages of star formation occur at scales of ~AU, which are 8 orders of magnitude smaller than the typical galactic scale (~ kpc). With the current computers, the best full-scale galactic simulations have a resolution of ~ pc, but in order to study the local effects of stellar feedback we need to reach sub-pc scales.

1.4 Formation of Stars

An overall picture of star formation has been long established (e.g. Shu et al. 1987, and references therein). Stars are formed in the densest parts of the molecular clouds. In these dense clumps molecules are formed protected, from external UV radiation. These parts collapse under their own gravity forming a protostar with a protoplanetary disk, resulting from the conservation of angular momentum. In this thesis we are interested in the interaction between molecular clouds and stars at scales of ~ 100 - 0.1 pc. We analyse how the gas collapses forming protostellar cores (which is our resolution limit) and the effect that the stellar feedback has on the surrounding molecular cloud. Individual protostars, binaries and disks are beyond our resolution.

To quantify the interplay between gravity, turbulence and other relevant processes that lead to the formation of a star, we use a number of physical quantities. The Jeans Mass represents a measure of the ability of a spherical mass of gas to collapse. A mass of ideal gas at a given temperature may be unstable (and therefore collapses) if its temperature is too low and therefore the thermal pressure is unable to give support to the gas, or the density too high and gravity is powerful enough to induce collapse. This instability is called the Jeans Instability (Jeans 1902). The Jeans mass (M_J) is defined as (Draine 2011):

$$M_J = \left(\frac{\pi k_B T}{Gm}\right)^{3/2} \frac{1}{\rho_o^{1/2}}, \tag{1.3}$$

where k_B is the Boltzmann constant, T the absolute temperature of the gas, m the mass of a molecule of the gas and ρ_o the average density of the cloud. It is worth noting that neither the temperature of the gas or the density of the cloud remains constant through the process of star formation. As the gravitational collapse progresses the cloud gets colder and denser and both effects reduce the Jeans Mass for that cloud.

The Jeans instability constitutes an oversimplified picture of the star formation process, as Jeans did not include on his analysis others sources of pressure that oppose the gravitational field such as magnetic fields or turbulence. We are also making strong assumptions such as the absence of gradients from external forces ($\nabla\phi = 0$). However, the Jeans mass constitutes a good estimate for gravitational collapse. For instance, if we substitute typical values for a core: $T = 10$ K and $\rho_{\rm o}$ = 10^5 part cm^{-3} (Stahler & Palla 2008), then we obtain a value for the Jeans mass of $M_J \sim 2$ M$_\odot$, which is reasonable considering the crudeness of the analysis.

Apart from the Jeans Mass, there is another important parameter that we will use to characterise and model our different clouds. This parameter is called the virial parameter, a dimensionless quantity that gives us an idea of how gravitationally bound is a mass of gas, by comparing the magnitudes of the kinetic and gravitational energy of the gas. It is often referred to as α (e.g. Dobbs et al. 2011a):

$$\alpha \equiv \frac{5R\sigma_v^2}{GM}, \tag{1.4}$$

where σ_v is the dispersion of velocities, M the mass of the cloud, and R its radius. A cloud is considered virialised if $\alpha \sim 1$, and totally unbound if $\alpha > 2$.

Lastly, to provide a time scale of the gravitational collapse, it is very common to use the free fall time $t_{\rm ff}$. The free fall time is defined as the time that it will take for a gaseous body to collapse on itself (Stahler & Palla 2008) and it is commonly written as

$$t_{\rm ff} = \sqrt{\frac{3\pi}{32G\rho_{\rm o}}}. \tag{1.5}$$

1.4.1 Star Formation Efficiency: Schmidt-Kennicutt Relation

Schmidt (1959) found an observational relation between the surface density of gas of the Galaxy ($\Sigma_{\rm gas}$) and the Star Formation Rate (SFR) surface density ($\Sigma_{\rm SFR}$):

$$\Sigma_{\rm SFR} = A\,\Sigma_{\rm gas}^{\rm N}, \tag{1.6}$$

where A is a constant, and N a positive exponent. This relation implies that the rate at which stars are produced is correlated with the concentration of gas in the disk of the galaxy. We find in the literature different values for N, all ranging between sublinear values $N < 1$ (Shetty et al. 2013), linear $N \approx 1$ (Bigiel et al. 2008) to super-linear $N \approx 2$ (Narayanan et al. 2012). In Fig. 1.11 we show a sample of different galaxies including normal disks and starburst galaxies, with a fitted line using least squares and a value of $N = 1.4$ from Kennicutt (1998).

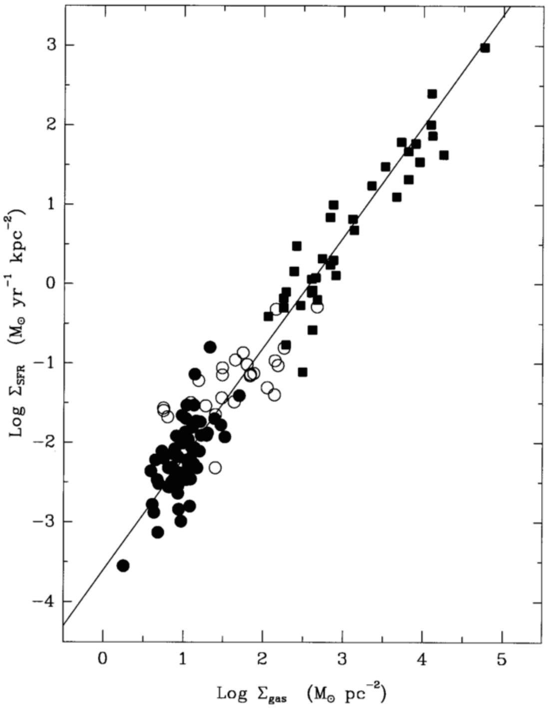

Figure 1.11: Schmidt-Kennicutt Relation from Kennicutt (1998) for different galaxies. The filled circles correspond to data from the normal galaxy disks, open circles the SFRs for the centres of normal disk galaxies, and the squares the starburst samples.

Heiderman et al. (2010) study the SFR and gas surface densities using young stellar objects and massive dense clumps in the Galaxy. They discovered that the SFR for these objects present higher values for the equivalent mass of gas than Kennicutt (1998) or Bigiel et al. (2008). Momose et al. (2013) study sub-pc structures in nearby galaxies, and found that if they extract the background from the sources, the exponent for the Schmidt-Kennicutt Relation raises from a value of $N = 1.3$ to $N = 1.8$. These two studies suggest that the Schmidt-Kennicutt Relation changes at sub-pc scales, specially in star forming clumps where the SFR is high. They both mention the difficulties of using tracers for the molecular gas, as they may introduce additional biases to the observations.

If we consider that most of the molecular gas available is transformed into stars, the star formation rates would be at least one order of magnitude higher than the ones observed in the Galaxy (Zuckerman & Evans 1974) and in nearby galaxies (Bigiel et al. 2008). Krumholz et al. (2005) consider that turbulence controls the star formation rate, assuming that all the gas compressed by turbulence above a certain density threshold will collapse and create stars. Other authors point out that strong magnetic fields (Allen & Shu 2000; Padoan & Nordlund 2011; Vázquez-Semadeni et al. 2011), or stellar feedback (Hopkins et al. 2011; Dobbs & Pringle 2013) may reduce the star formation efficiency. Simulations of molecular clouds (Clark & Bonnell 2004, 2005) and galaxies (Dobbs et al. 2011a) suggest that clouds are not globally bound, and thus have lower star formation efficiencies. There is also the possibility that galactic scale effects acting on the clouds may also change the way molecular clouds produce stars (Renaud et al. 2013). The reality is that all these processes may act together opposing gravitation.

1.4.2 Stellar Feedback

By stellar feedback we mean a set of various physical processes resulting from stellar evolution and that affect the ISM in different ways. Stellar feedback comprises stellar winds, radiation, supernovae, jets and stellar outflows.

If stellar feedback is sufficiently powerful, then the creation of new stars may be impeded. Divergent flows of matter (or radiation) from feedback may prevent further gravitational collapse, by injecting kinetic or thermal energy. This is commonly referred to as *destructive feedback*. On the other hand, stellar feedback could in some cases trigger star formation as the expanding shells may create overdense areas where new stars are created. This is referred to as *constructive feedback*.

Ionisation and Radiation from Massive Stars

Massive stars emit highly energetic photons able to ionise hydrogen. Strömgren (1939) studied for the first time the effect of highly energetic photons in the vicinity of massive stars (for a more recent review see Osterbrock & Ferland (2006) or Draine (2011)). The radiation dissociates the molecules in the envelope and ionises the resulting hydrogen atoms. The photons move forward in what is called the ionisation front, and they are consumed on each ionisation event. At some point, the rate of ionisations equals the recombination rate (the free electrons and hydrogen nuclei recombine via collisions), and the front is unable to move forward. The resulting sphere is called the Strömgren sphere.

Inside the sphere the temperature of the ionised gas is given by the heating/cooling processes. Apart from the hydrogen there are other metals (e.g. O and C) in the medium that are able to cool down the temperature of the gas. The temperature range for the ionised gas is 8000 - 10000 K, although this depends on the metallicity of the parental cloud (Haworth et al. 2015). The vast difference in temperature between the ionization front and the surrounding molecular environment ($T < 100$ K) causes the gas inside to expand supersonically heating up the surrounding medium. Some authors (Dale & Bonnell 2012; Walch et al. 2012) argue that ionisation is the most important feedback mechanism, able to destroy star forming regions .

Radiation from massive stars may also affect the ISM by injecting momentum to the gas particles. The gas absorbs the high energy photons from the stars, acquiring their momentum (the low energy photons interact mainly with the dust) and producing radiation-driven winds. Radiation pressure may disrupt clusters, even causing galactic winds (Murray 2011; Hopkins et al. 2012,

Figure 1.12: Star forming region NGC602 in the LMC (Gouliermis et al. 2012)

and subsequent works).

Stellar winds

In Figure 1.12 from Gouliermis et al. (2012) we observe a region of a molecular cloud forming stars and affected by stellar feedback. The young central cluster of stars has been formed in the last 5 Myr. This central cluster of stars was created from a previous molecular cloud which was rapidly dispersed by the wind emitted by the newly born stars. Strong hot winds sweep up the ISM creating a void structure or cavity, which is clearly visible in the picture. The shocked shell compresses the surrounding ISM triggering new star formation at its boundaries. In this case, Gouliermis et al. (2012) have identified 13 extra sub-clusters in the periphery of the region.

Shells and cavities similar to the one shown in Fig. 1.12 are abundant in our Galaxy. The Galactic Legacy Infrared Mid-Plane Survey Extraordinary (GLIMPSE) has surveyed 2/3 of the Galactic plane at IR wavelengths from 3.6 to 8.0 μm (Churchwell et al. 2006). In this catalogue there are more than 300 of these objects in our Galaxy. In Churchwell (2008) they consider these cavities created around O/B stars to have a central component of low density gas that is evacuated by the hypersonic wind coming from the star that forms the wind blown bubble (WBB). Surrounding the hypersonic winds there is a very hot region at temperatures able to ionise hydrogen ($T > 10^4$ K), and dominated by the pressure created by the shocked winds, that occupy the majority of the bubble. Then in the outer parts of the cavity where the hot gas meets the cold ISM, the hot gas starts ionising the ISM forming a dense shell of photoionised material or Photodissociation Region (PDR). A diagram illustrating the combined effects of winds and radiation feedback

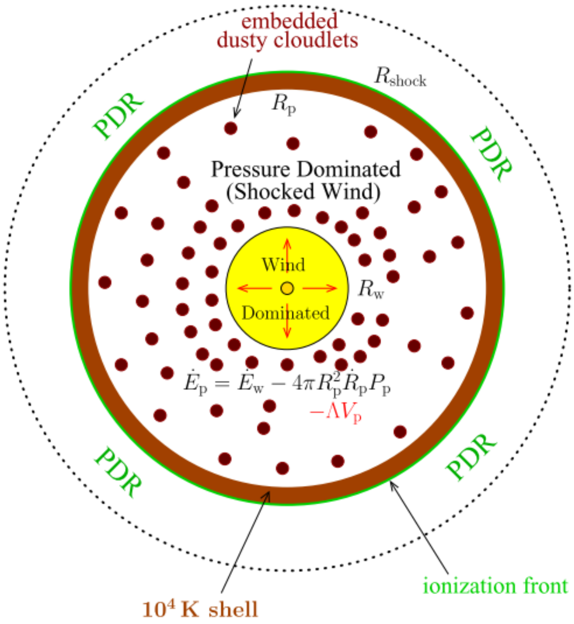

Figure 1.13: Schematics of a Wind Blown Bubble from Everett & Churchwell (2010)

is shown in Fig. 1.13.

Supernovae

Supernovae (SNe) constitute the most energetic feedback process in the ISM (Hensler 2010). When a very massive star dies, it injects momentum and thermal energy into the ISM heating it up. They produce the hottest phase in the ISM with temperatures of the order of $T \sim 10^6$ K (McKee & Ostriker 1977) providing an extra source of pressure for the ISM. There are two main types of SNe. The first kind (Type I SN) occurs in binary systems where at least one of the components is a very compact object (such us a white dwarf). The second kind (Type II SN) happens at the end of the life of a very massive star (> 8 M$_\odot$), when the thermal pressure produced by the nuclear reactions is no longer able to prevent gravitational collapse. Both types of SNe can be modeled using 4 phases (Draine 2011):

1. *Free expansion phase*: This phase lasts $\sim 10^2$ years and consists of very dense material expanding ballistically in the ISM at velocities much higher than the speed of sound. When the pressure of the shocked front exceeds the pressure of the ejecta, a reverse blastwave is also created.
2. *Sedov-Taylor phase*: In this phase that lasts over a period of $\sim 10^4$ years, the SNR behaves like a point source of energy left in a dense uniform medium of very low temperature, and modelled by a Sedov-Taylor explosion. In the late stages of this phase the hot gas of the interior cools emitting radiation.

3. *Snow-Plough phase*: After the Sedov-Taylor phase, the external parts of the SNR have cooled down, and they are practically at the same temperature as the surrounding ISM. However, the hot gas in the interior pushes out this cold perimeter acting like a snow-plough. This phase lasts until $\sim 10^5$ years after the explosion.

4. *Fadeaway phase*: In this phase the SNR becomes as cold as the surrounding ISM.

In addition to the injection of energy and momentum to the ISM, the SNe events increase the metallicity of the surrounding medium, as the heavier elements processed in the interior of the exploding star are expelled into the ISM. Both the Sedov-Taylor and the Snow-Plough phase are the most relevant to the timescales of our study.

Protostellar Outflows

Protostellar outflows are created in the early phases of star formation. They result from the interaction of the protostellar disk and the protostar, modifying the surrounding magnetic field that acts like a particle accelerator or collimator (see simulations by Lewis et al. 2015).

The scale of the protostellar outflows is of the order of ~0.1 pc (Duarte-Cabral et al. 2012), and thus they are not so relevant to the scale of our simulations. However, they are very important in sub-pc scales as they may be the responsible for clearing the protostellar envelope (Arce et al. 2010), and in highly populated clusters the protostellar flows of a star may affect its neighbours (Krumholz et al. 2014). They are also relevant in the absence of massive stars, as in this scenario they would constitute the only source of feedback.

1.5 Outline of Thesis

Our goal is to produce simulations from molecular clouds extracted from galactic models to study the combined effect of the galactic environment and stellar feedback on the star formation process. The rest of this thesis is organised as follows: In Chapter 2, we explain our numerical method for reproducing clouds extracted from galactic simulations, and how we resimulate them. We test how these clouds compare with other methods used in the literature, and we evaluate the advantages of using galactic clouds in Chapter 3. We include the effects of a multiphase ISM and the chemistry of H_2 and CO in Chapter 4, where we also produce synthetic observations of the galactic clouds. In Chapter 5 we include the effect of winds and SNe in our simulations. Lastly, in Chapter 6 we summarise our conclusions and point out directions that our future work could take.

2

Modelling Galactic Molecular Clouds in SPH

"Divide each difficulty into as many parts as is feasible and necessary to resolve it."
– Rene Descartes

2.1 Hydrodynamical Simulations

It is difficult to think that water is made of discrete particles if we observe the waves on the beach or a river flowing through a valley. Fluids behave as continuous entities that move and evolve *smoothly*. In fact, hydrodynamics was developed before the modern atomic theory was created, and it was some decades after the foundations of quantum theory were set, that a proper quantum description for a fluid was proposed. For the sake of this thesis the classical Newtonian description of a fluid, developed in the CXVIII and CXIX by Bernouilli, Euler, Navier and Stokes, is sufficient, although we follow a semiclassical approach when treating the ISM chemistry and cooling and heating.

According to the classical theory, the flow of a fluid is described by the Navier-Stokes equations. The first equation assures the conservation of matter in a fluid. If ρ is the density and $\vec{u}$ is the velocity field then

$$\frac{\partial \rho}{\partial t} + \nabla \cdot (\rho\, \vec{u}) = 0. \tag{2.1.1}$$

The second equation represents the conservation of momentum in the system

$$\rho \left(\frac{\partial \vec{u}}{\partial t} + \vec{u} \cdot \nabla \vec{u} \right) = -\nabla P + \mu \nabla^2 \vec{u} + \frac{1}{3} \mu \nabla (\nabla \cdot \vec{u}) + \rho \vec{g} + \sum_i f_i, \tag{2.1.2}$$

where μ is the viscosity of the fluid, $\vec{g}$ is the acceleration due to gravity, and f_i are any other

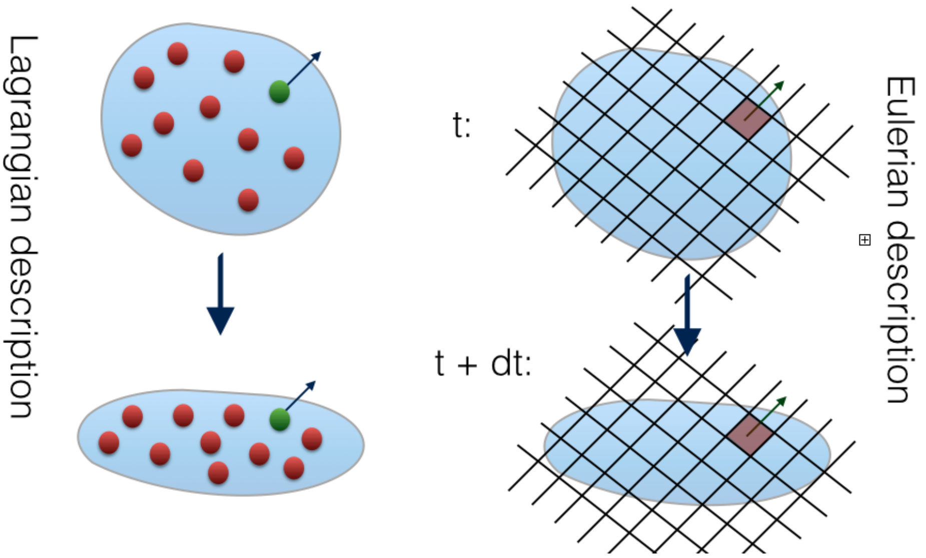

Figure 2.1.1: Evolution of the same parcel of fluid using Lagrangian and Eulerian description. After a small period of time dt, the parcel of fluid changes its shape. The fluid is the same in both cases. The Lagrangian description follows the particles over their evolution calculating the physical properties of each particle. The Eulerian study the properties of the fluid at certain localizations, in this case represented by the cells of a grid.

forces acting on the system. This equation expresses the change in the momentum of the fluid due to hydrostatic pressure (∇P), viscosity due to shear and compression (the two terms with the factor μ), gravity and other external forces. The third Navier-Stokes equation describes the conservation of energy

$$\rho\left(\frac{\partial e}{\partial t} + \vec{u}\cdot\nabla\vec{e}\right) = -P\nabla\vec{u} - \nabla\cdot\vec{q} + \sum_{j=1}^{3}\sum_{i=1}^{3}\tau_{ij}\frac{\partial u_i}{\partial x_j}, \tag{2.1.3}$$

where e is the energy, $P\nabla\vec{u}$ represents the hydrostatic work done on the system, $\vec{q}$ is the heat flow on the surfaces of the system, and the last term is the energy loss due to the viscous stress tensor τ_{ij}. This tensor is defined for a Newtonian fluid as follows:

$$\tau_{ij} = \mu\left(\frac{\partial u_i}{\partial x_j} + \frac{\partial u_j}{\partial x_i} - \frac{2}{3}\sum_{k=1}^{3}\frac{\partial u_k}{\partial x_k}\delta_{ij}\right). \tag{2.1.4}$$

To solve these complex second order coupled differential equations, we need to use numerical methods. Within the whole range of different computational schemes to solve the Navier-Stokes equations there are two big families of algorithms, Lagrangian and Eulerian. The Lagrangian algorithms follow the trajectories of the fluid elements, whereas the Eulerian study the variation of the physical properties of the fluid at certain locations.

In Fig. 2.1.1 we represent a small parcel of fluid that changes in time. On the left, we show the Lagrangian evolution, following the fluid particles that constitute the fluid during their evolution over time. On the right, we have the same parcel, but this time, as we are using an Eulerian method, we are computing the relevant fluid quantities at certain points represented here by the grid.

Each method has its advantages and disadvantages. For instance, the Eulerian grid introduces constraints on the geometry of the model. If the phase space changes dramatically with time, the current grid could not be used for the simulation. Therefore, it requires a huge computational effort to recalculate the grid on each timestep. On the other hand, implementing stellar feedback, or other physical phenomena that depend on vicinity, is less complicated for Eulerian algorithms, as we can readily find the adjacent cells (in a Lagrangian code we need to search for the particles that are nearby).

In Lagrangian codes we follow the evolution of particles as they evolve in the phase space and we are not restricted to the geometry of a grid. This represents an advantage for simulations that evolve into complicated structures and morphologies. Lagrangian algorithms have another advantage, as they follow the particles in their evolution, points in space with no particles require no computational time. Tracking the different flows in the simulations requires introducing 'test' particles, whereas it is done naturally in Lagrangian codes. In Eulerian codes if we have a void cell, we still have to solve the equations for that cell. On the other hand, many Lagrangian algorithms have problems when resolving shocks and complex fluid interfaces, needing to include additional terms to model those correctly.

To bridge the gap between these two families, in recent times, hybrid algorithms have been developed. These methods consider a grid of moving and changing cells (tessellation) created using special schemes, such as Voronoi tessellation (Okabe et al. 2000). These moving cells or *tessellae* (from the latin word of small tile) cover the whole phase space as tiles on a wall, with the advantage that these tiles can change in shape, size and position, following the fluid during its evolution. Each tessella has interfaces with its neighbours like a grid code, but because it is able to move, it provides a grid more flexible than a pure Eulerian code. These codes (e.g.AREPO, see Springel (2009)) represent an improvement with respect to Lagrangian codes when modeling interfaces of fluids, like the Kelvin-Helmholtz instability and improving with respect to Eulerian codes as the grid is now formed by small tessellae that may evolve into very complicated morphologies. One problem with this hybrid approach is that it requires extra computational effort. Computing the Voronoi tessellation on each timestep can be very demanding and may result in increased simulation times. These codes also need to include additional tracer particles to follow the evolution of the fluid.

For this thesis we use a Lagrangian code, that uses Smoothed Particle Hydrodynamics (SPH), and we illustrate the details in the rest of this chapter. We start by defining the fundamentals of SPH, and describe the particularities of the version of GADGET2 that we have used. After that, we detail how we increase the resolution of a given molecular cloud .

2.2 Fundamentals of Smoothed Particle Hydrodynamics

2.2.1 Introduction

Smoothed Particle Hydrodynamics SPH is a widely used Lagrangian algorithm, both in Astrophysics (Springel 2005; Bate et al. 1995; Hubber et al. 2011; Price & Federrath 2010) and in applied Sciences (Solenthaler & Pajarola 2009; Bonet & Kulasegaram 2000). It was introduced in the late 70's simultaneously by Lucy (1977) and Gingold & Monaghan (1977). The core of SPH is the interpolation of a function at a given point in space by summing over the surrounding particles.

Any continuous function A($\vec{r}$) can be written as

$$\langle A(\vec{r})\rangle = \int A(\vec{r}\,')\, W(\vec{r}-\vec{r}\,', h)\, d\vec{r}\,', \tag{2.2.1}$$

where W is an interpolation kernel, and the integration is over the solution domain. In SPH, W is typically known as the smoothing kernel, and h is called the smoothing length (Monaghan 1992) and represents a measure of the width of the smoothing kernel[1]. The kernel function W has to satisfy a series of conditions, so that $\langle A(\vec{r})\rangle$ represents accurately $A(\vec{r})$. First, it has to be a well behaved function and at least have defined first derivatives. W also needs a unique maximum at $\vec{r} = \vec{r}\,'$ and to be monotonically decreasing in every direction from that point. W also has to satisfy the following normalization condition

$$\int W(\vec{r}-\vec{r}\,', h)\, d\vec{r}\,' = 1. \tag{2.2.2}$$

Lastly, in the limit of null smoothing length

$$\lim_{h\to 0} W(\vec{r}-\vec{r}', h) = \delta(\vec{r}-\vec{r}\,'). \tag{2.2.3}$$

thus $\langle A(\vec{r})\rangle = A(\vec{r})$ in this limit. In SPH we discretise fluids by using particles to represent them. If we denote by N the total number of particles in the simulation we can transform the integral in Eq. 2.2.1 into a discrete sum

$$\langle A(\vec{r})\rangle = \sum_j^N m_j \frac{A_j}{\rho_j} W(\vec{r}-\vec{r_j}, h), \tag{2.2.4}$$

where the summation is over all the SPH particles, and we have used the density and the mass of the particles to produce an averaged sum. Now, we can define the magnitude A at any point in the space, for a discretised representation of the fluid. If $A = \rho(\vec{r})$ it is trivial to show that the density is calculated as

$$\langle \rho(\vec{r})\rangle = \sum_j^N m_j W(\vec{r}-\vec{r_j}, h). \tag{2.2.5}$$

By requiring the kernel W to have well defined first derivatives, this allows us to calculate

---

[1] Throughout this chapter we will use bracketed notation to represent the kernel averaged magnitudes.

the gradient of any field A. If we differentiate Eq. 2.2.4 we obtain

$$\langle \nabla A(\vec{r}) \rangle = \sum_j m_j \frac{A_j}{\rho_j} \nabla W(\vec{r} - \vec{r}_j, h). \tag{2.2.6}$$

This represents a large boost in speed as $\nabla W(\vec{r} - \vec{r}_j, h)$ can be calculated in advance and be stored in a table, and be used subsequently to calculate the derivatives of any physical variable.

2.2.2 The SPH Momentum Equation

In many occasions it is useful in SPH to compute the physical quantities by including the density in the calculations. For example we can apply the chain rule as follows,

$$\nabla \cdot (\rho \vec{u}) = [\vec{u} \cdot \nabla \rho + \rho \nabla \cdot \vec{u}], \tag{2.2.7}$$

and rearrange terms so that

$$\nabla \cdot \vec{u} = [\nabla \cdot (\rho \vec{u}) - \vec{u} \cdot \nabla \rho] \,/\rho. \tag{2.2.8}$$

For integrating Eq. 2.1.2, we need to calculate the gradient of the hydrostatic pressure. We can rewrite this as

$$\frac{\nabla P}{\rho} = \nabla \left(\frac{P}{\rho} \right) + \frac{P}{\rho^2} \nabla \rho. \tag{2.2.9}$$

Thus we have in SPH form

$$\left\langle \frac{\nabla P}{\rho} \right\rangle_i = \sum_j^N \frac{1}{\rho_j} m_j \frac{P_j}{\rho_j} \nabla_i W_{ij} + \frac{P_i}{\rho_i^2} \sum_j^N m_j \nabla_i W_{ij} = \sum_j^N m_j \left[\frac{P_i}{\rho_i^2} + \frac{P_j}{\rho_j^2} \right] \nabla_i W_{ij} \tag{2.2.10}$$

where $\nabla_i W_{ij}$ refers to the gradient of $W(\vec{r}_i - \vec{r}_j, h)$ calculated in the coordinates of particle i. Now, considering Eq. 2.1.2 and using no viscosity, gravity or external forces ($\mu = 0$, $\vec{g} = 0$ and $f_i = 0$)

$$\left(\frac{\partial \vec{u}}{\partial t} + \vec{u} \cdot \nabla \cdot \vec{u} \right) = -\frac{\nabla P}{\rho}. \tag{2.2.11}$$

Combining Eq. 2.2.11 and 2.2.10 gives

$$\left\langle \frac{D\vec{u}_i}{Dt} \right\rangle = -\sum_j m_j \left(\frac{P_j}{{\rho_j}^2} + \frac{P_i}{{\rho_i}^2} \right) \nabla_i W(\vec{r}_{ij}, h), \tag{2.2.12}$$

where we use the traditional notation for $r_{ij} = \vec{r}_i - \vec{r}_j$ and the Lagrangian derivative is

$$\frac{D\vec{A}}{Dt} = \left(\frac{\partial \vec{A}}{\partial t} + \vec{u} \cdot \nabla \cdot \vec{A} \right). \tag{2.2.13}$$

2.2.3 The SPH Energy equation

If the fluid has no viscosity ($\tau_{ij} = 0$ for all i,j), and there is no heat exchange ($\vec{q} = 0$) the change of thermal energy per unit mass for a gas can be written as

$$\frac{De}{Dt} = -\left(\frac{P}{\rho}\right)\nabla \cdot \vec{u}, \tag{2.2.14}$$

and in its discrete version for a particle i as

$$\left\langle\frac{De}{Dt}\right\rangle_i = -\left(\frac{P_i}{\rho_i^2}\right)\sum_j^N m_j \vec{u}_{ij} \cdot \nabla_i W_{ij}, \tag{2.2.15}$$

where $\vec{u}_{ij} = \vec{u}_i - \vec{u}_j$. However this equation is not symmetric with respect to a change in particles (i and j). However if we instead express the right hand side of Eq. 2.2.14 as

$$\frac{De}{Dt} = -\nabla\left(\frac{P\vec{u}}{\rho}\right) + \vec{u} \cdot \nabla\left(\frac{P}{\rho}\right), \tag{2.2.16}$$

using Eq. 2.2.10 and discretising the first term of the right hand side we can derive the thermal energy for the particle i as

$$\left\langle\frac{De}{Dt}\right\rangle_i = \sum_j^N m_j \left(\frac{P_j}{\rho_j^2}\right)\vec{u}_{ij} \cdot \nabla_i W_{ij}. \tag{2.2.17}$$

By taking the average of Eqs. 2.2.17 and 2.2.15 we obtain

$$\left\langle\frac{De}{Dt}\right\rangle_i = \frac{1}{2}\sum_j^N m_j \left(\frac{P_j}{\rho_j^2} + \frac{P_i}{\rho_i^2}\right)\vec{u}_{ij} \cdot \nabla_i W_{ij}. \tag{2.2.18}$$

2.2.4 Smoothing Length and Density

We study the effect of the different smoothing lengths in Fig. 2.2.1. We show the density of a simple mass field (two masses $m_1 = 1$ and $m_2 = 0.75$ situated at $x_1 = 0.3$ and $x_2 = 0.5$) for different smoothing lengths h and using the cubic kernel (Eq. 2.3.3). For the biggest smoothing length ($h = 0.5$ in black) the density field is not able to resolve the presence of two particles. Higher resolution (or smaller h) is needed to discriminate between the two masses. It is also important to note how the height of the peaks increases as the width is reduced, and the particles are resolved. This is because of the normalization condition of the smoothing kernel (Eq. 2.2.2). The total area comprised by the density function has to be equal to the total mass of the distribution. In the limit $h \to 0$ the peaks will be two Dirac's deltas $\delta(x - 0.3)$ and $\delta(x - 0.5)$, with heights weighted according to their masses.

The smoothing length does not need to be fixed for the total simulation space. A variable smoothing length allows a more precise description of denser zones in the fluid. Having a smaller h in the denser areas of the cloud increases the scale range of densities in the simulation while

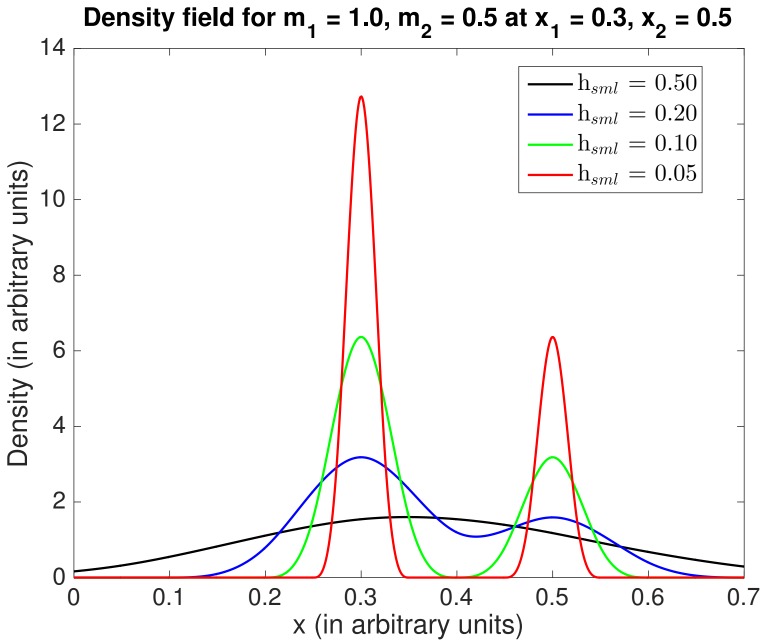

Figure 2.2.1: SPH Density for different smoothing lengths for the case of two masses using arbitrary units. For resolving the position of the two masses a small smoothing length is needed

using the same number of particles. The usual way of calculating the smoothing length for each particle is to define a number of neighbouring particles. Normally, the desired number of neighbours is fixed throughout the simulation.

In the literature there are two equivalent interpretations for SPH related to the smoothing length. The traditional point of view, referred by Hernquist & Katz (1989) as the "scatter" interpretation, considers the mass (and other relevant physical magnitudes) of a SPH particle as scattered around its position accordingly to the smoothing kernel and the smoothing length chosen. This is equivalent to considering the particle to be dispersed according to the smoothing kernel. The other point of view is the "gather" interpretation (also referred to by Hernquist & Katz 1989) where the value of a magnitude at a precise point in space is calculated by sampling all the neighbours using the smoothing kernel as the weighting function.

To calculate the a physical quantity $A(\vec{r})$ in the "scatter" interpretation and variable smoothing length we use the formula

$$\langle A(\vec{r})\rangle = \int A(\vec{r}\,')W(\vec{r}-\vec{r}\,',h'), \tag{2.2.19}$$

which can be discretised to

$$\langle A(\vec{r}_i)\rangle = \sum_j^N m_j \frac{A_j}{\rho_j} W(\vec{r}_{ij},h_j), \tag{2.2.20}$$

where $\vec{r}_{ij} = |r_i - r_j|$ and the value of A is calculated in each point using the respective smoothing length of every other particle. In the "gather" interpretation, the same quantity is computed using the smoothing length of the particle for which A is computed

$$\langle A(\vec{r})\rangle = \int A(\vec{r}\,')W(\vec{r}-\vec{r}\,',h), \tag{2.2.21}$$

which can be discretised to

$$\langle A(\vec{r}_i)\rangle = \sum_j^N m_j \frac{A_j}{\rho_j} W(\vec{r}_{ij},h_i). \tag{2.2.22}$$

In this case the smoothing length used to calculate the density is the one at the sampling point. Smoothing lengths for two given particles are in general different. This means that the force that the particle *i* exerts over the particle *j*, may be different than the force exerted on *i* by particle *j*. This violates Newton's Third Law and may cause problems. To fix this issue the most common approach is to symmetrise the smoothing length by making $h_{ij} = \frac{h_i+h_j}{2}$. For instance Eq. 2.2.6 becomes

$$\langle A(\vec{r})\rangle = \int A(\vec{r}\,')\frac{1}{2}\Big[W(\vec{r}-\vec{r}\,',h(\vec{r})) + W(\vec{r}-\vec{r}\,',h(\vec{r}\,'))\Big]\,d\vec{r}\,'. \tag{2.2.23}$$

For the discretised version of this equation we can define

$$W_{ij/2} = \frac{1}{2}\left[W(r_{ij},h_i) + W(r_{ij},h_j)\right], \tag{2.2.24}$$

and its derivative

$$\nabla_i W_{ij/2} = \frac{1}{2}\left[\nabla_i W(r_{ij},h_i) + \nabla_i W(r_{ij},h_j)\right]. \tag{2.2.25}$$

The density is now defined as

$$\langle \rho(\vec{r}_i)\rangle = \sum_j^N m_j W_{ij/2}, \tag{2.2.26}$$

which is the SPH symmetrised version of the continuity equation (Eq. 2.1.1).

2.2.5 Artificial Viscosity

In the previous formulation there is no impediment for two particles to occupy the same position in space. The major disadvantage of SPH is the need to introduce an artificial viscosity (Π_{ij}) to avoid this, and be able to model shocks and other non linear processes. We introduce this term into Equation 2.2.12 (Monaghan 1992):

$$\frac{D\vec{u}_i}{Dt} = -\sum_j m_j\left(\frac{P_j}{{\rho_j}^2} + \frac{P_i}{{\rho_i}^2} + \Pi_{ij}\right)\nabla_i W(\vec{r}_{ij},h_{ij}). \tag{2.2.27}$$

There are several diverse forms for this artificial viscosity in the literature. The most usual is one that relates the sound speed of the medium to the relative velocity of the particles. It is non zero if particles are approaching

$$\Pi_{ij} = \begin{cases} \dfrac{-\alpha \cdot c_{ij} \cdot \mu_{ij} + \beta \cdot {\mu_{ij}}^2}{\rho_{ij}} & \vec{u}_{ij} \cdot \vec{r}_{ij} < 0, \\ \\ 0 & \vec{u}_{ij} \cdot \vec{r}_{ij} \geq 0 \end{cases} \tag{2.2.28}$$

where α and β are the viscosity parameters and typical values are $\alpha \approx 0.5 - 1.0$ and frequently $\beta = 2\alpha$. c_{ij} and ρ_{ij} are the arithmetic averages of the speed of sound and density for a pair of SPH particles. Finally μ_{ij} is a parameter that depends on the direction of the relative movement between particles, and the smoothing length

$$\mu_{ij} = \frac{h_{ij}\vec{v}_{ij} \cdot \vec{r}_{ij}}{|\vec{r}_{ij}|^2}. \tag{2.2.29}$$

Note that μ_{ij} has the dimensions of a velocity. The addition of this artificial viscosity can change the thermodynamics of the simulation as it acts as a dissipative force that produces heat. However, it is needed to model non linear behaviours that are widely present in the ISM, such as shocks and instabilities.

2.2.6 Timestep and Courant–Friedrichs–Lewy condition

Defining the correct timestep is crucial in numerical integration. A large timestep introduces numerical errors, and when solving some integrals may lead to numerical instabilities. A very small timestep leads to many iterations and therefore requires extra CPU time. Finding the correct timestep is essential for hydrodynamical simulations and it is common practise to use the Courant–Friedrichs–Lewy (CFL) condition.

Consider a material wave travelling through a medium at sound speed c_s. The time for a wave to move between two points ($\vec{x}_1$ and $\vec{x}_2$) in the simulation is

$$t_s = \frac{|x_2 - x_1|}{c_s} = \frac{\Delta x}{c_s}. \tag{2.2.30}$$

We can consider these two points to be as close as possible in the simulation, that is, at the resolution limit. Hence, in order to reproduce properly the changes on the relevant physical properties of the fluid, such as density or temperature, we need a timestep (Δt) smaller than the time for the wave to travel the spatial resolution of the simulation. The fraction between these two quantities is a dimensionless number called the Courant–Friedrichs–Lewy constant, or just the Courant constant C_{cfl}

$$C_{\text{cfl}} = \frac{\Delta t}{t_s} = \frac{\Delta t}{\Delta x / c_s} = \frac{\Delta t \, c_s}{\Delta x}. \tag{2.2.31}$$

Normally C_{cfl} has values smaller than unity ~0.2 – 0.3, and we can calculate the timestep as

$$\Delta t = \frac{C_{\mathrm{cfl}}\,\Delta x}{c_s}. \tag{2.2.32}$$

Choosing the right timestep may require a deeper understanding of the physics of the simulation, as the CFL condition will fail when dealing with supersonic physics and shocks, as these events travel faster than the speed of sound.

Another important aspect of SPH is the possibility to have individual timesteps. As the different smoothing length allows us to simulate simultaneously a wide range of densities, this will mean that the densest parts will have a smaller smoothing length and therefore a smaller Δx (as $\Delta x \sim h$). If we use a single timestep to describe the whole simulation, we will need to use the timestep required for the densest parts of the phase space, resulting in wasting CPU time in the diffuse areas where a bigger timestep may be sufficient.

2.3 Particularities of GADGET2

2.3.1 Introduction

GADGET2 is a SPH code by V. Springel (Springel 2005) to run cosmological simulations. However its flexibility has allowed many groups to adapt it to other fields, and use it to model different astrophysical environments, from simulating galactic clusters to star forming molecular clouds. GADGET2 defines six different types of particles: Gas, Galactic Halo, Galactic Disk, Galactic Bulge, Stars and Sink Particles. For our purposes we are only interested in the gaseous component, to simulate the collapse of a molecular cloud, and the sink particles to model the star formation. So, we will use a hybrid SPH simulation where only the gaseous part evolves hydrodynamically and the sink particles will only interact with the gas through gravitation and accretion.

2.3.2 Hydrodynamics of Gas Particles in GADGET2

Hydrodynamic Equations

For computing the hydrodynamics of the gas, GADGET2 uses a fully conservative equation of motion as described in Springel & Hernquist (2002), improving Eq.2.2.12.

$$\left\langle \frac{D\vec{u}_i}{Dt} \right\rangle = -\sum_{j=1}^{N} m_j \left(f_i \frac{P_i}{\rho_i^2}\, \nabla_i W_{ij}(h_i) + f_j \frac{P_j}{\rho_j^2}\, \nabla_j W_{ij}(h_j) \right). \tag{2.3.1}$$

The coefficients f_i are defined by

$$f_i = \left(1 + \frac{h_i}{3\rho_i} \frac{\partial \rho_i}{\partial h_i} \right). \tag{2.3.2}$$

Equation 2.3.1 is symmetric with respect to any pair of particles i, j. The details of the derivation for these equations are included in the Appendix A.

GADGET2 Kernel

GADGET2 uses one of the most popular kernels in the literature: the spline cubic kernel (Hernquist & Katz 1989; Monaghan 1992; Springel 2005):

$$W(r,h) = \frac{8}{\pi h^3} \begin{cases} 1 - 6\left(\frac{r}{h}\right)^2 + 6\left(\frac{r}{h}\right)^3 & 0 \le \frac{r}{h} \le \frac{1}{2}, \\ 2\left(1 - \frac{r}{h}\right)^3 & \frac{1}{2} \le \frac{r}{h} \le 1, \\ 0 & \frac{r}{h} > 1. \end{cases} \tag{2.3.3}$$

where $r = |\vec{x_1} - \vec{x_2}|$. One of the major drawbacks of this kernel is that the second derivative is not a smooth function (Price 2012). As derivatives of the kernel are used to calculate derivatives of the physical magnitudes (Eq. 2.2.6), this may lead to numerical instabilities. For that reason it is more recommendable to use higher order kernels (such us the quintic) which present well-defined high order derivatives (Price 2012).

GADGET2 Internal Energy

Instead of computing the internal energy of the gas particles, GADGET2 uses a special entropic function, which depends on the specific entropy s (for details see Springel & Hernquist 2002). This function is defined as

$$A_j(s) \equiv \frac{P_j}{\rho_j}. \tag{2.3.4}$$

With this formulation, the modelling of shocks becomes easier, as the entropy of the SPH particle may vary even in the absence of sources/sinks. From this, we can define the specific internal energy as

$$e_j = \frac{A_j(s)}{\gamma - 1}\rho_j^{\gamma-1}. \tag{2.3.5}$$

Therefore to account for the internal energy of the SPH particles we include the following term in the Hamiltonian

$$H_{\text{therm}} = \frac{1}{\gamma - 1}\sum_i m_i A_i {\rho_i}^{\gamma-1}. \tag{2.3.6}$$

Artificial Viscosity in GADGET2

GADGET2 introduces an artificial viscosity tensor Π_{ij}. This viscosity reduces the kinetic energy of the particles transforming it into heat. This generates entropy at a rate:

$$\left\langle \frac{DA_i}{Dt} \right\rangle \bigg|_{\text{visc}} = \frac{1}{2}\frac{\gamma - 1}{\rho_i^{\gamma-1}} \sum_{j=1}^{N} m_j \Pi_{ij} \vec{u}_{ij} \cdot \nabla_i W_{ij}. \tag{2.3.7}$$

The viscosity tensor is computed in GADGET2 similarly to Eq. 2.2.28

$$\Pi_{ij} = -\frac{\alpha}{2}\left(\frac{c_i + c_j - 3\omega_{ij}}{\rho_{ij}}\right)\omega_{ij}, \tag{2.3.8}$$

where ω_{ij} is the relative velocity projected on to the separation vector provided if the particles approach each other, and otherwise $\omega_{ij} = 0$:

$$\omega_{ij} = \begin{cases} \dfrac{\vec{u}_{ij} \cdot \vec{r}_{ij}}{|\vec{r}_{ij}|} & \vec{u}_{ij} \cdot \vec{r}_{ij} < 0, \\ \\ 0 & \vec{u}_{ij} \cdot \vec{r}_{ij} \geq 0 \end{cases} \tag{2.3.9}$$

For small $\vec{r}_{ij}$ the viscosity might be divergent. This could be problematic as it will introduce spurious angular momentum when modelling shear flows. To limit the strength of the artificial viscosity GADGET2 follows the approach in Balsara (1995) and Steinmetz (1996) and introduces a viscosity limiter

$$\Pi_{ij}\Big|_{\text{limited}} = \frac{\eta_i + \eta_j}{2}\Pi_{ij}, \tag{2.3.10}$$

where

$$\eta_i = \frac{|\nabla \times \vec{u}|_i}{|\nabla \cdot \vec{u}|_i + |\nabla \times \vec{u}|_i}. \tag{2.3.11}$$

This represents a fraction of the solenoidal turbulent mode (responsible for the angular momentum transfer in shears), with the total turbulent field (compressive and solenoidal).

2.3.3 Gravity Calculation

To model molecular clouds, we will clearly need to include gravity. In SPH simulations, computing the gravitational potential requires calculating Newtonian gravity between each pair particles in the simulation. Solving the gravitational potential of a cloud by brute force (i.e. $\sim N^2$) comes with an implicit inefficiency: as gravity scales as $\propto r^{-2}$, particles that are very far away would have a very small effect compared with the interactions of the closest neighbours. GADGET2 solves this by using a common approach in the literature. GADGET2 calculates gravity using an octree as described in Barnes & Hut (1986). The principle of the octree can be seen in Fig 2.3.1. In the left panel we show a simple version of a SPH simulation with 3 particles. We refine the tree by subdividing cells with more than one particle into more cubes (with 8 smaller cells). If the cell has one particle (as cell 8) it will be consider as a *leaf* of the tree, and the refinement will end there for that leaf. If a cell has no particle in it, it will be not be considered as a branch or a leaf of the tree. If there is more than one particle in a given cell, we iterate the process and divide that cell into 8 more subcells, as shown in Fig. 2.3.2. That cell will be a *branch* of the tree and the new ones will be either leaves (if they only have one particle) or more branches (if they have more than one). GADGET2 stores the position of the centre of mass and the value of mass contained in every branch and leaf of the tree. The process is iterated until each particle is located on a leaf, and therefore the full structure of the tree is defined (Fig. 2.3.3).

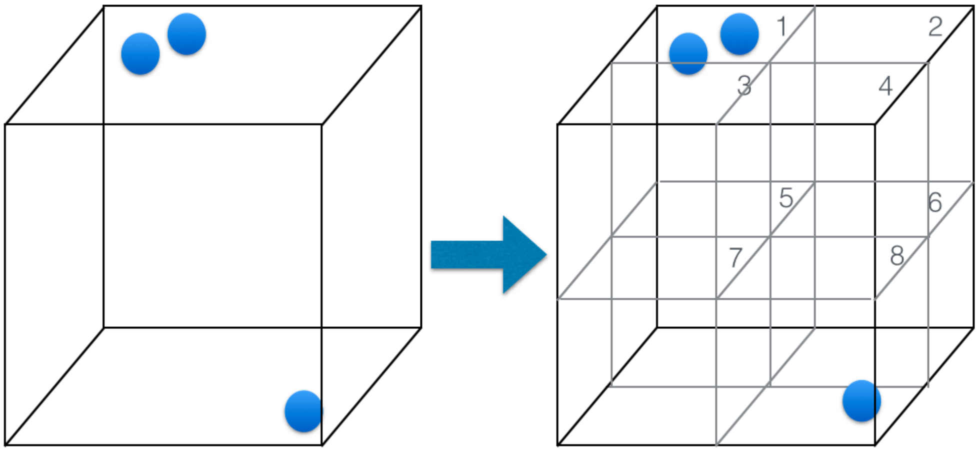

Figure 2.3.1: In this figure we show the division of a block of space with 3 particles into 8 different cells. The upper left cell has 2 particles and can be recursively divided into another 8 smaller cells.

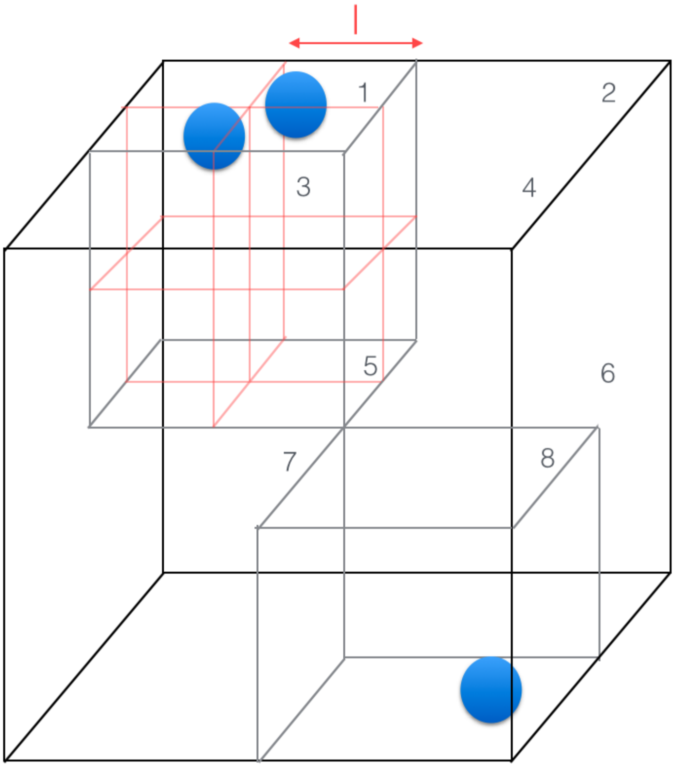

Figure 2.3.2: In this figure we show the next level of refinement in the tree structure. Cell 1 is recursively divided into 8 new subcells so that each particle is in one cell.

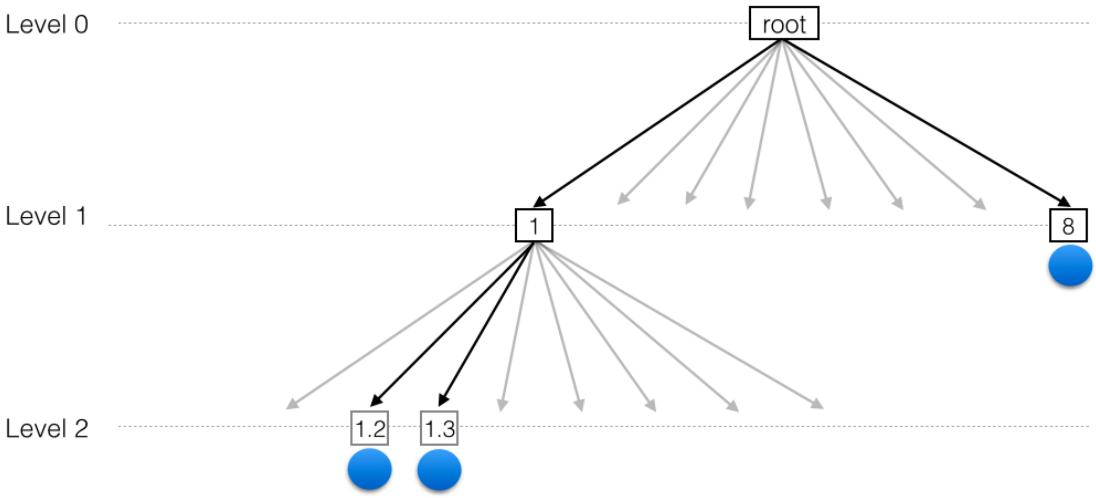

Figure 2.3.3: Tree structure of the 3 particle example shown above. Each node of the tree may have up to 8 children. The tree is complete once every particle is assigned to a final node (leaf) of the tree.

Once the tree structure is defined we can calculate the gravitational potential of our simulation. From each particle we calculate the potential of the mass structures around it. So, in our example in Fig. 2.3.3 if we are calculating the gravitational force experienced by the particle in cell 8, we walk up the tree until we reach the root node, and then we walk it down and reach cell 1 (that contains 2 particles). If cell 1 is sufficiently far away from 8, then we say that we do not *open* that cell, and we use the data about its centre of mass to compute the potential. For particle 1.2 (and 1.3) in cell 1, the procedure is the same, we walk up the tree until we reach node one, and then walk down through the branches of that node. If the particles are close enough we will *open* that branch reaching for the *leaves*. After that we will walk up the tree reaching the root node and expanding through the other branch that contains cell 8.

However, to perform the calculation of gravity, we still need to define which nodes are going to be treated as nearby and therefore be opened, and which ones will be considered far away and therefore part of a node where we will only consider the centre of mass. This is called the opening criterion. In Barnes & Hut (1986) they use the following geometric opening criterion

$$\theta < \frac{l}{D}, \tag{2.3.12}$$

where l is the size of the node, D is the distance from the node, and θ is a fixed accuracy parameter. This is a topological criterion as it only takes into account the length of the box and the distance between the particles. So, the effect of particles belonging to a branch that is far away will be computed using the averaged value of the branch, whereas the effect of particles in a nearby branch will be calculated using the values from the leaves.

Instead of this topological approach, GADGET2 uses a physical criterion calculating the ratio between the gravity interaction to the acceleration on that particle. For a node of mass M and size l, that is at a distance r of the particle, GADGET2 will open the node if

$$\frac{GM}{r^2}\left(\frac{l}{r}\right)^2 \leq \alpha\, |\vec{a}|, \tag{2.3.13}$$

where $\vec{a}$ is the acceleration of the node computed in the previous timestep and $\alpha \sim 1$ is a parameter. This method compares the magnitude of the error in truncation (when we do not open a far away node) and compares it with the actual force acting on the particle ($\vec{a}$). This is more suitable than a simple topological criterion, especially for cosmological simulations where gravitationally bound areas separate from each other due to the expansion of spacetime. The use of the octree method results in a gain in CPU time as it scales as $t \approx N$ log(N) versus the traditional $t \approx N^2$.

As two particles can get very close resulting in a huge gravitational force, it is customary to include some *softening* factor in the gravity computation to keep the value for the attracting force between two particles that are close within reasonable limits. If we have two particles i and j, the gravitational potential created is

$$\phi = -\frac{Gm_i m_j}{\sqrt{r_{ij}^2 + \epsilon^2}}, \tag{2.3.14}$$

where r$_{ij}$ is the distance between the two particles and ϵ is the gravitational softening length. Normally $\epsilon << r_{ij}$ but large enough to prevent large gravitational forces when solving the gravity tree (we choose $\epsilon = 0.01$ pc for our simulations). The softening length is especially important in simulations that include dark matter particles or sinks, as they are not be affected by artificial viscosity and therefore may get very close to each other.

2.3.4 Density Calculation

An octree is also used to find neighbours of SPH particles. GADGET2 follows the range-searching method devised by Hernquist & Katz (1989). The main difference between the gravity and neighbour trees is, that for the gravity the opening criterion only depends on the position of both particles and the acceleration of the particle in the current node (i). For the neighbour tree, it may depend on the properties of the distant particle j (for example smoothing length). This is solved by storing in the current node information about the maximum smoothing length of all particles contained in that node. GADGET2 uses equation (2.2.22) to calculate the density. As usual all SPH particles have the same mass, the smoothing length is the important parameter here. To calculate the smoothing length GADGET2 solves the following implicit equation

$$\frac{4\pi}{3} h_i^3 \rho_i = N_{\rm neigh}\, m_p, \tag{2.3.15}$$

where m_p is the average particle mass and $N_{\rm neigh}$ is typically a fixed number of neighbours ($\sim$ 50

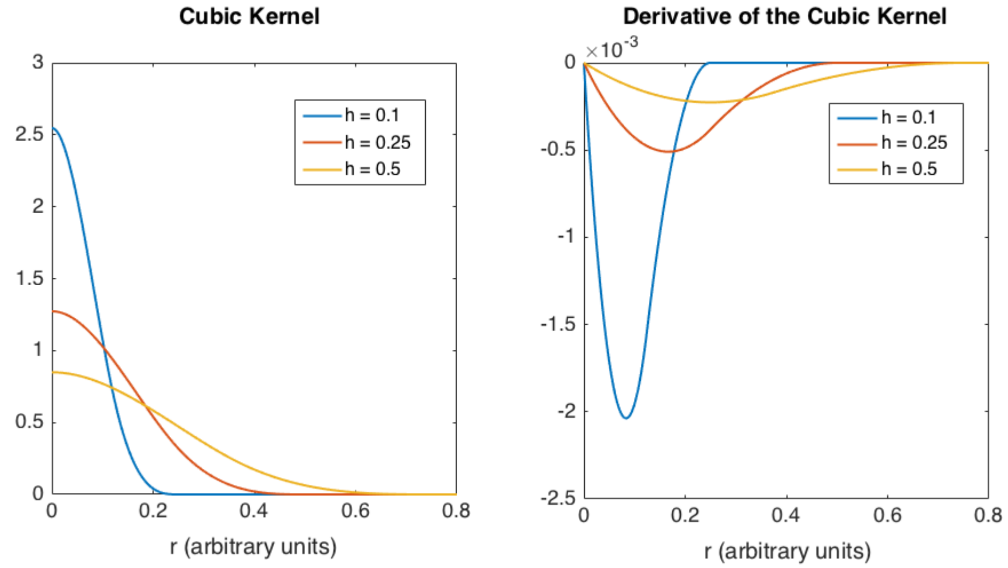

Figure 2.3.4: Cubic Kernel and first derivative for different smoothing lengths.

for GADGET2). This number is not arbitrary, a reduced number of neighbour would result in a low resolution simulation. A large number of neighbours $N_{\text{neigh}} > 100$ combined with a cubic spline kernel results in clumping or pairing of particles. It was argued that (see e.g. Price (2012)) this effect was caused by the flatness of the first derivative of the cubic kernel for small radius (as shown in Fig. 2.3.4). As the gradient of the kernel is used to calculate the repulsive force between particles (see Eq. 2.2.10), and hence for small gradients the repulsive force is negligible. However, Dehnen & Aly (2012) show that certain kind of kernels (Wendland (1995)) have an inflection point (as the cubic kernel), and there is no pairing observed. Dehnen & Aly (2012) claim that the pairing may be caused if the kernel has a negative Fourier transform. A negative Fourier transform of the kernel may lead to instabilities in the system causing the pairing for a high number of neighbours.

GADGET2 solves the neighbour searching equation using a Newton-Raphson bisection looking for the roots of this equation

$$f(h_i) \equiv \rho_i - \frac{3}{4\pi}\frac{N_{neigh}\, m_p}{h_i^3} = 0. \tag{2.3.16}$$

2.3.5 Integration Scheme and Timesteps

Once we have all the relevant quantities defined for both the gravitational and SPH part, we need to integrate the equations of motion. For integrating these equations GADGET2 uses a Kick-Drift-Kick leapfrog scheme, shown to be superior in performance to the Drift-Kick-Drift scheme (Quinn et al. 1997). The integration will occur in three stages for a given timestep:

- A initial Kick phase when the particle stays in the same position, but its momentum is updated accordingly to the force experienced by the particle (in the same way a that football player *kicks* the ball on a corner kick).

$$K_t(\Delta t) : \begin{cases} \vec{r}_i & \mapsto & \vec{r}_i \\ \vec{p}_i & \mapsto & \vec{p}_i + \vec{f}_i \Delta t, \end{cases} \tag{2.3.17}$$

where $\vec{f}_i$ is the force acting on particle i:

$$f_i^k = -\sum_j m_i m_j \frac{\partial \phi(\vec{r}_i - \vec{r}_j)}{\partial r_i^k}. \tag{2.3.18}$$

- A Drift phase where the momentum of the particle remains constant as the particle *drifts* in the space changing its position (as the ball flies towards the goal after the kick). The Drift will consist of integrating the particle trajectory using the momentum known from the previous timestep

$$D_t(\Delta t) : \begin{cases} \vec{p}_i & \mapsto & \vec{p}_i \\ \vec{r}_i & \mapsto & \vec{r}_i + \frac{\vec{p}_i}{m_i} \Delta t. \end{cases} \tag{2.3.19}$$

- A final Kick phase where the momentum of the particle is updated using the forces that have been recalculated after the Drift phase.

The usual integration scheme is given by the operator $U(\Delta t) = K(\Delta t/2)D(\Delta t)K(\Delta t/2)$ and that means that the particle experiences the force for half a timestep, moves during a full timestep and then its force is updated for another half timestep. The timestep is chosen according to the CFL condition (using Δx and the signal velocity ω_{ij} described in this chapter). Additional timestep criteria will be described in Chapter 4.

2.3.6 Parallelization Strategies

Large simulations require using High Performance Computers (HPC) that normally have multiple processors. We will perform simulations with more than 10 million particles, that include complicated physics and star formation. To use multiple processors, the first step is to subdivide the domain into different sub-domains, so that each processor controls one of those sub-domains. One simple approach is to divide the total volume into hierarchical orthogonal sections (as shown on the left panel fo Fig. 2.3.5). The space is divided into cells with the same volume, and each processor controls the particles in each cell. The main issue with this approach is that there may be some cells with few particles and others with too many, and CPU time is wasted as the less populated cells have to wait for the overloaded to finish their computation. We can solve this issue by dividing the number of particles and not the simulation volume. GADGET2 does this by transforming the 3D space into a 1D curve, the Peano-Hilbert curve. This curve divides the 3D (or 2D) space into small cells and *walks* through every cell just once. The Peano-Hilbert curve accepts different levels of precision if required.

This represents the first advantage of using this transformation. The curve allows different

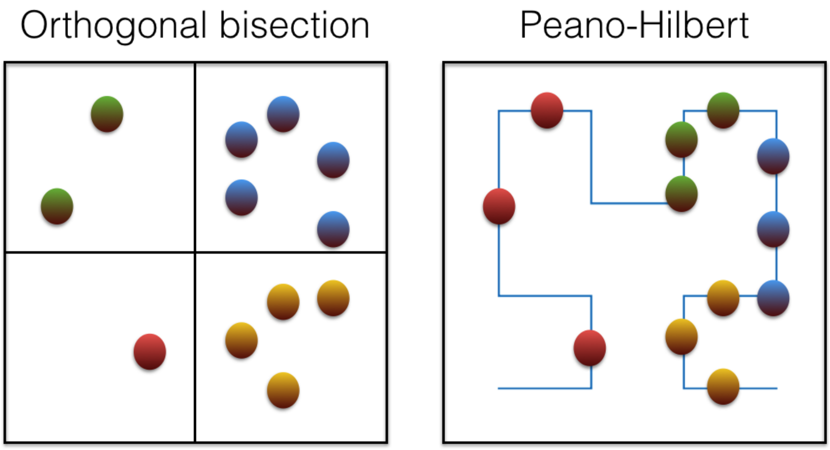

Figure 2.3.5: On the left panel how we distribute 12 particles in 4 orthogonal domains each one with its respective colour. On the left panel we have the same particles over a Peano-Hilbert curve and in different colours we show how the particles are distributed using this method.

levels of precision like the octree structure. If we are moving up on the tree, we can reduce the order of our Peano-Hilbert curve to find a 1D representation of the upper level of refinement on the simulation. The octree and the Peano-Hilbert structure are related. In the right panel of Fig. 2.3.5 we show the same particles of the left panel placed on a Peano-Hilbert curve. We have divided the 12 particles into 4 processors by using the Peano-Hilbert (represented by colours). In this case, each processor is controlling the same number of particles, so the work load is well balanced between them. Besides, it is clear that points which are close in the curve, are also close in real space, and therefore the processor responsible of them will control a region of the simulation that is physically connected.

2.3.7 Star Formation and Sink Particles

To fully model star formation, we would need to model a huge range of densities, from the diffuse areas of the ISM to protostellar densities. As the density of the gas increases during gravitational collapse, the timesteps become smaller and smaller such that the simulation becomes prohibitively slow.

To avoid this problem, the version of GADGET2 we are using includes sink particles which replace regions of very dense gas, and allow the simulations to continue. They are based on Clark et al. (2008) and Jappsen et al. (2005) which is based on Bate et al. (1995). The gas particles interact with each other through gravity and pressure forces, however the sink particles only interact with gas particles through gravity and accretion. Each sink will have a radius that will be fixed throughout the simulation and a density threshold. In our version of GADGET2 , these two quantities are free parameters that can be fixed at the beginning of the simulation. However, according to Bate et al. (1995) and Bate & Burkert (1997) it is highly recommended that the mass of the sink is

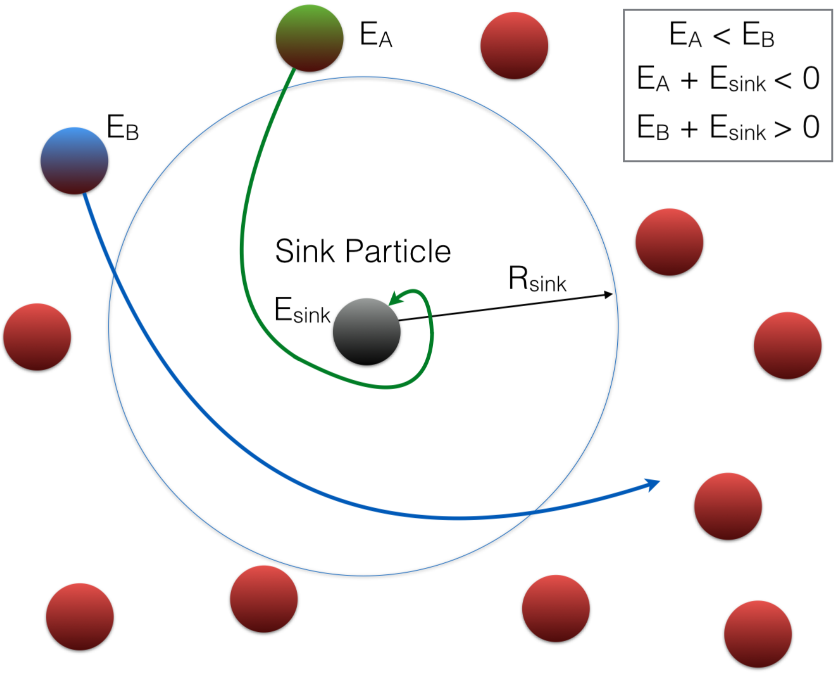

Figure 2.3.6: We show the sink particle (in grey) with its radius of influence and some SPH particles in colour. The blue particle enters the area of influence of the sink, but as it is not gravitationally bound it escapes. The green particle, on the other hand, is trapped by the sink and merges with it.

over the Jeans Mass of the cloud. Therefore, we have to choose these two parameters accordingly.

Creation of Sink Particles

The creation of a sink happens when the gas lying within the sink radius satisfies the following conditions:

1. The local density exceeds the density threshold of the sink.
2. The virial parameter of the system is $\alpha \leq \frac{1}{2}$.
3. If β represents the ratio of the rotational energy of the system with respect to gravity, then $\alpha + \beta \leq 1$, meaning that the kinetic energy due to translation and rotation is smaller than the gravitational energy.
4. The total mechanical energy of the system is negative.
5. A sink is created if the gas particles are converging ($\nabla \cdot \vec{v} < 0$), and the divergence of the acceleration of the particles is negative.

Accretion of Gas by Sink Particles

Once a sink particle is created, it may interact with the gas particles by accreting them. If a SPH particle lies within the sink radius, it may be accreted (as shown in Fig. 2.3.6). The SPH particle undergoes a series of test to determine if it is accreted:

1. The particle is gravitationally bound with the sink.
2. The angular momentum of the particle is small enough to form a bound orbit around the sink.
3. The gravitational influence of other sinks is smaller than the one accreting the particle.

This last check becomes important in very dense areas in the simulations where many sinks are clustered together. Once a SPH particle is accreted, it becomes frozen (or dead) in the simulation and it is ignored in further calculations. The sink will update its mass, angular and linear momentum, and position accordingly with the centre of mass of the SPH-sink particle system.

2.4 Method for Increasing the Resolution of a Galactic Cloud

Our goal is to simulate molecular clouds extracted from galactic simulations, using them as initial conditions for our version of GADGET2 . In order to use a cloud extracted from a full scale model and resimulate it, we need to find a method for increasing the resolution to the scales we want to sample. In doing so, the main physical invariants should be conserved: kinetic and gravitational energy, momenta, and of course the mass, density distribution and morphology of the cloud. Thus, one of the main caveats of the simulations is the resolution limit in a SPH simulation, which is given by the smallest smoothing length of the particles. The spatial physical properties of the system are smoothed by definition according to this length.

The resolution of the galactic clouds should also satisfy the criterion of Bate & Burkert (1997) and subsequent works. The smoothing length represents the distance around a given SPH particle at which it has the desired number of neighbours ($N_{\rm neigh} \sim 50$). Which is another way of saying that the smallest amount of mass that SPH can resolve is $M_{\rm res} \sim 2\, N_{\rm neigh}\, m_p$, and therefore any physical process (like gravitational collapse) that happens at smaller scales is missed. This sets a limit to the Jeans Mass of any clump of matter within the simulation. We show the typical values for a galactic GMC in Table 2.1. This indicates that we need to resolve 100 $M_\odot$ with $2N_{\rm neigh}$ =100. And therefore the resolving mass is $m_r = \frac{M_J}{100} \sim 1\ M_\odot$. As our initial particles have a mass of ~300 $M_\odot$, this implies that the factor F to increase the resolution is:

$$F = \frac{M_{\rm SPH}}{m_r} = \frac{312.5}{1} \sim 300 \tag{2.4.1}$$

To keep the relevant invariant quantities constant (see Appendix A for more detailed derivation) we will divide the mass of the initial particle by the factor F. But each new particle will have

Table 2.1: Typical parameters of a GMC

Typical values for a Molecular Cloud	
Total Mass of the Cloud:	$\sim 10^6$ M$_\odot$
Initial galactic SPH Particles Mass:	$M_{SPH} = 312.5$ M$_\odot$
Approximate Radius:	~ 100 pc
Average Density:	~ 100 cm^{-3}
Jeans Mass for T = 25 K:	$M_J \sim 100$ M$_\odot$

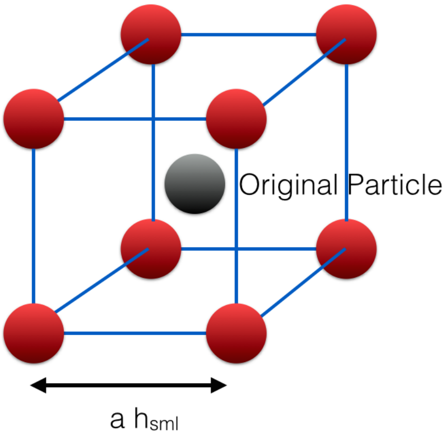

Figure 2.4.1: Cubic method for increasing resolution. The particles are placed in the corners of a cube of size $a \cdot h$ where h is the smoothing length and a is a free parameter normally set to 1.

the same velocity as the original to conserve momentum and energy. It is also worth mentioning that this factor F depends on the characteristics of each cloud, as the Jeans mass depends on its density. Thus, we need to use a method to increase the resolution of our clouds, able to work for an arbitrary F. In the following subsection we will explain the differences between methods.

2.4.1 Cubic Method

Our first choice was to follow the approach in (Dobbs 2015) and place 8 new particles in the corners of a cube as shown in Fig. 2.4.1. The cube has a size $a \cdot h$ where h is the smoothing length and a is a free parameter normally set to unity.

This method has the advantage that it is very simple to implement, and it has already been tested, and satisfies exactly the conditions for energy and moment conservation. However, it has two major drawbacks. The first one is the introduction of artificial structure as shown on Fig. 2.4.2. By placing the particles in a cubic structure we introduce an artificial pattern in the cloud. This is visible in the first snapshots of the simulation (Fig 2.4.7). The other one is that F is defined by the geometry of the method, and only certain quantities for F are allowed (9, 81, 729, etc...), lacking the flexibility to define F as the Jeans Mass limit of the cloud requires. Recursive iterations of this method will also cause particles placed on top of one another, making the search for neighbours

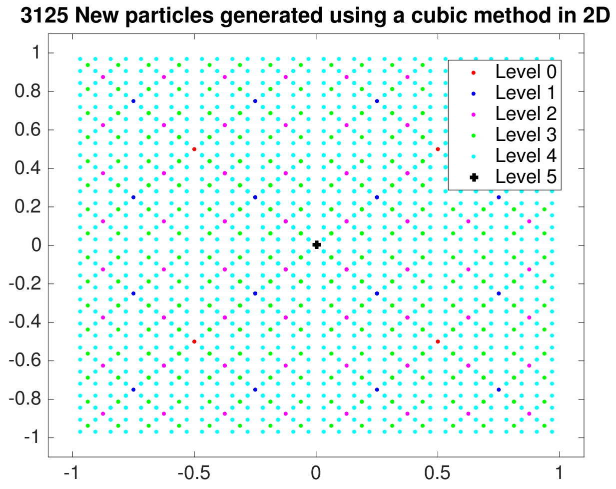

Figure 2.4.2: Cubic method for increasing resolution. It shows a 2D iteration scheme with 5 refinement levels

infeasible.

2.4.2 Spherical Method

For this method, we uniformly scatter the particles around a sphere of radius $a \cdot h$, where again the h is the smoothing length and a a free parameter.

To create the sphere we generate 3 random numbers x, y, z between $-a \cdot h < x, y, z < a \cdot h$. Then we calculate the radius r of the particle. If $r < a \cdot h$ then we generate a particle on that position. We iterate this process until we have the desired number of new particles (F - 1). This spherical method is fast and allows F to vary without any reasonable restrictions.

We have introduced the value a as a free parameter, to calculate the best size of the volume in which we are generating particles. Initially we used a value of $a = 1$. We tested this initial value by performing a χ^2 fit. First, we compute the density in the a sample of 1000 points r_i using the initial matter distribution ρ_o (from the initial cloud):

$$\rho_o = \sum_j m_j W(\vec{r}_i - \vec{r}^{o}_j, h_{ij}). \tag{2.4.2}$$

Then we choose a random value for a between $0.1 < a < 1.1$ and calculate the density field in the newly generated cloud ρ_hd

$$\rho_\mathrm{hd} = \sum_j m_j W(\vec{r}_i - \vec{r}^{hd}_j, h_{ij}). \tag{2.4.3}$$

After that, we calculate the χ^2 by using the following formula:

$$\chi^2 = \sum_i \left(\frac{\rho_{hd}(\vec{r}_i) - \rho_o(\vec{r}_i)}{\rho_o(\vec{r}_i)} \right)^2 . \tag{2.4.4}$$

We repeat this process iteratively as in a typical Markov Chain Monte Carlo. At the end of each iteration we check if $\chi_k^2 < \chi_{k-1}^2$. If the new χ^2 value is bigger than the previous one, we reject that value of a and randomly select a new one in the interval $0.1 < a < 1.1$. If the value of the new χ^2 is smaller, then we keep the value of a. To increase the sampling of phase space we vary a by 5%, during the iterations where we keep the old value for a.

The result of this algorithm after more than 3600 iterations was a value of $a \sim 1$ ($a = 0.9814811$), similar to our first assumption.

The main problem with the spherical method is that in the initial cloud, the density at a given point r_i is calculated by using the smoothing kernel and Eq. 2.2.5

$$\rho = \sum_j m_j W(\vec{r}_i - \vec{r}_j, h_{ij}). \tag{2.4.5}$$

For a given initial particle, the SPH density distribution follows the kernel, so ideally, the distribution of the new particles should be as close as possible to the kernel. The density profile of the new particles created using the spherical method, has a flatter profile (as shown in Fig. 2.4.3) underestimating the density in the central area where the initial particle lies, and overestimating it in the extremes.

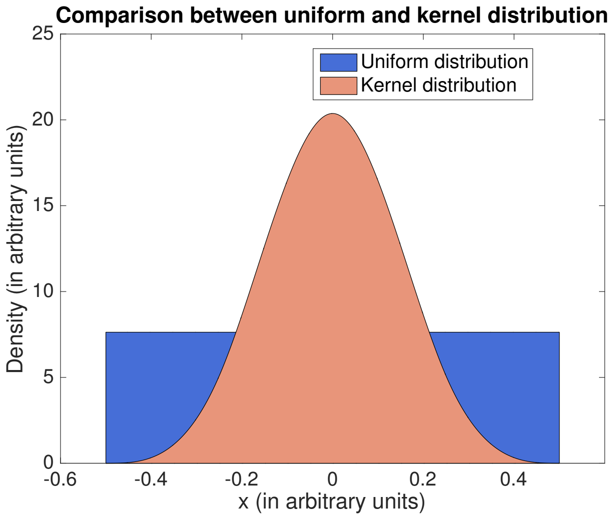

Figure 2.4.3: Density distribution for one particle using the smoothing kernel, and with a uniformly distributed sphere of particles. The spherical method overestimates the density in the outer parts and underestimates it in the centre.

Although this method represents an improvement with respect to the cubic, we are still changing the initial mass distribution of particles. An improvement will be to scatter the new particles following the kernel distribution.

2.4.3 Smoothing Kernel Method

For this method, we generate a distribution of particles that follows the SPH kernel, using the inverse sampling method. Let $P(x)$ be the cumulative probability distribution function, and $dP(x)/dx$ be the probability density. Let x, y be two sets of different random variables. Then the normalization condition for P has to be satisfied

$$\int \frac{dP}{dy} dy = \int \frac{dP}{dx} dx. \tag{2.4.6}$$

If y is a function of x: $y = f(x)$ and considering f as a well-behaved function then

$$\frac{dP}{dy} = \frac{dP}{df(x)} = \left|\frac{dx}{df(x)}\right| \frac{dP}{dx} = \left|\frac{d}{dx} f^{-1}\right| \frac{dP}{dx} \tag{2.4.7}$$

In our particular case, x is the uniform random distribution we have used to calculate the spherical method and y is the kernel function. Therefore, we need to calculate the inverse of f (f^{-1}) to be able to generate the kernel distribution using the uniform random number generator. So, the conversion function is

$$g(x) = \left|\frac{df^{-1}(x)}{dx}\right|. \tag{2.4.8}$$

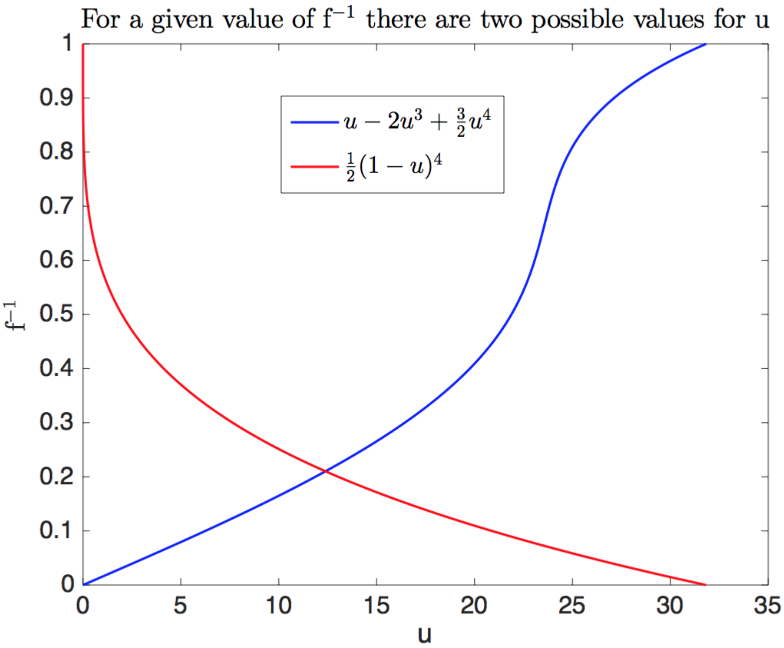

Figure 2.4.4: The function f^{-1} has 2 values for a given value of x.

If in our case $g(x) = W(x)$ and $W(x)$ is always positive, then

$$\int W(x)dx = \int df^{-1}(x) \rightarrow f^{-1} = \int W(x)dx. \tag{2.4.9}$$

Hence if $x = r/h$ and $dx = dr/h$

$$f^{-1}(x) = \int dxW(x) = \int dx\frac{8}{\pi h^2}\begin{cases} 1 - 6x^2 + 6x^3 & 0 \leq x \leq \frac{1}{2}, \\ 2(1-x)^3 & \frac{1}{2} \leq x \leq 1, \\ 0 & x > 1. \end{cases} \tag{2.4.10}$$

If $x < 1$

$$f^{-1}(x) = \frac{8}{\pi h^2}\begin{cases} x - 2x^3 + \frac{3}{2}x^4 & 0 \leq x \leq \frac{1}{2}, \\ \frac{1}{2}(1-x)^4 & \frac{1}{2} \leq x \leq 1. \end{cases} \tag{2.4.11}$$

However inverting this function is not trivial, as it does not have a unique value as Fig. 2.4.4 shows. To avoid this problem, we approximate the cubic kernel for a pseudogaussian distribution

$$G(x) = \frac{8}{\pi h^3}e^{-\frac{9}{2}x^2}, \tag{2.4.12}$$

where we have considered a Gaussian with $\mu = 0$ and standard deviation $\sigma = \frac{1}{3}h$, and arrange a different normalization factor to agree with the smoothing kernel $W(x)$. In Fig. 2.4.5 we plot the density distribution of the smoothing kernel and a pseudogaussian approximation, and the results are similar. We may be worried about the precision lost by introducing the pseudogaussian, but we have to bear in mind that we are already introducing noise from the random number generator and other sources.

The distribution given by 2.4.12 is easier to integrate and invert:

$$\int G(x)dx = \int df^{-1}(x) \rightarrow h^{-1} = \int G(x)dx. \tag{2.4.13}$$

Hence if $x = r/h$ and $dx = dr/h$

$$f^{-1}(x) = \frac{8}{\pi h^3}\int e^{-\frac{9}{2}x^2}dx = \frac{8}{\pi h^3}\frac{\sqrt{\pi}}{2}\frac{2}{\sqrt{\pi}}\int e^{-\frac{9}{2}x^2}dx. \tag{2.4.14}$$

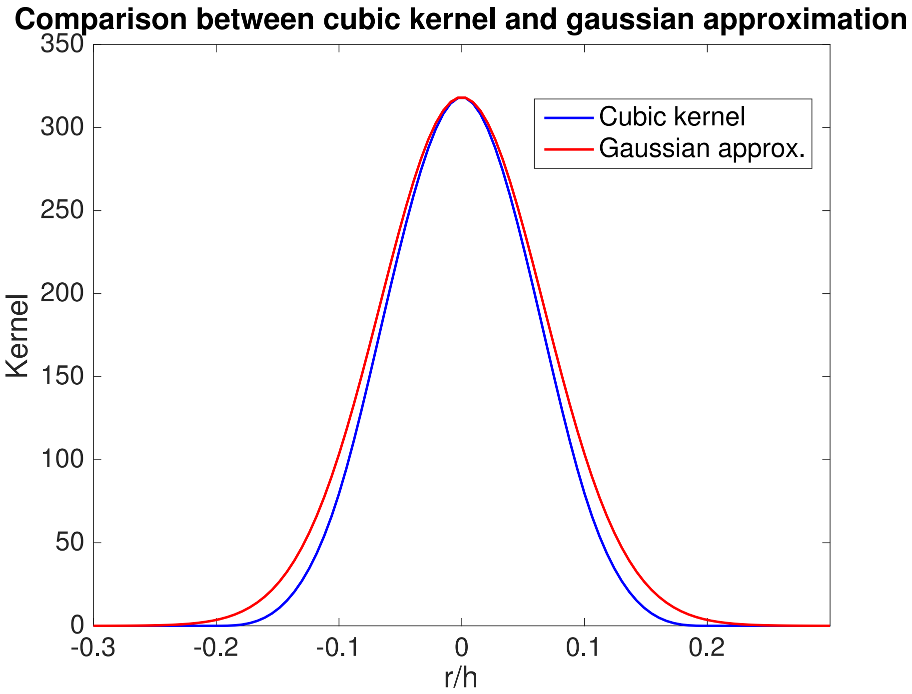

Figure 2.4.5: We show here the comparison between the density distribution of the spline and Gaussian kernel.

Now we make a change of variables $t = \frac{3x}{\sqrt{2}}$ and therefore $dt = \frac{3}{\sqrt{2}}dx$

$$f^{-1}(x) = \frac{8}{\pi h^3}\frac{\sqrt{\pi}}{2}\frac{\sqrt{2}}{3}\frac{2}{\sqrt{\pi}}\int e^{-t^2}dt. \tag{2.4.15}$$

And by identifying the Error Function $Erf(t) = \frac{2}{\sqrt{\pi}}\int e^{-t^2}dt$ and rearranging factors

$$f^{-1}(x) = \frac{8}{3h^3\sqrt{2\pi}}Erf(t) = \frac{8}{3h^3\sqrt{2\pi}}Erf\left(\frac{3}{\sqrt{2}}x\right). \tag{2.4.16}$$

In this case Erf has a unique value, so it is easier to find the inverse. In Figure 2.4.6 we present 1000 particles generated using this method. In comparison with the spherical uniform method we have a dense core of particles surrounded by a less dense area.

2.4.4 Comparison between Methods

The three methods described above are relatively easy to implement and they preserve the structure and global properties of the cloud reasonably well. If we define $\vec{r}_o \equiv (x_o, y_o, z_o)$ as the coordinates of the original particle and $\vec{r}_i \equiv (x_i, y_i, z_i)$ (with i ranging from 1 to F - 1) as the coordinates of the

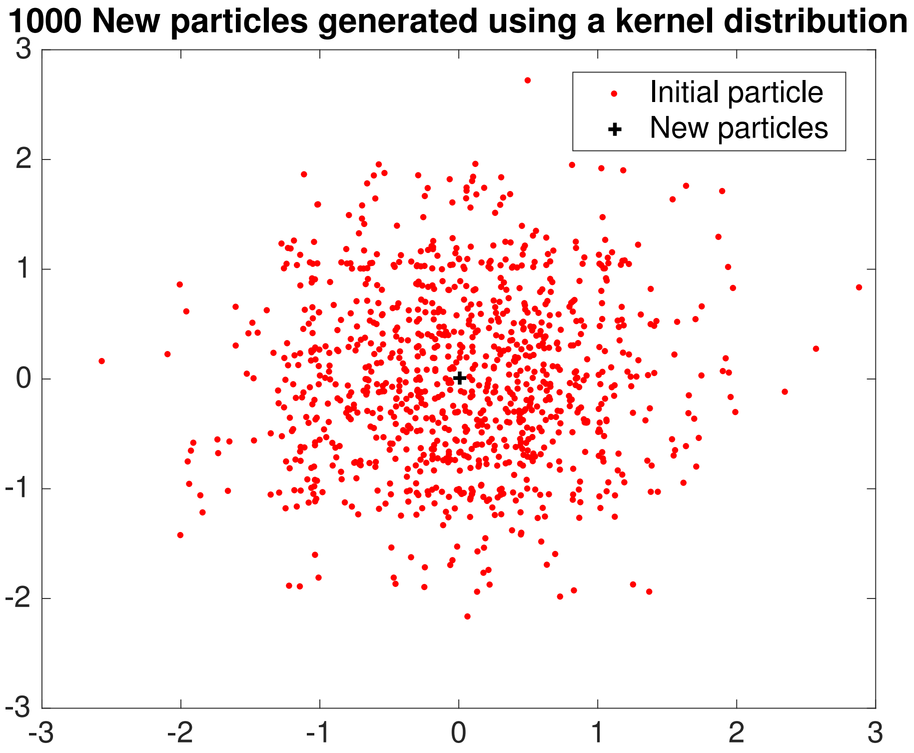

Figure 2.4.6: 1000 particles created using the kernel method.

new particles, we can define $\vec{\delta}_i \equiv (x_i - x_o, y_i - y_o, z_i - z_o)$ as the difference between the positions of the newly created particles and the original. For the cubic method, it follows that

$$\sum_{k=1}^{N} \delta_k = 0. \tag{2.4.17}$$

For the spherical and kernel method this is approximately true

$$\sum_{k=1}^{N} \delta_k \simeq 0. \tag{2.4.18}$$

In Fig. 2.4.7 we present the initial state of a cloud, comparing the original resolution, to the new cloud generated using the three methods described above. The three methods keep the original morphology of the cloud, but the cubic produces a cloud with a grainier aspect. The spherical and kernel method give similar results (it is very difficult to differentiate between them). To check the introduction of new structure in the refined clouds, in Fig. 2.4.8 we show the power spectrum of the x coordinate of the new particles for the three methods using the function PSD in Matlab. As expected the power spectrum for the cubic method is not flat. This means that at different scales we are generating different structures. On the other hand, both spherical and kernel present flat spectra, indicating that the random selection of particles is not introducing additional structure to the system.

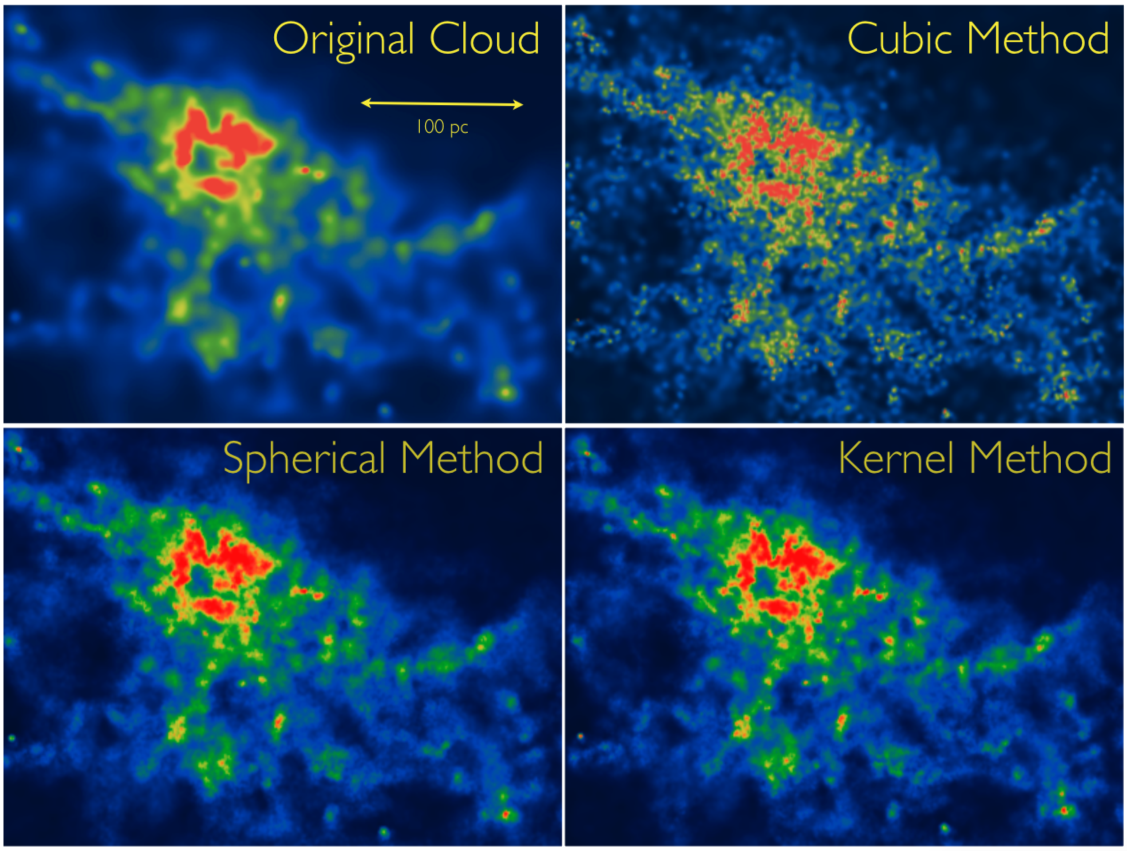

Figure 2.4.7: First snapshot of the three methods compared to the original cloud. The methods conserve the morphology of the clouds

It is worth mentioning that in all the tests we have performed, the initial differences in the density profiles were smoothed out, after a few timesteps. Because of the smoothing, any small difference in the system moves to a minimum in energy space, and therefore the systems evolve similarly. Apart from the fact that new structure is added, the cubic method, is less suitable for our purposes as the increase in resolution has to be done in discrete amounts given by the refinement levels. We need flexibility to study a sample of molecular clouds very different in sizes, shapes and velocity profiles. For these reasons we choose to use the SPH kernel method to generate the initial conditions of our simulations.

2.4.5 Summary

In this chapter we have explained in detail the tools needed to perform simulations of molecular clouds selected from full scale galactic models. We will be using a Lagrangian SPH code called GADGET2 that allows us to solve the hydrodynamical and gravitational equations using individual smoothing length and timesteps, widely used and tested in the community. We also include sink particles to model star formation. Lastly we have explained three possible methods for increasing the resolution of the clouds we wish to simulate and we have chosen the one that reproduces the

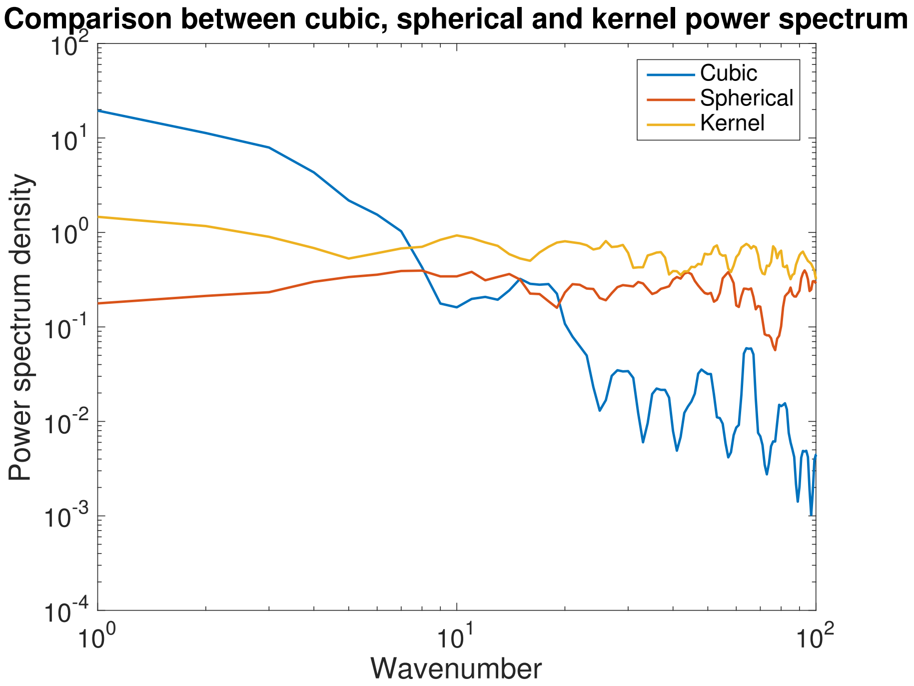

Figure 2.4.8: Comparison of the power spectrum for the x coordinate of the new particles for the three methods.

density profile most accurately. Our next step is to carry out simulations of molecular clouds extracted from galactic simulations and compare them with the other initial conditions used in the literature.

3

Comparing the Star Formation Process in Galactic Clouds and Turbulent Spheres

> *"I always thought they were balls of gas burning billions of miles away"*
> – Pumbaa (The Lion King)

3.1 Introduction

In the previous chapter we described a method to extract molecular clouds from galactic simulations preserving their main physical properties: morphology, energy budget and both linear and angular momentum. Our aim in this chapter is to test whether the inherited properties from the parent galaxy simulation play a role in the star formation process, by comparing to clouds set up without the context of a galaxy.

In the last decade there have been a large number of different numerical simulations modelling star formation using Lagrangian and Eulerian codes. However, one of the limitations of these simulations is the choice of initial conditions. The most typical approach to model star formation at GMC scales (100 pc or less) is to assume a uniform turbulent sphere (e.g. Bate et al. 2002; Clark & Bonnell 2006; Bate 2009; Clark et al. 2011; Girichidis et al. 2011; Federrath et al. 2014). In these simulations the sphere collapses under its own gravity forming filaments with the help of the initially imposed turbulent field. When using grid codes to model star formation, it is common to adopt periodic boundary conditions, considering a periodic box filled with turbulent gas (e.g. Gammie & Ostriker 1996; Offner et al. 2009; Padoan & Nordlund 2011; Federrath & Klessen 2012; Myers et al. 2013) as an initial setup. Others study the effect of colliding masses of turbulent gas to model the large-scale origin of molecular clouds by using planar colliding flows as initial conditions (e.g. Heitsch et al. 2006; Vázquez-Semadeni et al. 2006; Hennebelle et al. 2008; Banerjee et al. 2009; Ntormousi et al. 2011; Clark et al. 2012b). One limitation of using colliding flows is that the geometries normally used are simple, consisting of two different turbulent masses of gas crashing at an angle of 180°, which compress the gas in the interface and enhance star formation there, neglecting the effect of shear between the flows. Walch et al. (2012) model clouds as fractal structures, although their main focus is on examining the propagation of Hii regions into structured clouds (see also Gritschneder et al. 2009). Most simulations adopt an imposed turbulent velocity field to model the dynamics of the ISM.

All these methods have given us a picture of the star formation process in molecular clouds. However, the phase space of these initial conditions is fairly restricted by their own geometry (a sphere of gas which can be bigger or smaller, heavier or lighter, and the turbulence inside can be more or less powerful). Our method allows us to study the clouds taken from their natal environment in a simulated galaxy. Before we include more complicated physics in the simulations we intend to examine how the evolution of galactic clouds compare to the more usual initial conditions. In this chapter we compare 5 clouds extracted from galactic simulations, with three turbulent spheres of gas.

3.2 Galactic Clouds

We start with the galaxy simulation described in Dobbs & Pringle (2013) and shown in the background of Figure 3.2.1. They use the sph code sphng to perform one of the most realistic galactic simulations to date. It includes self-gravity and a galactic potential with two components: one logarithmic following Binney & Tremaine (1987) and a spiral perturbation based on Cox & Gomez (2002). For the spiral potential they chose 2 arms, as that is the case for most symmetric galaxies. Creating molecular clouds requires the formation of cold areas in the ISM therefore in Dobbs & Pringle (2013) they include ISM cooling and heating following Glover & Mac Low (2007a,b). They also model the H_2 chemistry using the same approach as Bergin et al. (2004). We will explain the chemistry and the ISM cooling-heating in further detail in Chapter 4. For the stellar feedback, instead of using complicated schemes that include winds and radiation pressure (Agertz et al. 2012; Hopkins et al. 2011) they use a simpler approach following Dobbs et al. (2011b). They assume feedback from SNe and consider that each SN injects 10^{51} erg, including an efficiency parameter $\epsilon \leq 1$. They inject this energy whenever a gravitationally bound pocket of gas exceeds the density of 1000 cm^{-3}. The total energy injected from stellar feedback is

$$E_{SN} = \epsilon \frac{M_{H_2}}{160 M_\odot} 10^{51} \text{ erg}. \tag{3.2.1}$$

Only the molecular hydrogen contributes to the stellar feedback, and the factor 1/160 comes from the assumption of a Salpeter IMF (see Salpeter 1955) with limits 0.1 and 100 $M_\odot$. To extract the clouds from the galaxy we select a box of gas ($L \sim 100$ pc) which includes the cloud, and in-

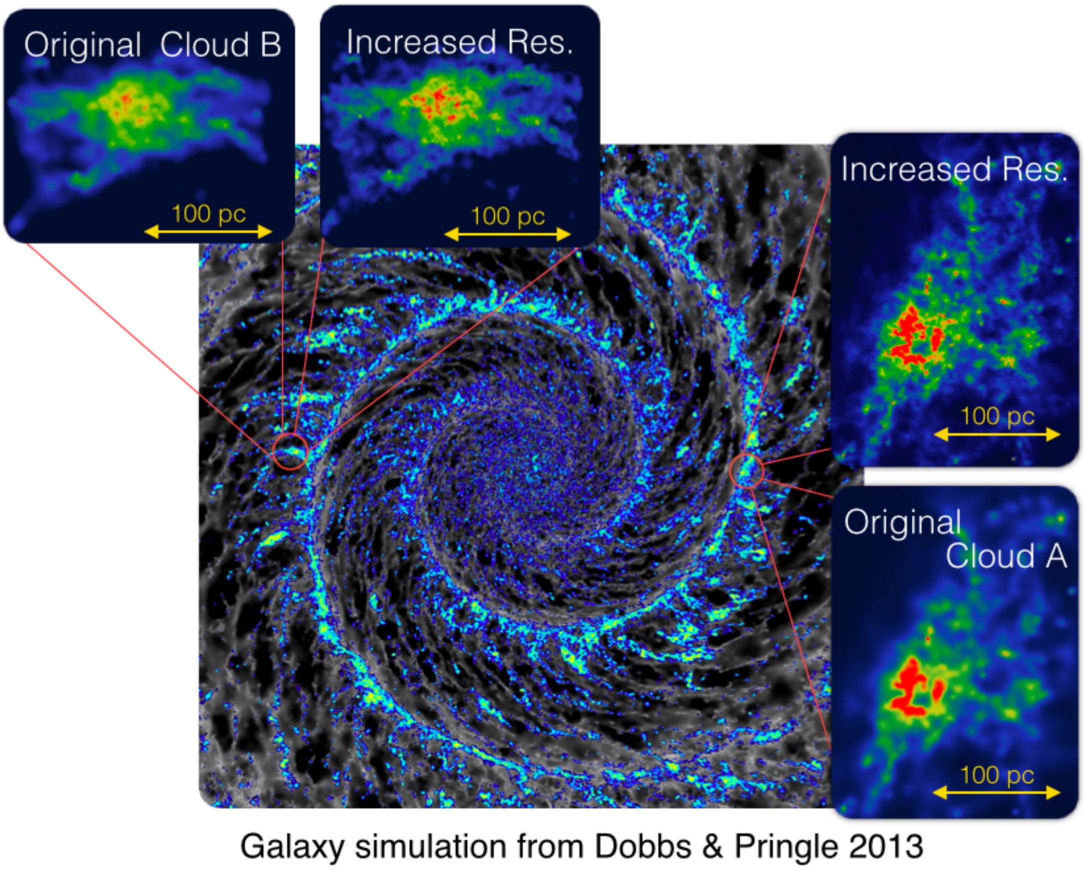

Figure 3.2.1: Top-down view of the simulated galaxy showing the position of two selected clouds. On the top left, we display the column density plot of an inter-arm cloud (Cloud B), with both the original and increased resolution. On the right, we show the column density plot of an arm cloud (Cloud A) at both resolutions.

crease the resolution by a factor of F following the SPH kernel method described in Chapter 2. The SPH particle mass in the galaxy simulation is 312.5 $M_\odot$, and the giant molecular clouds (GMCs) contain $\sim 10^4$ particles, hence $500 \leq F \leq 1000$.

Figure 3.2.1, shows the galactic simulation at 250 Myr from which we have selected two clouds, one inside a spiral arm (Cloud A), and the other in an inter-arm region (Cloud B), both with an approximate radius of 100 pc. We display these two clouds in the two insets of Figure 1, with the original and increased resolution. In Fig. 3.2.2 we show the velocity dispersion of Cloud A compared to Larson's relation. Both Cloud A and B are found to exhibit a velocity dispersion relation of $\sigma \propto r^{1/2}$ (Dobbs (2015) shows a number of clouds roughly following this relation).

Although the original galactic simulation included the prior evolution of these clouds, it did not contain sink particles, or followed star formation in detail. We traced back the gas in Cloud A to a time of 240 Myr in order to follow the preceding stages of Cloud A's evolution when the gas was less gravitationally bound (we call this model Early A). Lastly we wanted to test if the method of extracting galactic clouds is robust, given the large increase in resolution. Hence, we

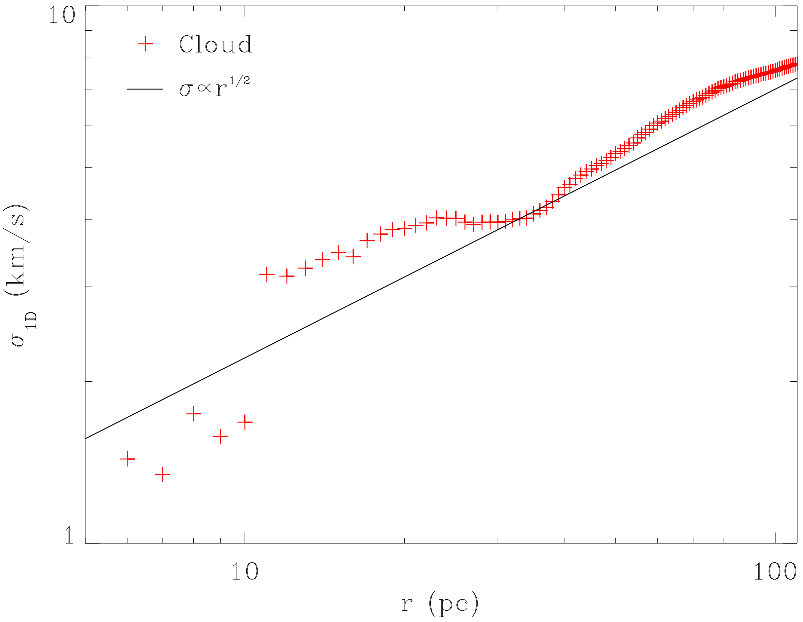

Figure 3.2.2: In this Figure we compare the velocity dispersion of the galactic Cloud A with the ideal velocity dispersion of a turbulent sphere generated using the method explained in this section.

have selected two clouds in a spiral arm taken from a simulation by Dobbs (2015), with a original particle mass of 3.85 $M_\odot$ (Cloud C and D). For these clouds, we only increase the resolution by a factor of $F = 30$, obtaining a mass for the particles of $\sim$0.1 $M_\odot$. The details for these clouds are included in Table 3.1.

3.3 Creating Turbulent Spherical Molecular Clouds

From the three usual choices in the literature (turbulent spheres, colliding flows and fractal molecular clouds) we have used turbulent spherical clouds as a benchmark. The main reason for this choice is that it is the most common way of generating initial conditions, and it allows us to match the properties of the galactic and spherical clouds easily. We follow the approach in Dobbs et al. (2005) based on Dubinski et al. (1995) and similar to Bate et al. (2003).

We set up three spheres (Sphere A, B, C) to compare them with Clouds A, B and C. We match the physical properties of the spheres with the clouds by selecting a similar virial parameter. To create a turbulent velocity field we use a grid algorithm generating Gaussian turbulence in Fourier space, and applying the inverse Fourier transform to reproduce the velocity field. We obtain an incompressible turbulent field, that is divergence free, by using the velocity potential $\vec{A}$

$$\vec{u} = \nabla \times \vec{A}. \tag{3.3.1}$$

The initial power spectrum of our velocity field follows a Gaussian velocity field according

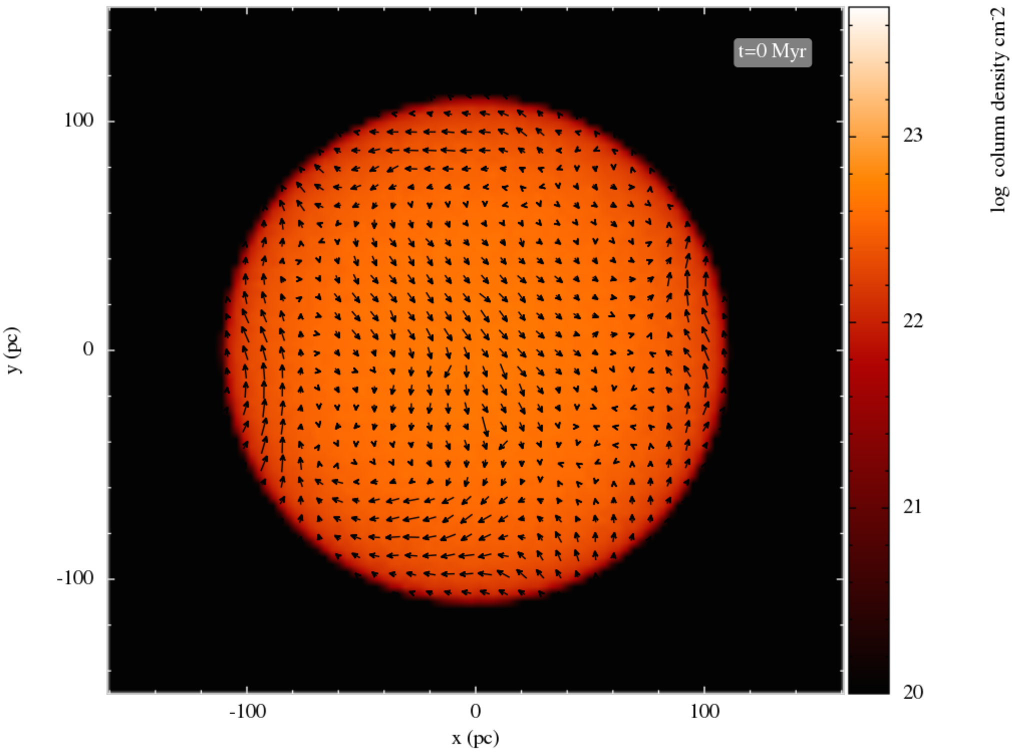

Figure 3.3.1: Column density plot of the initial state for Sphere A. The projected velocity field is superposed on the density plot.

to

$$P(k) \equiv \langle|\vec{u}_k|\rangle^2 \propto \vec{k}^{-n}. \tag{3.3.2}$$

We choose $n = 4$ so that the velocity scaling relation goes as $\sigma \propto r^{\frac{1}{2}}$ (Myers & Gammie 1999), comparable to the galactic clouds. We generate $\vec{A}$ in Fourier space sampling its components $(\vec{A}_k)$ from a grid of wavevectors (k_x, k_y, k_z) and the following formula

$$\vec{A}_k = |\vec{k}|^{-(n+2)/2}(C_x e^{i\theta_x}, C_y e^{i\theta_y}, C_z e^{i\theta_z}). \tag{3.3.3}$$

We choose the coefficients C_i and the phases θ_i so that the vectors generated by $\vec{A}_k$ satisfy Eq. 3.3.2. We extract the C_i's from a Rayleigh distribution, and the phases from a random distribution between $0 < \theta < 2\pi$. Then the inverse Fourier transform of $\nabla \times \vec{A}_k$ is

$$\vec{u} = \frac{1}{2\pi} \sum_{\vec{k}} i\vec{k} \times \vec{A}_k e^{i\vec{k}\cdot\vec{r}}, \tag{3.3.4}$$

and the velocity field in real space becomes

$$u_x = \frac{1}{2\pi} \sum_{-k_x^{max}}^{k_x^{max}} \sum_{-k_y^{max}}^{k_y^{max}} \sum_{-k_z^{max}}^{k_z^{max}} |\vec{k}|^{-(n+2)/2} \Big[k_z C_y sin(\vec{k}\cdot\vec{r} + \phi_y) - k_y C_z sin(\vec{k}\cdot\vec{r} + \phi_z)\Big], \tag{3.3.5}$$

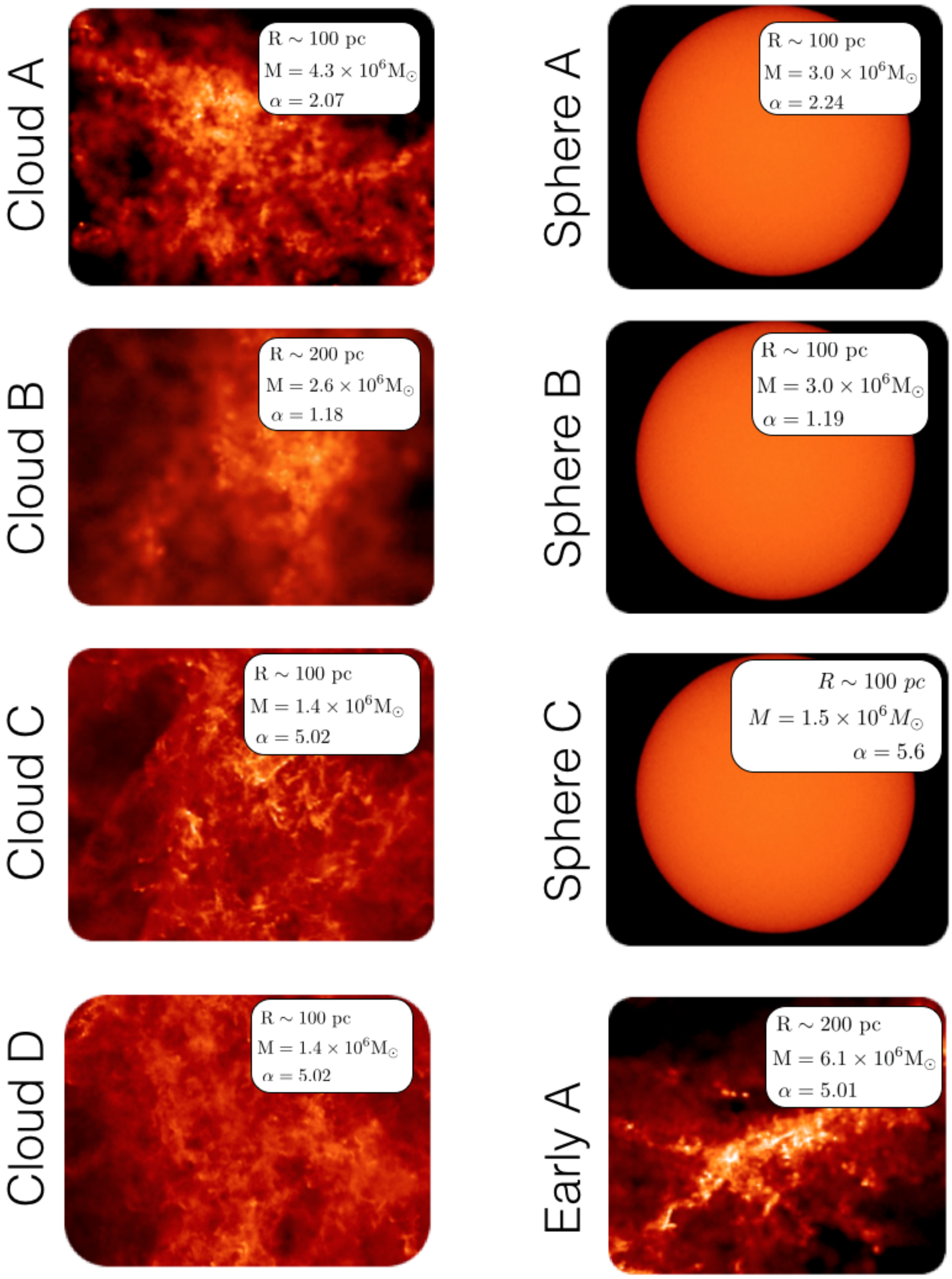

Figure 3.3.2: Column density plot of the initial state for the eight clouds described in this chapter. We include the masses, radius and virial parameters.

Table 3.1: Mass, radius, velocity dispersion, virial parameter, number of particles, factor for increasing resolution F, resolved mass (M_r) and Jeans mass for each simulated cloud.

Cloud	Mass ($M_\odot$)	R (pc)	σ (km/s)	α	Part #	F	M$_r$ ($M_\odot$)	M$_J$ ($M_\odot$)
Early A	6.1×10^6	200	11.48	5.01	1.07×10^7	550	56	1600
Cloud A	4.3×10^6	100	8.75	2.07	9.60×10^6	700	45	700
Sphere A	3.0×10^6	100	7.60	2.24	1.00×10^7	N/A	36	760
Cloud B	2.6×10^6	100	5.17	1.18	1.01×10^7	1000	26	900
Sphere B	3.6×10^6	100	6.08	1.19	1.00×10^7	N/A	30	840
Cloud C	1.4×10^6	100	7.80	5.02	1.09×10^7	30	12	1230
Sphere C	1.5×10^6	100	8.52	5.63	1.00×10^7	N/A	15	1186
Cloud D	1.5×10^6	100	7.73	4.78	1.07×10^7	30	12	1203

$$u_y = \frac{1}{2\pi} \sum_{-k_x^{max}}^{k_x^{max}} \sum_{-k_y^{max}}^{k_y^{max}} \sum_{-k_z^{max}}^{k_z^{max}} |\vec{k}|^{-(n+2)/2} \left[k_x C_z sin(\vec{k} \cdot \vec{r} + \phi_z) - k_z C_x sin(\vec{k} \cdot \vec{r} + \phi_x) \right], \tag{3.3.6}$$

$$u_z = \frac{1}{2\pi} \sum_{-k_x^{max}}^{k_x^{max}} \sum_{-k_y^{max}}^{k_y^{max}} \sum_{-k_z^{max}}^{k_z^{max}} |\vec{k}|^{-(n+2)/2} \left[k_y C_x sin(\vec{k} \cdot \vec{r} + \phi_x) - k_x C_y sin(\vec{k} \cdot \vec{r} + \phi_y) \right]. \tag{3.3.7}$$

We define the values for the k_i^{max} by the size of the grid (L_x, L_y, L_z), e.g. $k_x = 2\pi/L_x$.

We adjust the amplitude of the turbulent velocity field so that the velocity dispersion of the turbulent sphere is comparable to the equivalent galactic cloud. Then we change the mass of the sphere so that the virial parameters are similar. In Fig. 3.3.1 we present the column density plot of the initial state for Sphere A. The projected velocity field is superposed on the density plot. In Fig. 3.3.2 we show the 8 clouds with their masses, radii and virial parameters. Also, in Table 3.1 we have included the number of particles in each simulation, the factor F for increasing the resolution of the cloud, and the resolved SPH mass (M_r) compared to the Jeans mass for the cloud. To calculate M_J we consider a temperature of 25 K and a volume-based density.

3.4 Details of the simulations

Although observed clouds are very cold, $T \sim 10$ K, we performed isothermal simulations with 50 K which ensures that the Jeans mass is well resolved (Bate & Burkert 1997). We also ran simulations with 20 K, which gave similar overall results (see Fig. 3.4.1). In the left panel of the figure we show Cloud A simulated with 20 K, whereas on the right we show the results of the 50 K simulation. The global structure of both clouds is similar, but in the colder cloud the filaments

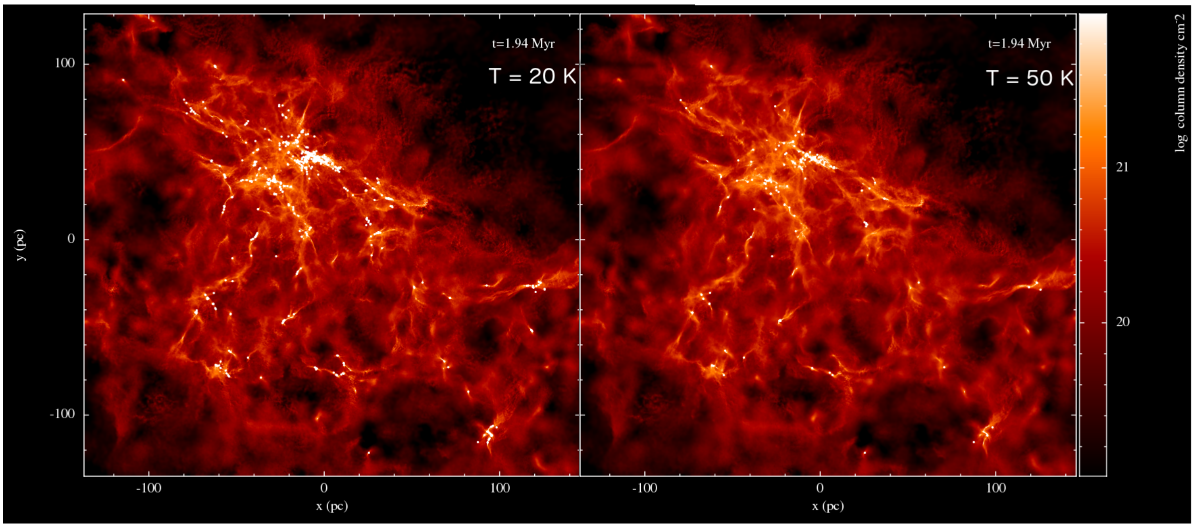

Figure 3.4.1: Column density plots of the clouds 2 Myr in the simulation. In the left panel we show Cloud A simulated at 20 K and in the right panel the same cloud modelled at 50 K.

manage to collapse further, and they are thinner, and produce more sink particles. We include sink particles similar to Bate et al. (1995) at densities of $\rho_{\rm sink} = 1.6 \times 10^4$ cm^{-3} with a sink radius $R_{\rm sink}$ = 0.1 pc using the implementation in Clark et al. (2008) (based on Jappsen et al. 2005). These parameters ensure that the minimum mass of a sink

$$m_{sink} = \frac{4}{3}\pi R_{sink}^3 \rho_{sink} > M_J, \tag{3.4.1}$$

is over the Jeans Mass for each cloud with a temperature of 50 K.

We run simulations of the GMCs for 16 Myr and the spheres for 24 Myr, which corresponds to at least 3 free fall times for all of the clouds. We do not include the galactic potential in our simulations (as described in Dobbs et al. 2006). We tested its impact on Early A, the biggest cloud, but there were no major differences. The rotational period of the galaxy at the radius of our clouds (~ 220 Myr) is much greater than the simulation time of our clouds, and the clouds do not traverse between the spiral arms and interarm regions in any of our calculations.

3.5 Comparing the evolution of the galactic clouds with the turbulent spheres

We demonstrate the column density plots of the eight clouds 5 Myr after the first star is formed in Figure 3.5.1 (except for Early A). In the galactic simulation Early A evolves into Cloud A after 10 Myr. Therefore, in Figure 3.5.1 we show Early A at 15 Myr, to compare it with Cloud A at 5 Myr. If we include the galactic potential Early A would move in an orbit around the galactic centre. For this plot we show Early A rotated accordingly. All clouds show a complex filamentary network and are highly structured, whether using the initial conditions from the galaxy, or the turbulent

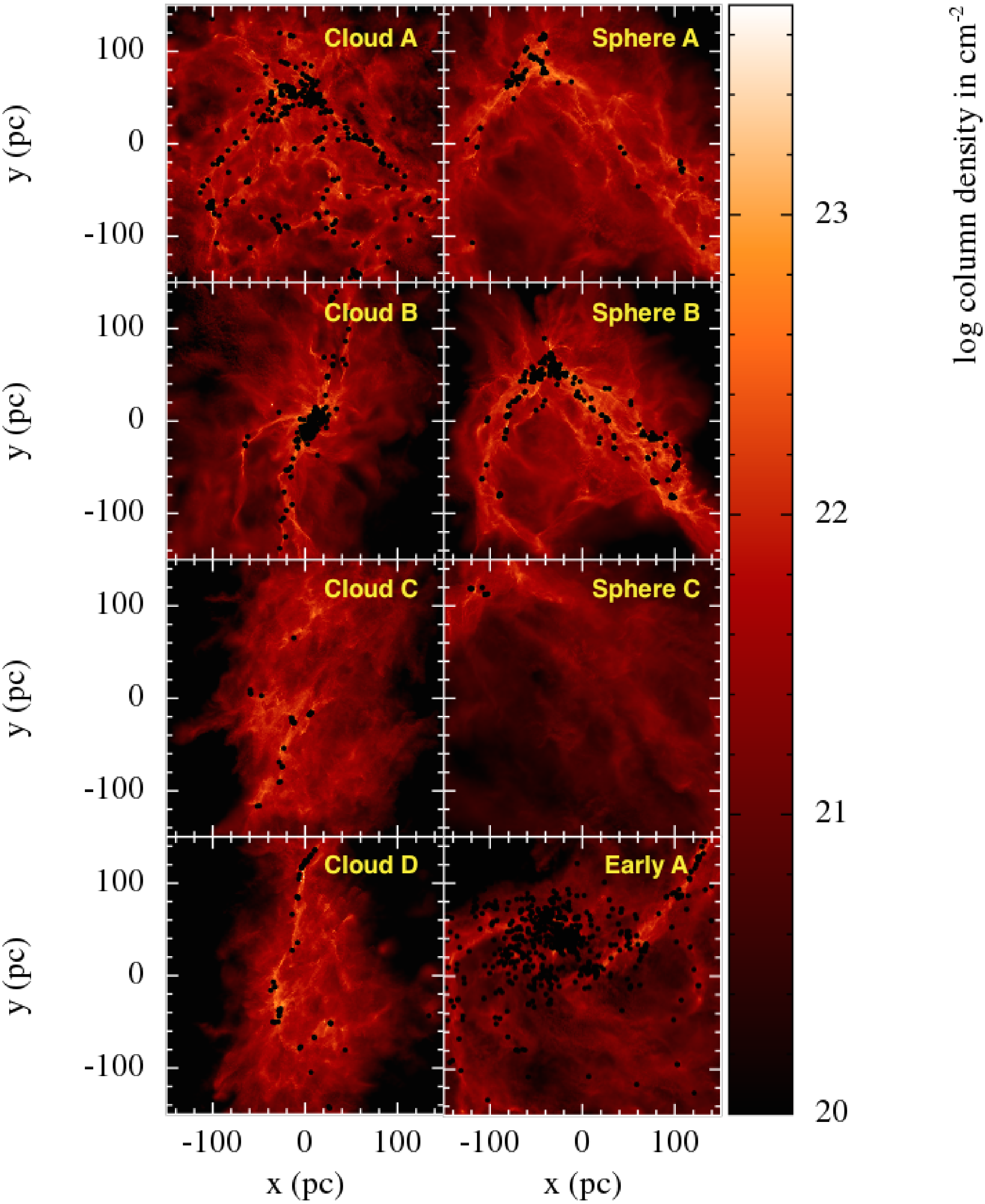

Figure 3.5.1: Column density plots of the clouds 5 Myr after the first star is formed are shown except for Early A (which is shown at 15 Myr to compare it with Cloud A). The sink particles are represented by black dots. The galactic clouds show a variety of density configurations, with Cloud A showing a rather complex network of filaments, Cloud B and Early A being dominated by one main long dense filament, and Cloud C and D appearing as rather diffuse and barely substructured cloud. Sphere A and B are dominated by two dense filaments that coalesce in the centre of the cloud. Sphere C has expanded so that we only show a portion of the cloud.

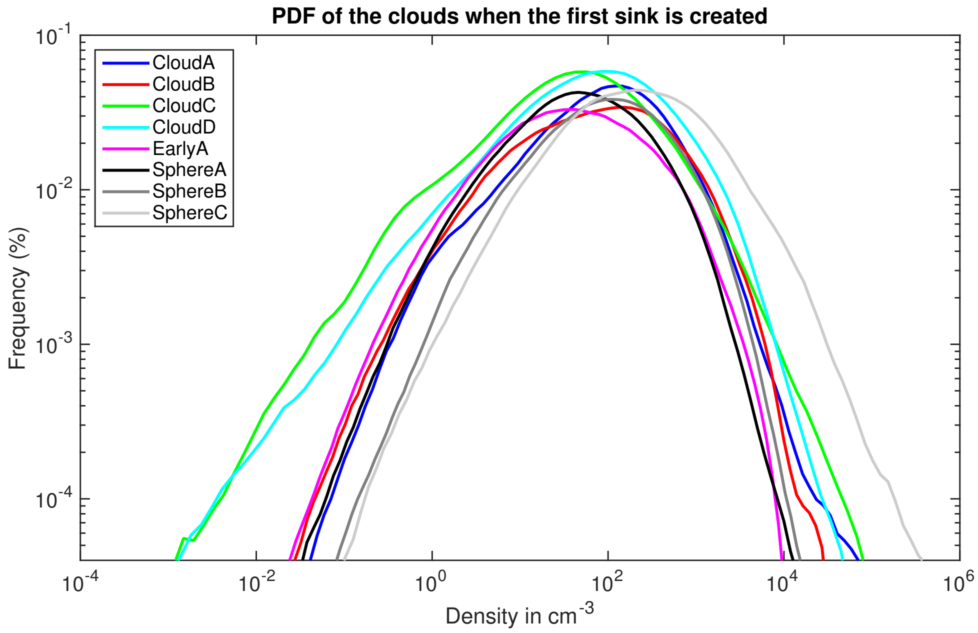

Figure 3.5.2: Density PDFs are shown for all the simulated clouds. The clouds have similar PDF compared with the turbulent spheres. Cloud C and D have more diffuse gas than the rest of the clouds, and as Sphere C has evolved for longer, the high density tail is larger.

spheres (except for Sphere C that has expanded considerably). The main structures in Clouds A and B reflect the galactic structure - the most dominant filaments in each are aligned with a spiral arm and inter-arm spur respectively. If we compare Cloud A and Sphere A we can see that star formation is more widespread in Cloud A, rather than restricted to one or two main filaments, as is the case for Sphere A. For both Cloud B and Sphere B, the cloud evolution and location of star formation is dominated by one or two long filaments. Both Cloud A and Early A have two main filaments and a cluster of stars in the centre. However, the evolution of Early A is altered by the large number of sink particles formed at early times. Cloud C and D have formed far fewer stars and has less dense features compared to all other clouds, even though they start from a similar unbound state (as e.g. Early A, even though it will evolve into a virialised cloud). If we zoom from the figure showing Sphere C, we find a similar structure to the other two spheres, with two long filaments coalescing in the centre. However, Sphere C is so unbound that it expands in our simulation with very few overdense areas.

In Figure 3.5.2 we show the density PDF (Probability Density Function, e.g. see Vázquez-Semadeni (1994)) for all the clouds at the time when the first sink particle is created. The PDFs show good agreement between the spheres and galactic GMCs. All PDFs are similar, except for Cloud C and D, which stand out for containing significantly more low density gas when compared to the other clouds. We observe that the PDF of Sphere C is shifted towards high densities, but this is because the first sink is created 12 Myr in the simulation, and although the cloud is globally unbound, turbulence has had more time to create highly dense areas in the filaments. In the first stages of the simulation, the PDFs for the turbulent spheres are obviously narrower in comparison to the rest of the GMCs.

In Figure 3.5.3 we show the star formation rate defined as SFR(t) = $\dot{M}_*$(t), where $\dot{M}_*$(t) is the time derivative of the mass contained in sinks. We have used bins of 0.1 Myr. In colours we show the SFR of the galactic clouds. The star formation process is similar for A, B and Early A, starting almost from initialisation, as these clouds already have overdense regions. Once the initial star formation burst is over, the SFR decreases during the remainder of the simulation because there is less gas available (as it has been accreted by the sinks). For Cloud C, the star formation rate behaves differently - it increases slowly, and is significantly lower than the other clouds during most of the simulation. For Cloud D the SFR is also lower compared to Clouds A and B, but after 5 Myr it is half way between A and B and Cloud C. This and the observation that Sphere C has a very low SFR, indicates that the initial resolution (or F) is not a factor. That said, there may be some selection effect from the simulations of Dobbs (2015) as they have higher resolution and stellar feedback, resolving the velocity field at smaller scales

In grey scale we depict the SFR of the spheres. We have set the origin of time when the first sink is formed. Sphere A, B and C need 7, 6 and 12 Myr to create the first sink respectively. Sphere A and B need another 4 - 5 Myr to reach the peak of the SFR, but at later times their SFRs are very similar to the GMCs.

Whilst the SFRs of Cloud A and B are in agreement with the spheres, Cloud C and D have lower SFR than Early A, but higher than Sphere C, even though these five clouds have similar virial parameters. We suspect this could be a consequence of the large scale velocity field. We include a velocity map of the clouds 5 Myr after the first sink is created in Figure 3.5.4. For Sphere A and B, the velocity field mainly traces the gravitational collapse in the main filaments where star formation happens. For Sphere C the velocity field also traces the gravitational collapse but the diffuse filaments are outside the range of Fig. 3.5.4 as the velocity field in Sphere C is clearly divergent. Cloud B also presents a velocity field dominated by the gravitational field. The velocity field for Cloud A and Early A shows stronger rotation, but there is still convergence in the centre where stars are forming. Cloud C has a particular velocity field inherited from the galactic simulation. It has a strong pair of divergent flows in the northern and southern regions, which results in the disruption of the cloud, inhibiting star formation. In Cloud D we can also notice these shear flows, although they are not as strong as in Cloud C, specially in the northern part of the cloud. This suggests that the shear flows in Figure 3.5.4 are responsible for the difference in star formation rate for Cloud C and D. The effects of the different velocity fields are clearer when visualising the evolution of the clouds and spheres in a movie.

If we define the total star formation efficiency as SFE = $M_*/M^o_{\rm cl}$ where M_* is the total mass contained in sinks and $M^o_{\rm cl}$ the initial mass of the cloud. The total star formation efficiencies we obtain for all cases are high ($\sim$ 50%) compared with the observed $\sim$ 5% (e.g. Bigiel et al. 2008; Evans et al. 2009). However, we have not included magnetic fields or feedback processes which

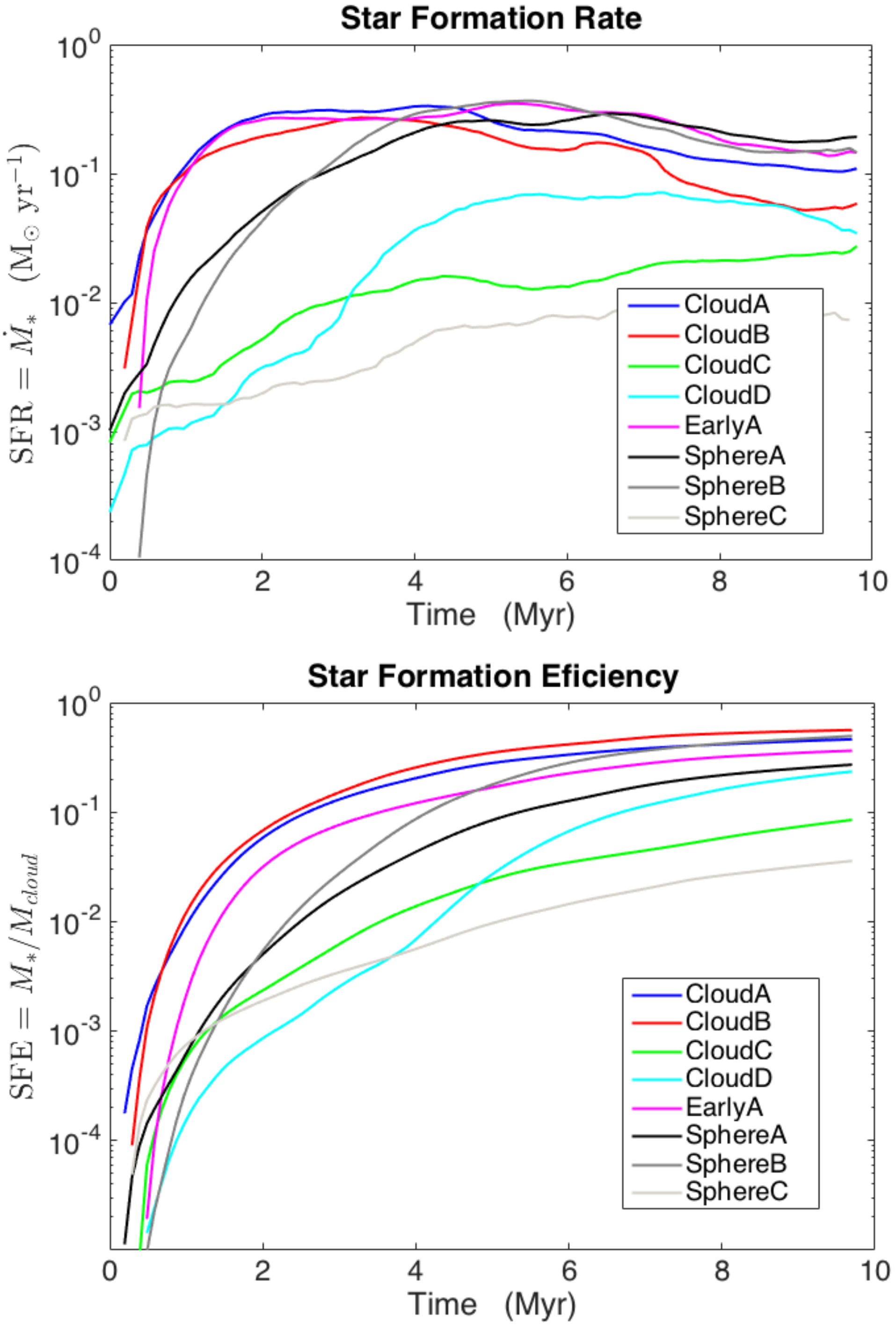

Figure 3.5.3: Top Panel: In colours we show the SFR for the galactic clouds. Clouds A, B and Early A present a similar behaviour creating stars in the beginning and gradually decreasing afterwards. The efficiency for Cloud C and D is much lower. In grey scale we show the SFR for the spheres. We have set the origin of time when the first sink is created. Bottom Panel, we show the star formation efficiency using the same colour scheme.

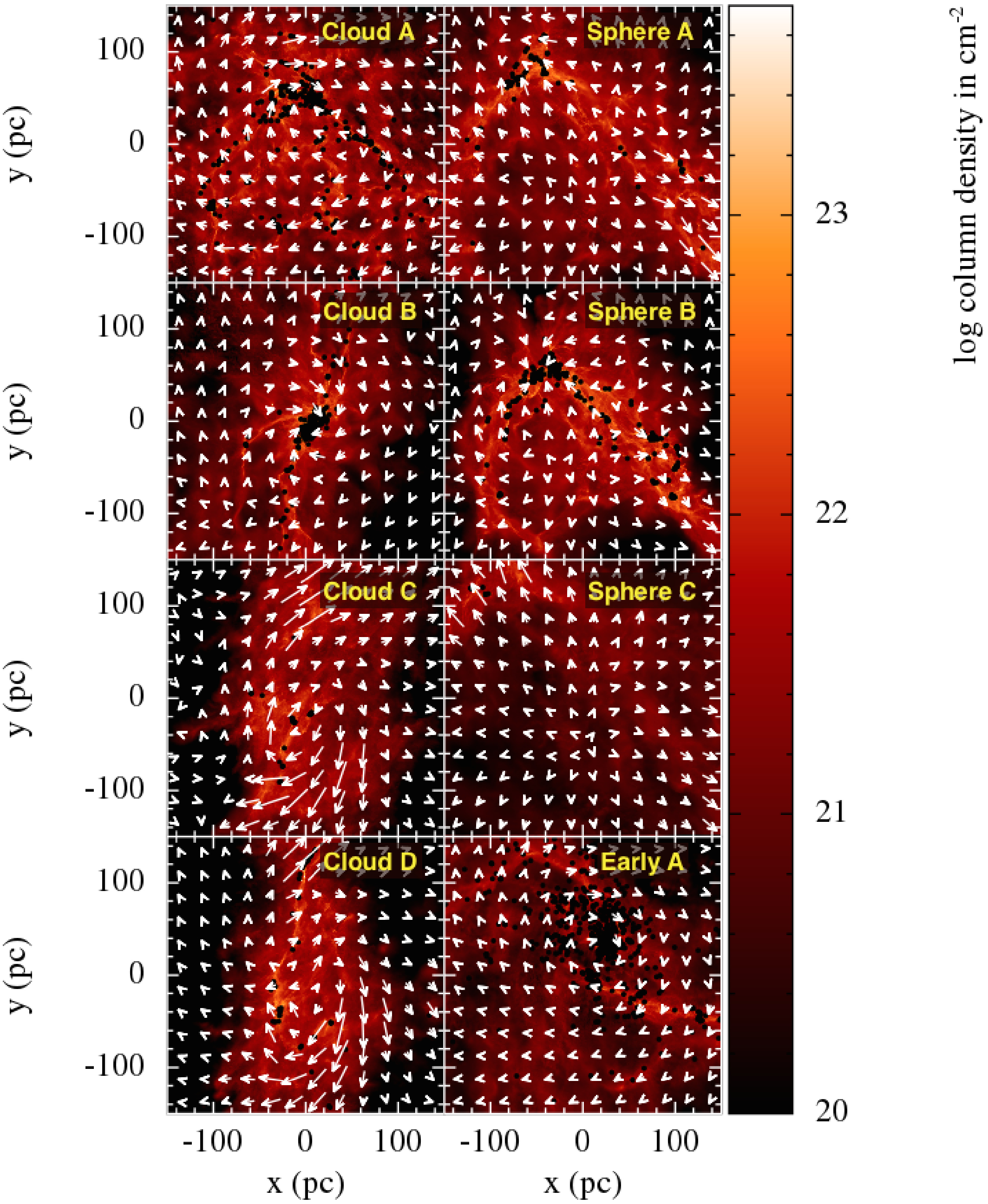

Figure 3.5.4: Projected velocity field (in white arrows) superposed on the column density maps for the clouds at 5 Myr, after the first star is formed (except for Early A that we show it at 15 Myr to compare it with Cloud A). In the spheres, the velocity field follows the direction of the gravitational collapse, and the highest velocities are in the vicinity of a filament. Cloud B also presents a velocity field dominated by gravitational collapse. For Early A and Cloud A the velocities inherited from the galactic simulations are more important than those arising from the gravitational collapse (except in the densest areas). The shear flows inherited from the galaxy inhibit star formation in Cloud C and D.

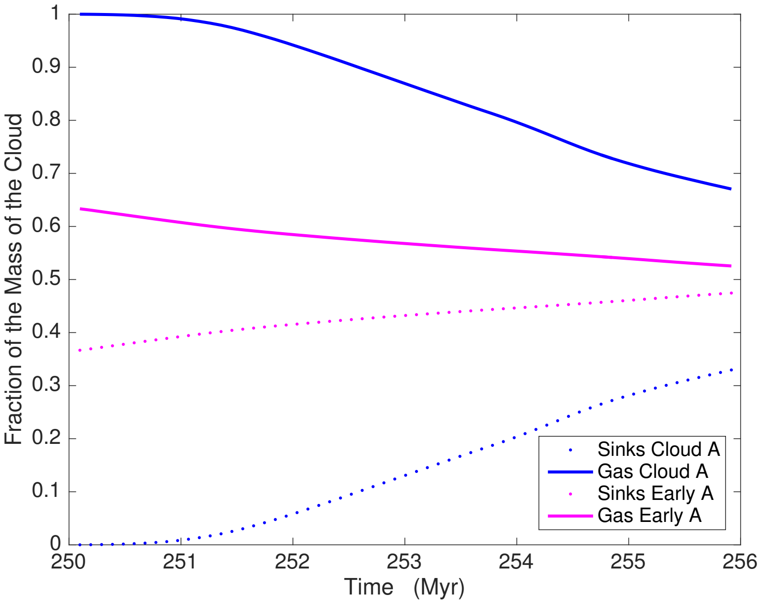

Figure 3.6.1: Evolution of the fraction of the mass of the cloud captured in sinks and in gas for Cloud A and Early A. In this case we are using the simulation time for the galaxy to compare both clouds at the same stage.

likely reduce the efficiencies to smaller values $\sim 10-20\%$ (e.g. Price & Bate 2009; Dobbs et al. 2011b; Federrath & Klessen 2012, 2013; Dale et al. 2014).

3.6 Star Formation History

The galactic clouds form stars immediately in the simulations. This suggests that starting with turbulent spheres misses some star formation history (SFH). Also there are differences in stellar content between the galactic simulations, Early A and Cloud A (the galactic simulations do not use sinks). We study the SFH by tracing back the gas that constitutes Cloud A 10 Myr earlier in the galactic simulation (Early A). In Fig. 3.5.1 we show Cloud A and Early A at 255 Myr in the galactic simulation time. We have rotated the column density plot of Early A as it would appear in the galactic simulation. We observe that the overall structure of both clouds is similar: both clouds have two long filaments coalescing in the centre of the cloud. However, they are different entities, even though they come from the same cloud in the galactic simulations. The filaments in Cloud A have denser gas compared to Early A. This is because Early A has been forming sinks for longer time ($\sim$ 10 Myr more), and these sinks have been trapping dense gas for a longer period of time.

In Fig. 3.6.1 we present the evolution of the fraction of mass of the cloud in the gaseous component (solid lines) and in sinks (dotted lines) for Cloud A and Early A. To avoid confusion we use the time in the galactic simulation, and show the first 6 Myr of Cloud A. Cloud A starts as entirely gaseous, and after 6 Myr, 30% of the mass is already in sinks. Initially Early A also starts as completely gaseous, but this occurs at 240 Myr. In the re-simulated clouds, Early A has

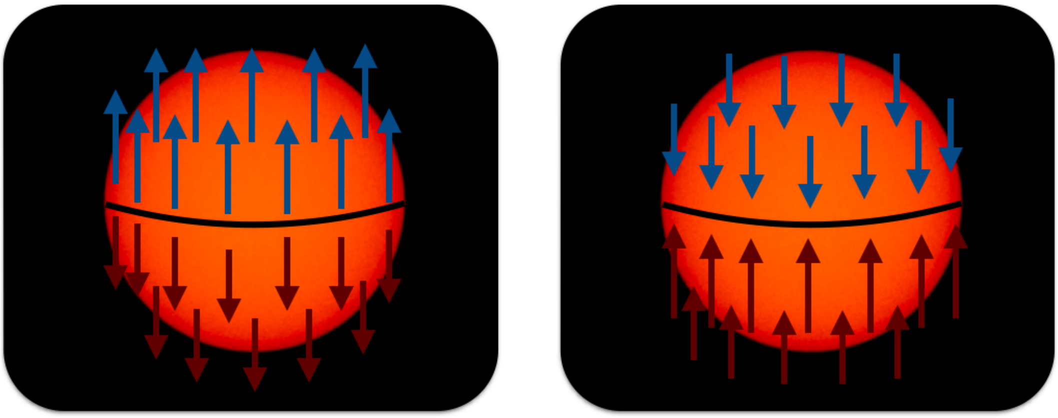

Figure 3.7.1: Example of two spheres of gas with a peculiar velocity field. On the right panel, we have a sphere that is being stretched out by a velocity field that points upwards in the northern hemisphere and downwards in the southern. On the left panel we have the opposite case. The average velocity for both spheres is close to zero. The velocity dispersion of both cases is similar, (as the average is zero) it is basically the average of the square of the modulus of the velocity

10 extra Myr to form more sinks. So, at 250 Myr, Early A has more than 30% of its mass in sinks. The overall virial state of the cloud also differs when the mass is in sinks or the gaseous component.

We expect the SFR to be reduced when including stellar feedback. The winds, HII regions, SNe will disperse the dense material around the sinks, stopping the accretion of gas by them. Thus we may expect the SFH of Cloud A and Early A to be more alike, as less gas is going to form stars, so the difference would be less extreme.

3.7 Characterizing the Velocity Field

The results from this chapter suggest that the velocity field inherited from the galactic simulations plays an important role in the star formation process. It seems worthwhile to try to characterise the velocity field using some parameters to assess the ability of a given cloud to form stars. The first parameter, already introduced in Chapter 1 is the virial parameter α. It gives us information about the global gravitational state of the cloud, by comparing the gravitational field with the velocity dispersion of the gas. One limitation of the virial parameter is that the velocity dispersion does not depend on the direction of the velocity field.

For a cloud with a random velocity field, with the gas in each part of the cloud moving in a different direction, the virial parameter can be a good indicator of star formation, as there are no preferred directions in the velocity field. On the other hand, if we imagine a spherical cloud divided in two hemispheres (like the one shown on the left panel of Fig. 3.7.1), and the velocity field points upwards in the northern hemisphere and downwards in the south, it is very unlikely that this cloud may form stars, as it will be dispersed. Even if the gravitational force of this special cloud is strong enough to eventually hold the cloud together, the star formation process will happen at later times compared to a sphere with a non-ordered velocity field. In contrast, for the other cloud represented on the right panel of Fig. 3.7.1, the velocity field is compressing the gas in the cloud facilitating the star formation process and yielding a faster and greater SFR. The average velocity for both clouds is equal to zero, and the velocity dispersion, as long as the amplitude of the velocity field is equal but reversed in sign, is the same for both hemispheres. If both spheres have the same mass, as the virial parameter depends only on the mass and velocity dispersion of the cloud, it will be the same for both spheres.

This oversimplified and extreme example shows us that a more detailed description of the velocity field is needed to characterise the star formation process. We are limited when studying the effect of the velocity field if we use as initial conditions turbulent spheres/boxes or colliding flows. In these cases we are imposing the initial velocity field via initial conditions. For colliding flows, we are artificially forcing a scenario similar to the right panel of Fig. 3.7.1. As our galactic clouds have complex morphologies and velocity fields inherited from the galactic simulation, it is easier to notice the effect of the velocity field.

We also characterise the velocity field in terms of the average of the radial component of the velocity defined as $\langle \vec{r} \cdot \vec{u} / \vec{r} \rangle$, and average axial component of the velocity defined as $\langle |\vec{r} \times \vec{u}| / \vec{r} \rangle$. In order to be able to compare different clouds we normalise these parameters using the velocity dispersion of each cloud. We define

$$\beta_u = \frac{1}{\sigma_u} \left\langle \frac{\vec{r} \cdot \vec{u}}{|\vec{r}|} \right\rangle, \tag{3.7.1}$$

and for the axial component we define

$$\gamma_u = \frac{1}{\sigma_u} \left\langle \frac{|\vec{r} \times \vec{u}|}{|\vec{r}|} \right\rangle. \tag{3.7.2}$$

With these three dimensionless parameters (α, β_u, γ_u) we may describe the gravitational and kinetic state of a given molecular cloud. For each timestep we calculate the average of the radial and axial components of the velocity of each particle and average it by the initial velocity dispersion of the cloud. As all particles have the same mass the results are mass averaged. When there are no sinks the SFR is zero, after which we calculate α, β_u, γ_u for the clouds from the moment when the first sink is created for a period of 10 Myr.

In Fig. 3.7.2 we show the evolution of the SFR for the clouds as the mass averaged virial parameter changes. Cloud C and D start from an unbound state and evolve into a bound state as they create filaments where sinks are formed.

We show the relation between the SFR and β_u in Fig. 3.7.3. We see that, in general, a negative β_u implies a high SFR. The results are mass averaged so the denser parts of the clouds have a higher contribution. That is why even though Cloud C and D are expanding globally, both

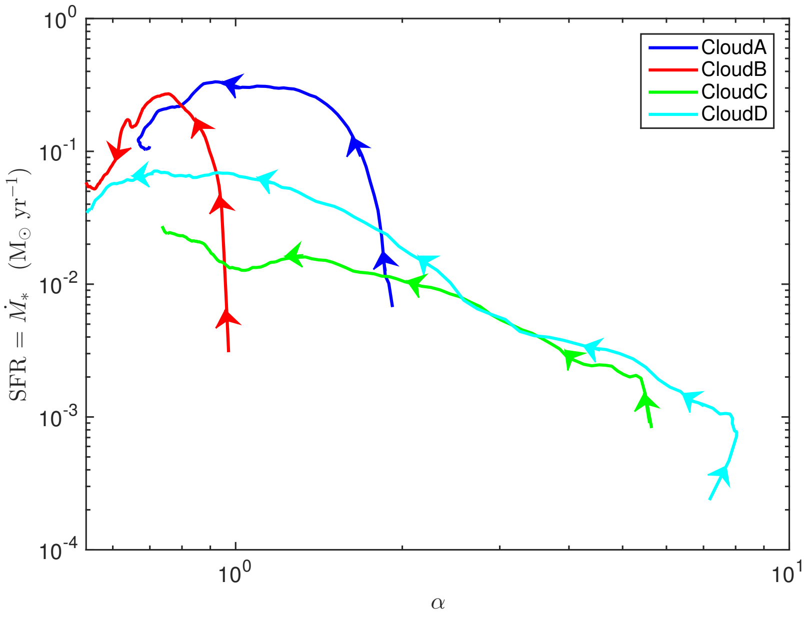

Figure 3.7.2: SFR for different clouds versus the virial parameter as it changes during the simulation. Even though Cloud C has a virial parameter comparable with Cloud D, its SFR is smaller than for the rest of the clouds. Clouds A and B also have similar SFR despite having different virial parameters.

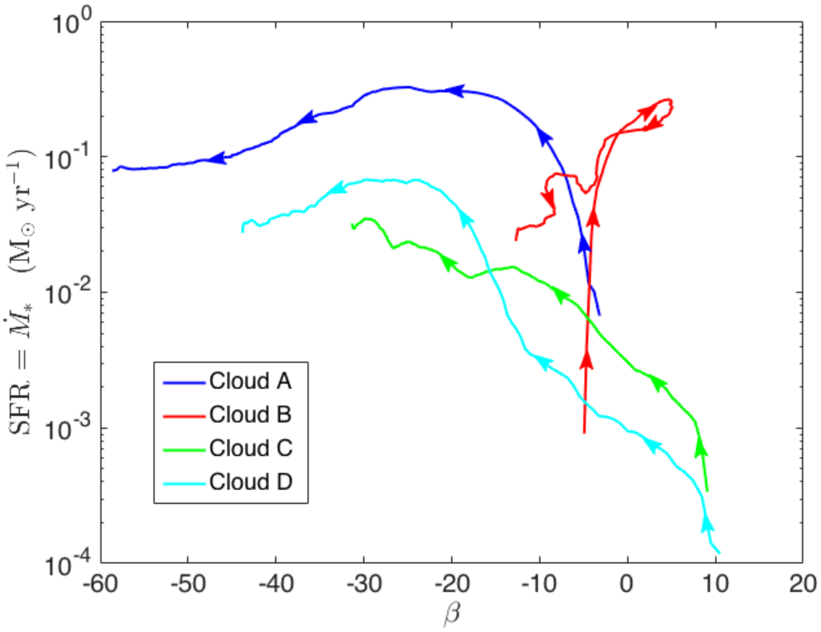

Figure 3.7.3: SFR for the different clouds versus β_u.

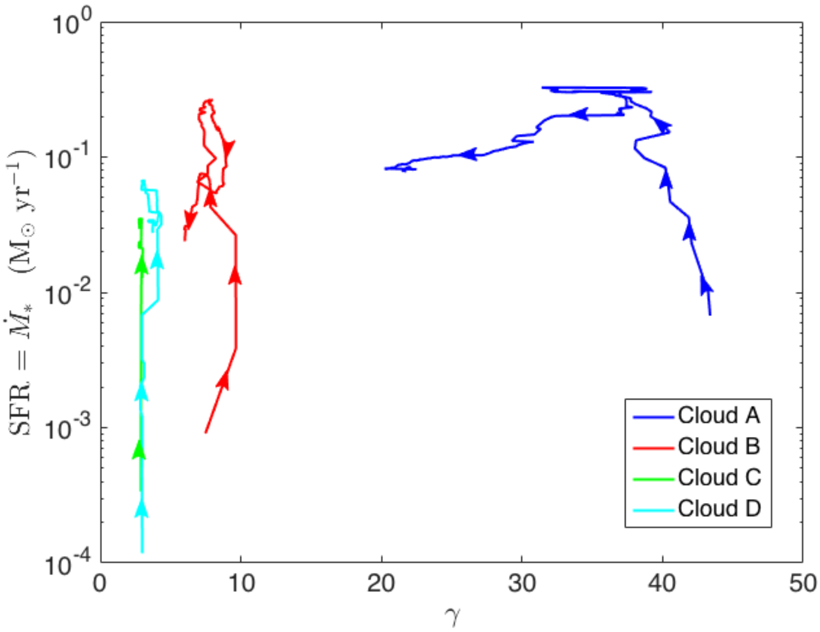

Figure 3.7.4: SFR for the different clouds versus γ_u.

have negative β_u as the simulation evolves. In Fig. 3.7.4 we show the average axial velocity of the clouds. Both clouds C and D are dominated by galactic shear, so their axial velocities are small during most simulation. Cloud A presents high values of γ_u as it is a cloud that is rotating. The horizontal branch of Cloud A at later times may indicate that the gas is being trapped in sinks and the remaining gas tends to be low density gas with high velocity.

These are preliminary results that have only been tested in 4 clouds. Ideally we need to test a greater sample of GMCs to study the influence of the velocity field characteristics in the star formation process. It would be interesting to study the evolution of clouds extracted from different parts of the galaxy and see how the values of α, β_u, γ_u are related to the SFR of each cloud, and compare them to other methods of studying the velocity field, such as the ones used by Federrath & Klessen (2012); Konstandin et al. (2015); Renaud et al. (2014).

3.8 Conclusions

In this chapter we showed the results of performing numerical simulations of clouds that have been extracted from galactic simulations. We selected five clouds and modelled three turbulent spheres that resemble three of the galactic clouds as closely as possible. We explored the differences and similarities of using turbulent spheres and GMCs as initial conditions to model the star formation process. The main advantage of the GMCs compared to the turbulent spheres is that they provide a wider variety of morphologies and velocity structures which influence the clouds' evolution and properties.

There are some clear similarities between the simulated GMCs and turbulent spheres, their PDFs are similar and generally the star formation rates are also analogous. Although the initial PDFs of the spheres are narrower, they eventually become comparable to most of the GMCs at late times. The spheres also have comparable SFRs once they have evolved and formed dense areas able to produce stars, except perhaps for Sphere C that constitutes a bad choice for initial conditions of a star forming cloud. However in some instances the GMCs can evolve to show different behaviour from each other, and the spheres, dependent on their initial conditions. The velocity field from larger (galactic) scales affects the morphology, kinematics and can effect the star formation in those clouds.

Another advantage with respect to turbulent spheres is that as well as modelling clouds in different environments (for example arm and inter-arm regions), we can also study different stages of their evolution. We found that Cloud A and Early A, which should be the same cloud, have different morphologies due to following sink particle creation in Early A. Our results are somewhat extreme, as we do not include feedback and the star formation rate in Early A is far too high. However this highlights that likely all simulations of isolated clouds will miss a previous star formation history. This problem can perhaps be lessened when using galactic or spiral arm scale simulations (Dobbs 2015) and tracing clouds back to earlier stages.

The influence of the inherited properties appears to have as much impact on star formation as the virial parameter of the clouds. For instance, Cloud C and Early A have similar virial parameters, but the star formation rate of Early A is more comparable to the other models, whereas in Cloud C it is partially inhibited by the inherited shear flows. Spheres can be divergent or convergent but they do not represent other aspects of the galactic flows such as shear. Our conclusions are in agreement with Federrath & Klessen (2012). They find that the compressive and solenoidal components of a turbulent velocity field (quantified by the mode mixture parameter b) have a large impact on star formation. This constitutes the main advantage of the GMCs, enabling different environments which would be difficult to reproduce with turbulent spheres.

In this chapter we have also described an attempt to characterise the star formation process in terms of two more dimensionless quantities (β_u, γ_u) in addition to to the virial parameter. However due to the limited number of clouds studied, we believe that we need to extend this analysis to a a more statistically representative sample of clouds, to be able to draw more solid conclusions.

4

Chemistry in Cold Galactic Molecular Clouds

"Chemistry is, well technically, chemistry is the study of matter. But I prefer to see it as the study of change."
– Walter White (Breaking Bad)

4.1 Introduction

In the previous chapter we produced simulated clouds to model the star formation process with more variety than the more conventional turbulent spheres. However, we used isothermal simulations at a low temperature, and we included no chemistry in our galactic clouds. In this chapter, we describe the ISM heating/cooling algorithm that provides a more realistic description for our simulated clouds and allows us to model a multiphase ISM. With stellar feedback (Chapter 5) gas will heat up to 10^6 K, and therefore we need to be able to model gas at a wide range of temperatures. We will also describe the models we have chosen to simulate the chemistry of H_2 and CO in our galactic clouds, so that we can trace the formation of molecular hydrogen from atomic. As H_2 is very difficult to observe, we will analyse the relationship between H_2 and CO in our clouds, producing synthetic observations of the clouds to calculate the X-factor in our simulations.

This chapter is organised as follows. First we describe the chemistry models used for H_2 and CO. Then we explain the cooling and heating processes we include. In the following section we present the tests we performed. The final section of this chapter details the different results from the simulations, thermal properties, and chemical abundances. We end comparing our clouds with observations producing synthetic maps of CO.

4.2 Chemistry Model

The ISM harbours a complex network of chemical reactions, involving a great diversity of molecules (from the simple H_2 to the complex PAHs) that contribute to heating and cooling. In this thesis we are mainly interested in modelling the formation of molecular hydrogen and CO. We choose H_2 because it is the most abundant molecule in the ISM and is where star formation occurs, and CO because it is widely used as a H_2 tracer.

4.2.1 H_2 Chemistry

H_2 is the most abundant molecule in the ISM. To model its creation and destruction we use a model based on Bergin et al. (2004) (also used in Pettitt et al. 2014; Dobbs et al. 2008). We consider the evolution of the concentration of molecular hydrogen as

$$\frac{dn(H_2)}{dt} = C(H) - D(H_2), \tag{4.2.1}$$

where C and D represent the creation and destruction of hydrogen respectively. The majority of the H_2 molecules forms in the surface of dust grains. We model this process in terms of a temperature-dependent grain formation rate of H_2, R_{gr}(T), in a similar way as Hollenbach et al. (1971)

$$R_{gr}(T) = 2.2 \cdot 10^{-18} S \sqrt{T} \quad (cm^3 s^{-1}). \tag{4.2.2}$$

The first term in R_{gr} is a constant and accounts for the relative average densities of dust and hydrogen on the ISM and other conversion factors. The following term S, represents the efficiency of the formation of H_2 in dust grains that we set to a constant value of $S = 0.3$, although in practice this efficiency depends on both the gas and dust temperature (Cazaux & Tielens 2004, and references therein). Lastly the $\sqrt{T}$ represents the thermal movement of the gas, and in conjunction with density, determines the probability of collision between gas and dust. The creation of hydrogen depends on the amount of atomic hydrogen and the total number of hydrogen atoms in a region, $n = n(H) + 2n(H_2)$, hence

$$C(H) = R_{gr}(T)\, n(H)\, n. \tag{4.2.3}$$

We consider two main processes for the destruction of H_2, the action of cosmic rays and photodissociation. We assume the effect of cosmic rays to be constant, $\zeta_{CR} = 6 \cdot 10^{-18}$ cm^3 s^{-1} (Bergin et al. 2004). This term is low unless the column density of molecular gas becomes large. We model the photodissociation by first considering the photodissociation for unshielded H_2. We assume its rate to be constant with $\zeta_o = 4.17 \cdot 10^{-11}$ cm^3 s^{-1}, for a cloud at T = 100 K with a density of 100 cm^{-2} and considering local thermodynamical equilibrium (Draine & Bertoldi 1996). This term represents the total number of photons available to dissociate a molecule of hydrogen in the proximity of a star. However, in a molecular cloud these photons can be absorbed and re-emitted at longer wavelengths by the dust and the H_2 itself. For the photons absorbed by dust we follow

Draine & Bertoldi (1996) and consider a factor of dust absorption:

$$f_{dust} = e^{-\tau_{d,1000}}, \tag{4.2.4}$$

where $\tau_{d,1000}$ is the optical depth of dust for the UV radiation at 1000 Å with value $\tau_{d,1000} = 2 \cdot 10^{-21}[N(H) + 2N(H_2)]$, where N(H) and N($H_2$) represent the column densities for atomic and molecular hydrogen respectively. Lastly the outer parts of molecular H_2 regions can also self-shield the inner parts of the cloud. For the self-shielding of H_2 we use the fitting formula from Draine & Bertoldi (1996):

$$f_{shield} = \frac{0.965}{(1 + x/3)^2} + \frac{0.035}{\sqrt{1+x}} e^{-8.5 \cdot 10^{-4} \sqrt{1+x}}, \tag{4.2.5}$$

where $x = N(H_2)/5 \cdot 10^{14}\ cm^2$ and we assume a Doppler broadening parameter $b = 3km/s$. Hence the total destruction of H_2 is

$$D(H_2) = [\zeta_{CR} + \zeta_o f_{shield} f_{dust}]\ n(H_2). \tag{4.2.6}$$

For the chemistry we consider that all the hydrogen is either in an atomic or molecular state, neglecting any amount of HII for these calculations, as we are modelling cold areas of the ISM. We define aH_2, the hydrogen abundance for each gas particle, as:

$$aH_2 = \frac{n(H_2)}{n(H) + 2n(H_2)}. \tag{4.2.7}$$

4.2.2 CO Chemistry

For modelling the chemistry of CO we also follow Pettitt et al. (2014) which is based on Nelson & Langer (1997). They consider a simplified model that assumes the direct transformation between C^+ and CO. The process starts with an ionised atom of carbon that interacts with a molecule of hydrogen creating a hydrocarbon and emitting the excess energy with a photon:

$$C^+ + H_2 \rightarrow CH_2^+ + \gamma. \tag{4.2.8}$$

The rate of this reaction is defined as k_o. CH_2^+ interacts with the surrounding H_2 rapidly becoming either CH or CH_2 (denoted by CH_x). This reaction is much faster than Eq. 4.2.8. Lastly, the resulting hydrocarbon CH_x interacts with neutral oxygen to obtain CO:

$$O + CH_x \rightarrow CO + H_x + \gamma. \tag{4.2.9}$$

Once the CO is created, it is a relatively stable molecule, and it is destroyed mainly by photodissociation. Nelson & Langer (1997) do not consider self-shielding for the CO. As for the H_2 we model the CO production rate as

$$\frac{dn(CO)}{dt} = C(C^+) - D(CO), \tag{4.2.10}$$

where C and D stand for the rates of creation and destruction of CO. For the creation of CO we consider

$$C(C^+) = k_o n(C^+)\, n\, \beta, \tag{4.2.11}$$

where $k_o = 5 \cdot 10^{-16}$ ($cm^3 s^{-1}$) is the rate of Eq. 4.2.8. β is a measurement of the rate at which Eq. 4.2.9 occurs, and it is defined as

$$\beta = \frac{k_1 X(O)}{k_1 X(O) + G_o[\zeta_{CH_x}/n(H_2)]}, \tag{4.2.12}$$

where $k_1 = 5 \cdot 10^{-10}$ ($cm^3 s^{-1}$) and X(O) is the numerical abundance of neutral oxygen. G_o represents how much the UV field differs from the standard ISM value (Habing 1968), and we consider it to be standard ($G_o = 1$). The factor ζ_{CH_x} accounts for the photodissociation of the hydrocarbon:

$$\zeta_{CH_x} = 5 \cdot 10^{-10} e^{-\tau_{d,1000}}. \tag{4.2.13}$$

We assume that the formation of CO only happens in the densest (and therefore molecular) parts of our simulation, and that is why for calculating $\tau_{d,1000}$ for CO, we use the column density of H_2. For the destruction of CO we consider only photodissociation from UV sources (mainly nearby OB stars). Hence, if $\zeta_{CO} = G_o \cdot 10^{-10} e^{-\tau_{d,1000}}$ then

$$D(CO) = \zeta_{CO}\, n(CO). \tag{4.2.14}$$

To calculate the column densities we assume a fixed length L_{chem} that we set as a parameter at the beginning of the simulations

$$N(H_2) = L_{\rm chem}\, n(H_2), \tag{4.2.15}$$

$$N(CO) = L_{\rm chem}\, n(CO). \tag{4.2.16}$$

Similarly to the H_2 we define aCO as the CO abundance.As we are selecting GMCs from the galactic scale simulations, our clouds are denser on average than the galaxy they come from. This increases the column density of H_2, that is used to calculate the self-shielding of H_2, and the dust absorption for both H_2 and CO.

4.3 Cooling-Heating Model

In reality molecular clouds likely consist of an intermixed gas: the molecular regions are surrounded by CNM and WNM. The temperature range in the ISM is still wide (10 - 10^4 K Glover & Mac Low 2007a; Field et al. 1969) without including stellar feedback. In the previous chapter we performed isothermal simulations of molecular clouds at very low temperatures, without considering the different phases of the ISM. To simulate the thermodynamics of our clouds, we use one of the most complex models available, detailed in Glover & Mac Low (2007a).

Table 4.1: Different cooling mechanisms considered by Glover & Mac Low (2007a) ordered by the temperature range where they are more effective.

Temperature Range	Process	Reference
T > 8000 K	Resonance lines for H, He and another heavy elements	Sutherland & Dopita (1993)
T < 10000 K	Interaction of electrons with dust grains and PAH	Wolfire et al. (2003)
T ~ 2000 K	Collisions of C^+ with H_2, neutral hydrogen and free electrons	Silva & Viegas (2002)
T ~ 2000 K	Collisions of O with H_2, neutral hydrogen and free electrons	Silva & Viegas (2002)
T ~ 2000 K	Collisions of Si^+ with H_2, neutral hydrogen and free electrons	Silva & Viegas (2002)
T < 200 K	Molecular Transitions of H_2 (transitions $J = 2 \rightarrow 0$ and $J = 3 \rightarrow 1$)	Le Bourlot et al. (1999)
$T_{gas} > T_{dust}$	Collisional transfer of energy between gas and dust	Hollenbach & McKee (1989)

In Chapter 2 we defined the specific internal energy of a gas particle in GADGET2 as

$$e_j = \frac{A_j(s)}{\gamma - 1}\rho_j^{\gamma-1}. \tag{4.3.1}$$

For the isothermal runs the entropic function $A_j(s)$ remains constant for all the particles. However, in a non-isothermal environment each gas particle suffers a net loss (or gain) of temperature that we express as

$$\Lambda = \Lambda_{cool} + \Gamma_{heat}, \tag{4.3.2}$$

where Λ_{cool} accounts for the net heat loss of the gas due to various effects, and Γ_{heat} the net heat gain. It is worth noting that Λ is positive when the gas loses heat and negative when it gains heat. We have modified our version of GADGET2 so that Eq. 4.3.3 is now

$$e_j = \frac{A_j(s)}{\gamma - 1}\rho_j^{\gamma-1} - \Lambda. \tag{4.3.3}$$

To compute the value of Λ for each particle we have included the Glover & Mac Low (2007a) subroutines in our version of GADGET2 . These subroutines allow a wide range of temperatures ($T \sim 10$ - 10^4 K) and in each regime, different species dominate the cooling and heating budget. We include a summary of the different processes modelled in Table 4.1.

Table 4.2: Different heating mechanisms considered by Glover & Mac Low (2007a).

Heating Vector	Process	Reference
UV	Photoelectric emission that happens in PAHs , and dust grains when subjected to a UV field	Wolfire et al. (2003)
FUV	Photodissociation of H_2 by far-ultraviolet radiation	Black & Dalgarno (1977)
FUV	Excitation of H_2, by far-ultraviolet radiation	Draine & Bertoldi (1996)
Dust	H_2 formation on dust grains,	Duley & Williams (1993)
Cosmic Rays	Ionisation by cosmic rays,	Goldsmith & Langer (1978)
Dust	Collisional transfer of energy between gas and dust	Hollenbach & McKee (1989)

We have not included in Table 4.1 the cooling due to collisional dissociation of H_2 and collisional ionisation of H, because the authors claim that those processes are not very essential in their simulations. Glover & Mac Low (2007a) treat all the cooling from emission lines in the optically thin limit. This approximation is good for practically the whole range of temperatures and densities, except in the very dense areas of the clouds. However, in these areas most of the hydrogen is in molecular form, and the majority of the carbon and oxygen is trapped in CO molecules. Under these conditions the photoelectric heating by dust ceases to be an efficient way of heating, and the main coolant are the lines of C^+ and C (see Fig. 4.3.1). Hence, Glover & Mac Low (2007a) claim that the errors of extending the optically thin limit to this regime are not so relevant.

In Table 4.2 we show all the processes that Glover & Mac Low (2007a) consider in their heating algorithm which determine Γ. They neglect the heating by soft X-rays, and the photoionisation of carbon and silicon, considering them not as crucial as the processes mentioned in Table 4.2. In Fig. 4.3.1, extracted from the thesis of Pettitt (2014), we present the cooling and heating curves given by the mechanisms listed in Tables 4.2 and 4.1.

To calculate the column densities needed in the Glover & Mac Low (2007a) cooling and heating subroutines we employ a fixed length (50 pc) which is representative of the dense structures in the interior of our clouds. We also define two more parameters T_{max} and T_{min} as the limits for the temperature of each particle.

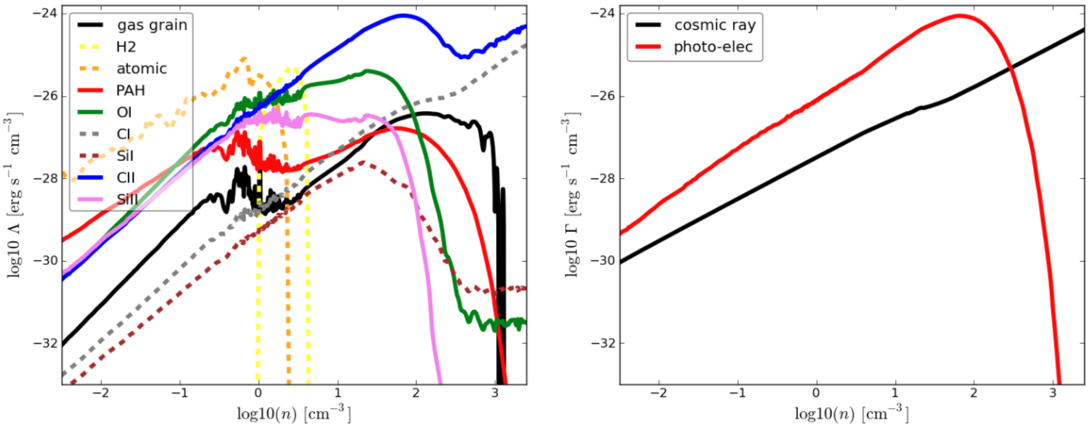

Figure 4.3.1: Main cooling and heating process as a function of the particle density. Extracted from Pettitt (2014).

4.4 Integration Scheme

The size of the timestep is limited by the Courant condition C_{cfl}. This means that the internal energy of a SPH particle affects its individual timestep by changing the speed of sound of the gas. As we introduce the cooling and heating we are modifying the temperature of the gas, and therefore this should be reflected on the individual timestep of the particles. To avoid a large and instantaneous increase in the internal energy of the gas particles, we have modified GADGET2 so that the fraction of change of the internal energy of the particle is always smaller than a fixed parameter $\eta_{\mathrm{cool}} = 0.3$ (following Glover & Mac Low (2007a)). Hence, the internal energy satisfies

$$\eta_{\mathrm{cool}} \leq \frac{|e_j^{\mathrm{old}} - e_j^{\mathrm{new}}|}{e_j^{\mathrm{old}}}. \tag{4.4.1}$$

If the change in internal energy is greater than η_{cool} for the next integration, we will reduce the integration timestep accordingly. We include Δt_{cool} in the global check along with the gravitational and hydrodynamical timestep (and select the smallest one). The new internal energy after calculating the cooling/heating rate (e_j^{new}) is

$$e_j^{\mathrm{new}} = e_j^{\mathrm{old}} - \Lambda\ \Delta t_{\mathrm{cool}}, \tag{4.4.2}$$

hence we can define the cooling timestep (Δt_{cool}) as

$$\Delta t_{\mathrm{cool}} = \frac{|e_j^{\mathrm{old}} - e_j^{\mathrm{new}}|}{\Lambda}. \tag{4.4.3}$$

In general, the introduction of cooling-heating reduces considerably the global timestep of the simulations. However given the short timescales for the chemistry, the general timestep of a particle can be too large to compute the chemistry with reasonable accuracy and numerical stability. Hence for integrating chemistry we use a subcycling scheme (using an adapted algorithm from Pettitt et al. (2014)). For a given general timestep ($\Delta t_{\rm o}$) we divide the integration process into smaller stages. For each particle we calculate the change in the $\rm H_2$ composition using the equation 4.2.1 (and subsequent). With that rate $\Delta n(H_2)$, we calculate the timestep needed to destroy all the molecular hydrogen in that particle

$$0 = n(H_2) + \Delta n(H_2)\,\Delta t_{\rm test} \rightarrow \Delta t_{\rm test} = -\frac{n(H_2)}{\Delta n(H_2)}. \tag{4.4.4}$$

If $\Delta t_{\rm test}$ is negative, it means that we are generating $\rm H_2$ in that timestep. If $\Delta t_{\rm test} > 0$ it means that in the current timestep $n(H_2)$ will become negative. We avoid it by dividing the integration into smaller timesteps ($n_{\rm steps}$). In doing so, we recompute the ratio of $\rm H_2$/H on each stage enhancing the stability of the integration scheme. By default we perform the $\rm H_2$ integration in $n_{\rm steps} = 200$ (even if $\Delta t_{\rm test} < 0$). However this number is increased if the depletion time $\Delta t_{\rm test}$ is 20 times smaller than the current timestep $\Delta t_{\rm o}$

$$\frac{\Delta t_{\rm o}}{\Delta t_{\rm test}} > 20. \tag{4.4.5}$$

Therefore $n_{\rm step} = MAX(10\frac{dt_{\rm o}}{\Delta t_{\rm test}}, 200)$ and the subcycling timestep is

$$\Delta t_{\rm H_2} = \frac{\Delta t_{\rm o}}{n_{\rm step}}. \tag{4.4.6}$$

We perform the integration on each $\Delta t_{\rm H_2}$ by calculating $\Delta n(H_2)$ and the molecular and atomic concentrations of hydrogen using

$$n(H_2)_{\rm i+1} = n(H_2)_{\rm i} + \Delta n(H_2)\,\Delta t_{\rm H_2}, \tag{4.4.7}$$

and

$$n(H)_{\rm i+1} = n_{\rm p} - 2\,n(H_2)_{\rm i+1}. \tag{4.4.8}$$

Where $n_{\rm p}$ is the total number of hydrogen atoms available. We may have to subcycle further to account for the smaller timescales of CO. Hence, within the $\rm H_2$ subcycle loop we calculate the change in CO concentration ($\Delta n(CO)$) using Eq. 4.2.10, and calculate a subcycling timestep for CO using a similar analysis

$$\Delta t_{\rm CO} = \frac{\Delta t_{\rm H_2}}{n_{\rm stepCO}}. \tag{4.4.9}$$

To clarify, the global simulation timestep $\Delta t_{\rm o}$ may be limited by the gravitation force, the hydrodynamics or the ISM cooling and heating. For each particle GADGET2 selects the smallest of these three quantities. Once the chemistry subroutine is called, we integrate using Δt_{H_2}, which is a fraction of $\Delta t_{\rm o}$, to compute the evolution of $\rm H_2$. Lastly, we use $\Delta t_{\rm CO}$ (a fraction of Δt_{H_2}) to calculate the evolution of CO. In general,

$$\Delta t_{\rm o} > \Delta t_{H_2} > \Delta t_{\rm CO}. \tag{4.4.10}$$

4.5 Tests

To test the cooling-heating algorithm, we perform a simulation of a galactic disk with an initial temperature of $T = 2000$ K and run it in the SPHNG code used in Dobbs et al. (2014a) and in our version of GADGET2 . The results are presented in Fig.4.5.1. The range of temperatures is similar, although the turning point in our version of GADGET2 is shifted towards smaller densities.

Then we compare our version of the chemistry with the data from Pettitt et al. (2014). In Fig. 4.5.2 we show the abundances of H_2 and CO versus the overall density of the gas. We present our results in Fig. 4.5.3. Here we are comparing a GMC (Cloud A) with a whole galaxy allowing us to reach higher densities. The overall behaviour of the chemistry is comparable, changing the slope around 10^{-23} g cm^{-3}. Both models show signs of saturation at high densities, corresponding to all the hydrogen in molecular state and all the carbon contained in CO molecules.

We test the chemistry further by comparing the evolution of the most and least virialised clouds (B and C) with a turbulent box of similar characteristics. The box has dimensions of 150 pc, a total mas of $4 \cdot 10^6$ M$_\odot$, and it is simulated with 10^6 particles each with a velocity that ranges randomly from -1 km s^{-1} to +1 km s^{-1} in any direction. We initialise the gas with a temperature of 50 K and run it for 5 Myr. We use the same $L_{\rm chem}$ and $L_{\rm cool}$ as for the clouds. In the following figures we show the mass averaged fraction of H and C in molecular form compared to the total density of the cloud. To calculate it, we bin the number density in 50 intervals and add the H_2 or CO abundance in each interval dividing it by the total number of particles in that density bin. As we are basically counting SPH particles (which have the same mass) the results are mass averaged. Lastly we normalize the molecular content, so that both quantities are equal to one when all the available H or C is in molecules.

If we compare our H_2 abundances (Fig. 4.5.4) with the results from Glover & Mac Low (2007b) (Fig. 4.5.5) we find that our model produces H_2 in a similar manner, although in Glover & Mac Low (2007b) the cloud becomes molecular at lower densities. There is a difference between the two clouds, Cloud C being able to produce hydrogen at lower densities. The turbulent box does not have time to reach number densities over 1000 cm^{-3}, but its behaviour is similar to the less virialised Cloud C. It is counter intuitive that the less virialised cloud is more molecular at a given density than Cloud B. This may be due to the fact that we are using the same column length to calculate the extinction, even though the morphology of the clouds is different. As we can notice on the column density plots from the previous chapter Cloud B is substantially denser and therefore should have a larger $L_{\rm chem}$. The effect at high densities is not so important, as the gas is fully molecular for $n > 10^5$ cm^{-3} in both cases.

For the case of the CO we present the mass averaged fractions in Fig. 4.5.6 and compare them with the results from Glover & Clark (2012) in Fig. 4.5.7. In Glover & Clark (2012) they compare different CO algorithms, and one of them is the Nelson & Langer (1997), labeled in the figure as NL97. We observe that the results are also similar, saturating around 10^3 cm^{-3}.

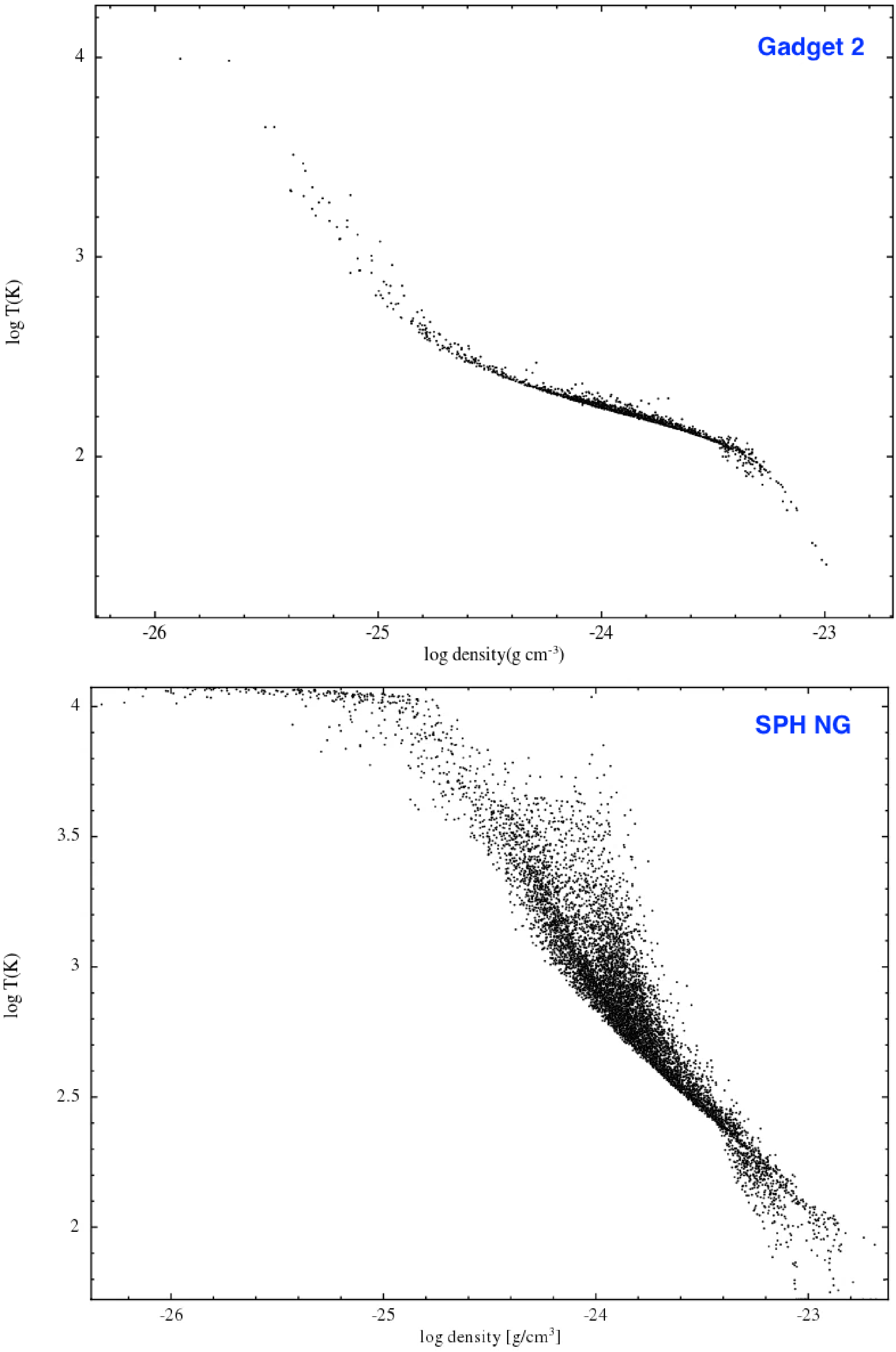

Figure 4.5.1: Temperature versus Density Histogram.

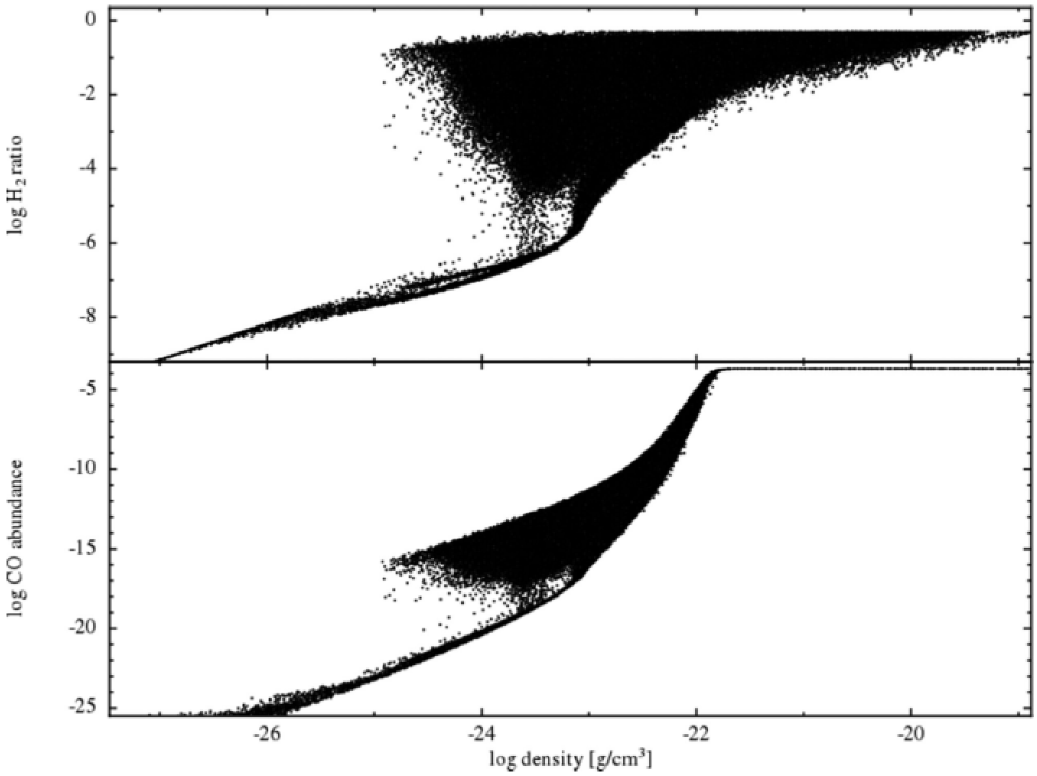

Figure 4.5.2: H_2 (top) and CO abundance (bottom) versus the particle density of a four armed disk galaxy (from Pettitt et al. (2014)).

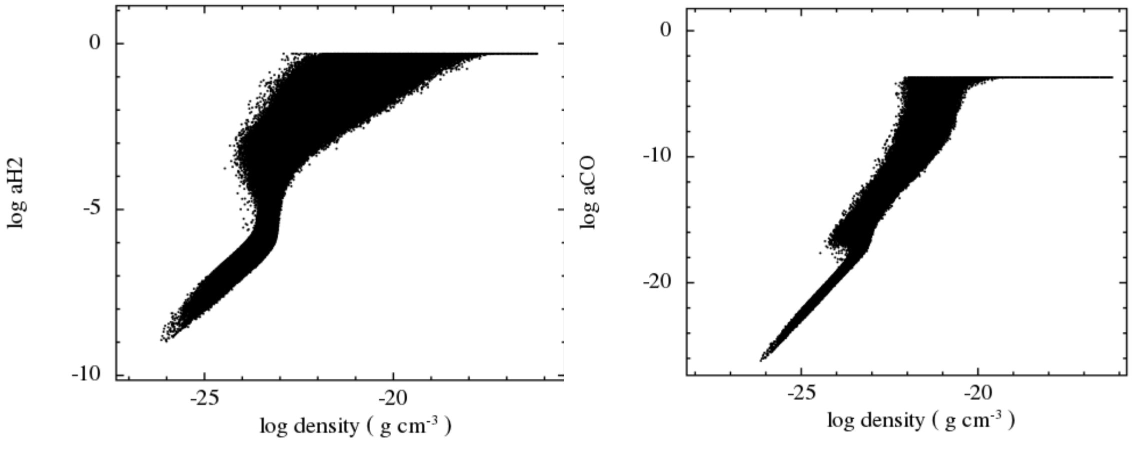

Figure 4.5.3: Abundances of H_2 and CO vs. SPH particle density for Cloud A.

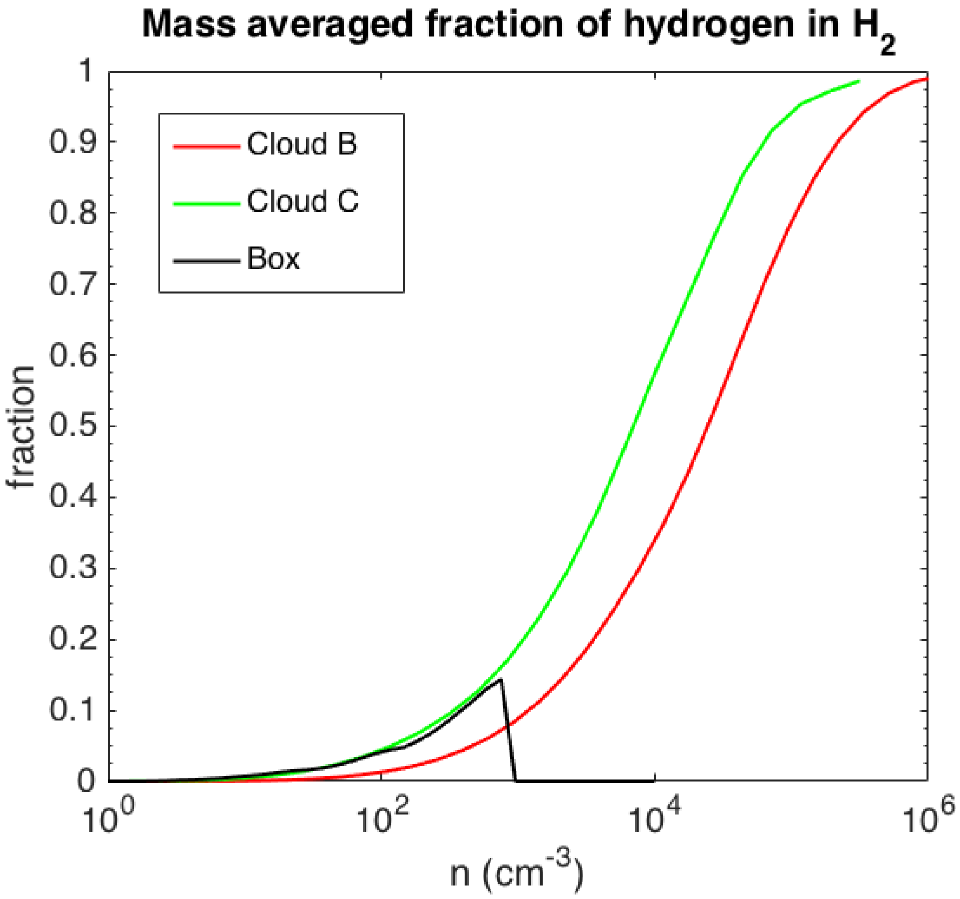

Figure 4.5.4: Mass averaged H_2 abundance in our models.

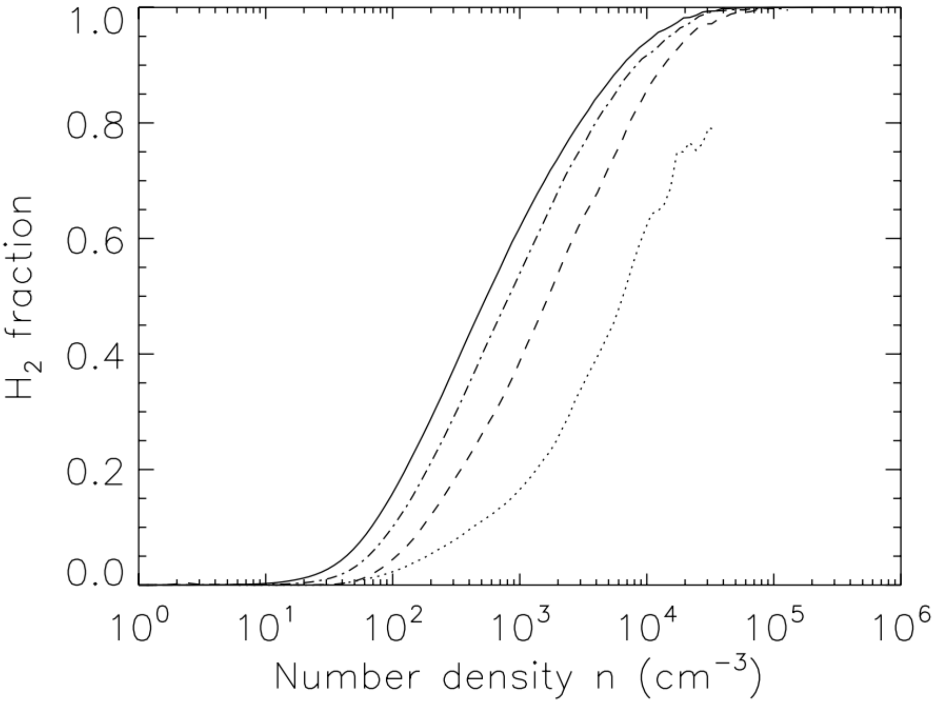

Figure 4.5.5: Mass averaged H_2 abundance from Glover & Mac Low (2007a).

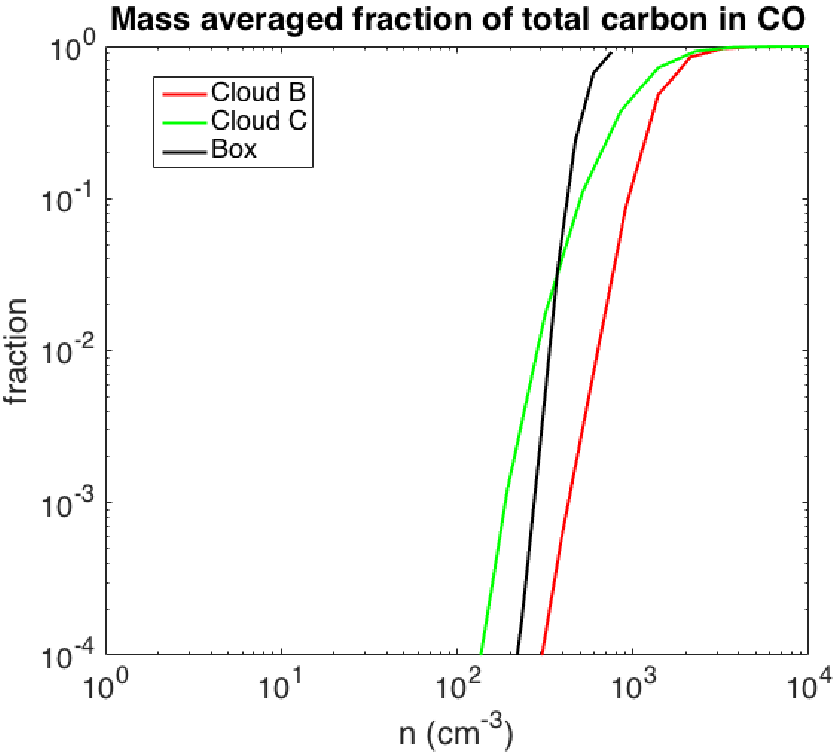

Figure 4.5.6: Mass averaged CO abundance in our models.

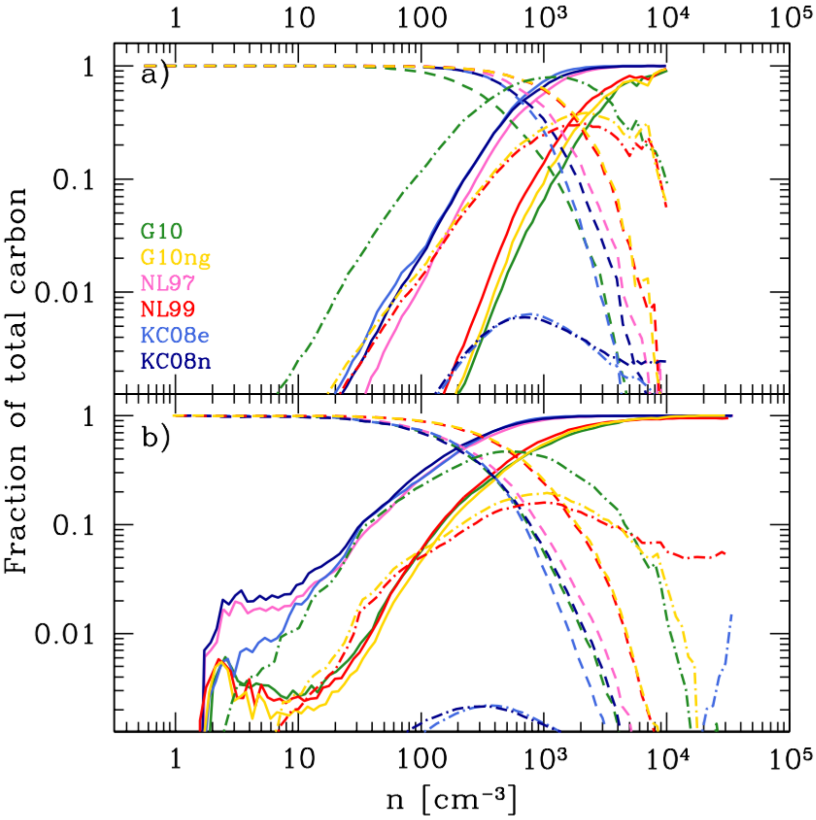

Figure 4.5.7: Mass averaged CO abundance from Glover & Clark (2012).

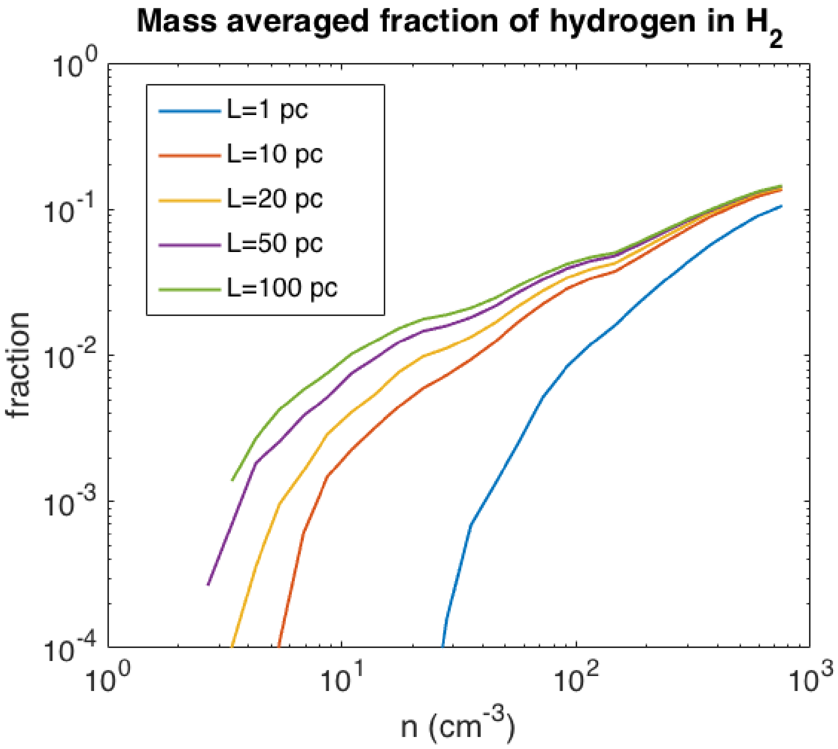

Figure 4.5.8: Hydrogen molecular fraction vs density for different column density lengths

4.5.1 Dependance of the chemistry on the Extinction

To calculate column densities we use a very simple method (see Eq. 4.2.15, 4.2.16), especially when compared to TREECOL, or use the density gradient as suggested by Gnedin (2014). Our chemistry models of H_2 and CO depend on the extinction via the dust absorption fraction $f_{\rm dust}$ and the shelf shielding of H_2. To calculate these two magnitudes we use column densities of H_2 calculated with a fixed length, and therefore our estimation of $N(H_2)$ may have an impact on the chemistry of our clouds. In this section we perform a series of tests in the turbulent box, to avoid the effect of the inherited properties of the GMCs. We run the same turbulent box described above, but considering different $L_{\rm chem}$ = 1, 10, 20, 50 and 100 pc.

We show the evolution of the mass averaged H_2 fraction of the box in Fig. 4.5.8. At relatively high densities the effect of the different $L_{\rm chem}$ is not so aparent (especially if $L > 10$ pc). The bigger differences occur in the diffuse medium. In this regime a larger $L_{\rm chem}$ implies a better self-shielding of H_2, reducing the photodissociation rate.

The case for the CO is different. We show the results of our simulations in Fig. 4.5.9. For number densities in the range $10 - 10^2$ cm^{-3} the difference between the models is not very large (except for the case of $L_{\rm chem}$ = 1 pc, where the destruction of CO (see Eq. 4.2.14) caused by the photodissociation from UV sources, is high as the extinction is reduced). However, we observe considerable differences (a few orders of magnitude) for the effect of different $L_{\rm chem}$ at number densities larger than $n \sim 10^2$ cm^{-3}. In Nelson & Langer (1997) the creation of CO is regulated

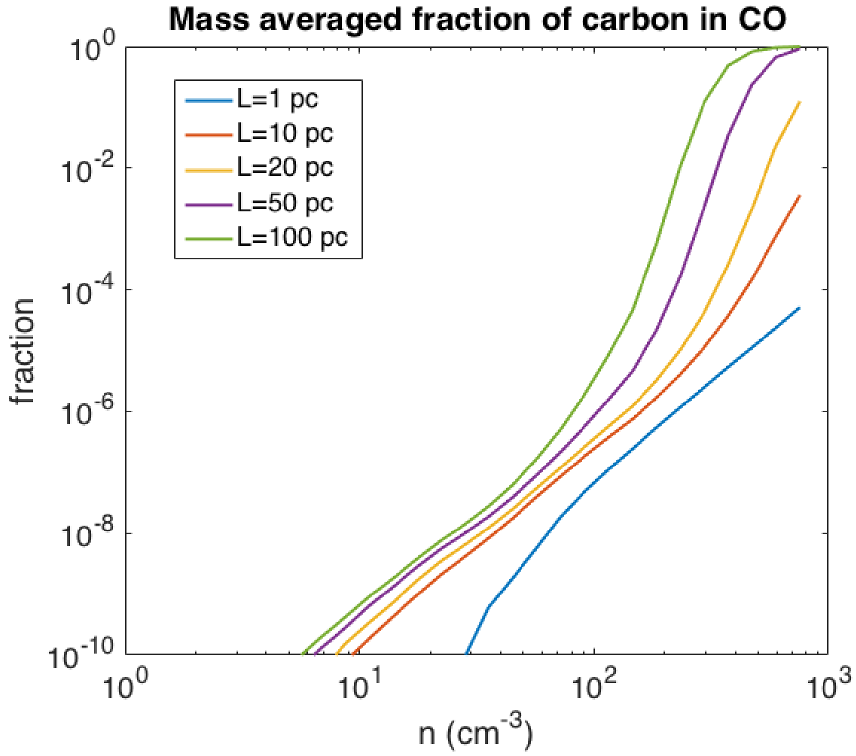

Figure 4.5.9: C molecular fraction vs density plot for different column density lengths

by the dissociation of the hydrocarbon CH$_x$ via Eq. 4.2.12. Hence, at relatively high densities the elevated column density (or extinction) protects CH$_x$ from photodissociating and therefore the carbon atom is not released to form CO. Provided that the box runs reach even higher densities, the CO abundances would saturate as they do for the GMCs.

4.6 Results

4.6.1 Details of the Simulations

In the previous chapter we introduced four clouds extracted from galactic simulations, Cloud A, B, C and D. In Table 5.1 we recap the details of the initial conditions of these four clouds. These simulations will also constitute a benchmark, to compare to those with feedback in the next chapter. We initialise all the clouds with a temperature of 50 K, and the gas is in an atomic state ($aH_2 = 0$ and $aCO = 0$). The fiducial values we have used for the abundances of O and C are $X(O) = 4.5 \cdot 10^{-4}$ and $X(C) = 2.0 \cdot 10^{-4}$ respectively. We choose $T_{min} = 20$ K, satisfying the Jeans Mass criterion everywhere in the cloud. We calculate the column densities for the chemistry using a fixed length of 20 pc, instead of the full-size of the clouds ($\sim$ 100 pc). The column densities are used to calculate the shielding from UV radiation. We argue that molecules exist in the densest areas, and therefore using the total size of the cloud would cause an overestimation of the molecule shielding.

Table 4.3: Mass, radius, velocity dispersion, virial parameter and number of particles of each simulated cloud.

Cloud	Mass ($M_\odot$)	R (pc)	σ (km/s)	α	Part #	F	M$_r$ ($M_\odot$)	M$_J$ ($M_\odot$)
Cloud A	4.3×10^6	100	8.75	2.07	9.6×10^6	700	45	700
Cloud B	2.6×10^6	100	5.17	1.18	1.01×10^7	1000	26	900
Cloud C	1.4×10^6	100	7.80	5.02	1.09×10^7	30	12	1230
Cloud D	1.46×10^6	100	7.73	4.78	1.07×10^7	30	12	1203

4.6.2 Thermal Properties of the Clouds

In the previous chapter we studied the results from isothermal simulations with a temperature of 50 K (we also run another simulation at $T = 20$ K and the results were comparable). In Fig. 4.6.1 we show the mass weighted temperature of the cloud over time, defined as

$$\langle T(t)\rangle = \frac{\sum_{i,j,k} T(i,j,k)\,\rho(i,j,k)\,\Delta V(i,j,k)}{M_{gas}}. \tag{4.6.1}$$

Where we grid the cloud and $T(i,j,k)$, $\rho(i,j,k)$ and $\Delta V(i,j,k)$ are the temperature, density and the volume of each cell of the cloud. We grid the central region of each cloud (-100 pc < x,y < 100 and -50 < z < 50 pc) and calculate the average temperature using Eq. 4.6.1. The size of each cell is 2 pc. We notice that the average temperature remains low during the simulation time ($T <$ 25 K) for the four clouds, hence the choice of temperature in the isothermal simulations shown in Chapter 3 is reasonable. However, the clouds present a range of temperatures typical of the ISM (20 - 10^4 K). This can be observed in Fig. 4.6.2 where we illustrate a 2D histogram with the temperature for all the gas particles in Cloud B. We observe that a major fraction of the particles lie very close to the 20 K limit. This explains why the average temperature of the clouds is so low, although the clouds present a range of temperatures typical of the ISM without considering feedback.

In Fig. 4.6.3 we observe a cross section at $z = 0$ of the four clouds at 2 Myr in the simulation, noticing three regimes in the clouds:

1. *Cold Medium (T < 50 K)*: in the densest parts of the clouds where sink particles are formed[1].
2. *Warm Medium (T > 800 K)*: constituted by warm diffuse gas in the periphery of the clouds.
3. *Intermediate Medium (T ~ 100 K)*: serves as a transition between the two other phases.

In Cloud A we observe islands of intermediate medium mixed in with the cold gas, mainly arising from the global rotation of the cloud. Due to the rotation of the cloud, some regions with more angular momentum move slightly outwards, in some cases into lower density gas where

---

[1] The sinks are projected on to the plot, hence some of them appear in a hot area but they belong to a different z coordinate, and are plotted on the z = 0 plane.

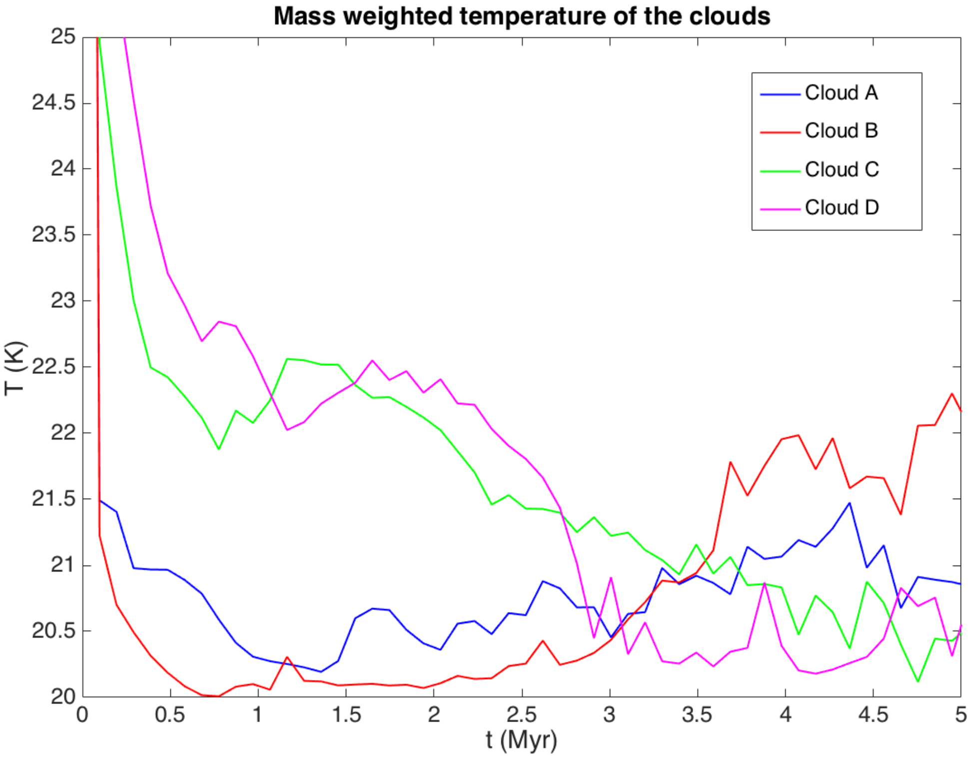

Figure 4.6.1: Evolution of the density averaged temperature of the clouds during the simulation.

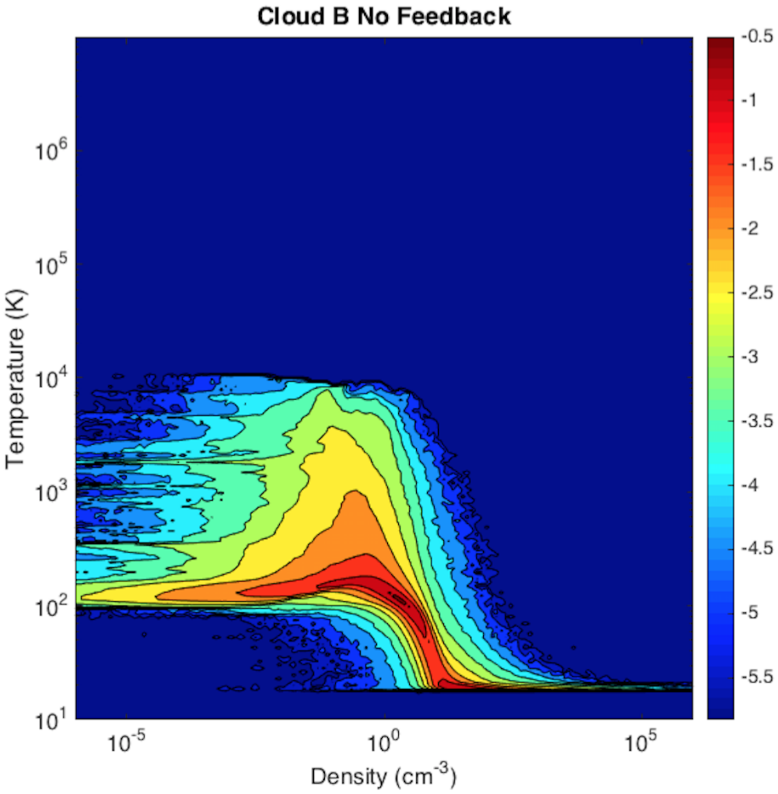

Figure 4.6.2: Temperature vs. density histogram.

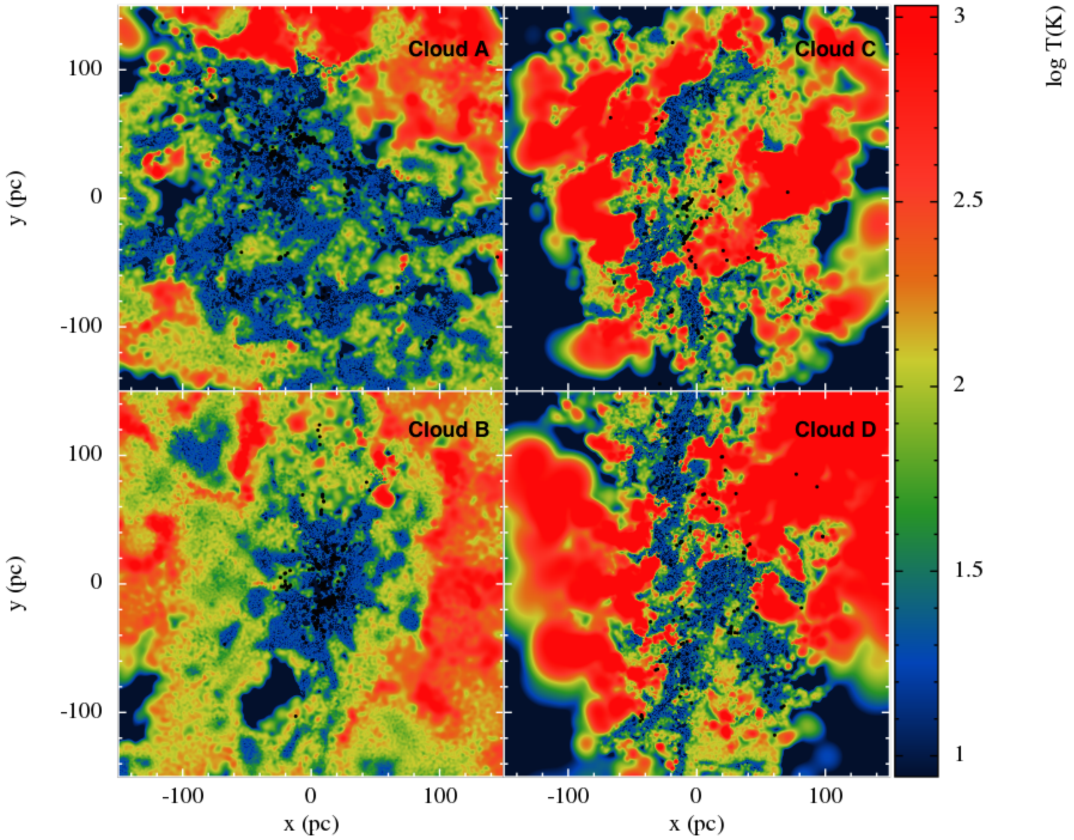

Figure 4.6.3: Cross section of the clouds (at $z = 0$) showing the temperature at 2 Myr in the simulation.

they expand and heat up. Cloud B shows a central cold area, surrounded first by the intermediate regime and then by the warm neutral medium. The temperature map for Clouds C and D are similar. There is a central cold area in both clouds, but we observe small structures of warm gas in the deepest part of the clouds. This mixture is caused by the global shear in the clouds inherited from the galactic simulations. This shear mixes the warm external gas with the colder dense parts of the clouds.

4.6.3 Chemical Properties of the Clouds

In this section we explore how the molecules of H_2 and CO are formed in our simulated clouds. In Fig. 4.6.4 we plot the temporal evolution of the mass averaged molecular abundance aH_2. The black dotted line represents $aH_2 = 0.5$ (the cloud being in a total molecular state). To calculate the abundance of a species X we use

$$\langle a_X \rangle = \frac{\sum_{i,j,k} \; a_X(i,j,k)\, \rho(i,j,k)\, \Delta V(i,j,k)}{M_{gas}}. \tag{4.6.2}$$

Where we have gridded the clouds in the same way as for the temperature (-100 pc < x,y <

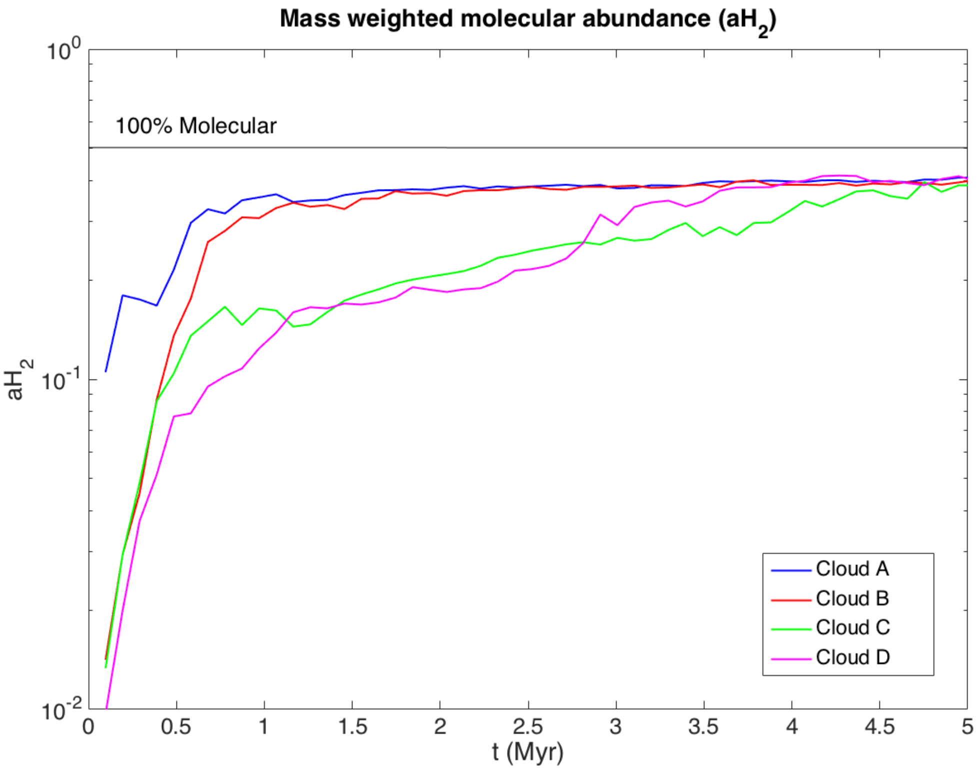

Figure 4.6.4: Evolution of the hydrogen molecular fraction of the clouds in time.

100 and -50 < z < 50 pc), and a_X represents the abundance of species X in a certain cell. Although Cloud B is more virialised than A and should collapse faster, it has a lower aH_2 in the beginning. Both clouds reach a highly molecular state swiftly and after that they create molecules at a slower rate. For Cloud C and D the evolution is different. It takes them almost 5 Myr to reach the molecular levels of A and B because in the early stages the molecular creation is slower although it faster at late times. Molecular gas is denser, and Clouds A and B have a higher initial distribution of dense gas favouring the formation of molecules there. Clouds C and D, on the other hand, need time to create dense areas where the molecules can exist.

In Fig. 4.6.5 we show the CO (solid) and C^+ (dashed) mass average abundances for the clouds. When comparing clouds, the behaviour of the CO is similar to the H_2, Cloud A and B form molecules faster than the other two.

In Fig. 4.6.6 (from Clark et al. (2012b)) we present the abundances for H_2, CO and neutral and ionised carbon for one of the colliding flows they simulated. The main difference with our data is that the GMCs form H_2 from the very beginning of the simulation. This is presumably due to the initial conditions. In Clark et al. (2012b) they start the simulations with a flow of gas of uniform density (1 cm^{-3}), whereas our GMCs have overdense areas inherited from the galactic simulations. These high density areas allow the formation of H_2 very early in the simulations, whereas in Clark et al. (2012b) some time is needed to create overdensities where molecules are

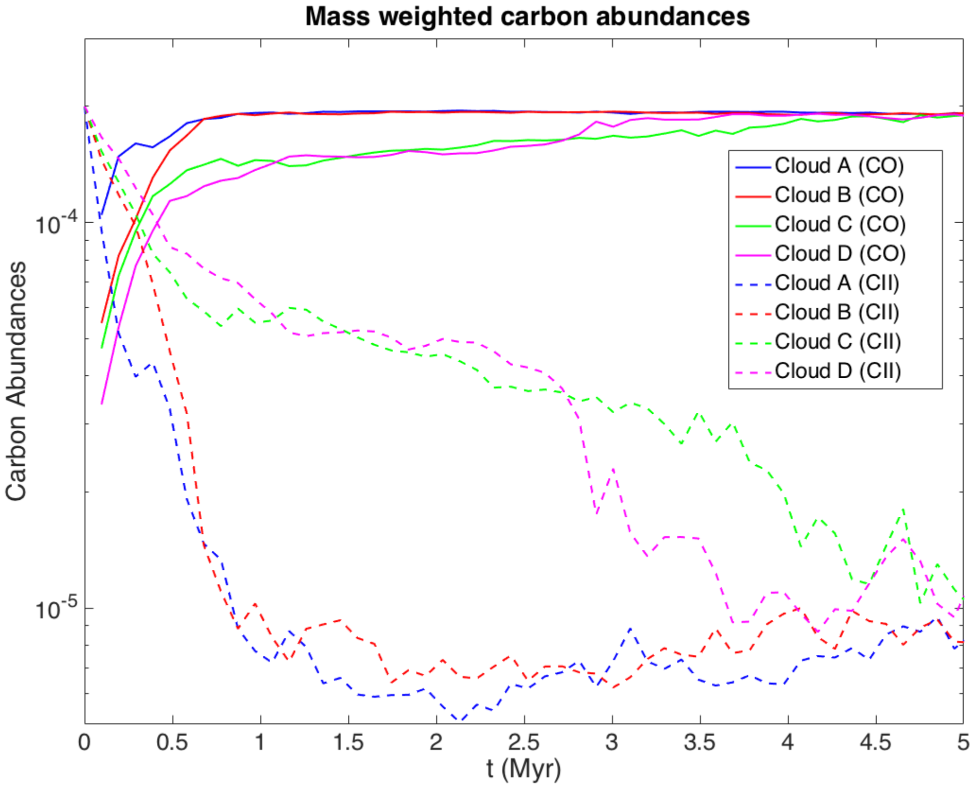

Figure 4.6.5: Evolution of the carbon abundances of the clouds in time.

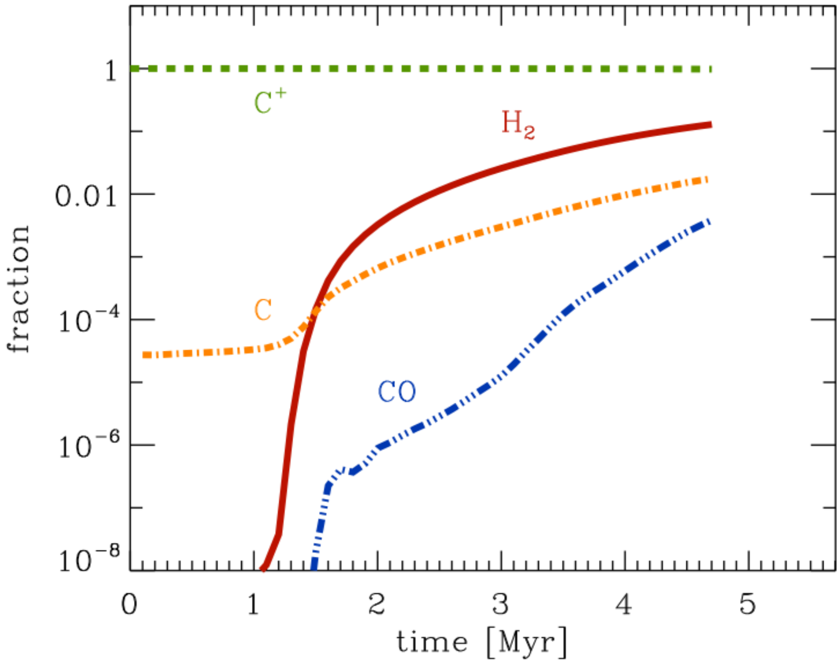

Figure 4.6.6: Time evolution of the different molecular fractions from the high speed flow from Clark et al. (2012b).

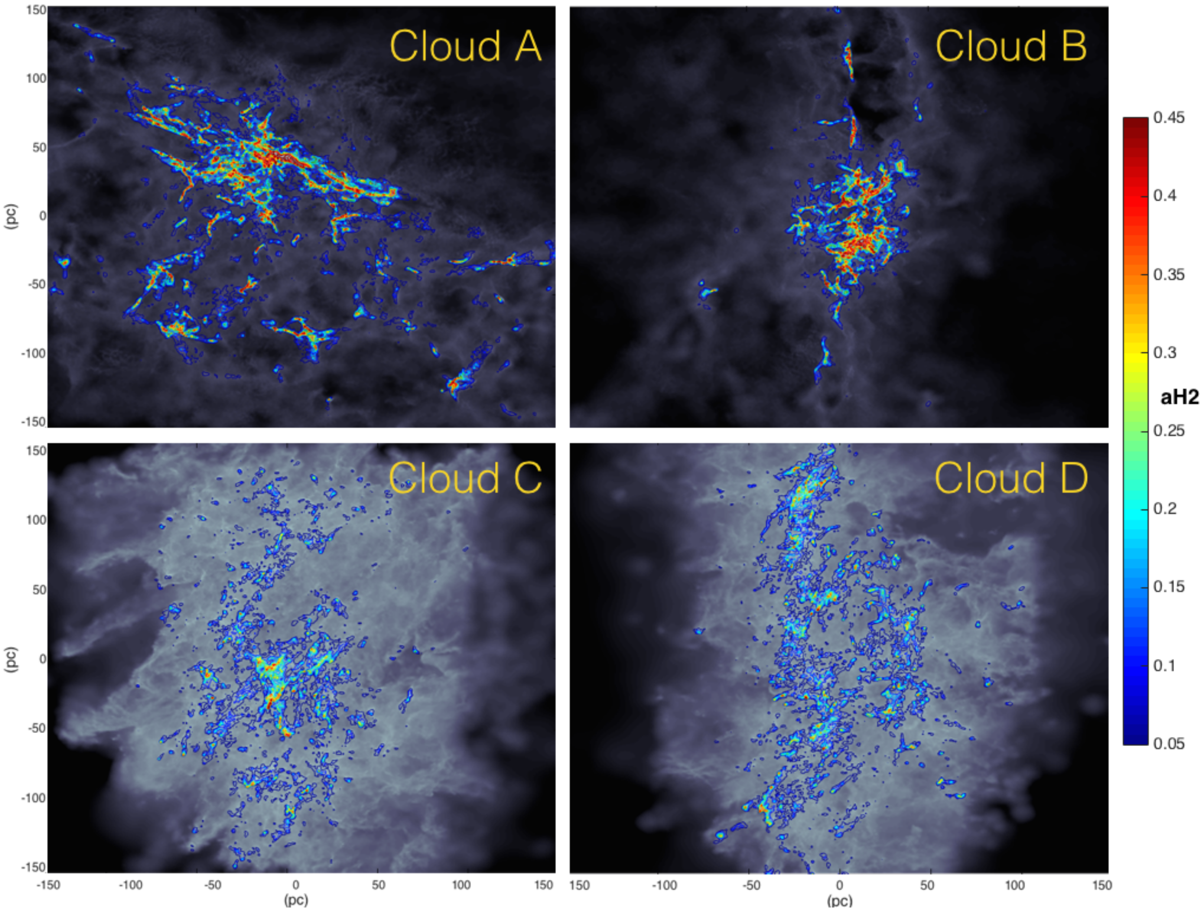

Figure 4.6.7: Column density plots of the clouds with the density averaged abundance of H_2 in the line of sight overlaid at 2 Myr in the simulation.

formed. The creation rate of H_2 for the flows is similar to Clouds A and B, increasing very abruptly in the beginning and changing to a flatter profiles at later times.

The CO abundance in our case increases sharply when compared to Clark et al. (2012b), reaching our simulation limit of $X(C) = 2\cdot 10^{-4}$ very early, whereas in Clark et al. (2012b) the CO fraction continues growing during the 5 Myr of their simulation, suggesting that it may be a consequence of the initial conditions, or a combination of the initial conditions, and the fact that the algorithm from Nelson & Langer (1997) produces CO faster than the chemical network considered in Clark et al. (2012b).

To study the distribution of H_2 in the molecular clouds we have prepared a column density plot, where we have overlaid the average of aH_2 over the line of sight (along the z axis) at a time of 2 Myr (Fig. 4.6.7). We see that Clouds A and B have larger dense areas where the gas is molecular. This is in accordance with the global evolution of the clouds in Fig. 4.6.4. We also see a richer filamentary structure in the molecular regions of A and B compared to C and D.

The filamentary structure is more patent in the column density plot of CO. In Fig. 4.6.8

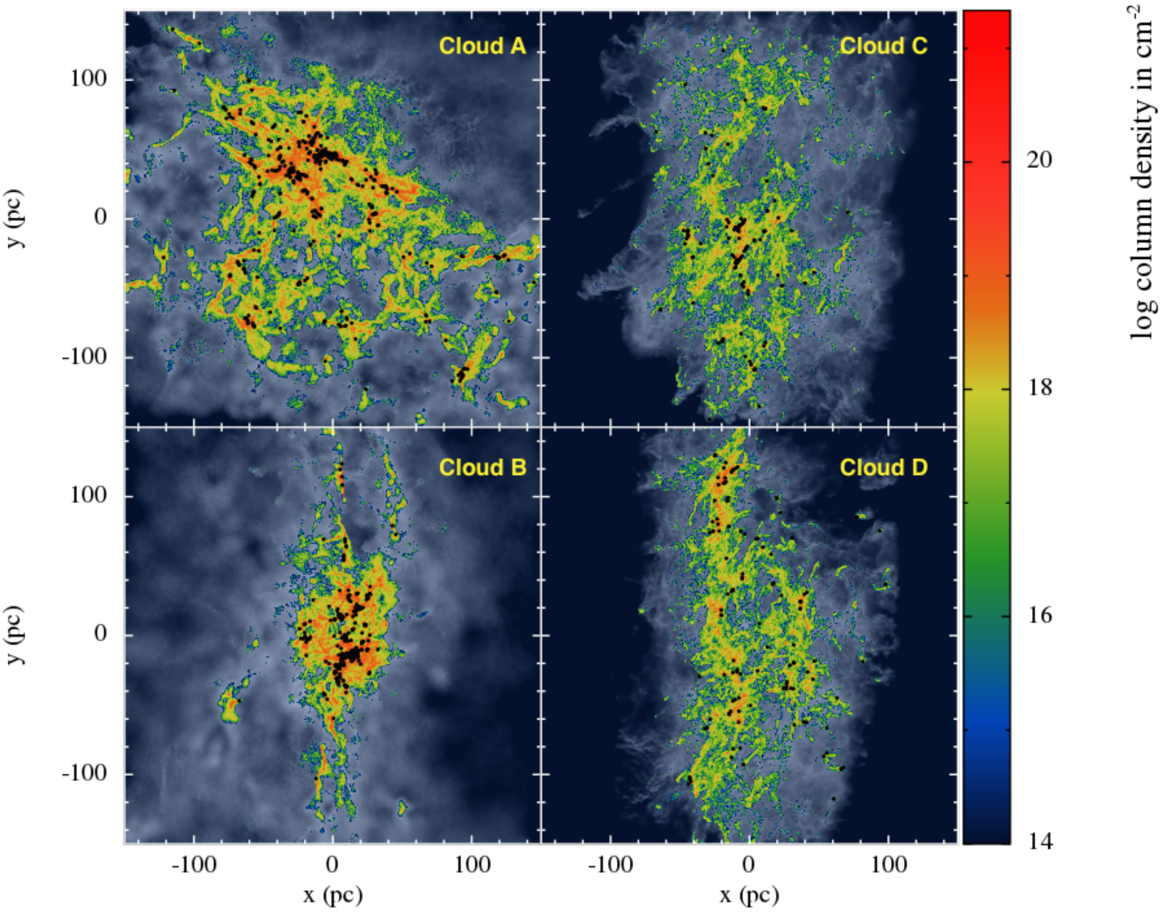

Figure 4.6.8: Column density plots of the clouds with the column density of CO overlaid at 2 Myr in the simulation.

we show the $N(CO)$ overlaid over the total column density for the four clouds at 2 Myr in the simulation. The CO abundance is again greater in Cloud A and B than in C and D. The molecular gas traces the densest areas of the clouds, and therefore the star formation process. All the sink particles are positioned in areas of high molecular fraction. Even isolated sinks in cloud C and D present an envelope of molecular material when we zoom in.

We present a 2D histogram of the CO abundance (aCO) and the temperature for Cloud A in Fig. 4.6.9. We observe that the vast majority of molecular gas is at temperatures lower than 200 K. Although high abundances of CO correspond with cold molecular gas (~ 20 K), there is a significant fraction of CO at temperatures of the order of ~ 100 K.

4.6.4 Comparison with Observations

We compare the column densities of H_2 and CO with observations in this section. We calculate the column densities as if we were an observer in the galactic disk viewing the XZ plane and integrating over the Y axis of our clouds. We employ a resolution of 100 x 100 pixels per cloud. We use

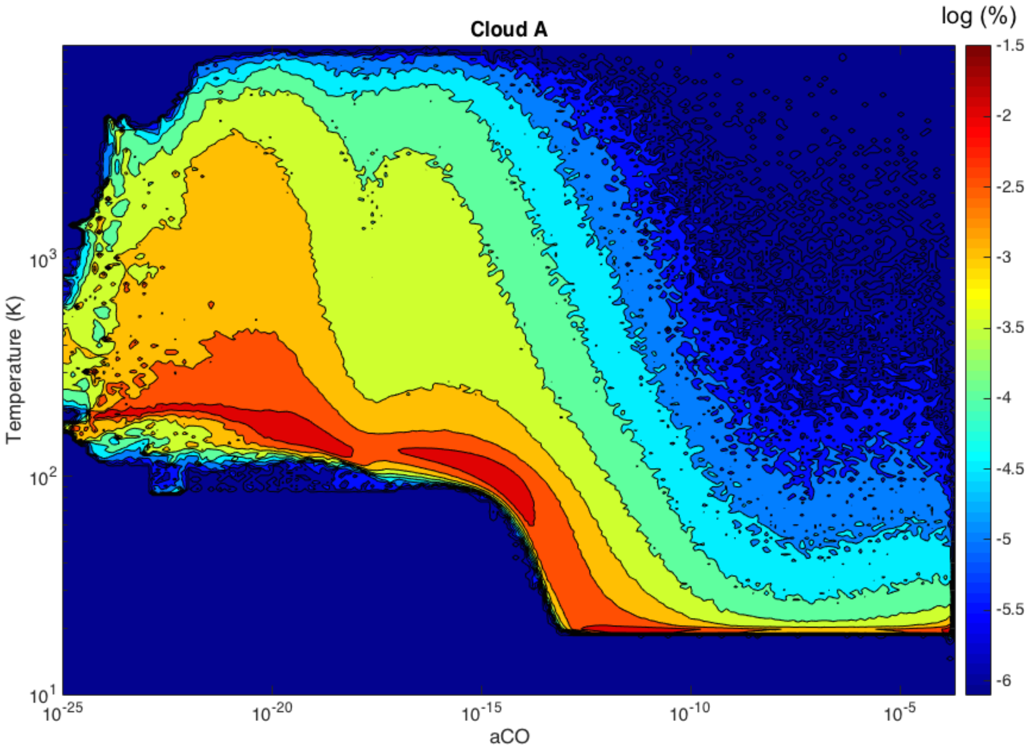

Figure 4.6.9: 2D histogram of the CO abundance and temperature of Cloud A at 2 Myr in the simulation in the left panel.

the same data as in Duarte-Cabral et al. (2015) (Federman et al. 1980; Baudry et al. 1981; Ungerer et al. 1985; Burgh et al. 2007; Sheffer et al. 2008). In Fig. 4.6.10 we present a 2D histogram of the column densities for H_2 and CO for the four clouds at 2 Myr. We include the observations represented by coloured circles.

The observational points lie close to the column densities from the simulated clouds. At low densities the observations seem to have a flat tail. In our clouds we reach smaller CO column densities than in the observations. At high densities the self-absorption becomes large and observing CO is difficult and requires using other wavelengths. In our simulations the high density tail is constrained by the parameter $X(C)$ (carbon abundance) of our model, which denotes the limit for the production of CO in our clouds.

The distribution for individual simulated clouds (not shown) is thinner, suggesting that the scatter in the observations may be caused by sampling over different types of clouds. The low density tail is smaller for Cloud A and B compared to Cloud C and D. The most frequent hydrogen column density for all the clouds is $\sim 10^{23}$ cm^{-2}, which is an order of magnitude higher than the largest column density from observations. These high column densities occur when we integrate over the central areas of our clouds that are highly populated with dense clumps. These regions of the clouds represent areas where the dust extinction is high, and therefore very difficult to observe. Another possibility is that we may be overestimating the CO column density. The model we use

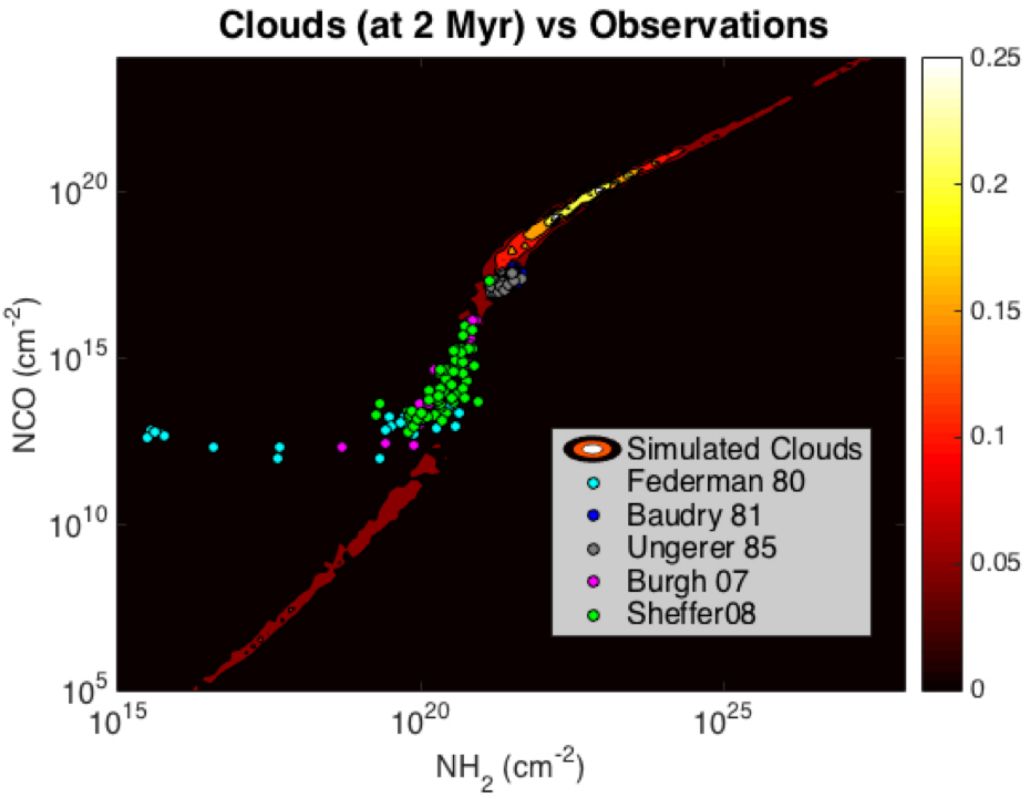

Figure 4.6.10: Comparison of NCO vs. NH2 for all the clouds compared with observations

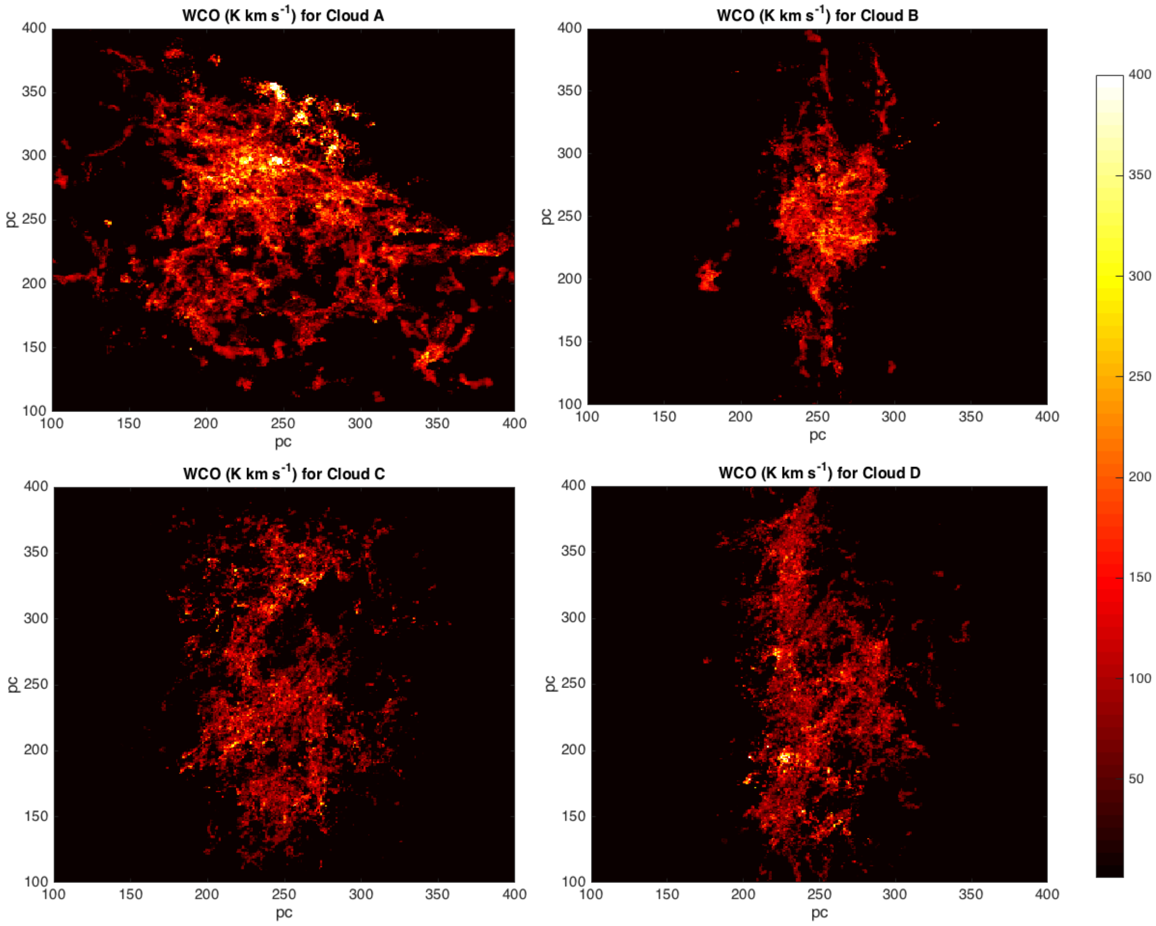

Figure 4.6.11: Synthetic observations of the clouds produced using TORUS and considering LTE at 2 Myr

to compute the column densities of CO was designed to work in galactic-scale simulations, where the maximum densities are not so high. At those densities the carbon atoms form other compounds that we do not consider (e.g. CH, HCN or PAHs). Our model assumes all the carbon available (given by X(C)) produces CO. Besides, at high densities and very low temperatures the CO freezes on the surface of dust grains and disappears from the gaseous phase, reducing the concentration of CO.

Using the radiative transfer code TORUS we have produced synthetic observations of the clouds considering local thermodynamical equilibrium (LTE) and the velocity gradient technique from Santander-García et al. (2012), again following Duarte-Cabral et al. (2015). Assuming LTE provides a reasonable measure of the distribution of CO, although we may overestimate the CO intensity (Duarte-Cabral et al. 2015). In Fig. 4.6.11 we present the integrated intensity of CO (W_{CO}) for the four clouds. Both clouds A and B have stronger emission than C and D, as expected.

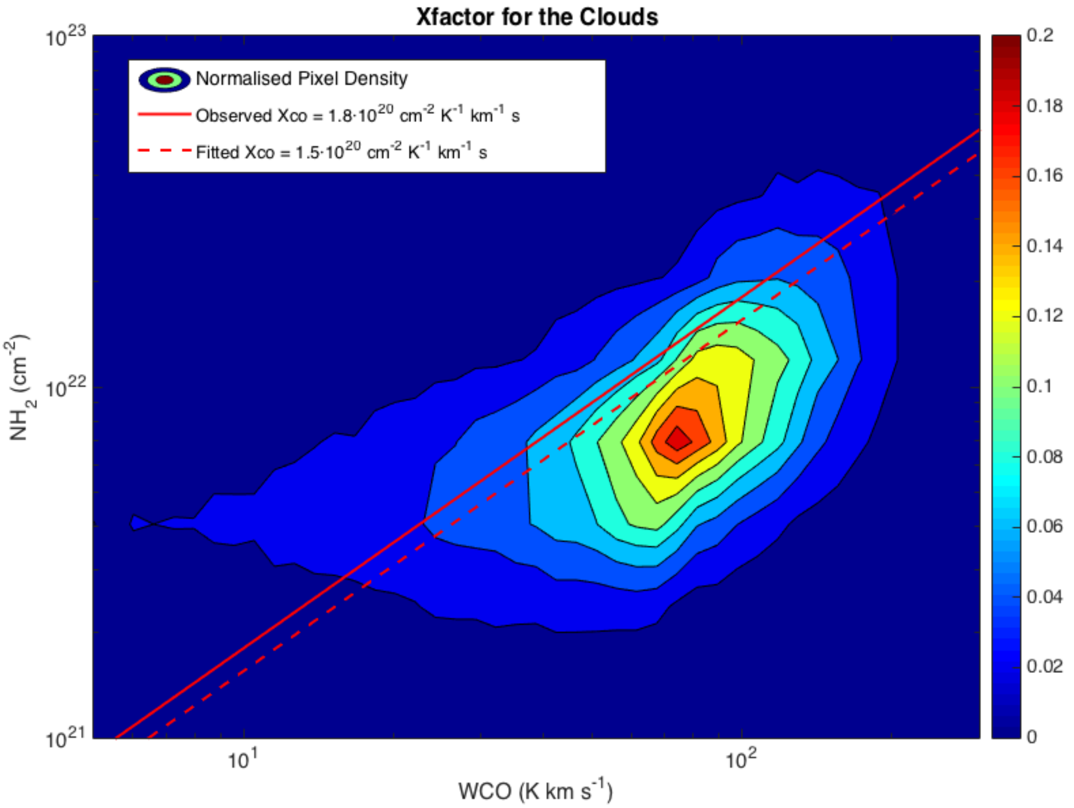

Figure 4.6.12: Pixel density of the H_2 column density and CO intensity for the 4 Clouds. We have included the observed value from Dame et al. (2001).

Lastly, we compare how our simulated observations compare to the actual X_{CO} from Dame et al. (2001). In Fig. 4.6.12 we present the pixel density distribution for the clouds comparing them with the value from Dame et al. (2001) of $X_{CO} = 1.8 \times 10^{20}$ cm^{-2} K^{-1} km^{-1} s. To obtain the value of X_{CO} we calculate the median of the distribution of points. This line separates the total number of points leaving 50 % of the points at each side of that line. We obtain a value of $X_{CO} \sim 1.5 \times 10^{20}$ cm^{-2} K^{-1} km^{-1} s, 20 % below the value from Dame et al. (2001).

4.7 Discussion

In this chapter we have described the ISM cooling and heating algorithm, and the two models we use to compute the chemical abundances of CO and H_2 in the clouds. We find that the density averaged temperature of the clouds is low (~ 25 K), although overall the gas exhibits a wide range of ISM temperatures (20 - 10^4 K), comparable with other simulations like Clark et al. (2012b). Grassi et al. (2014) test their newly developed KROME network (that depends on the number density and the extinction) using a collapsing sphere of gas, but do not reproduce the high temperatures of the diffuse medium (1000 K or higher) for sub-solar metallicities.

Our clouds do not present a homogeneous structure, only Cloud B features one cold and molecular central area or filaments. Because of their different morphologies, our clouds show complex temperature maps (as shown in 4.6.3). The differences between clouds may be related to their velocity fields. For instance, the central area of Cloud B is cold and surrounded by intermediate gas. In the lower density clouds dominated by galactic shear, they also contain areas (~ 5-10 pc of radius) with warm temperatures (~ 800 K).

The CO and H_2 trace the denser areas of the clouds, and therefore their distribution is similarly affected by the characteristic structures of each cloud. Unsurprisingly the virialised clouds are more molecular, with strongly molecular filaments. Cold dense areas are highly molecular, although there is a considerable fraction of intermediate gas that is also highly molecular.

The CO and H_2 abundances we obtain at given densities are very similar to those in Duarte-Cabral et al. (2015) and Pettitt et al. (2014) (see Figures 4.5.2 and 4.5.3). This is not surprising since we use the same algorithm for H_2 and CO formation. However our clouds are almost completely molecular, compared to the fractionally molecular clouds in galaxy simulations studied by Duarte-Cabral et al. (2015) (see also Dobbs et al. 2014a). The main difference between the models is that we reach higher densities in our clouds, indicating that the resolution we attain here is necessary to correctly recover realistic molecular fractions of dense clouds. One other difference is that the models used in Duarte-Cabral et al. (2015) is that those models include stellar feedback, but we check the impact of feedback on the chemistry in the next chapter.

We compare our simulations with data from surveys following Duarte-Cabral et al. (2015). We find that our model overestimates the production of CO at high column densities. This is because the Nelson & Langer (1997) algorithm overproduces CO as it does not consider neutral carbon (only CO and C^+). Other models which consider grain surface recombination for the C^+, have smaller rates of CO production, as there is less C ions available to form molecules (Glover & Clark 2012). Also, Glover & Clark (2012) argue that Nelson & Langer (1997) algorithm produces CO at faster rate than other more complex models. This can also explain why our CO production is faster than in Clark et al. (2012b). As in Pettitt et al. (2014) our limit for producing CO is the simulation parameter $X(C)$, and in those dense areas all the carbon atoms are in molecular form. As we reach higher densities in our clouds, the overproduction of CO becomes more important in our simulations than in the works of Pettitt et al. (2014) and Duarte-Cabral et al. (2015). Including in our models carbon freezing on dust grains at high densities may improve our CO chemistry model.

We also produce synthetic observations using the radiative transfer code TORUS and considering LTE. We find a value for the X-factor of $X_{CO} \sim 1.5 \times 10^{20}$ cm^{-2} K^{-1} km^{-1} s, which is 20 % below the value from Dame et al. (2001), but there is considerable scatter on the observational value depending on the method used to measure it (see Pineda et al. (2008) for more details). Our results are also comparable (within the uncertainties) to other models including Duarte-Cabral et al. (2015) (2.5×10^{20} cm^{-2} K^{-1} km^{-1}) and Smith et al. (2014) (2.2×10^{20} cm^{-2} K^{-1} km^{-1}).

5

Feedback within Galactic Molecular Clouds

"In all your travels, have you ever seen a star go supernova? ... I have. I saw a star explode and send out the building blocks of the Universe. Other stars, other planets and eventually other life. A supernova! Creation itself! I was there."
– Brother Cavil (Battlestar Galactica)

5.1 Introduction

Stellar feedback plays an important role modulating the star formation rate in molecular clouds. Massive stars emit winds during their lifetime, heating the ISM, creating cavities and ionising their surroundings. By the end of their lives, massive stars die in a supernova explosion that injects energy in their surroundings, modifying the shape the cloud, and chemically enriching the ISM with new metals. The star formation rate in our galaxy and in nearby galaxies is, at least, an order of magnitude smaller than expected if we consider the total mass of molecular gas in the galaxy (Zuckerman & Evans 1974; Krumholz & Tan 2007). Stellar feedback is a plausible explanation for this difference as feedback may reduce the SFR (Bate 2009; Kim et al. 2012; Walch et al. 2012; Dale et al. 2013a). At smaller scales (pc), feedback may also trigger star formation as it creates overdensities where new stars can be formed (Dale et al. 2005; Gouliermis et al. 2012; Colin et al. 2013).

The problem of modelling feedback presents two issues: first selecting which mechanisms we include in the simulation, and then choosing the most appropriate way of injecting feedback in the clouds. As we mentioned in Chapter 1, by stellar feedback we consider a series of physical phenomena which includes SNe, stellar winds, radiation pressure and ionising photons. There is still a debate about which mechanism is more important. Dale et al. (2014) present results of combined simulations of photoionization and momentum driven winds from O stars. The effect of the winds is modest compared to the photons. Hensler (2010) claims that SNe are the most important feedback effect, and some authors like Padoan et al. (2015) argue that only the SNe are sufficient to drive turbulence in the ISM (supporting Mac Low & Klessen (2004)). Dobbs et al. (2011b) claim that the feedback from SNe is necessary to maintain a population of unbound clouds. However, before a SN occurs, the parental star has been emitting winds and radiation modifying their surroundings. Rogers & Pittard (2013) study the combined effect of winds and SNe. Winds create cavities and passages in the turbulent clouds, reducing the impact of the later SNe, as the hot gas escapes through the areas excavated by winds. Hopkins et al. (2012) and Agertz et al. (2012) present very complex feedback models that include winds, SNe and momentum deposition by photons. In particular Agertz et al. (2012) consider winds from massive stars, stellar mass loss by low mass stars, feedback from two types of SNe and momentum deposition by photons. Again Agertz et al. (2012) emphasise the importance of pre-SN feedback, as it modifies the effect of SNe. Recent works such as Gatto et al. (2015); Girichidis et al. (2015) study the differences in effect of the SNe feedback when it is 'peak - driven', meaning that the supernovae occurs in a very dense area of the cloud, or 'random driven' where the energy is injected randomly in the cloud. They found differences between these two scenarios, and Girichidis et al. (2015) suggest that the coupling between the cloud and the feedback is only effective in the random driven SNe in diffuse areas of the cloud.

Observationally, the importance of feedback from massive and young stars is unquestionable. However, there is still some debate about the particular role of the different feedback components. Massive stars emit UV photons that heat up the surrounding medium, acting as a source of radiation pressure in the early times of the cluster, and generating thermal pressure via ISM heating at later stages of their evolution (Lopez et al. 2010). The influence of stellar winds is still debated. The energy injection from winds is at least, an order of magnitude smaller, but the radiation couples inefficiently with the ISM (Güdel et al. 2008), making uncertain which mechanism dominates (Rogers & Pittard 2014; Rosen et al. 2014).

Many simulations that model the effect of stellar feedback do not include gravity (e.g. Haworth et al. 2012; Rogers & Pittard 2013). However we believe that gravity is crucial to assess how the feedback affects the star formation process. Most feedback effects cause divergent flows of matter or energy coming out from the stellar source. Gravity acts in opposition to these forces, and we consider it is important to understand the detailed balance between gravitation and feedback. In simulations without gravity the formation of filaments is difficult, although they are fundamental in the star formation process (André et al. 2014).

To model feedback in molecular clouds most simulations use initial conditions that are oversimplified (e.g. Rogers & Pittard 2013; Dale & Bonnell 2012; Federrath 2015), although some studies try to explore the parameter space. For instance, Walch et al. (2012) varies the fractal dimension (related to the exponent of the density power spectrum) to study the effect of feedback in different configurations of a turbulent sphere. There are some concerns about choosing a simple model as initial conditions. In the previous chapters we argue that turbulent spheres fail to reproduce the vast repertoire of morphologies from galactic molecular clouds. In particular, the inherited velocity field affects the SFR, hence it may also modify the effects of feedback in GMCs.

There are also different approaches in the literature to model the feedback injection in the simulations. In grid based codes, the simplest way of modelling feedback is to inject energy in the cell that contains the stellar source (Vázquez-Semadeni et al. 2010). This can be improved by injecting feedback in the cells that are at a certain distance from the source. This distance may be fixed as in Agertz et al. (2012) where they inject momentum to the 26 adjacent cells, or variable as in (Colin et al. 2013) where they calculate the Strömgren radius at each timestep and inject feedback accordingly.

In particle based codes, the simplest method consists of injecting feedback searching for the particles close enough to the stellar source. For instance, Dobbs et al. (2011b) inject SNe feedback in all the gas particles within a certain radius from the source of feedback. Some improvements can be included, especially if used at smaller scales or simpler geometries. Dale & Bonnell (2008) propose a mechanism to inject feedback called the *working face* algorithm. They look for the particles directly facing the source by ray-tracing and calculate the feedback injection by assigning statistical weights to the different rays that cross a gas particle.

The effect of the feedback can be studied in a global context using galactic simulations (Dobbs et al. 2008; Hopkins et al. 2011; Agertz et al. 2012), however this approach does not resolve the effect of feedback on sub-pc scales. Other works like Dale et al. (2012); Colin et al. (2013); Rogers & Pittard (2014) model feedback on smaller scales, but these studies do not account for the global galactic effects. In this chapter we study the effect of feedback from winds and SNe in molecular clouds that have been extracted from galactic simulations. In previous chapters we analysed the influence of the galactic context in the star formation process of these clouds, and here we will discuss the effect of stellar feedback on different GMCs. We choose two feedback processes, one that acts over a period of time (momentum deposition by winds) and another with an instantaneous effect (SNe). We performed initial tests to include momentum deposition by photons following Hopkins et al. (2011) but the momentum injection was at least an order of magnitude smaller than the winds. In future works it would be a good idea to introduce ionising radiation acting in conjunction with the winds.

This chapter is structured as follows. We discuss the feedback algorithm in the following section. Then in section 3 we describe the effect of winds in simulated clouds, and study the effect of SNe in section 4. We discuss the properties of a simulation with SNe and winds in section 5 and proceed to discuss the temporal evolution of the clouds in section 6. In section 7 we analyse CO column density maps, and lastly, in section 8 we summarize and discuss the main results of

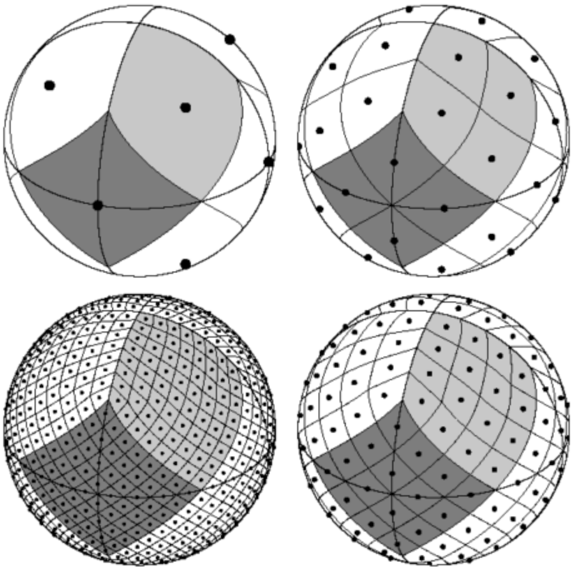

Figure 5.2.1: Sphere divided using a HEALPIX scheme. Clockwise from the upper left we present the sphere divided in 12, 48, 192 and 768 corresponding to the resolution parameter N_{side} = 1, 2, 3, 4 (Gorski et al. 2005, from)

this chapter.

5.2 Method

Simulating feedback in molecular clouds requires solving two issues. The first consists of deciding how the feedback is going to be injected spatially, and the second is deciding the magnitude of that injection at each timestep. In our simulations we trace the star formation by using sink particles (Dale & Bonnell 2008; Bate 2009). Some other simulations simply place the source of feedback in the centre of the cloud (Rogers & Pittard 2014; Dale et al. 2014). We then inject feedback into a sphere around each sink particle (similar to Dale & Bonnell 2008; Dobbs et al. 2011a) with a radius R_{feed}.

5.2.1 Modelling Feedback using a HEALPIX sphere

In the first tests we performed we did not take into consideration the distribution of gas around the sink particle. On each timestep we searched for the particles around the sink and injected the total amount of feedback divided by the number of particles within a distance R_{feed}. We found that when the majority of the sphere was empty and some gas particles were concentrated in a small area of that sphere, the feedback injection they received could be extreme. To avoid that situation, we decided to divide the sphere into different cells using a HEALPIX scheme (Gorski et al. (2005)). We chose HEALPIX because it is widely used in the literature and its subroutines were already included in our code as part of the TREECOL algorithm (Clark et al. 2012a). HEALPIX provides a fast and scalable way of dividing a sphere in pixels of the same area covering cells of the same volume. From now on, we will use the word pixel to refer to a patch on the surface of the sphere, and cell to describe the quasi-conical volume under each pixel. Each pixel has the same area, and therefore, each cell covers the same volume. The number of pixels scales as $N_{\mathrm{pix}} = 12 \cdot N_{\mathrm{side}}^2$ where N_{side} is an integer greater or equal to one. This allows us to select the number of cells to reach the required precision. We choose $N_{\mathrm{side}} = 2$, which yields $N_{\mathrm{pix}} = 48$ cells or pixels. In Fig. 5.2.1 we show 4 divisions of a sphere corresponding to $N_{\mathrm{side}} = 1, 2, 3, 4$. The utilisation of the HEALPIX sphere increases the numerical stability of the algorithm at a relatively low computational cost.

5.2.2 Injecting Feedback from Winds

With our resolution, the sink particles represent stellar cores. Because we cannot resolve individual stars, or an IMF, we differentiate between the mass of the sink (M_{s}) and the mass of the O/B stars contained in the sink particle (M_*). To define the stellar mass we include an additional parameter to the simulations W_{eff} fixed at the beginning of the simulation, which represents the fraction of the mass of the sink that will be creating winds.

$$M_* = W_{\mathrm{eff}}\, M_{\mathrm{s}} \tag{5.2.1}$$

We only inject feedback if $M_* \geq 8\, M_\odot$. From the moment a sink particle is created (t_*^{o}), it will be injecting feedback from winds unless that sink becomes a supernova at $t = t_*^{\mathrm{SN}}$ (t_*^{SN} can again be fixed for a given simulation). To calculate feedback injection from winds we roughly follow Dale & Bonnell (2008). The winds affect all the particles in a healpix sphere of radius $R_{\mathrm{feed}} = R_{\mathrm{w}}$ around the sink. We performed multiple tests for different values of R_{w}, finding that if we choose a small radius, winds would only affect a few particles. These particles will have a huge kick from the feedback which may potentially induce numerical problems. On the other hand if we select a large radius we may be injecting feedback in areas not causally related. For those reasons we consider $R_{\mathrm{w}} = 50 \times R_{\mathrm{sink}} = 5$ pc (corresponding to the area causally connected on an average timestep). According to Dale & Bonnell (2008) the total mass lost by an O/B star can be modelled as

$$\dot{M} = 10^{-5} \left(\frac{M_*}{30 M_\odot}\right)^4 M_\odot\, yr^{-1}. \tag{5.2.2}$$

We calculate the stellar mass M_* by setting the parameter $W_{\mathrm{eff}} = 0.75$, to reflect that not all the mass in a clump forms stars. This value is significantly higher than for example galactic simulations (Dobbs et al. 2011b). We chose a relatively high value for the parameter, whereby the effects of feedback are clearly visible on any cloud. We select the same value of W_{eff} for the two clouds to be able to compare them, although the average mass of their sinks does differ, e.g. Clouds C and D, feature sinks with masses $M_{\mathrm{s}} \leq 30 M_\odot$, whereas in Clouds A and B, the sinks have higher masses and therefore $M_{\mathrm{s}} > M_*$. In general, the total mass loss converted into momentum is

$$\Delta\vec{p} = \Delta m\, \vec{v}_{\mathrm{w}} = \vec{v}_{\mathrm{w}}\, \dot{M}\, t_{\mathrm{step}}, \tag{5.2.3}$$

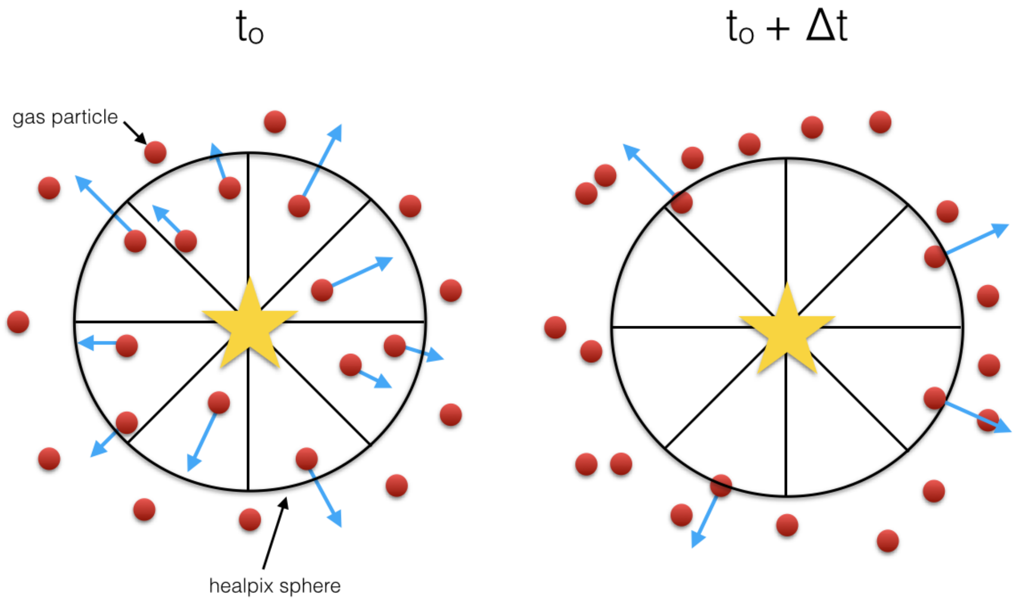

Figure 5.2.2: Injection of stellar winds using a HEALPIX scheme. In the left panel we portray a distribution of gas particles (represented by red circles) around a sink particle (represented by the star). We show a simplified version of the HEALPIX sphere divided in 8 cells. The total amount of the momentum injection from winds will be divided by the number of pixels or cells. In each cell the corresponding strength of the winds is also divided by the number of particles in the cell. This is represented by large arrows for the cells with only one particle and small arrows for the cells with two particles. The winds point in the outward direction of the sphere. In the right panel, we show the evolution of the system after a small period of time Δt, some of the gas particles have escaped the sphere and the winds are injected only in the particles that remain within the radius of influence.

where $\vec{v}_{\rm w}$ is a parameter representing the terminal velocities of the winds and $t_{\rm step}$ is the current timestep. We set $|\vec{v}_{\rm w}| = 1000$ km/s (Dale & Bonnell 2008), and choose the direction so that $\vec{v}_{\rm w}$ points radially outwards. The change in the velocity caused by the momentum injection from winds is

$$\Delta\vec{v} = \frac{\Delta\vec{p}}{m_p} = \vec{v}_{\rm w}\,\frac{\dot{M}}{m_p}\,t_{\rm step}, \tag{5.2.4}$$

where $t_{\rm step}$ is the current timestep and m_p the mass of a SPH particle. To compute the momentum increase of each particle in our model ($\Delta\vec{p}_{\rm i}$) we divide the total velocity injection by the number of pixels ($N_{\rm pix}$). Then on each timestep we count all the gas particles present ($N_{\rm j}$) in a given cell of the sphere around the sink. The velocity injection of each gas particle in the j-th cell is then

$$\Delta\vec{v}_i = \frac{1}{N_{\rm pix}N_j}\vec{v}_{\rm w}\frac{\dot{M}}{m_p}\,t_{\rm step}, \tag{5.2.5}$$

where $N_{\rm j}$ is the number of particles included in the j-th cell.

Table 5.1: Summary of the simulations, including the mass, virial parameter, feedback mechanism and time when the simulation stops ($t_{\rm end}$). The models have all been carried out without feedback as well (see Chapter 4).

Cloud	Mass ($M_\odot$)	α	Feedback	$t_{\rm end}$ (Myr)
Cloud A	4.3×10^6	2.07	Winds	0.7
Cloud B	2.6×10^6	1.18	Winds	1.0
Cloud C	1.4×10^6	5.02	Winds	2.0
Cloud D	1.46×10^6	4.78	Winds	2.0
Cloud B	2.6×10^6	1.18	SNe	1.0
Cloud B	2.6×10^6	1.18	SNe & Winds	1.35

5.2.3 Modelling Supernovae

For modelling supernovae we use the same healpix scheme as for the winds. The supernova event takes place only once and when the sink age is larger than $t_*^{\rm SN}$. We inject $E_{\rm SN}^O = 10^{51}$ erg in a sphere of radius $R_{\rm SN}$. This energy is injected 50% as momentum deposited on the gas and 50% as thermal energy. As for the winds, we include $SN_{\rm eff}$ as an extra parameter to vary the efficiency of SNe changing the total energy injected per sink,

$$E_{\rm SN} = SN_{\rm eff} \cdot E_{\rm SN}^O \tag{5.2.6}$$

Following an analysis similar to winds, the momentum injection on each particle is given by

$$\Delta \vec{v}_i = \sqrt{\frac{E_{\rm SN}}{N_{\rm pix}\, N_{\rm j}\, m_{\rm p}}}. \tag{5.2.7}$$

The thermal energy per unit mass deposited by the supernova event is

$$\Delta e_i = \frac{E_{\rm SN}}{2N_{\rm pix}\, N\, m_{\rm p}}. \tag{5.2.8}$$

A SN event represents an incredible injection of energy and momentum in one timestep. We select $SN_{\rm eff} = 0.50$, considering that SN events happen in a longer timeframe than the simulation, and if a sink particle hosts more than one massive star it is unlikely to see two SN events in the timescales of our simulations. We select a larger region for SNe ($R_{\rm SN} = 10$ pc), to reduce numerical effects when injecting a large amount of energy and momentum in just one timestep. We also linearly decrease the amount of injected energy from the position of the sink to $R_{\rm SN}$. Even though there are not many particles with temperatures higher of $T = 10^6$ K, we have set a temperature ceiling of $T = 10^7$ K in case some particles receive such a large internal energy injection that timesteps are cripplingly small. After undergoing a supernova the sink is no longer emitting feedback.

Table 5.1 shows a summary of the simulations presented in this chapter, including those with just winds.

5.2.4 Improvements not included in the model

As discussed in the previous section, we fix the radius for the winds. An alternative could be to use a variable radius. We examined the possibility of using a variable radius, based on the terminal velocity of the wind $v_{\mathrm{w}} = 1000$ km/s (Churchwell et al. 2006) and timestep

$$R_w = v_{\mathrm{w}} t_{\mathrm{step}}. \tag{5.2.9}$$

We also included a lower limit for the radius so that $R_{\mathrm{w}} \geq 2\ R_{sink}$. However, we found that in the very dense areas the timesteps were minuscule, and R_{w} became $R_{\mathrm{w}} = 2\ R_{sink}$ in practice. For this small radius there are not many gas particles where feedback is injected, which may mean the feedback is not being modelled well. In tests we observed that in these scenarios, particles were ejected dramatically and they did not produce a well defined wind blown bubble (WBB).

We also investigated using the Initial Mass Function (IMF) to produce a statistical population of stars. After a sink is formed, we randomly sample to assign a stellar population to the sink. We use a random distribution that follows the Kroupa (2001) IMF. If we expect that the sink would contain a massive star, we update the stellar mass M_* correspondingly, and also calculate the time t_*^{SN} for that particular M_* (following Hansen, Carl J.; Kawaler 1994). We then continue to update the sink particle, adding new stars and potentially new massive stars until the SN phase is reached. However, this implied an increase in the parallel computing overhead as it requires to synchronise the sink particles.

Having populations of stars associated with each sink particle is probably more involved than we need here, but we plan to look at a simpler scheme where we simply assign one ore more massive stars to each sink particle when it is created (or becomes sufficiently massive). We would assign the masses such that the total amount of massive star formation agrees with that expected from an IMF.

5.3 Effect of Stellar Winds

In this section we study the effect of winds, focusing on two different clouds, one that is undergoing gravitational collapse (Cloud B), and another that is being disrupted by galactic shear (Cloud C). We wish to understand the interplay between the inherited velocity field and the stellar feedback from winds. We are aware that the mass of our sink particles is more representative of a core as defined in Chapter 1, but for the sake of simplicity in this section we will use the terms sink/sink particle or star indistinctly.

5.3.1 Effect of Stellar Winds in a Dense Cloud

In this section we explore if the winds are able to disrupt the structure of a very dense cloud, and affect how the new stars are formed. We have selected Cloud B from the previous simulations because it is the most virialised cloud, and it has a central region that produces a highly bound cluster. From our 4 GMCs, Cloud B has an inherited velocity field with less shear or rotation.

We have run the simulation for 1 Myr and in Fig. 5.3.1 we present the evolution of the central region of Cloud B under the influence of the stellar winds. In a short period of time (less than 1 Myr) a cavity with an approximate radius of 20 pc is created. This WBB is created mainly by the first sink that can be observed in the second panel of Fig. 5.3.1. The rest of the sinks are formed at later stages and a great fraction of them are born in dense areas created by the winds in the periphery of the cavity.

In Fig. 5.3.2 we present column density plots of Cloud B after approximately 1 Myr for the simulations without winds (left) and with feedback from winds (right). There is a strong filamentary structure in the non-feedback case in the centre of the cavity, that does not exist in the case with winds. The winds sweep out all the material leaving a void. There are denser areas in the case without feedback suggesting that the winds may disrupt the gravitational collapse. Specifically the most prominent structure (situated approximately at x = 20 pc and y = -10 pc) in the non feedback case is almost one order of magnitude less dense in the simulation with winds.

The simulations also have different sink properties. For the case without winds the cloud created 58 sinks of an average mass of $\sim$ 820 $M_\odot$ and a total mass of $\sim 4.7\cdot 10^4$ $M_\odot$. The cloud with winds has 99 sinks with an average mass of $\sim$ 185 $M_\odot$ and a total mass of $\sim 1.8\cdot 10^4$ $M_\odot$. This may indicate that winds reduce the accretion of matter onto sinks. However, winds create a larger number of overdense areas (even though they are not as dense as in the non-feedback case), that allow the formation of a greater number of less massive sinks.

We illustrate the effect of the feedback on the velocity field in Fig. 5.3.3, where we show the projected velocity field over the column density for Cloud B. The velocity field for the non-feedback case is mainly dominated by gravitational collapse (left panel). There is a change in the velocity field in the central region, as the winds are dispersing it preventing or at least reducing collapse, whereas with winds the velocity field of the cloud (right panel) is no longer dominated by gravitational collapse. We observe a spherical pattern pointing outwards in the middle of the main WBB. We also notice another spherical pattern below the large cavity. In contrast to the simulation with no winds, the strongest flows in the feedback run are in the most diffuse areas. The hot gas from the winds escapes through the *least effort* path (also observed in Hopkins et al. 2011; Dale et al. 2013b; Rogers & Pittard 2014), puncturing the cloud and reducing the pressure created from the hot gas inside the cavity.

A temperature cross section (z = 0 pc) of the same area of the cloud is shown in Fig.

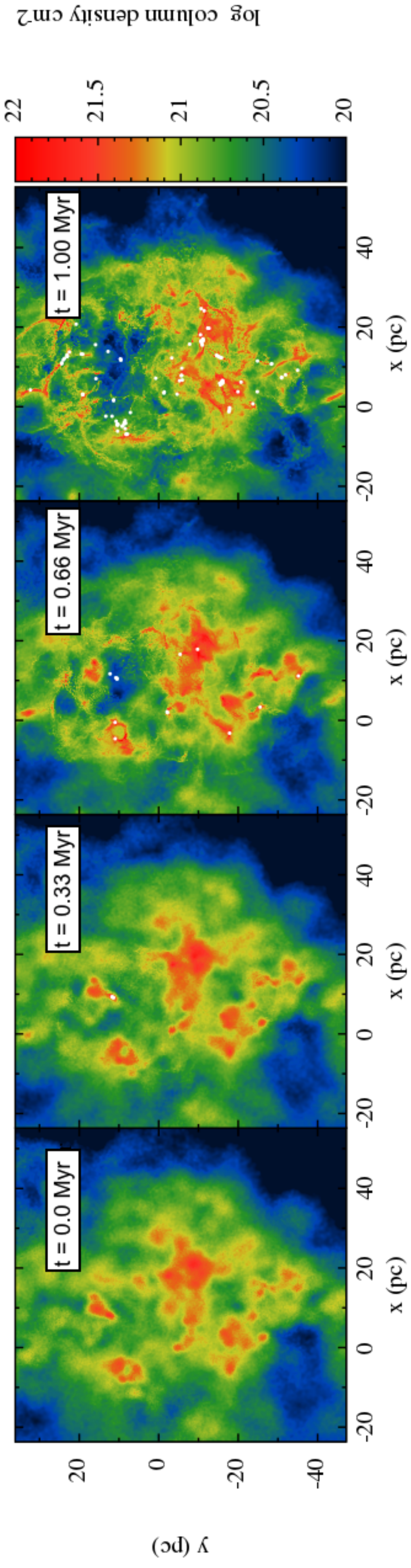

Figure 5.3.1: Evolution of the central region of Cloud B under the effect of stellar winds.

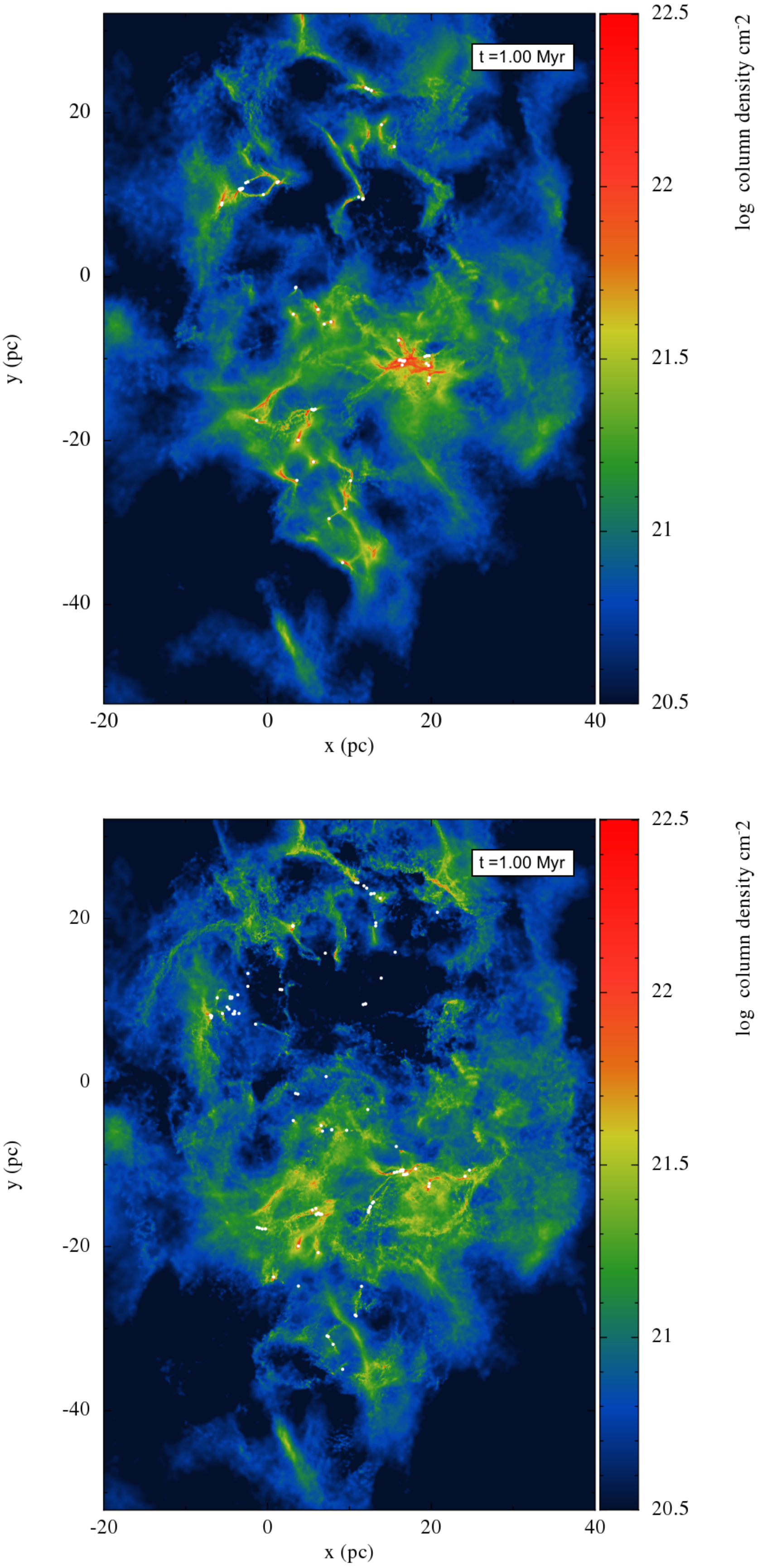

Figure 5.3.2: Column density render of Cloud B at 1 Myr of evolution. In the top panel we present the non-feedback run, and in the bottom panel the simulation that includes feedback from winds.

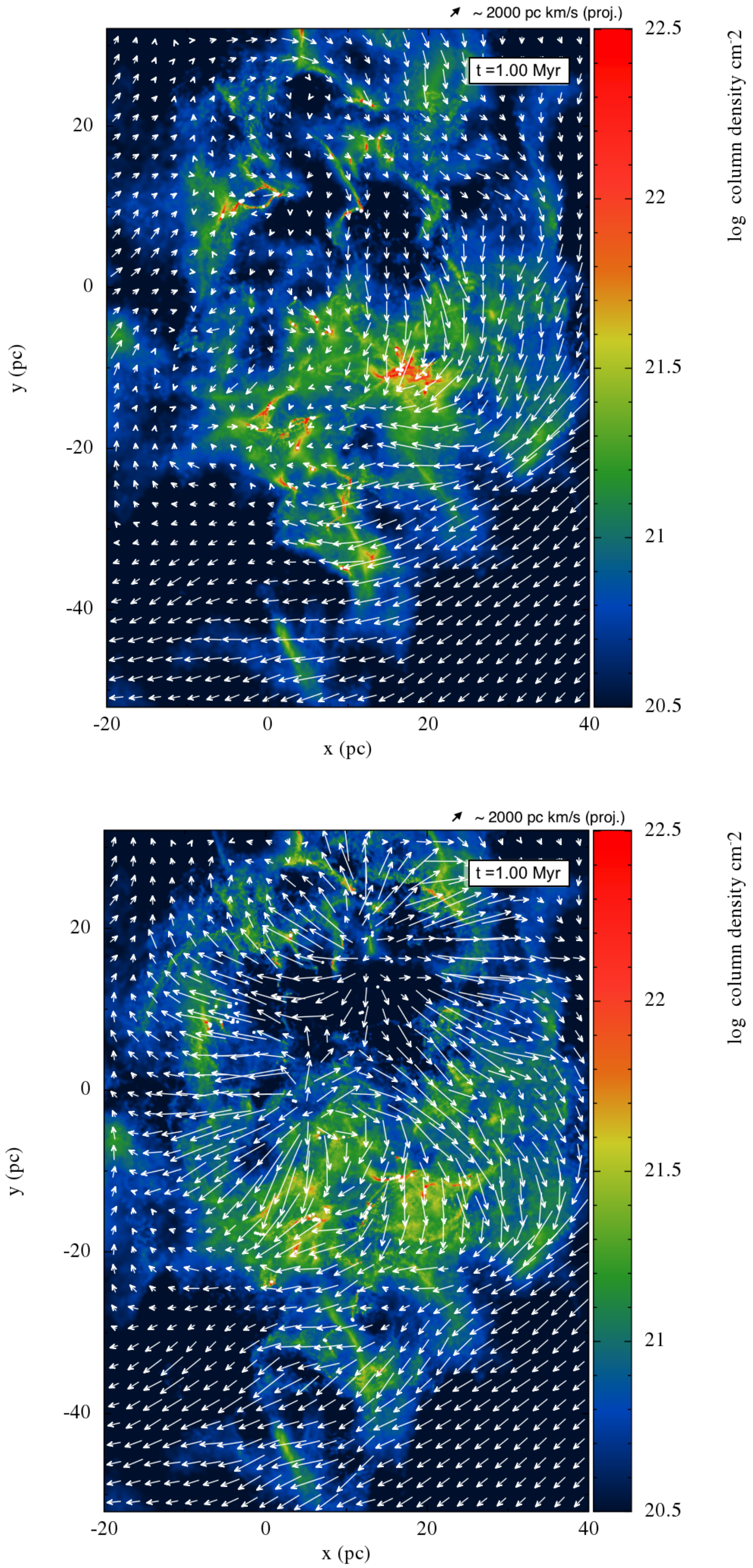

Figure 5.3.3: Column density render of Cloud B at 1 Myr in the evolution with the projected velocity field. The top panel shows the non-feedback run, and the bottom panel the simulation that includes feedback from winds. The size of the arrow on top of the figure gives an indication of the value of the projected velocity.

5.3.4 (note different scales for the temperature). For the simulation without feedback there is a very uniform value around ~ 50 K. There is one relatively large region in the centre with very cold temperatures. For the winds run, we observe a wide range of temperatures. The gas in the feedback case is also cold in the southern area of the figure. However, we have at least 3 areas with very high temperatures (~ 10^6 K) that coincide with the diffuse regions where the gas escapes. The central dense region remains cold as the hot diffuse gas travels around it.

In Fig. 5.3.5 we show the CO column densities for both simulations. The resulting structure in the simulation with winds is similar to the column density plots, with the CO simply reflecting the underlying differences in the structure with and without winds.

To study the effect of winds over the different scales of the clouds, we have averaged the main physical properties. We locate the centre of mass of the cloud and create concentric shells where we average the density, temperature and molecular fraction aH_2, and we sum the mass of sinks. The results are shown in Fig. 5.3.6. In the bottom right panel we present the cumulative mass of the sinks at a given radius. As we mentioned before, winds decrease the accretion of gas by the sinks. However, there are no sinks at more than 50 pc from the centre, and this restricts the effect of the winds outside the central area. This is also clear for the rest of the panels included in this figure. There is no apparent difference in the profiles for the density, temperature or molecular fraction if the distance from the centre of mass is bigger than 50 pc.

We present the density profiles of Cloud B in the top left panel of Fig. 5.3.6. Both runs show the same overall behaviour, with a dense central region and diffuse external areas. As shown in the column density plots of the central region (Fig. 5.3.2), the winds are able to reduce the density, but they also broaden the central area by a small fraction. The temperature profile (shown in the top left panel of Fig. 5.3.6) presents differences only in the central region where the effect of the winds heating up the ISM is clear. They elevate the average temperature of the centre of the cloud more than an order of magnitude (also in accordance with the temperature cross section shown in 5.3.4). The averaged molecular fraction as a function of the radius is shown on the bottom right panel of Fig. 5.3.6. In the central region, the averaged molecular fraction is slightly higher for the simulation with winds than for the non-feedback case. This happens because there is significantly more gas trapped in sinks for the run without feedback. This dense gas would have a higher molecular fraction, but if it is accreted by sinks it is not included in our calculations.

As a summary, the effects of winds in a highly bound GMC are patent only around the areas where sinks are formed. The winds disrupt the gravitational collapse, reducing the accretion of gas by sinks, and escape following the less dense areas of the clouds. The winds do not seem to affect highly the molecular composition of the cloud, although there is a substantial increase in the temperature of this central area.

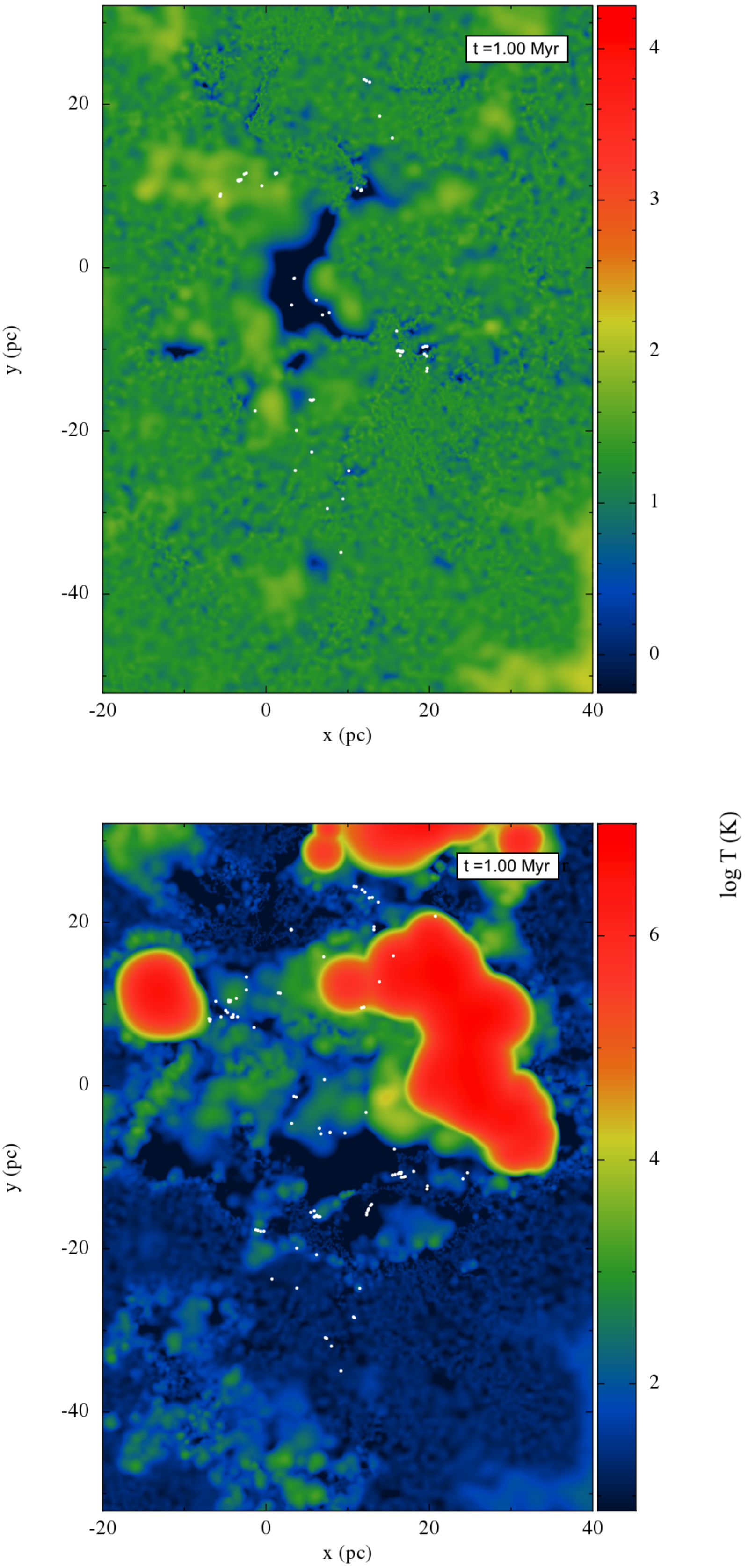

Figure 5.3.4: Temperature cross section ($z = 0$) of Cloud B at 1 Myr in the evolution with the projected velocity field. In the top panel we present the non-feedback run, and in the bottom panel the simulation that includes feedback from winds. Note that the temperature scale is different for the two plots.

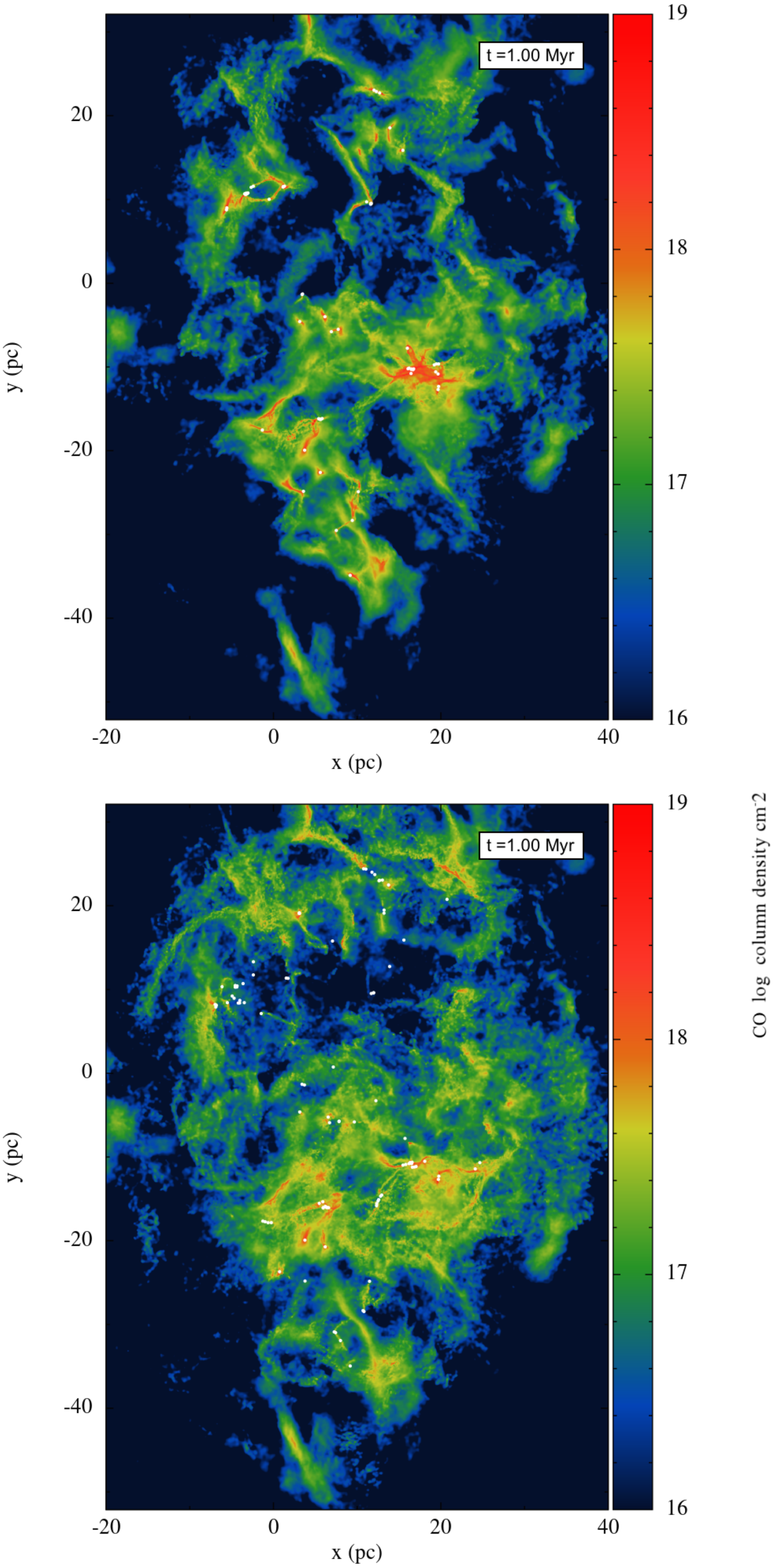

Figure 5.3.5: CO Column density render of Cloud B at 1 Myr in the evolution with the projected velocity field. In the top panel we present the non-feedback run, and in the bottom panel the simulation that includes feedback from winds.

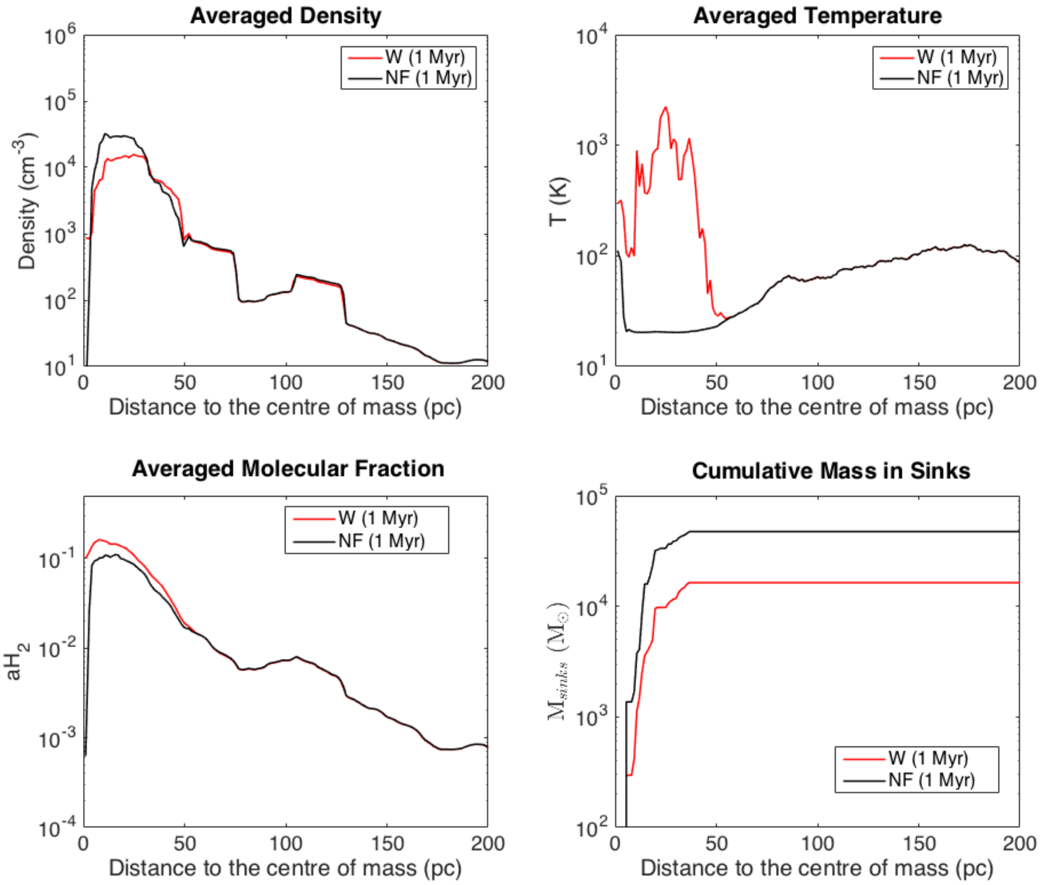

Figure 5.3.6: Variation of the properties of Cloud B with the distance to the centre of mass. We show the averaged density in the top left panel and averaged temperature in the top right. The molecular fraction is presented in the bottom left, and we show the cumulative mass in sinks in the bottom right.

5.3.2 Effect of Stellar Winds in a Cloud Dominated by Galactic Shear

In this section we study the effect of the winds in a cloud that is not globally collapsing, and instead is dominated by galactic shear. We run cloud C for 2 Myr, a longer period of time because the mass of the sinks and consequently the intensity of the winds is smaller.

In Fig. 5.3.7 we present the evolution of the central area of Cloud C at four different times. The distribution of sinks in Cloud C is not restricted to the central area. Cloud C is affected by shear over larger scales, and sink formation occurs in the filaments created in every region of the cloud. We have selected the region of the cloud most populated with sinks to closely observe the effects of winds in this cloud, but there are still some stars created in the outer regions.

The evolution of the central area seems to be largely unaffected by the stellar winds, at least during the first 1 Myr of simulation. Even though the sinks are emitting winds from the moment they are created, their effect over the surrounding areas is less powerful, and the inherited velocity field from the galaxy still dominates the dynamics of the cloud. The winds represent approximately 10% of the strength of the cloud's own velocity field (~1 km/s vs. ~10 km/s). The winds weakly interact with the complex network of filaments which are stretched and deformed by the galactic shear.

However, in the centre of the panel at 1.28 Myr we observe a shell of expanding gas surrounding a cluster of sinks, and in the last panel we see a cavity in the bottom centre of the cloud that has been created by the winds. In Cloud B the central cavity has a radius of approximately 20 pc, whereas in this case the cavity has a smaller size (~ 10 pc).

Fig. 5.3.8 presents the column density of Cloud C with and without winds. The overall aspect of both runs is similar, except in the central cavity created at the bottom of the image. In contrast with Cloud B, the winds do not disrupt the dense areas in this cloud. The strong velocity field of Cloud C may be the reason for this difference.

The global velocity field of the cloud does not vary substantially from the non feedback case (see Fig. 5.3.9), featuring a strong shear flow from the northeast to the southwest of the cloud (the values for the velocity in this cloud are an order of magnitude larger than for Cloud B). Furthermore the sinks in this cloud are less massive and therefore the wind strength is reduced (Eq. 5.2.2). Hence, the velocity field is practically unaffected by the feedback.

The temperature field is shown in Fig. 5.3.10. The winds heat up the ISM to temperatures of the order of $T \sim 10^6$ K, as for Cloud B. There is a hot bubble of gas whose position is slightly shifted compared to the position of the cavity in the column density map.

The molecular properties of both runs of Cloud C are similar. This is shown in Fig. 5.3.11, where we present the column density plots for CO. The main difference is the presence of two

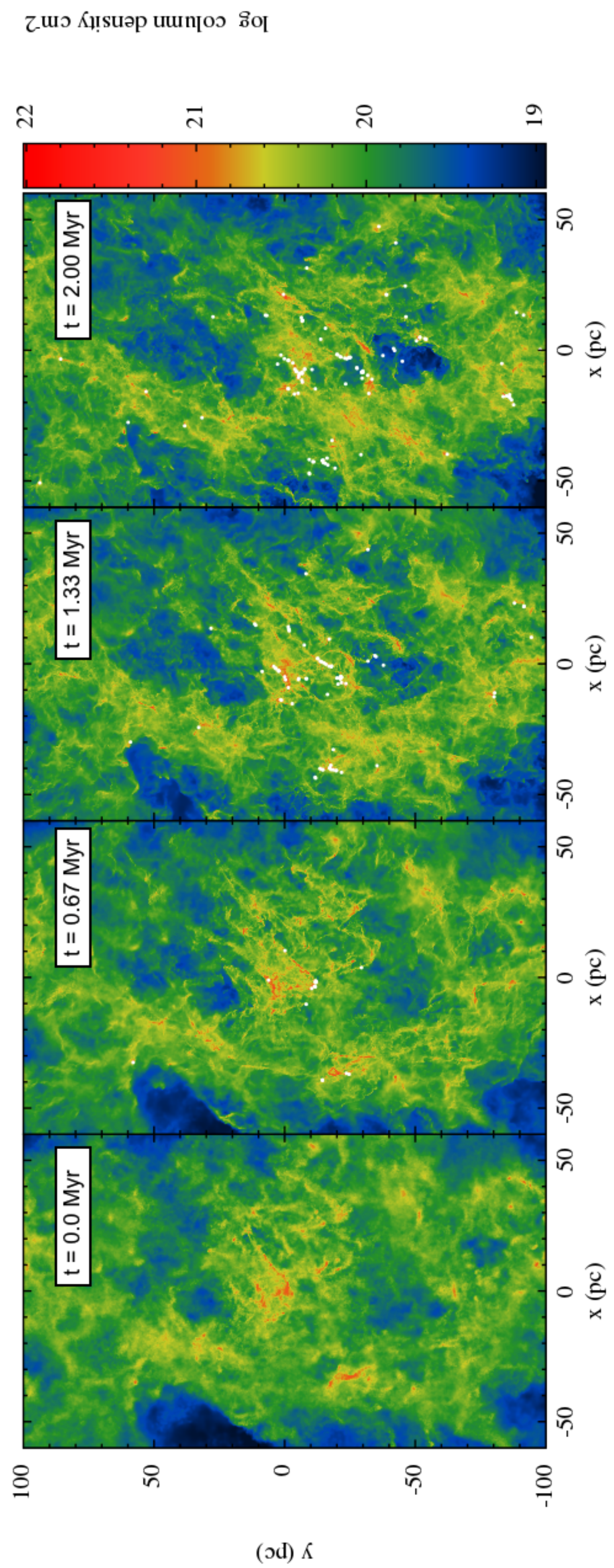

Figure 5.3.7: Evolution of the central region of Cloud C under the effect of stellar winds.

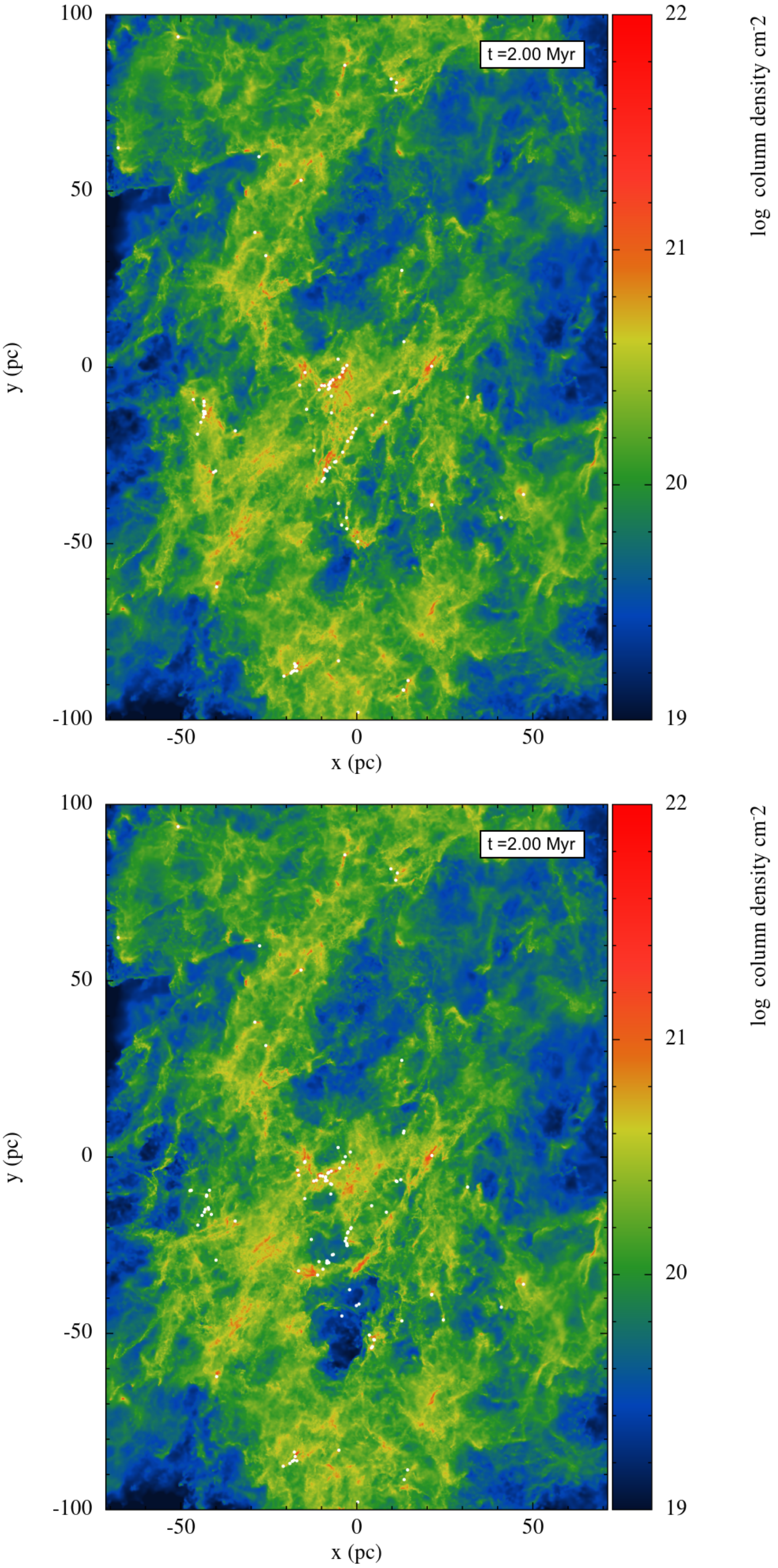

Figure 5.3.8: Column density render of Cloud C at 2.0 Myr in the evolution. In the top panel we present the non-feedback run, and in the bottom panel the simulation that includes feedback from winds.

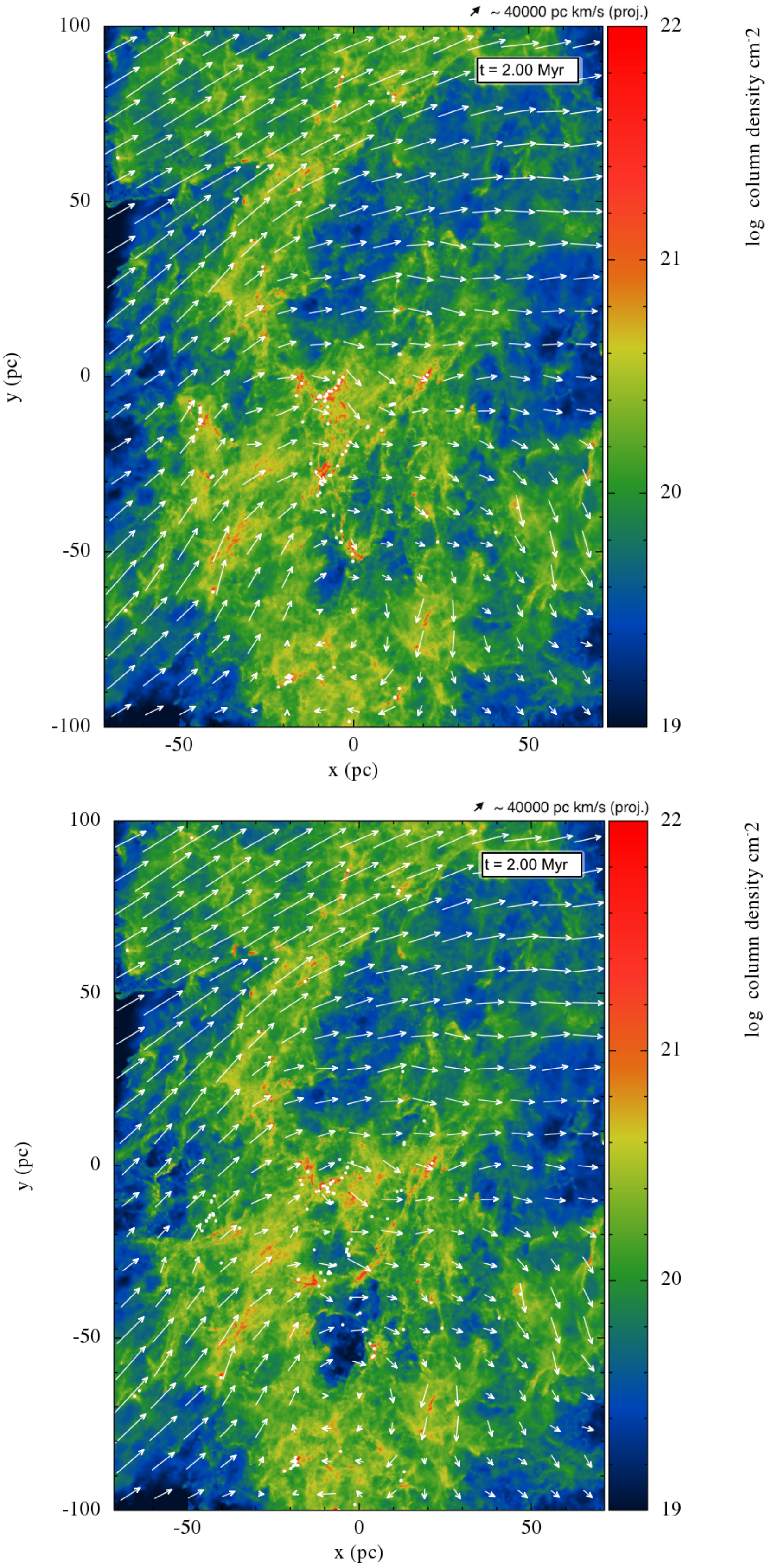

Figure 5.3.9: Column density render of Cloud C at 2.0 Myr in the evolution with the projected velocity field. In the top panel we present the non-feedback run, and in the bottom panel the simulation that includes feedback from winds. The size of the arrow on top of the figure gives an indication of the value of the projected velocity.

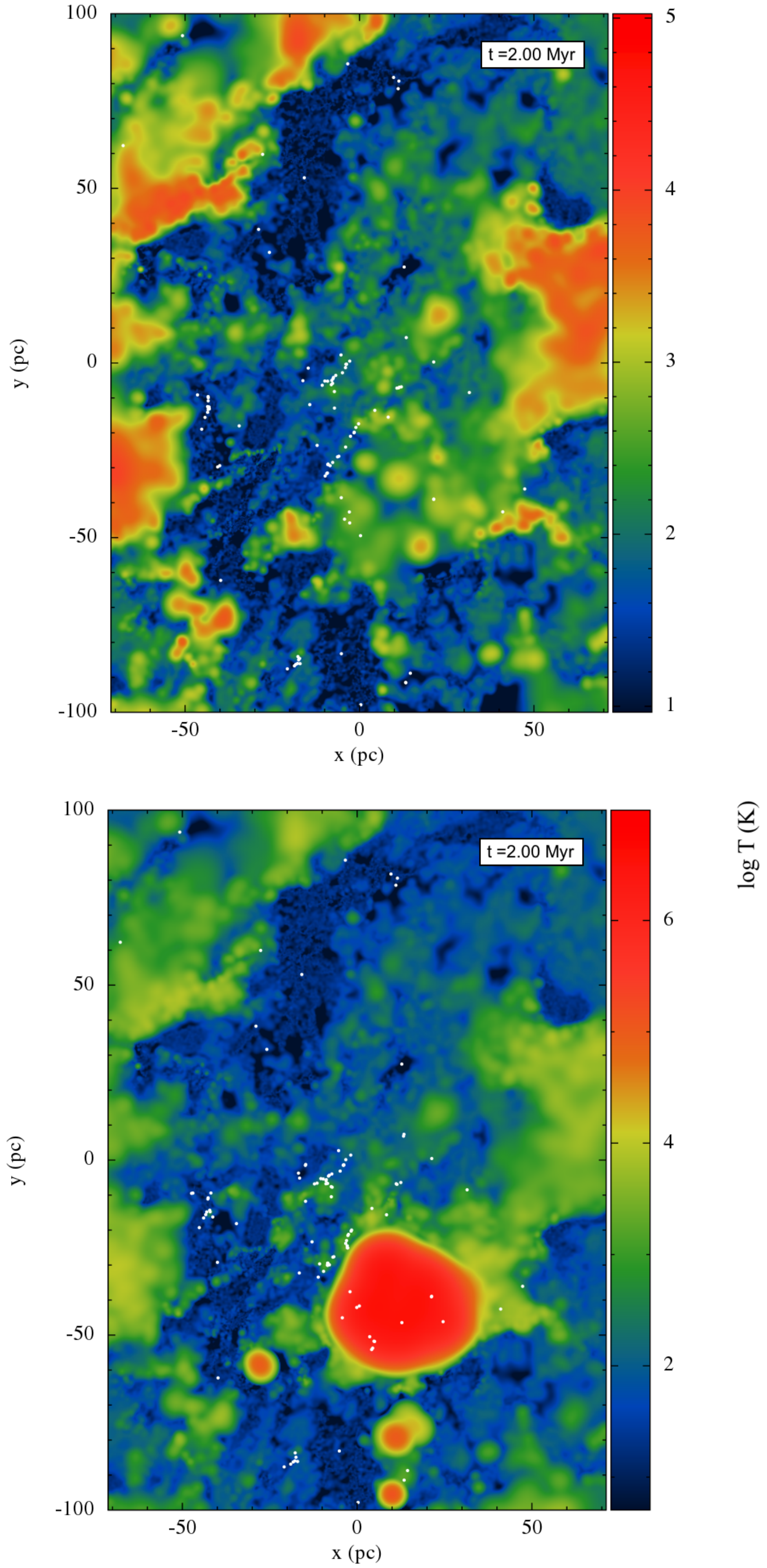

Figure 5.3.10: Temperature cross section (z = 0 pc) of Cloud C at 2.0 Myr. In the top panel we present the non-feedback run, and in the bottom panel the simulation that includes feedback from winds. Note that the temperature scale is different for the two plots

cavities with low concentrations of CO: the central in the bottom of the figure and another one in the west (which is more visible in the CO column density figure).

Proceeding in the same way as for Cloud B, we have computed the radial averages for density, temperature, molecular fraction and mass in sinks, for both runs of Cloud C. In the top left panel of Fig. 5.3.12 we present the averaged density for both runs of Cloud C. The density profiles are almost identical and they present a flat slope. The averaged molecular fraction of both runs is shown in the bottom left panel of Fig. 5.3.12. As for the averaged densities, the molecular fractions are almost identical. The temperature profile of Cloud C (shown in the top right panel of Fig. 5.3.12) changes when winds are injected. The feedback heats up the cloud raising the temperature of the ISM. The increase of temperature happens throughout the cloud as the sinks are widespread.

In the last panel of Fig. 5.3.12 (bottom right) we present the cumulative mass contained in sinks at each radius from the centre of mass. In both cases there are sinks at large radii (>100 pc), however the mass in sinks is reduced by the feedback. The number of sinks in the run with no winds is 116 with a total mass of $1.4{\cdot}10^4$ $M_\odot$, giving an average sink mass of 120 $M_\odot$. For the simulation with winds there are 104 sinks with a total mass of $6.7{\cdot}10^3$ $M_\odot$, so the average mass of sink in the winds case is 64 $M_\odot$. The winds reduce the number of sinks by a factor of 10%, but they also reduce by a half the mass of the sinks. This reduction in mass is caused by the winds preventing the accretion of mass by the sinks, even if they do not cause a great impact on their surroundings.

To summarise, these results suggest that feedback from winds does not affect the molecular fraction of the cloud independently of its geometry. Stellar winds are injected locally, and only have an effect in the surrounding areas. In this respect, the inherited morphology and velocity field of the cloud play an important role on how the feedback affects the clouds. We performed further tests for different values of W_{eff}, and as the parameter decreases, as expected the effect of winds was less obvious However, for W_{eff} over a certain level (e.g. $W_{\text{eff}} > 0.3$ for Cloud C), the SFR were still similar.

5.4 Effect of SNe

In this section we study the effect of the SNe in Cloud B (the most virialised). We set $t_*^{\text{SN}} = 0.1$ Myr, which is the time between the creation of the sink and the SN event. We are aware that the life of a massive star is longer, ∼10 Myr for a 15 $M_\odot$ (Hansen, Carl J.; Kawaler 1994), but we choose this time for two reasons. First, to perform a direct comparison of SNe with winds. Second, we argue that as Cloud B has already evolved in a galactic simulation with no sink particles, the overdensities in reality already would have created sinks.

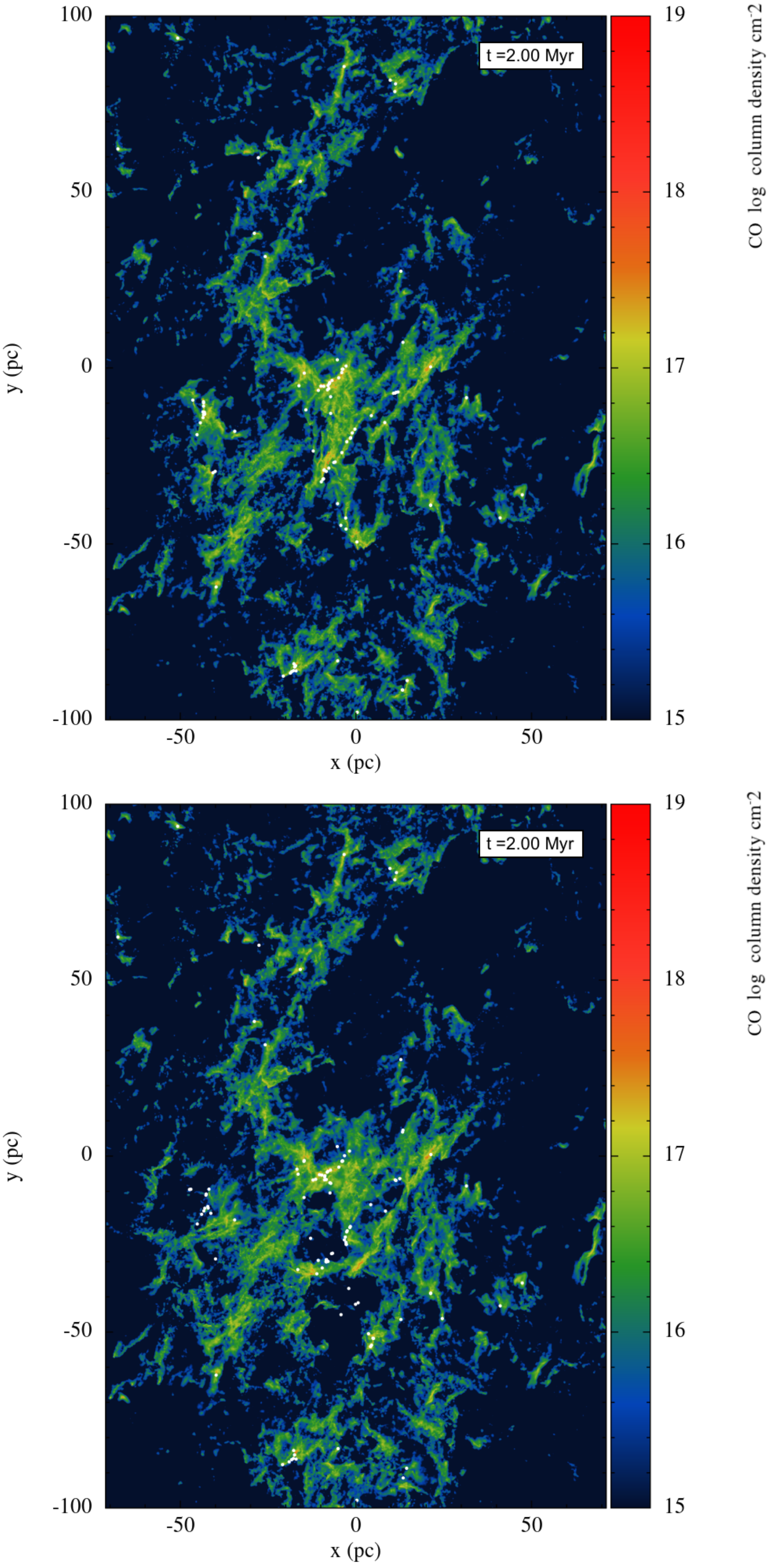

Figure 5.3.11: CO Column density render of Cloud C at 2.0 Myr. In the left panel we have the non-feedback run, and in the right panel the simulation that includes feedback from winds.

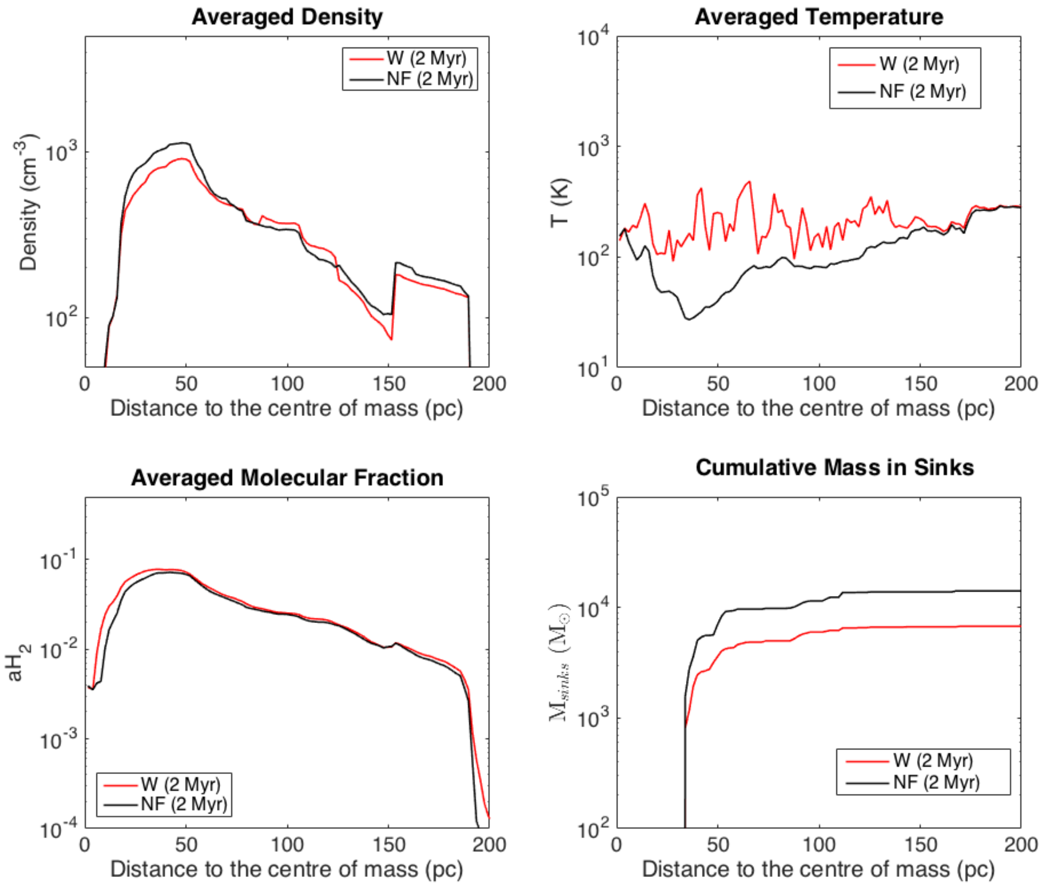

Figure 5.3.12: Variation of the properties of Cloud C with the distance to the centre of mass. We show the averaged density in the top left panel and averaged temperature in the top right. The molecular fraction is presented in the bottom left, and we show the mass in sinks in the bottom right.

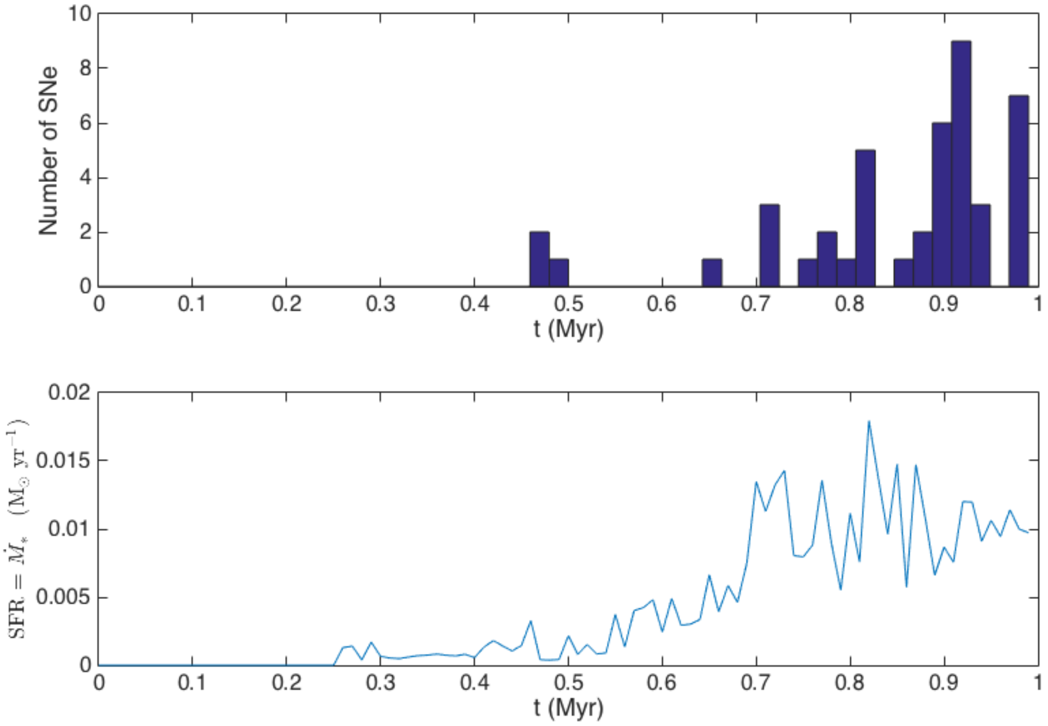

Figure 5.4.1: Comparison of the number of SNe with the SFR. In the top panel we show the number of SNe over time (in bins of 0.02 Myr), and in the bottom panel the SFR.

Figure 5.4.1 presents the SN events in the simulation compared with the SFR. In the top panel we have the number of SNe over time (in bins of 0.02 Myr), whereas in the bottom panel we show the SFR. There is a delay between the peaks in the SFR and in the SNe events, and the total number of SNe during the first Myr of the simulation is 44. To have an idea of where and when the SNe take places, in Fig. 5.4.2 we represent the spatial distribution of these 44 SNe. We have included a colour bar to show the moment when the SNe event occurs. Early SNe correspond to bluish dots in opposition to late ones, that are represented by reddish circles.

Cloud B with SN feedback evolves similarly as in the case with winds. The energy and momentum injected by the SNe disperse the gas creating cavities around the sink particles. In Fig. 5.4.3 we compare the column density of Cloud B at the end of the simulation with SNe (in the right panel) with the winds case (in the left panel). In both cases the cloud is disrupted by feedback, although the winds appear to have a greater effect.

Sinks emit winds for a long period of time compared with the timestep of the simulation (which can be as small as a year). We inject the energy of the SNe in one single timestep. Thus, instead of the continuous flow from winds, we have 44 instantaneous injections of energy and momentum, and this modifies the structure of the central cavity. Fig. 5.4.4 presents the velocity field of the simulation with SNe (in the right panel) and the case with winds (in the left panel). We observe a SN taking place (one of the dark red circles in Fig. 5.4.2) close to the top left corner of

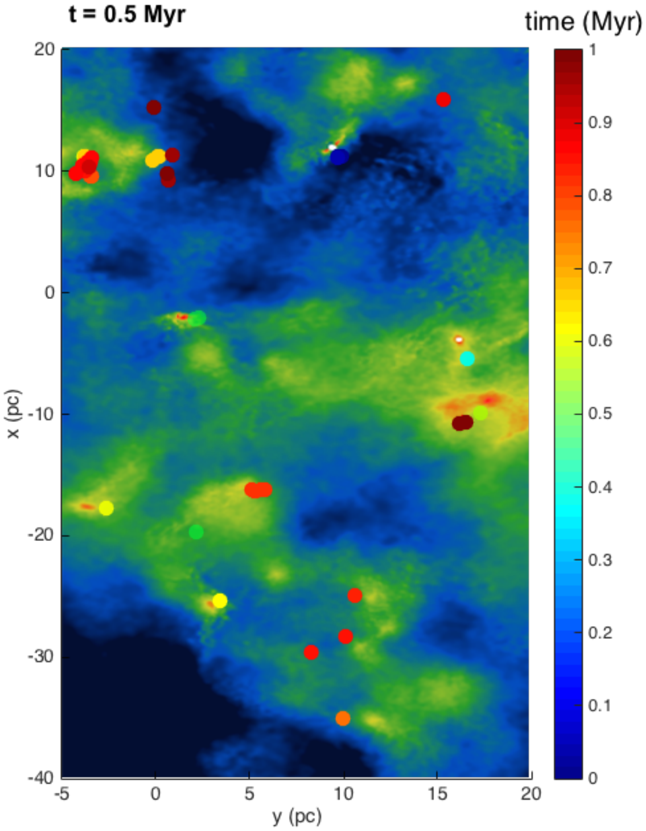

Figure 5.4.2: Spatial distribution of the different SNe. Colours of the points reflect the time when the SN event happens. The background is a scaled column density map taken at 0.5 Myr.

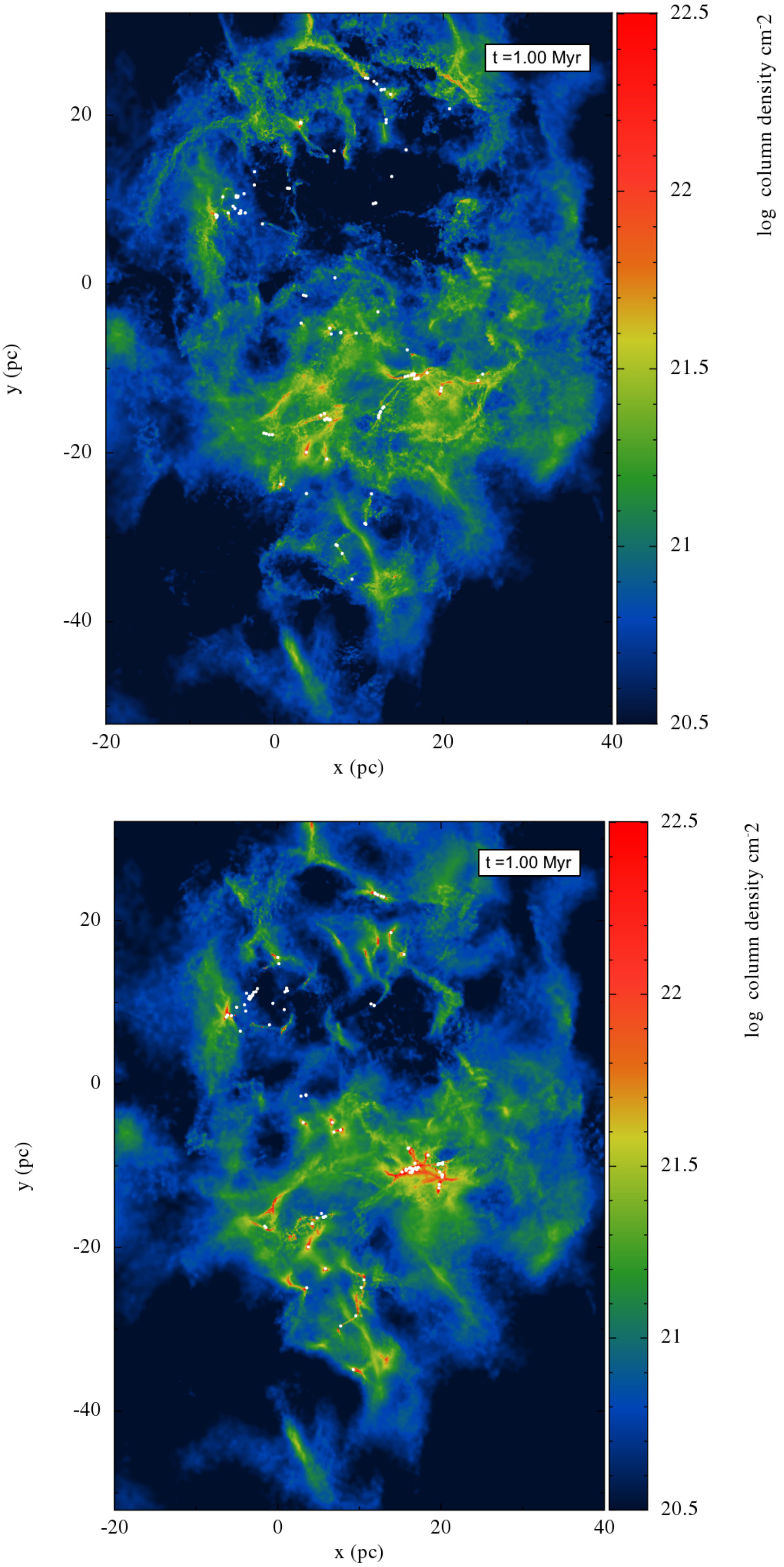

Figure 5.4.3: Column density render of Cloud B at 1Myr in the evolution. In the top panel we show the run with winds, and in the bottom panel the simulation that includes feedback from SNe.

the figure. The rest of the velocity field is more similar to the non feedback run, than to the case with winds.

The temperature maps also change compared to the run with winds. The instantaneous action of the SNe heats the ISM for a moment, but after the event, the warm gas cools down. In the simulations with winds the gas has a continuous source of heat (via injection of kinetic energy) and therefore the temperature of the gas does not decrease. In Fig. 5.4.5 we show the temperature cross section of Cloud B for the case with with winds (left panel) and the case with SNe (right panel). We selected a cross section at $z = 4$ pc, as it is the approximate depth of the SN event observed at this time. The temperature of the gas around the SN event is considerably higher than in the non feedback case ($\sim 10^5$ K) but an order of magnitude smaller than in the winds run. The other warm structure ($T \sim 10^3$ K) present in the right panel of Fig. 5.4.5 is the result of two SNe occurring at approximately 0.8 Myr, which has since cooled down.

One remarkable characteristic we find observing the CO column density maps (Fig. 5.4.6) is that the central dense filamentary structure contains at least as much CO as in the non feedback run. The SNe feedback in that area is not effective enough to push that dense material to the periphery of the cavity or to simply destroy it.

For the SNe case we present the radial average of different physical parameters compared to the case with winds at 1 Myr in Fig. 5.4.7 (clockwise from the upper left: density, temperature, molecular fraction and mass in sinks at a given radius). The mass contained in sinks at a given radius is very similar. As the feedback for this cloud is mainly restricted to a radius of 50 pc around the centre of the cloud, the profiles for the average temperature, density and molecular fraction are also very similar for large radii. At lower radii we find that for the case with SNe the temperature is very high at distances smaller than 10 pc, corresponding with the SN event in the upper left corner of Fig. 5.4.4. Apart from that, the rest of the cloud is considerably colder than in the case with winds (even in the central region for radii between 20 and 50 pc). The density profile in the core of the cloud is almost two orders of magnitude higher than in the winds run and practically one order of magnitude larger than in the non feedback case. The central filamentary structure (very prominent and well defined for the SNe run), which we also noted above is strong a CO feature, probably corresponds to the peaks in the density and molecular profiles. These results suggest that feedback from SNe could generate localised dense and molecular regions. This idea has been proposed in other works including Ballesteros-Paredes et al. (1999), who suggest that flows from a supernova might generate clouds, and more recently, Dawson et al. (2015) who study a GMC between two Milky Way supershells, arguing that the collision of the two shells has formed this GMC. This central increase in density affects the molecular fraction. Hence, for the SNe simulations the central region is more molecular than in both the non feedback run and in the winds case.

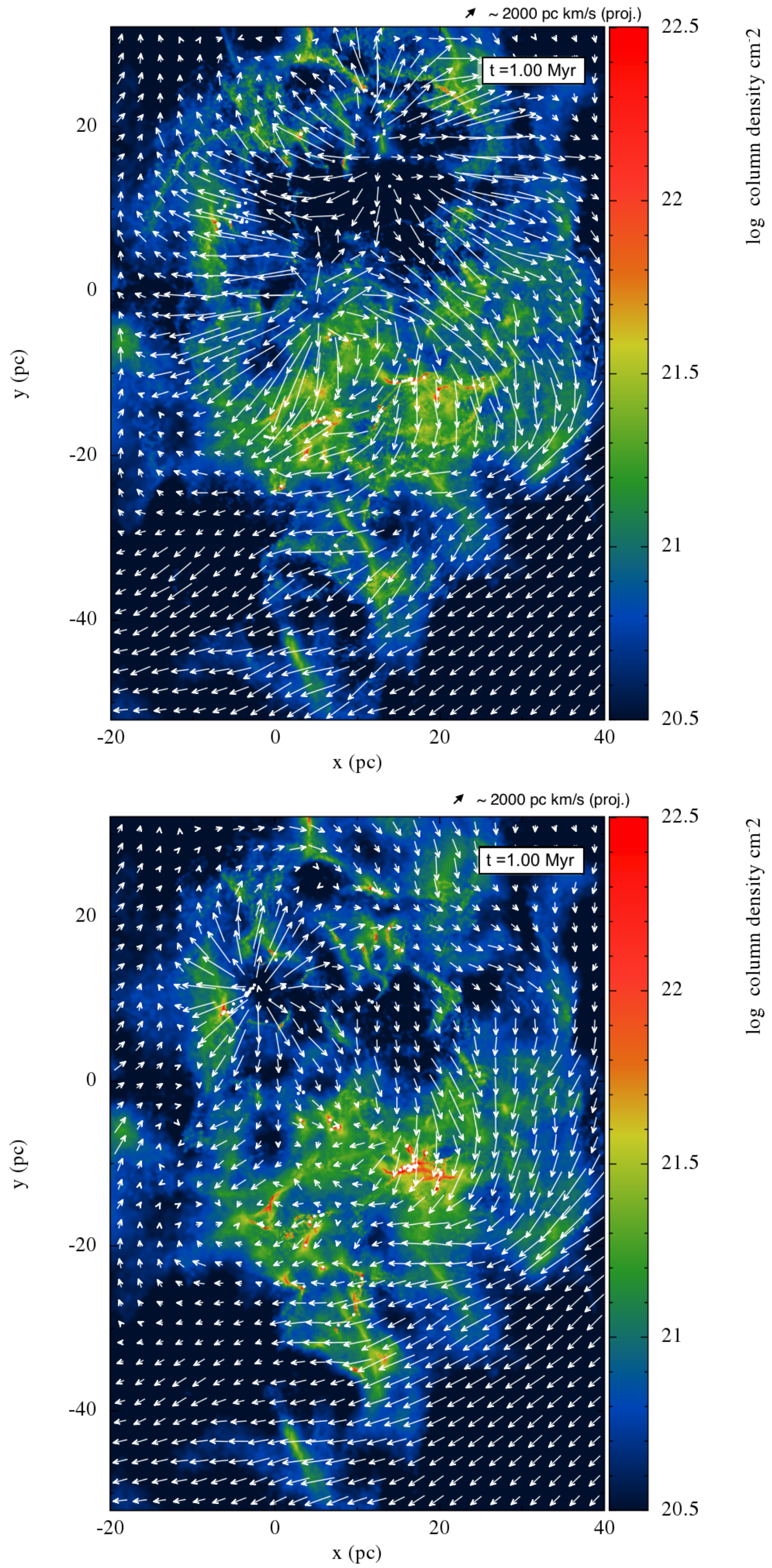

Figure 5.4.4: Column density render of Cloud B at 1 Myr in the evolution with the projected velocity field. In the top panel we present the run with winds, and in the bottom panel the simulation that includes feedback from SNe. The size of the arrow on top of the figure gives an indication of the value of the projected velocity.

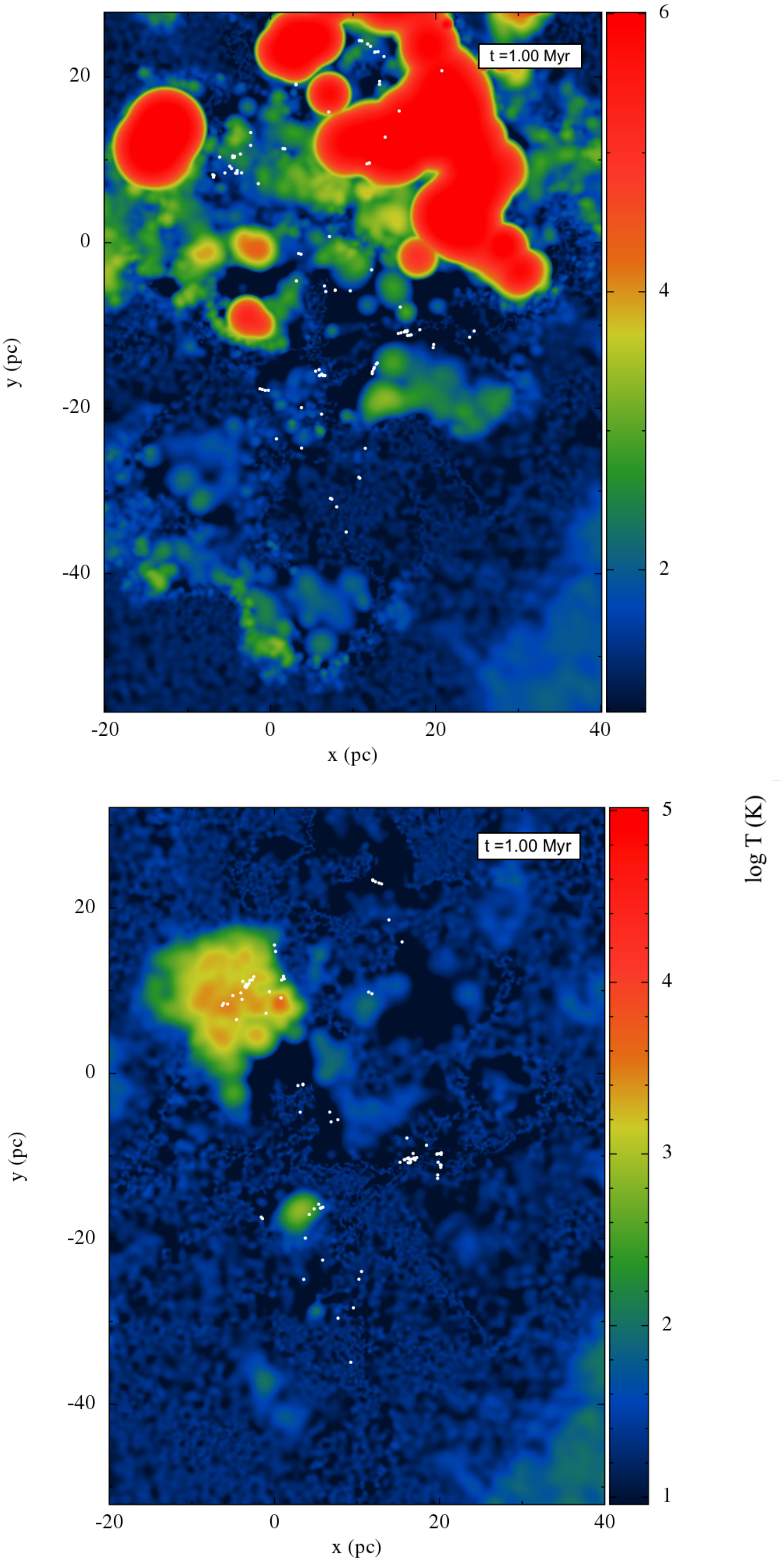

Figure 5.4.5: Temperature cross section (z = 4 pc) of Cloud B at 1 Myr in the evolution with the projected velocity field. In the top panel we show the run with winds, and in the bottom panel the simulation that includes feedback from SNe. Note that the temperature scale is different for the two plots.

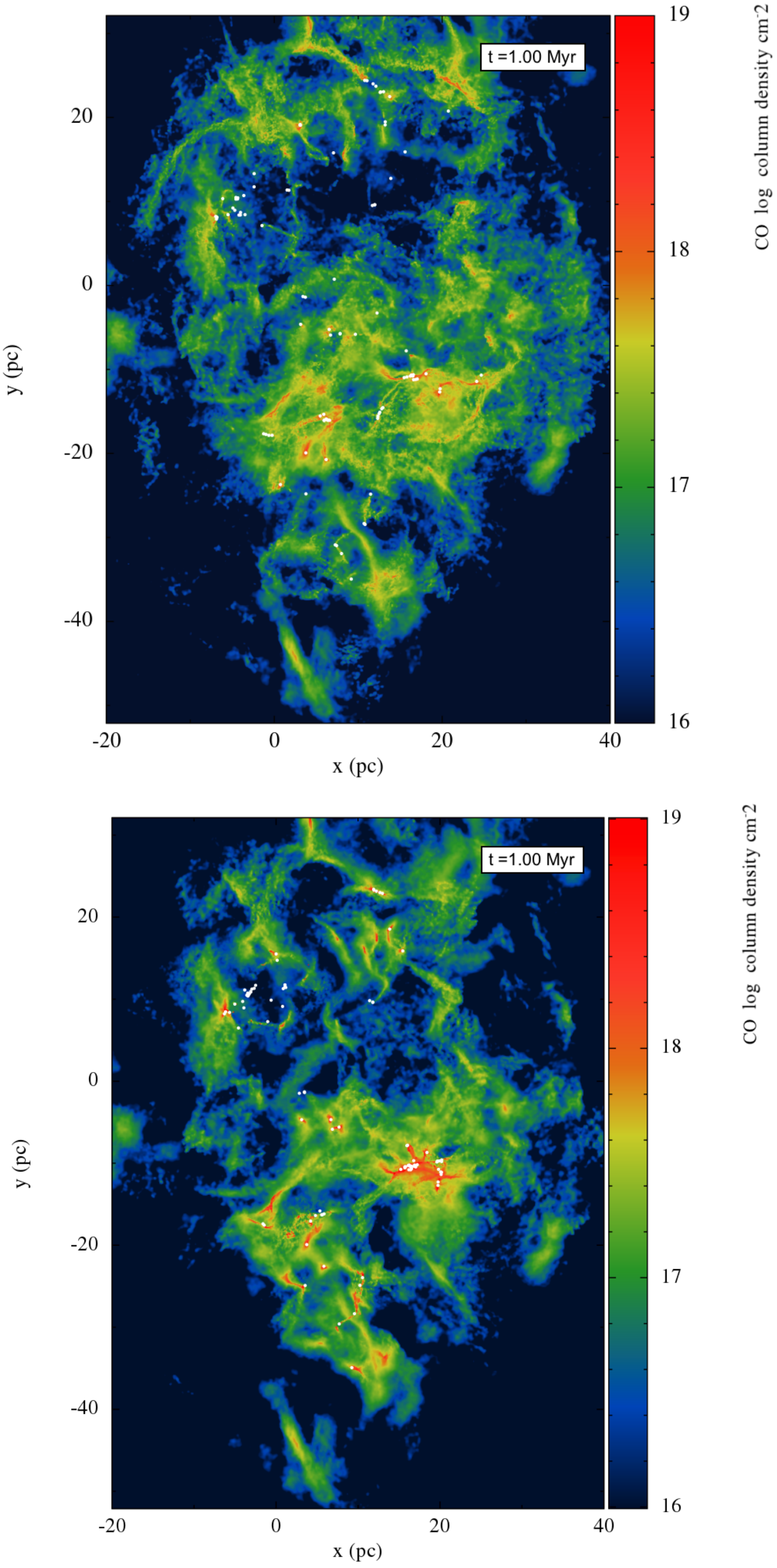

Figure 5.4.6: CO Column density render of Cloud B at 1 Myr in the evolution with the projected velocity field. In the top panel we present the run with winds, and in the bottom panel the simulation that includes feedback from SNe.

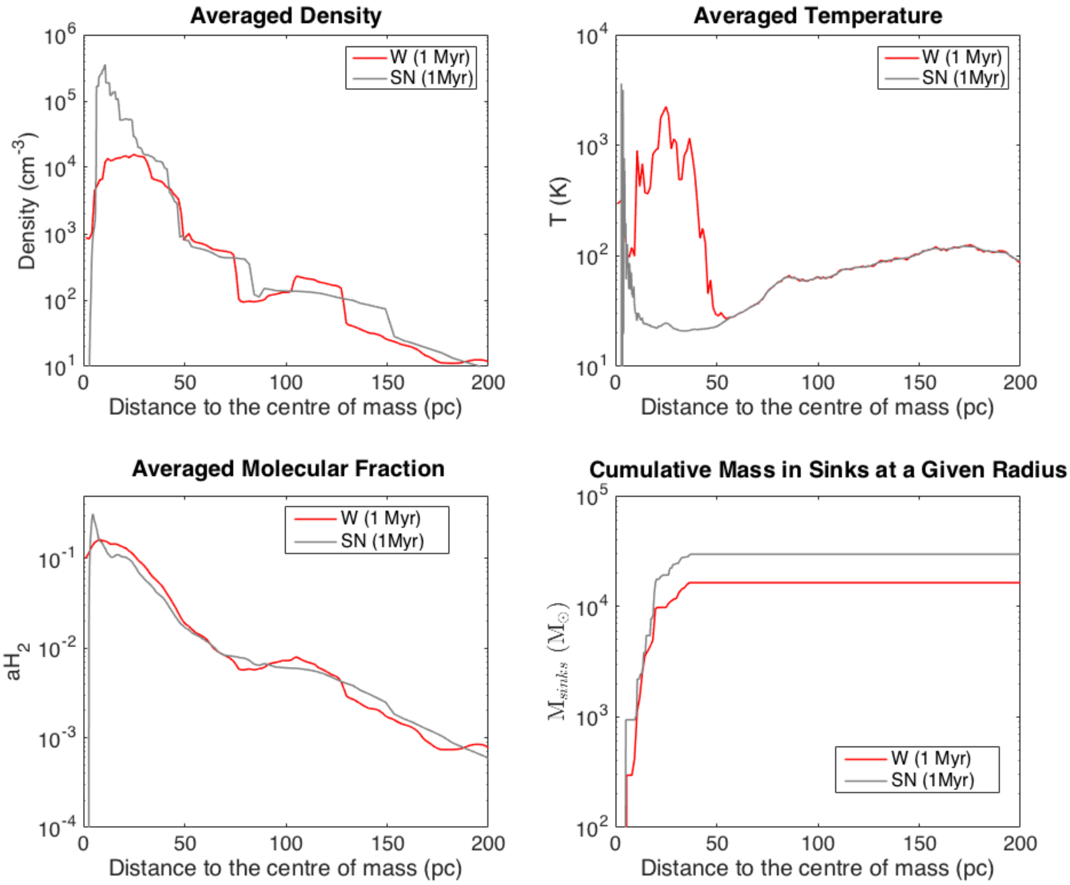

Figure 5.4.7: Variation of the properties of Cloud B with the distance to the centre of mass. We show the averaged density in the top left panel and averaged temperature in the top right. The molecular fraction is presented in the bottom left, and we show the cumulative mass in sinks in the bottom right.

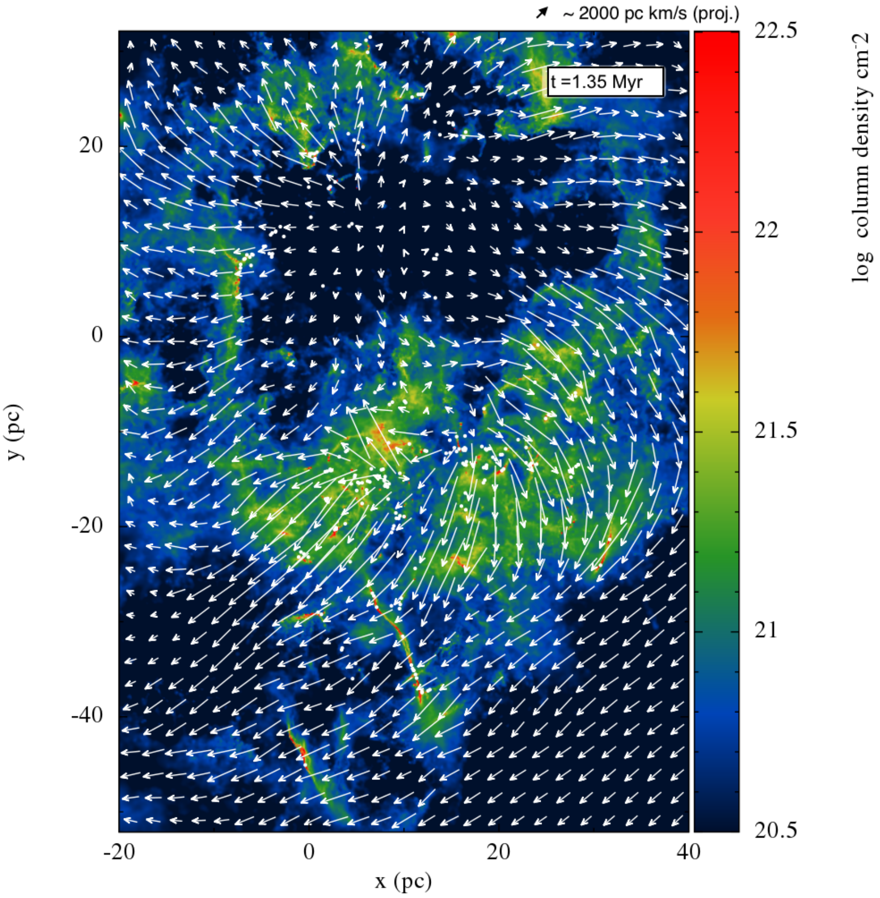

Figure 5.5.1: Column density render of Cloud B at 1.35 Myr in the evolution with the projected velocity field for the winds and SNe simulation.

5.5 Combined Effect of SNe and Winds

In this section we study the combined effects of winds and SNe. We use Cloud B with feedback from winds at 1 Myr as initial conditions. We stop the winds and set $t_*^{SN} = 0.7$ Myr, so that the first SN event happens shortly after 1 Myr (i.e. corresponding to sink creation just after 0.3 Myr). The rest of the sinks will produce SNe following the order of their creation. The simulation stops at 1.35 Myr. In Fig. 5.5.1 we present the column density map of Cloud B with the projected velocity field at 1.35 Myr. The large cavity has continued to expand. The central dense area is disrupted by several SN events, and the velocity field in that area is modified by the SNe. We observe the effect of these SN events in the shape of shells and other dense areas resulting from multiple nearby SNe in the CO map of the central area shown in Fig. 5.5.2. There are considerable number of sink particles that do not possess a molecular envelope, because it was dispersed by feedback. This depletion of gas by feedback happens as soon as the first stars are formed ($\sim$ 1 Myr) in accordance with models for the clusters in the LMC (Chandar et al. 2010). The temperature range of this cloud is also wide (20 - 10^6 K) as for the other feedback cases. As shown in Fig 5.5.3, we present a histogram similar to Fig. 4.6.2 but for Cloud B. We observe a significant fraction of hot gas ($T > 10^6$ K) that was not present in the non feedback run Fig. 4.6.2. With feedback there are

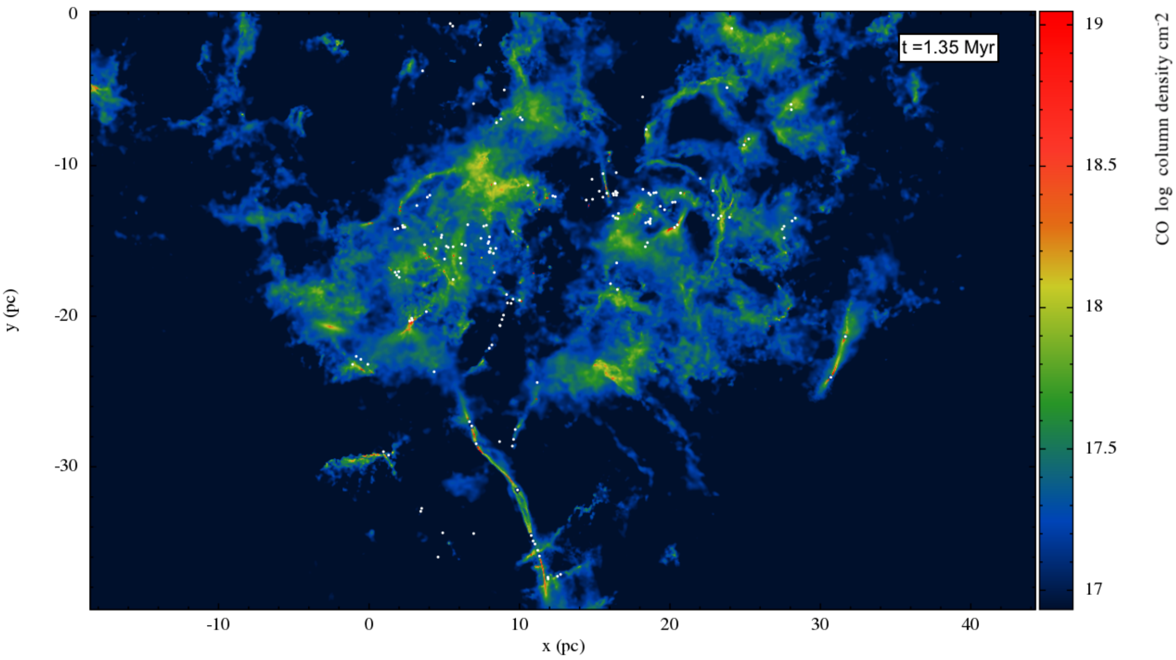

Figure 5.5.2: CO Column density render of the central area of Cloud B, modelled with winds and supernovae, at 1.35 Myr.

particles occupying the space between the hot and the warm ISM phases. When compared with Gatto et al. (2015), the state of our cloud is more similar to the 'peak driving' feedback in their work, as the 'random driving' the gas is more diffuse and with a stronger high temperature tail.

We study the variation of the properties of the cloud in Fig. 5.5.4. We show the average density, temperature, molecular fraction and number of sinks, for the three simulations of Cloud B that include feedback. All the models show fairly similar behaviour. The average density for the run that includes winds and SNe is higher than for the other simulations. The results here are in agreement with the SNe run, where multiple instantaneous injections of energy and momentum enhance the formation of dense areas.

5.6 Evolution of the Physical Properties of the Clouds

In this section we compare the evolution over time of different properties of the clouds (with and without feedback). We start by studying the SFR of the clouds represented in Fig. 5.6.1. We define the SFR as SFR(t) = $\dot{M}_*$(t), where $\dot{M}_*$(t) is the time derivative of the mass contained in sinks, as we did in Chapter 3, but over a shorter time period. For the simulations without feedback we use bins of 0.1 Myr, whereas for the simulations with winds we use bins of 0.01 Myr.

In general, winds reduce the SFR. For clouds A and B the reduction is considerable (nearly half) while for clouds C and D the SFRs are slightly reduced with winds. This is consistent with

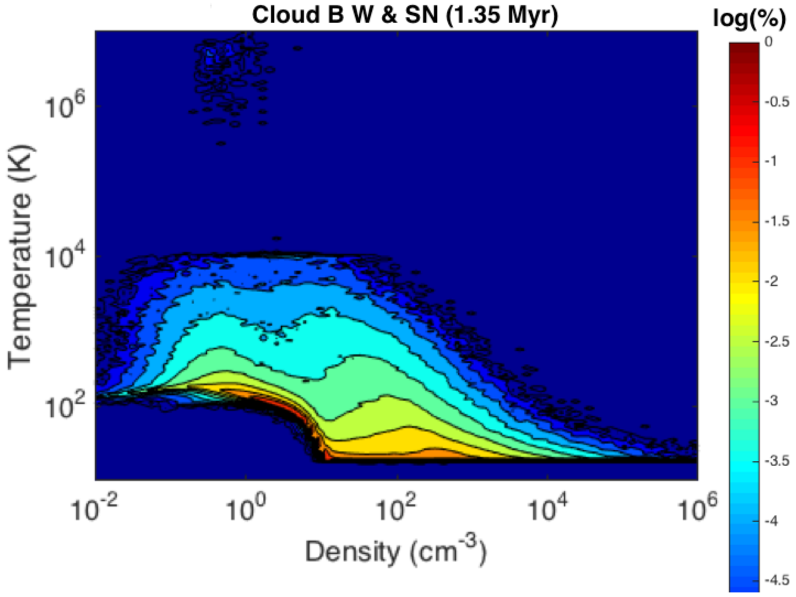

Figure 5.5.3: Temperature vs. density histogram.

the previous analysis of the effects of winds. The SFR of the run with only SNe of Cloud B presents a different behaviour. Initially, the SNe reduce the SFR and at later times in the simulation the SFR is comparable to the non feedback case. In the case of feedback from winds and SNe we also observe an increase in the SFR, although it is not clear how significant this is. One possible explanation for this increase is accretion by sinks. With winds accretion is difficult, but sinks which are no longer emitting winds may accrete SNe ejecta. SNe also contribute to the formation of dense areas that lead eventually to the formation of more sinks.

Fig. 5.6.2 shows the star formation efficiency defined as SFE(t) = $M_*(t)/M_g(0)$, where $M_g(0)$ is the initial mass of the cloud. We present the results as a percentage, and again the non feedback runs are shown with dashed lines, the feedback from winds as solid lines, and the SNe run with dotted lines (red for the SNe only and black for the combined run with winds).

As the SFR is the time derivative of the SFE divided by the initial mass of the cloud, both figures are related. We observe that the stellar feedback from winds substantially reduces the efficiency for clouds A and B (again by half). For cloud C and D the SFE is reduced by a smaller amount. In the run with only SNe, the SFE is higher than the case with winds, reaching almost the SFE of the non feedback simulation. When we include SNe in the run with winds, the SFE also increases approaching the non feedback case.

In Fig. 5.6.3 we show the variation of the virial parameter over time. We calculate the density-averaged velocity dispersion of the cloud on each timestep considering the other parameters constant. Therefore we neglect the change in size of the cloud over time, although this effect is smaller than 10% for the simulation times considered here. In the non feedback scenarios, the clouds become more virialised as they collapse and form more filamentary structures reducing

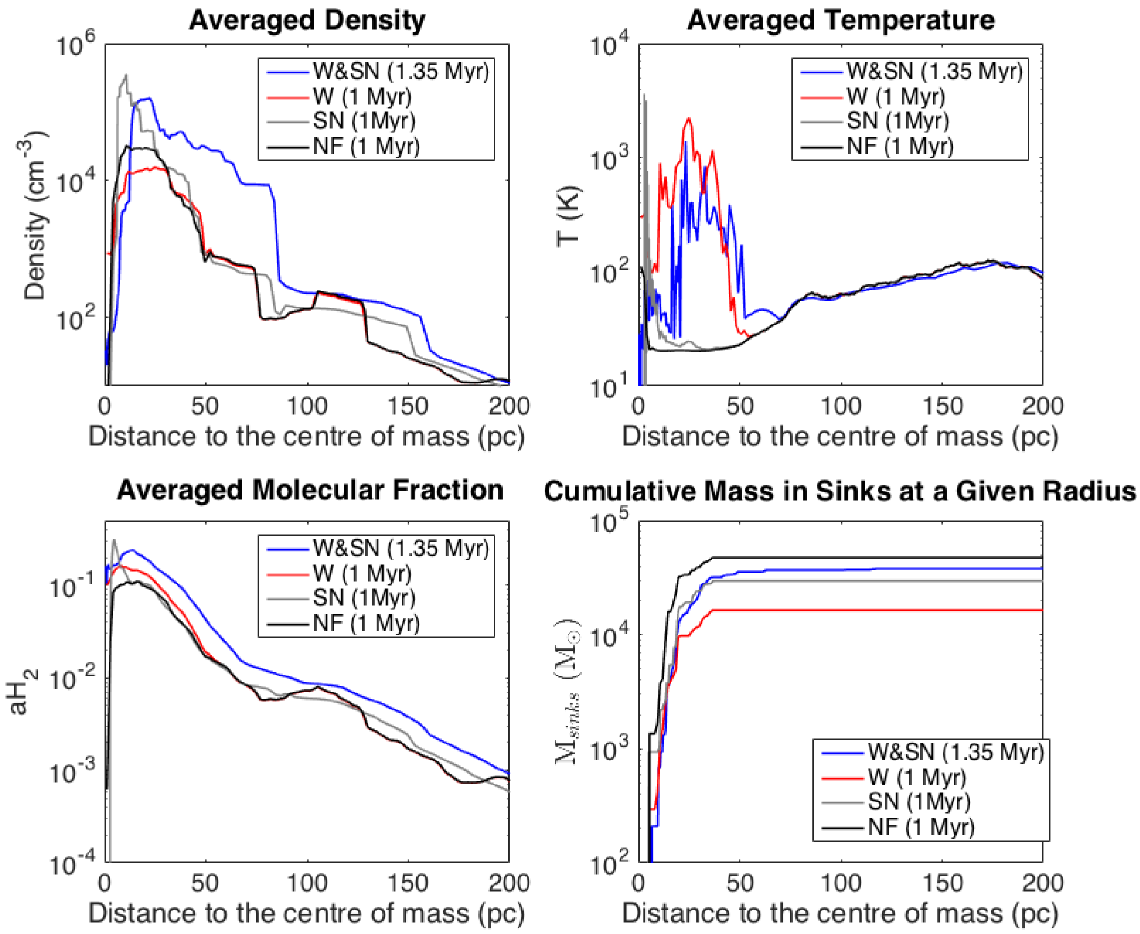

Figure 5.5.4: Variation of the properties of Cloud B with the distance to the centre of mass for all the feedback runs. We show the averaged density in the top left panel and averaged temperature in the top right. The molecular fraction is presented in the bottom left, and we show the mass in sinks in the bottom right. In this case we compare the 3 simulations that included feedback.

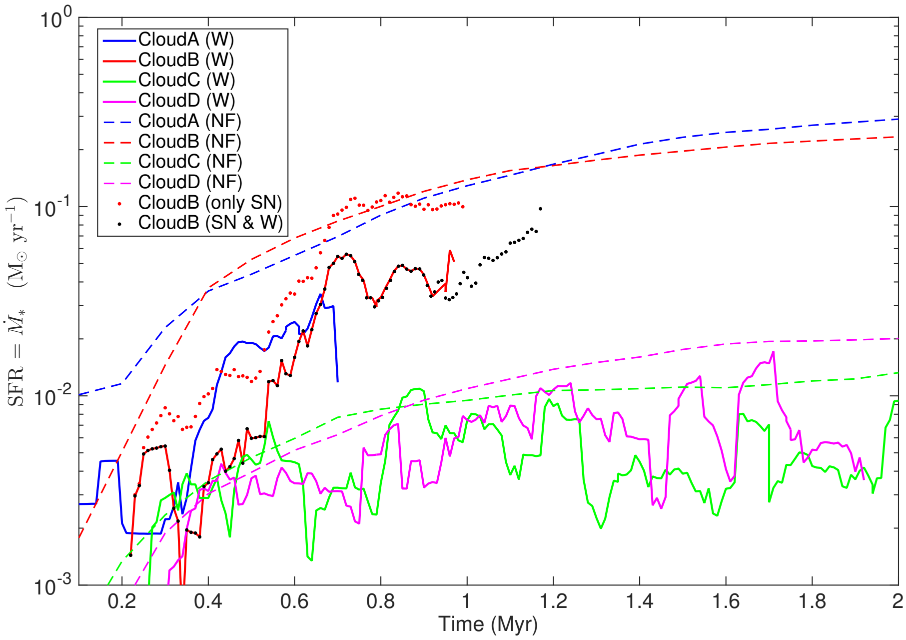

Figure 5.6.1: Star Formation Rate for the 4 clouds. We show with dashed lines the non-feedback runs, in solid the simulations with winds and with a dotted line the case with SNe.

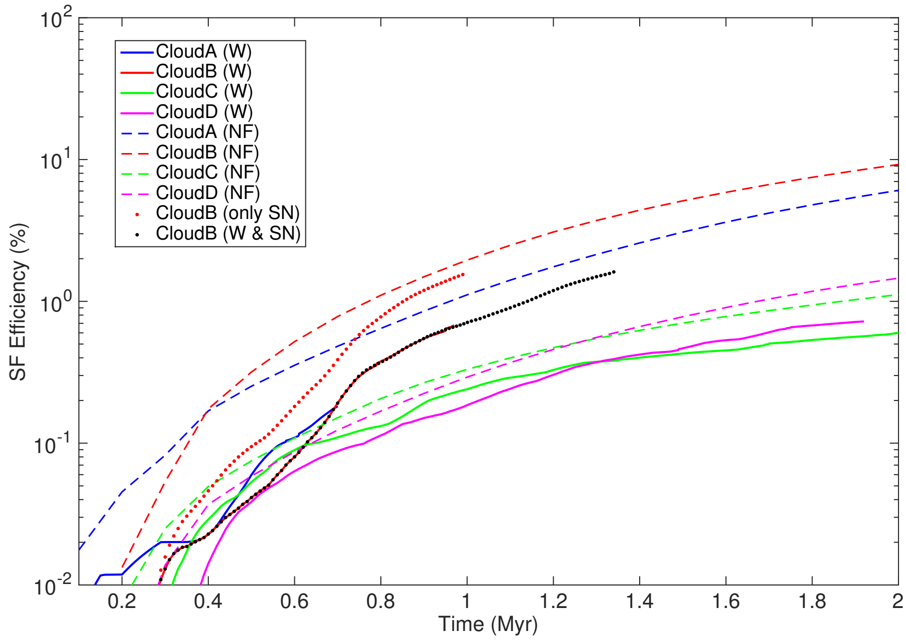

Figure 5.6.2: Star Formation Efficiency for the 4 clouds. We show with dashed lines the non-feedback runs, in solid the simulations with winds and with dotted lines the cases with feedback from SNe.

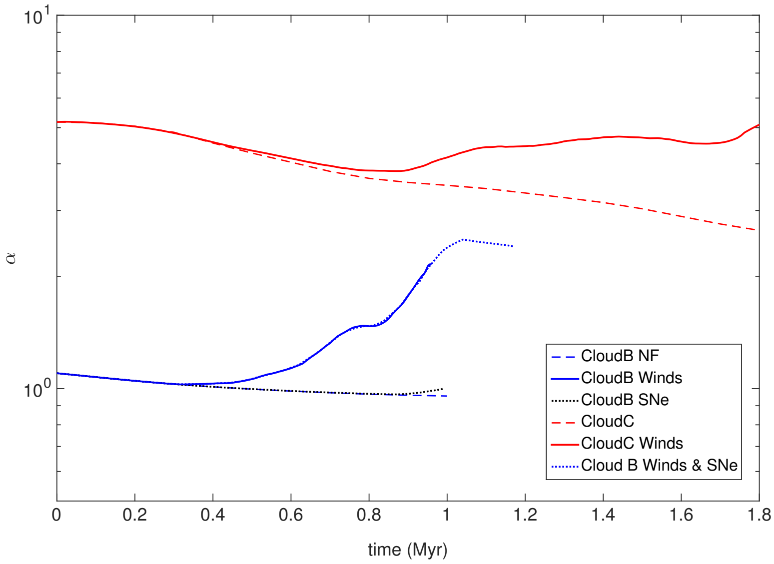

Figure 5.6.3: Variation of the virial parameter with time for clouds B and C

the velocity dispersion. Winds on the other hand, increase significantly the velocity dispersion of the clouds, and the effect is more patent for Cloud B than for Cloud C. The effect of the SNe is minuscule, and we do not think that the difference is conclusive.

We analyse the temporal evolution of the density averaged molecular factor aH_2 in Fig. 5.6.4. We do not find great differences between the feedback runs for a given cloud, suggesting that feedback does not have a great impact on the chemistry. It is worth noting that Fig. 5.6.4 shows density average molecular fraction, and in very dense areas the cooling is highly effective and therefore gas affected by feedback is able to reduce its temperature without severely affecting its molecular composition.

5.6.1 Energy Budget of the Cloud

To examine why the effect of winds is much more pronounced than the SNe we present the total thermal and kinetic energy of the clouds in Fig. 5.6.5. We express the energies of the clouds in $E_{\rm SN}^{O} = 10^{51}$ erg units. Once the gas temperature has settled (we initialise the clouds at $T = 50$ K), the thermal energy for the non feedback case remains practically constant. Note that at 1 Myr both clouds have the same thermal energy, even though Cloud B is practically twice as massive as Cloud C. This is because Cloud C possess more diffuse gas, that is at a higher temperature. For the kinetic energy there is a decrease due to the fact that more gas is captured in sinks, and is not accounted for. The kinetic energy of both clouds is an order of magnitude larger than the thermal.

The behaviour for the SNe run is again very similar to the non-feedback scenarios, suggesting that the energy (thermal and kinetic) injected is quickly radiated away. The density varies in the area affected by the SNe, at least, by two orders of magnitude. Hot shocked gas (T $\sim 10^6$ K)

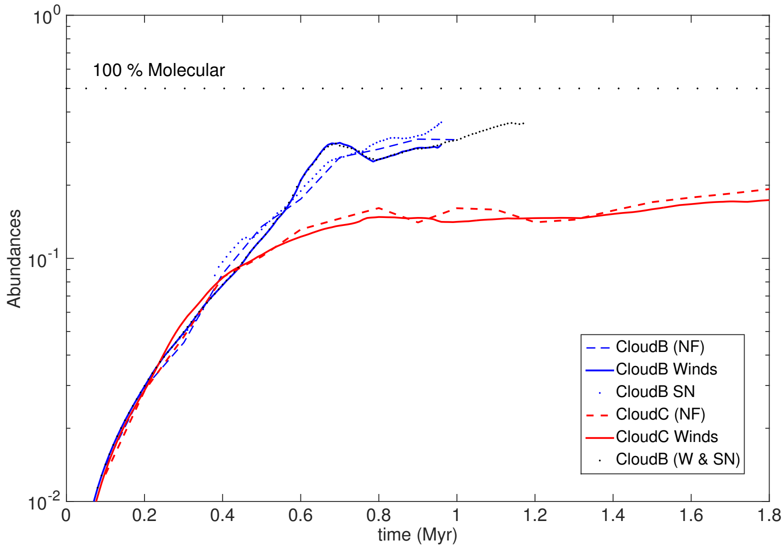

Figure 5.6.4: Variation of the average molecular fraction with time for clouds B and C

has different cooling times ranging from ∼ 100 yr for $n \sim 10^3$ cm^{-3} (see e.g. Agertz et al. (2012); Sutherland & Dopita (1993)) to ∼ 1 yr for the very dense areas ($n \sim 10^6$ cm^{-3}). The cooling in these dense regions is very efficient, and therefore the gas around the sink is able to lose the injected energy swiftly.

Winds shock the ISM, increasing considerably the thermal energy of Cloud B, as the continuous injection of energy impedes the cooling of the hot gas. There is however a substantial difference between the two clouds. For Cloud B the increase in the thermal energy is approximately of a factor 10, whereas for Cloud C winds double the thermal energy of the cloud. This difference in the effect of feedback is in agreement with the difference in the star formation rate of the clouds. As suggested in previous sections, the characteristics of the cloud affect the way feedback interacts with the gas, and how it couples with the ISM. The effect of winds is also clear in the kinetic energy of the clouds. Again for Cloud B this is greater than for Cloud C.

We also include the radial profiles of the thermal, kinetic an potential energies (absolute value) for the clouds in Fig. 5.6.6. We have used the spherical shell approximation to calculate the potential energy. The thermal energy profiles are similar to the temperature, as expected (the binning for this figure is coarser than for the others). The injection of kinetic energy from the winds is more visible again in Cloud B than in C, and clearer in the central area of Cloud B, as discussed before. The feedback seems to have little impact on the gravitational energy of the clouds, only causing differences at short radii for Cloud B.

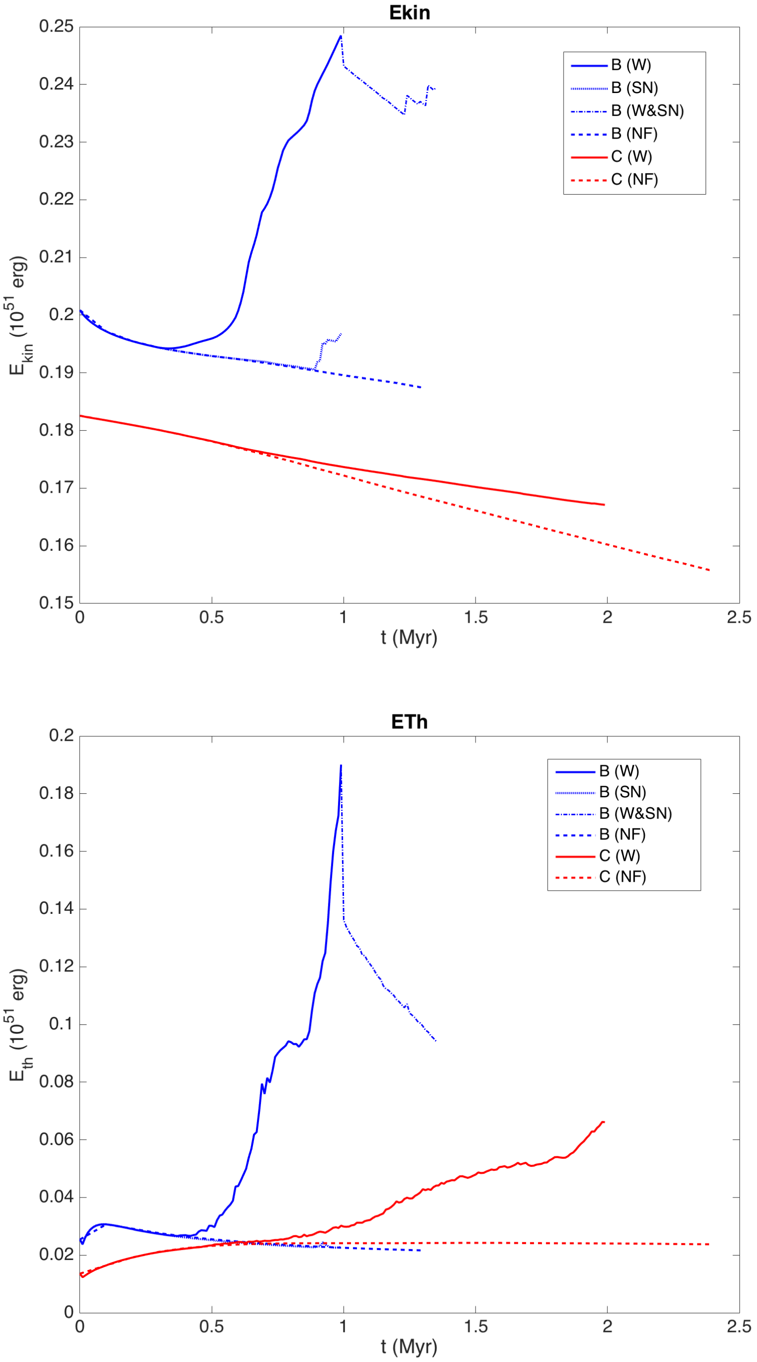

Figure 5.6.5: Evolution of the kinetic and thermal energy of the clouds.

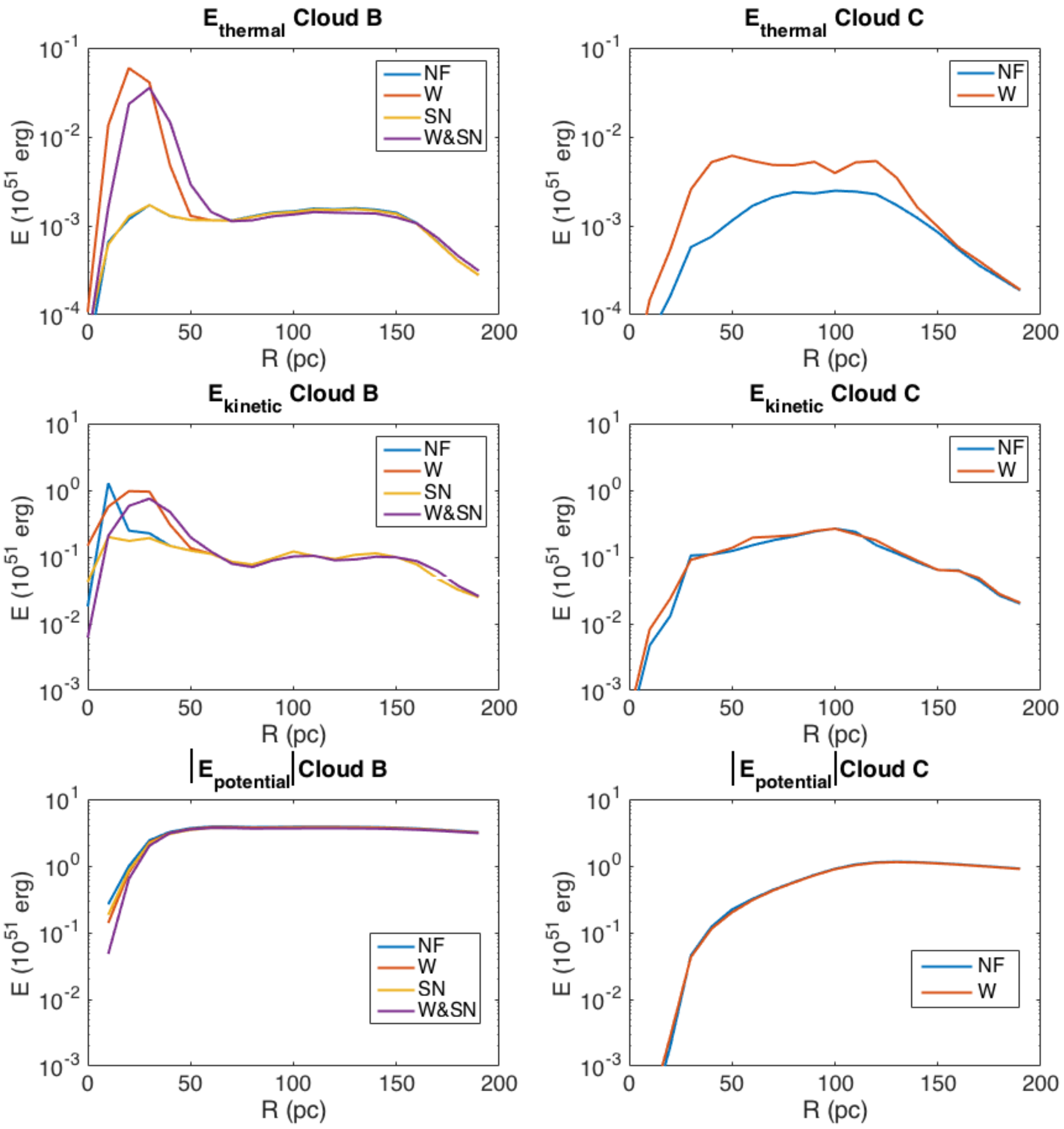

Figure 5.6.6: Thermal, kinetic and potential (absolute value) energy profiles of the simulations.

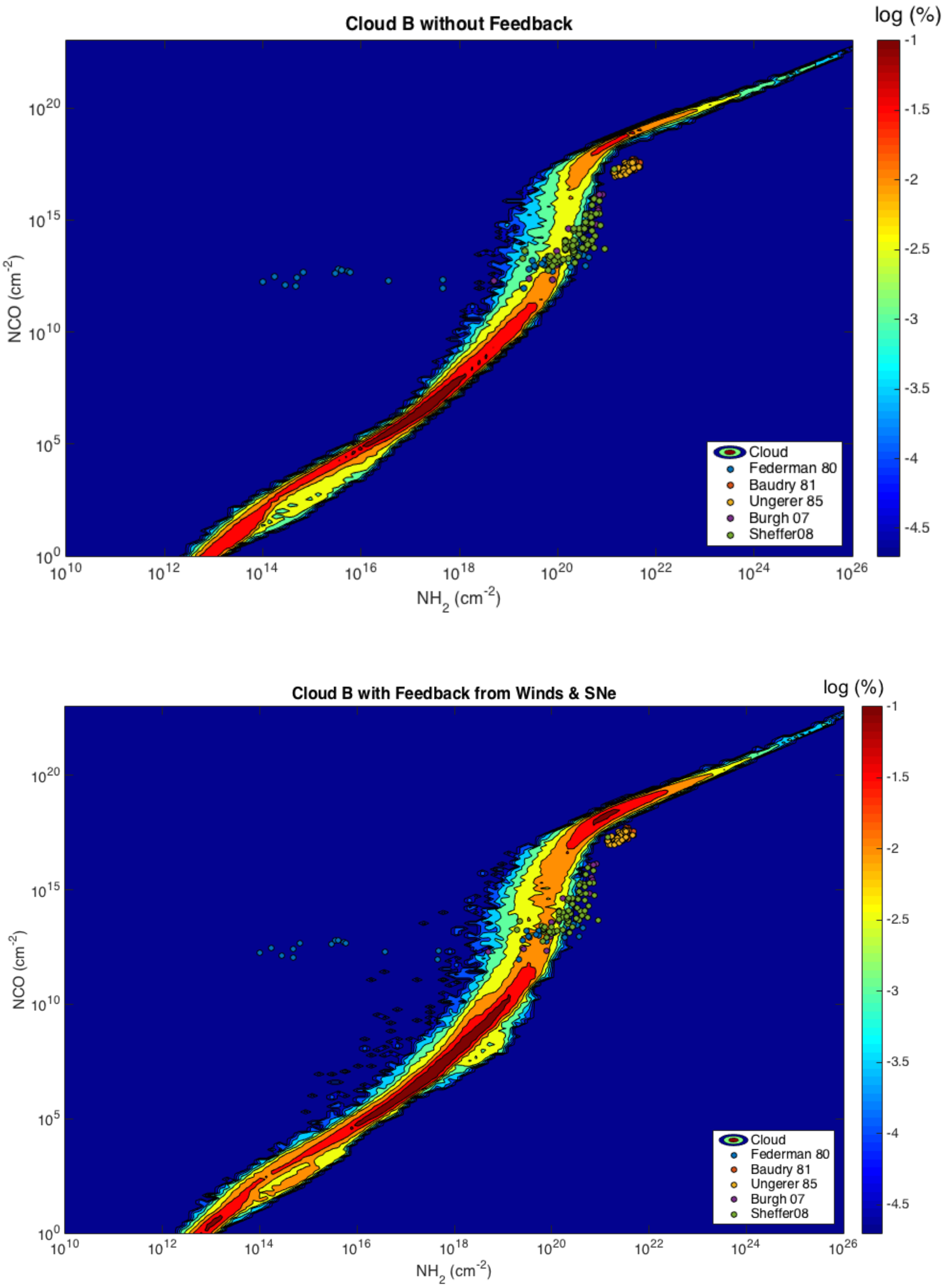

Figure 5.7.1: Comparison of the column densities with data from different surveys and Cloud B. The left panel is for the case without feedback and the right panel is for the case of feedback from winds. Results are taken at 1 Myr for the non feedback case and at 1.35 Myr fo the case with winds.

5.7 CO Column densities

In Chapter 4 we compared our results without feedback with observations (Federman et al. 1980; Baudry et al. 1981; Ungerer et al. 1985; Burgh et al. 2007; Sheffer et al. 2008), following Duarte-Cabral et al. (2015). Instead of using a 100 x 100 grid for calculating the column densities, we have increased the resolution to a 500 x 500 grid so that the small scale effects of the feedback may be resolved. We integrate over the Y axis. As the feedback may eject gas at larger distances, we have increased the z range to calculate the column densities from -50 < z < 50 to -100 < z < 100 (pc). Therefore the column density plots for the non-feedback case shown here may be slightly different from Fig. 4.6.10.

For the case of a highly virialised cloud (Cloud B), we present the results in Fig. 5.7.1. The left panel shows the non feedback case, and the right panel the run with winds and SNe (at 1.35 Myr). The overall shape of the distribution is similar with and without feedback. This is in agreement with the CO column density plots (Fig. 5.3.5, 5.3.11 and 5.4.6).

The maximum at high densities ($\sim 10^{22}$ cm^{-2} for $N(H_2)$ is more prominent for the feedback case. SNe enhance the production of dense areas in the cloud, increasing the creation of CO. For the low density tail, there is not much difference between the models. In the simulation with SNe the dispersion at the end of this tail is slightly higher, probably provoked by the mixing caused by the different SN events.

5.8 Discussion

In this chapter we have performed simulations of molecular clouds that include feedback from winds and SNe. We started by analysing the effect of winds in two clouds with different velocity structures. The shocked gas from the winds punctures the main wind blown bubble and escapes through the diffuse areas of the clouds. This is also observed in other works such as Rogers & Pittard (2014). In our simulations winds impede the formation of stars in all the clouds, mainly by stopping accretion onto sinks (see also Dale & Bonnell 2008), but also through dispersing the gas. In comparison to these previous works though, we model GMCs with a wider variety of typically more realistic morphologies. We find that the clouds' inherited properties from the galaxy have a notable effect on the amount and effects of feedback.

The structures and velocity fields of Cloud B and C are very different, and this leads to differences in the strength and effect of the winds. As well as the density, or virial parameter, of the cloud leading to more star formation and feedback, we also find that the velocity field is significant. The effect of the velocity field (which in turn arises from the global galaxy model) in these two clouds can be explained by two factors.

1. The production of sink particles depends on the properties of the velocity field (see Chapter 3). Therefore the strength of the feedback from winds depends also on the inherited properties of the cloud.

2. The velocity structure of the cloud modifies the effects of winds. The intrinsic velocity field for the non feedback case is stronger in Cloud C than in Cloud B (see e.g. Fig 5.3.9 and 5.3.3). The velocity ratio $\frac{v_{winds}}{v_{gas}}$ is of the order of 1 for Cloud B, and 0.1 for Cloud C. Hence, the winds are more important for the velocity structure of Cloud B than C.

With stellar feedback, we see lower star formation rates compared to those in Chapter 3, and which are in better agreement with observations. The SFR is relative to the initial mass of the cloud. To compare with observed clouds we use the star formation efficiency rate SFER(t) = SFR(t) / M_{cloud} (as defined in Dale et al. (2014)). We find values of 0.004 Myr^{-1} for Cloud C and 0.015 Myr^{-1} for Cloud B. This is comparable to or even lower than observations, where SFER ~0.015 - 0.030 Myr^{-1} (Evans et al. 2009). The SFEs for Cloud C (~0.01) and Cloud B (~0.02) are also smaller compared to other computational works (in Dale et al. (2014) they are of the order 0.05 - 0.20). But we note that our simulation times are relatively short, and that particularly for Cloud C (where in Chapter 3 we saw that the star formation rate grew with time), the star formation rate may increase.

Feedback from winds significantly increases the virial parameter of the clouds. The effect is more important for Cloud B, as feedback changes its state from gravitationally bound to unbound. Whereas Cloud C is always unbound during our simulations. The de-virialisation effect of feedback has also been observed in other simulations like Colin et al. (2013).

Unlike other studies at larger scales (e.g. Duarte-Cabral et al. (2015)), who find that feedback decreases the molecular content in galaxies, we find that feedback has little impact on the amount of CO and H_2. This is likely because at higher resolution, we produce denser and colder gas which is less readily disrupted by feedback, and because at sub-pc scales stellar feedback can effect lower density, rather than solely high density gas.

We find that SNe tend to be less effective compared to winds, and the energy and momentum injected by the SNe do not seem to couple to the gas (i.e. dense gas is not so effected by the SNe). This is in agreement with Rogers & Pittard (2013), who claim that 99% of the energy from the SNe escapes through holes and cavities created by winds. Our results are also consistent with Fierlinger et al. (2015) who find SNe are not so important on smaller scales (~ 10 pc) where winds inject twice as much energy as SNe, whilst Ibáñez-Mejía et al. (2015) find that SNe do not inject enough energy to maintain turbulence. However other studies that suggest that SN are the most effective feedback mechanism (Hensler (2010)), and other numerical work which claims that SN and photodissociation are more effective than winds (Geen et al. 2015). One reason SNe may be less effective is that although they heat the gas up to over 10^6 K, efficient cooling leads to a fairly rapid decrease in temperature. Hot gas emits energetic photons that are able to escape the cloud, using the corridors created in the clouds by the winds (Rogers & Pittard 2013), and exporting the energy from the SNe outside the cloud onto the galactic scales. The reduction of the energy coupling between SNe and the gas in the cloud is also observed in other simulations (e.g. Walch & Naab (2015)).

This shocked hot gas emits in the X-ray and has been observed in many star forming regions like the Rosette nebula (Townsley et al. 2003), the extended Orion Nebula Cloud (Güdel et al. 2008), or the 30 Doradus region (Lopez et al. 2010; Rosen et al. 2014), between others. These observations represent a fantastic window to understand the dynamics of the interplay between the ISM and the stellar feedback. The diffuse X-ray emission detected in many of these regions is thermalised (Rogers & Pittard 2014), meaning that is emitted because the shocked gas is hot, although its temperature varies depending on the characteristics of the star forming region. Typically the X-ray spectrum has a peak around 1 keV (Stahler & Palla 2008), but it can be smaller as in the Rosette and Orion nebula (Townsley et al. 2003; Güdel et al. 2008), or higher like the X-ray emission from the Arches cluster (Wang et al. 2006). This difference in the characteristics of the spectrum may be caused by the distinct origin of the X-ray radiation. Particles accelerated by stellar feedback travel through the surrounding inhomogeneous medium colliding with dense shells from other feedback events. This collision causes a strong deceleration. Hence, apart from thermal emission, we also find X-ray Bremsstrahlung in the GMCs (Townsley et al. 2003; Wang et al. 2006).

Note that we have been using the words "stellar feedback" to refer to the cause of the X-ray emission. We do so because it is still debated which feedback mechanism may be responsible for it. It is typical to assume that the thermal X-ray emission is caused by the mechanical power of stellar winds (Townsley et al. 2003; Güdel et al. 2008). This certainly is the case for very young star forming regions, which did not have the time for the formation of SNe. In a SN event the injection of energy happens in a very short period of time, less than a year (Draine 2011), and the gas is able to cool down considering the usual timescales for the clouds (~ Myr). Therefore, for a mid-size cloud, even if there is a SNR in the cloud, the gas would typically be at temperatures too low to produce X-ray radiation. Observations of well known HII regions like 30 Doradus, show that the star formation process occurs in different stages, each generation affecting the next one (De Marchi et al. 2011; Doran et al. 2013). In this region, an older generation of stars (~ 20 Myr) produces feedback which triggered the formation of the bright cluster in the centre of the region containing massive stars that are a few Myr old. These stars also coexist with protostellar objects covered in dusty envelopes that will eventually disperse liberating newly born stars within them. Therefore, a SN event happening recently may be the cause of the hot gas emitting X-ray thermal radiation. This possibility is supported by the increased metallicity observed in the diffuse component of these complexes (see e.g. Lopez et al. (2014)).

The clouds simulated in this Chapter have a similar size as 30 Doradus, and in the non-feedback runs that cover longer timescales (~ 10 Myr), we observe the existence of different generations of stars. However when we include feedback we are restricted by the short simulation times, and having multiple generations of stars in one cloud becomes unfeasible. Our results suggest that the cause for the diffuse X-ray emission is the mechanical injection of winds, as this is the only mechanism able to keep the temperature of the diffuse gas over 10^4 K (which corresponds to a thermal emission of 4 eV approximately) for a significant period of time. We have shown that a fraction of the gas is at temperatures of the order of $5 \cdot 10^6$ K, corresponding with a thermal emission of $\sim$ 1.5 keV, and therefore able to emit X-rays. We also observe that the cooling time for gas subject to feedback from SNe is comparable to observations $\sim 10^4$ yr (Kavanagh et al. (2011)), so in the absence of the winds the gas loses temperature rapidly, and it is not able to emit X-ray. Our simulations support the idea that the diffuse X-ray emission is mostly produced by stellar winds.

There are differences between our work and the above studies which may further effect the impact of feedback. So for example Rogers & Pittard (2013) only model a small patch of a GMC, and do not include self gravity. In our simulations, we model a whole GMC and the inclusion of self gravity likely leads to denser gas and / or a convergent velocity field which counters the effects of feedback. Thus it is unsurprising that feedback appears particularly effective at dispersing the clouds modelled in Rogers & Pittard (2013). Again our spatial scales are larger, and initial conditions much more complex compared to other studies (Dale et al. 2014; Geen et al. 2015; Fierlinger et al. 2015) and even Walch et al. (2012) who model fractal clouds. Furthermore some of these models simply place a star particle emitting feedback at the centre of the simulation Geen et al. (2015); Fierlinger et al. (2015). Our results suggest that the different morphology of clouds may have an impact on the level, and effectiveness of feedback on the gas dynamics of the clouds.

There are further caveats to our models, in addition to not including ionisation. Some of our results, such as the triggering of star formation by SNe, are based on tests of only one cloud. Ideally we would want to base any generalisation of this result on a larger sample. We have also not simulated our clouds for as long a timescales as we would like. Computing time is even more problematic than usual with our more realistic conditions for several reasons:

1. The simulations present very dense areas in the beginning causing a reduction of the timestep for particles in those regions.
2. The GMCs generate sinks very early in the simulation, and these sinks start producing winds the moment they are created. The effect of the winds is twofold: first they shock the nearby gas reducing the timesteps for those particles, and they increase the computing time as there is a larger number of MPI instructions. This second effect is not so relevant for SNe as they are modelled in one timestep.
3. The inherited velocity field of the GMCs may also slow the simulation by reducing the timestep in regions with a large range of velocities.

We are also aware that we may be overestimating the mass of massive stars in our sinks (calculated via the W_{eff} parameter). A relatively large fraction of our sinks are assumed to constitute massive stars, whereas ideally the fraction of massive stars should reflect the observed stellar IMF (Kroupa 2001). For future work we will likely consider a more realistic stellar production model for our sinks. For instance, we could assign a value of M_* to each sink according to the observed IMF, every time a sink is created, which is then fixed for the remainder of the simulation.

6

Conclusions and Future Work

"After all, tomorrow is another day"
– Scarlett O'Hara (Gone with the wind)

6.1 Conclusions

In this thesis we have aimed to build a bridge between the simulations of molecular clouds at galactic and sub-pc scales. We produced isolated molecular clouds that still retain the characteristics from their galactic context, and we find that the influence from the galaxy should not be disregarded. Clouds with different morphologies and in particular distinct velocity fields, do not evolve and generate stars in the same way. The effects of the star formation process (e.g. stellar feedback) are also altered by the morphology and velocity structure of the cloud.

In the first chapter of this thesis we described the most important aspects about star forming molecular clouds. We synthetised the main properties of the ISM and molecular clouds focusing on stellar feedback. In Chapter 2 we described GADGET2, a SPH code we use to model galactic molecular clouds. In the second part of this chapter we described our method for increasing the resolution of a given galactic cloud. For each original SPH particle in the cloud, we generate a fixed number ($F - 1$) of new particles using a random distribution which follows the SPH kernel of the original particle. We tested this method for different values of F in the range 10 - 1000. We compared our method with 2 other ways of increasing the resolution of a given cloud in SPH (cubic and spherical), and found that the SPH kernel method is the one that conserves the initial density field with more fidelity, avoiding introducing any additional structure in the cloud (Fig. 2.4.8).

We selected four galactic clouds from two different simulations in Chapter 3 and compared them with three turbulent spheres. We matched the virial parameter α of the turbulent spheres to the first 3 clouds (A, B and C). We generated the turbulent velocity field of the spheres following Dobbs et al. (2005) and making their velocity dispersion comparable with Cloud A. We traced the gas that constitutes Cloud A ten million years back in the galactic simulation, and extracted the resulting cloud (Early A). We found that the density PDF at the time the first sink is formed for all the clouds is similar although dependent on the particular characteristics of the clouds. We analysed the SFR for the clouds and spheres and compared them setting time of origin as the moment when the first sink is created. For the galactic clouds this occurs very early in the simulation, whereas for the spheres the time for the formation of the first sink increases with the virial parameter. The star formation rate depends on the initial velocity field of the clouds, so even though Cloud C and Early A have a similar virial parameter, Early A is more efficient at creating stars. To parameterise the velocity field we included two extra parameters β_u and γ_u, that are related to the divergence and curl of the velocity field. High SFR occurs for small β_u and γ_u at least for the four galactic clouds. We are aware that this is a reduced sample of clouds and we would like to test these parameters in a statistically representative set of clouds. We compared the star formation histories of Early A and Cloud A in this chapter. Early A should become Cloud A after 10 Myr. However, sinks are formed in the beginning of the simulation in Early A and they accrete gas during 10 yr, depleting the cloud of gas and modifying its properties.

In Chapter 4 we described models including chemistry and the ISM cooling/heating (clouds A, B, C and D). We found that the average temperature of the clouds is low (~ 25 K), but their temperature range encompasses temperatures across the neutral ISM (10 - 10^4 K). The complex velocity field of Cloud C and D mixes the gas, bringing warm diffuse gas from the periphery of the cloud into the central and cold parts, creating small bubbles of diffuse gas in the centre of the cloud. The clouds not affected by galactic shear (Clouds A and B) become molecular in a shorter period of time. We also compared our clouds with observations, and found that our models overestimate the existence of CO at large column densities, where probably part of the CO is frozen on the surface of dust grains. Using the radiative transfer code TORUS we produced synthetic observations for the clouds and calculate a value for the X-factor of $X_{CO} \sim 1.5 \times 10^{20}$ cm^{-2} K^{-1} km^{-1}, which is 20% smaller than the value from Dame et al. (2001).

We studied the effects of feedback from winds and SNe in Chapter 5. We included winds in the simulations of the most virialised cloud (B) and the cloud most affected by shear (C), to study the impact of the feedback in clouds with very different velocity fields. The effect of winds is greater in Cloud B, where the winds oppose the homogeneous gravitational collapse, than in Cloud C which has a intricate network of filaments. This difference may be explained by two factors. First, sinks in Cloud B are more massive and emit powerful winds (the velocity field is responsible for the difference in the mass of sinks). The second reason is the complex structure of Cloud C. Winds escape through the most diffuse areas, and Cloud C has a very complex structure with mixed dense and diffuse areas. We also included SNe in Cloud B to test the difference between the two types of feedback. The continuous injection of momentum by winds is more effective disrupting the cloud than the instantaneous series of SNe events. We found that the SNe feedback can create denser areas than in the case without any feedback.

Although the fact that Cloud C is subjected to a strong galactic shear is independent of the resolution, the cloud's complex filamentary structure could be enhanced as a result of the initial resolution of the cloud. In the galactic simulations, Cloud C has an initial resolution which is ~20 times higher than Cloud B. Well resolved filamentary structures in Cloud C would look as pseudo-spherical entities in Cloud B. We present an example of this in Fig. 6.1.1b where we show Cloud C rendered at different resolutions. Although the SPH kernel method preserves the density profile of the cloud, it does not include additional structure. A spherical mass of gas would be converted into a spherical mass of gas made of more SPH particles, whereas in a real molecular cloud, that mass presumably has some internal structure. This constitutes a limitation of our method, but could be alleviated by successively resimulating a section of galaxy, or galactic cloud in the manner of Clouds C and D.

Apart from this resolution effect, using molecular clouds extracted from simulated galaxies provides us with a more realistic set of initial conditions. The inherited velocity field affects the evolution of the cloud (independently of the resolution used), and has an impact on the way new stars are formed. The effect of the stellar feedback also depends on the inherited properties of the cloud.

6.2 Future work

In this section we summarise the next steps that may be taken to understand the effects of galactic context in star forming molecular clouds.

6.2.1 Enhanced Star Formation by SNe

The results presented in this thesis regarding the effect of SNe in molecular clouds are restricted to only one cloud with a particular morphology. To extract more general conclusions, this study should be extended to a wider range of clouds, including shear dominated clouds like C and D. If the SNe explosions enhance the formation of dense areas in these clouds, it would be a strong indicator that SNe feedback triggers star formation.

The coupling between SNe and the ISM is also important at galactic scales, as SNe may drive ISM turbulence (Padoan et al. 2015), or be responsible for the vertical distribution of temperatures in the galaxies (Agertz et al. 2009). Different models of galaxy formation in a cosmological context (e.g. Agertz et al. 2011; Kimm et al. 2015) point out the importance of the small scale (~ pc) effects in the evolution of galaxies. Studying the effect of SNe in molecular clouds at high

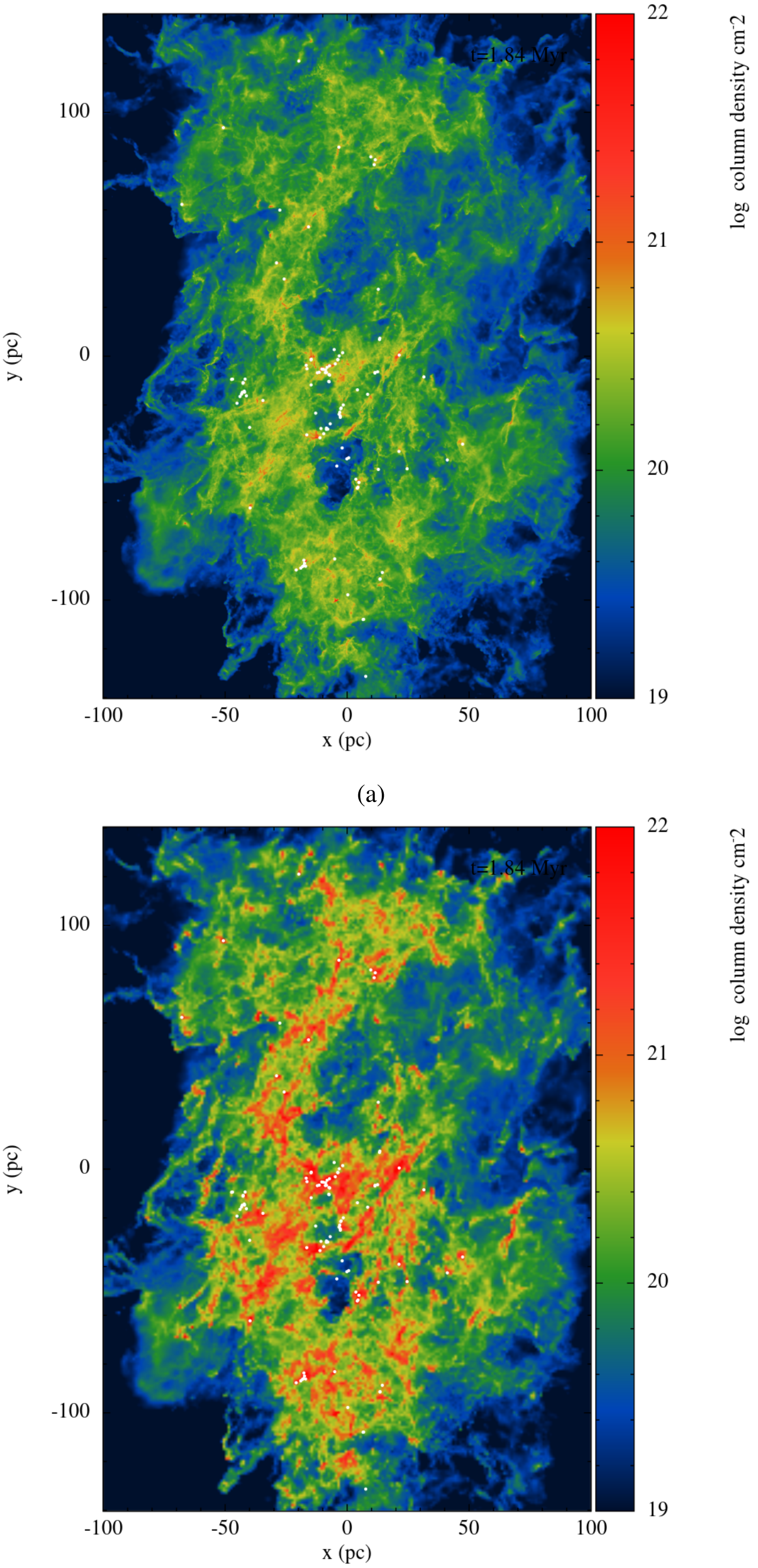

(a)

(b)

Figure 6.1.1: Column density render of Cloud C after 2.0 Myr of evolution. In (a) we show the high resolution render, and in (b) the low resolution. Well defined filaments in top left panel become *blurred* structures in the low resolution case.

redshift may help to understand the formation of galaxies and their evolution in a cosmological context.

6.2.2 Resolution Effects on GMCs

Analysing the effects of the resolution when implementing feedback would also be desirable. The clouds directly extracted from galactic simulations (A and B) do not feature such small scale (e.g. sub pc) structure compared to clouds C and D, which have been extracted from a resimulation of a section of galaxy. As such, Clouds A and B require a greater increase in resolution. The section of a galaxy simulation was limited by only containing a few massive clouds which tended to be unbound, but ideally we would also perform simulations of Clouds A and B with $F \sim 20$, i.e. requiring a smaller increase in resolution.

6.2.3 Synthetic Observations

In Chapter 4 we showed the synthetic observations for the clouds using the TORUS radiative transfer code. We assumed LTE, however synthetic observations that include non-LTE radiative transfer are more realistic, and would allow to have better constraints on the X-factor. The radiative transfer code produces CO intensities, that are ideal to compare with data from real observations (see e.g. Drabek et al. 2012; Lopez et al. 2014). Apart from including a larger sample of clouds, one idea would be to change the position of the observer when post-processing. Particularly when considering stellar feedback, holes or shells may have quite different morphologies depending on the viewing angle (Haworth et al. 2013). Changing the position of the observer in the simulated galaxy may alter the observed properties of the cloud. To illustrate this point, in Fig 6.2.1 we show the CO column density for the winds run of Cloud B. The top panel presents the column density calculated on the xy plane, and the bottom panel the column density of the xz plane. Even though it is the same cloud in both pictures, there are differences. We do not observe the central cavity in the right panel, hence in a first impression, the cloud seems to be less affected by the winds in the xz plane than in the xy.

Our CO maps could be compared with real cloud CO maps in a number of ways. These could include:

1. Estimating the parameters β_u and γ_u for observable clouds and compare them with our simulations, or similarly, measuring the relative fractions of solenoidal and compressive turbulence in the clouds with and without feedback (using an analysis similar to Brunt & Federrath (2014)).
2. Using a statistical tool such as Principal Component Analysis (PCA) of the CO intensity (e.g. Bertram et al. (2015)) would allow to compare the structure of observed and simulated clouds at different scales (we do not have data of the spatial structure of clouds in the line of sight direction). Another possibility in this direction is to compare the formation of

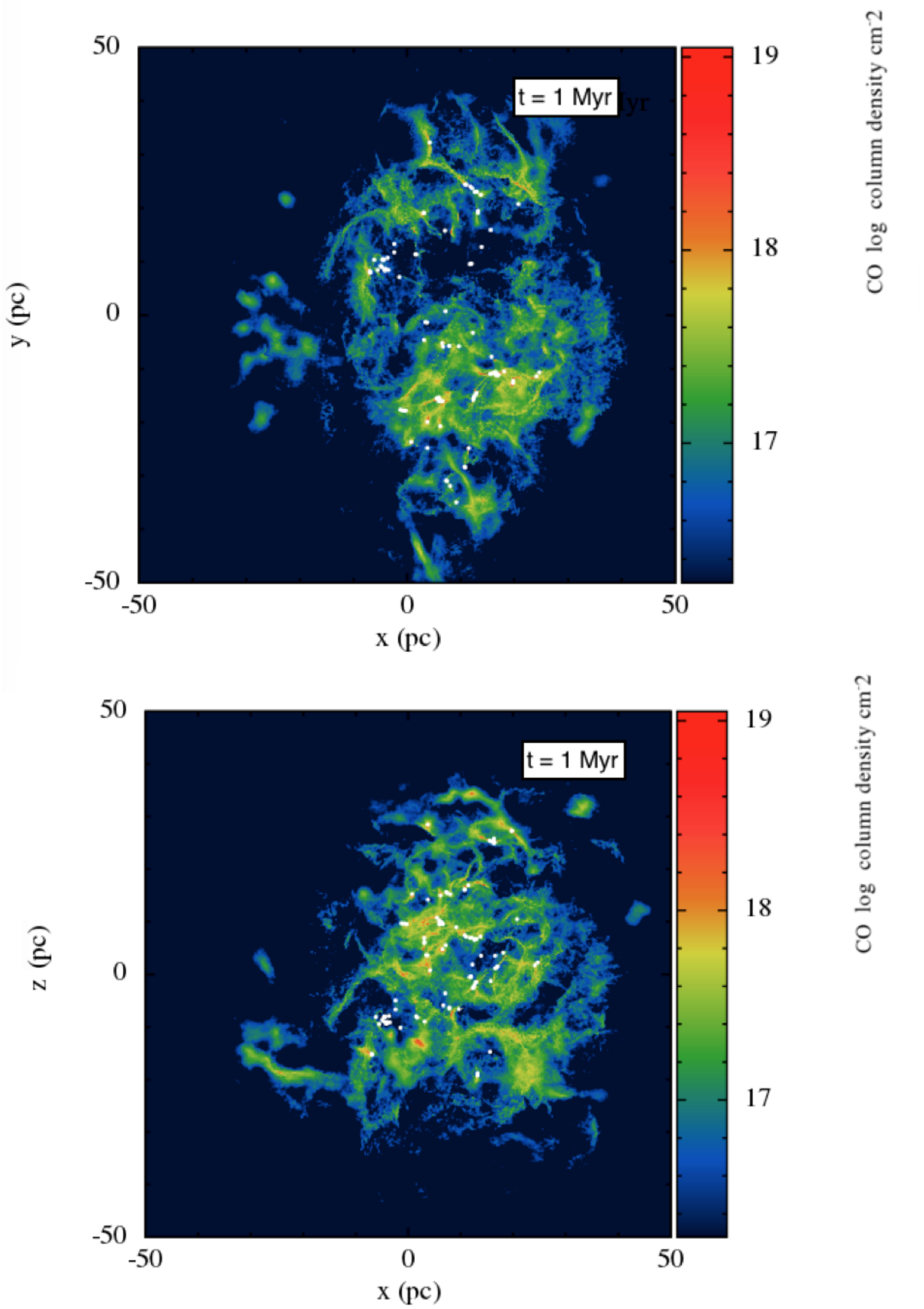

Figure 6.2.1: CO column density of Cloud B for the run with winds, calculated on the *xy* plane (top) and on the *xz* plane (bottom).

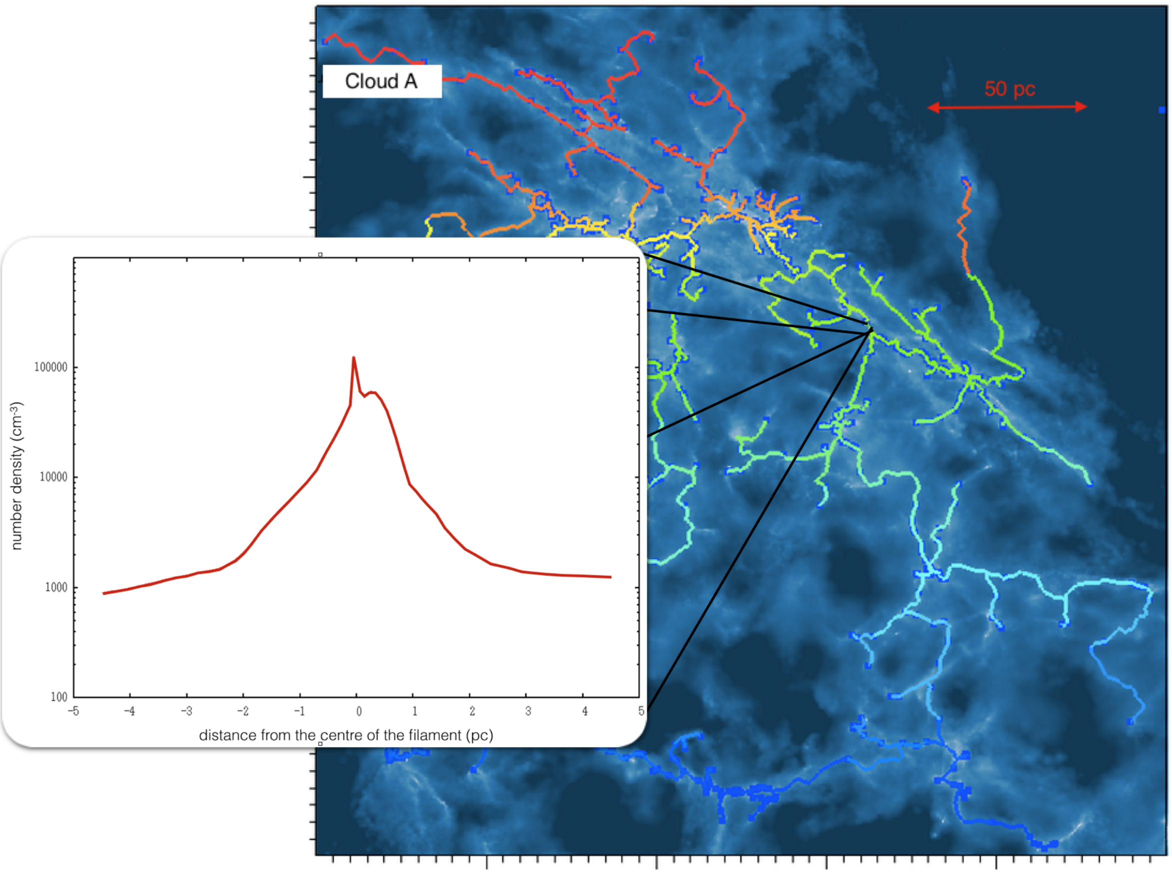

Figure 6.2.2: We show the column density map of Cloud A, with the filaments found with DISPERSE. The colour denotes the ordinal number of the filament. The cumulative density profile of a filament is also shown on the picture.

small scale structure by comparing the matter power spectrum employing an excursion set formalism (Hopkins 2011).

3. Using the algorithm DISPERSE (Sousbie 2011; Sousbie et al. 2011) to find filamentary structures in our clouds, and compare them to the results of other works (e.g Palmeirim et al. (2013)). Once the filaments are identified, different quantities can be calculated: average radial profiles of H_2 column density, lengths, masses and aspect ratios. In the right panel of Fig. 6.2.2 we show the results of using DISPERSE on Cloud A. The colour denotes the ordinal number of the filament, whereas we present an cumulative density profile of a filament from that cloud in the right panel. Furthermore, our resolution allows to compare the distribution of masses of cores in the filamentary structure (similar to the observational work by Peretto et al. (2012)).

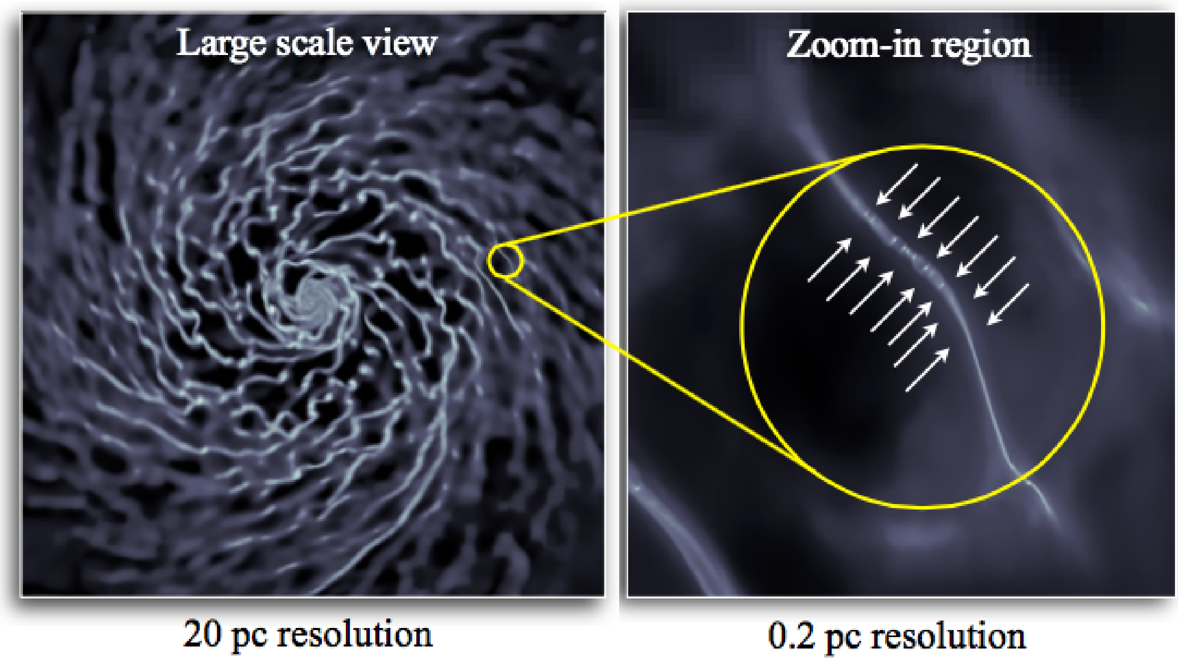

Figure 6.2.3: Left Panel: Simulation of a galaxy performed using the AMR code RAMSES. Right Panel: Zoom in simulation of a galactic filament with molecular clouds in it. RAMSES allows to *tag* certain areas of the simulation for increasing their resolution (Credit: Oscar Agertz).

6.2.4 Testing the Results with Other Codes

To explore if the results presented in this thesis depend on the type of code used, it would be advantageous to simulate the clouds with another code. The AMR code RAMSES (Teyssier 2002) has been modified to include stellar feedback (Agertz et al. 2012), sink particles (Padoan et al. 2012), magnetic fields Masson et al. (2012) and a radiative transfer suite Rosdahl & Blaizot (2012). Therefore it constitutes a good tool to quantify the impact of galactic environment and stellar feedback on star formation in molecular clouds.

An advantage of using RAMSES is that instead of increasing the resolution, certain areas can be tagged in the simulation for further refinement. This means that only those areas are refined further, whilst the rest of the galaxy is at a much lower resolution. An illustration of this is shown in Fig. 6.2.3. After performing our first simulations in SPH and comparing them with clouds modelled with RAMSES, using some hybrid code such as AREPO, could also be a possibility.

6.2.5 Modelling other large scale galactic or extragalactic effects

The clouds included in this thesis are extracted several kpcs from the centre of the galaxy. So the environment in our simulated clouds is completely different to, for example, regions close to the Galactic Centre. Strong tidal effects and higher radiation rates are present in this hostile environment (Kruijssen et al. 2014). Clark & Glover (2014) simulated $G0.253 + 0.016$ ("The Brick") a molecular cloud in the Galactic Centre. They found an increase in the SFR when compared to the central molecular zone, if they assume that the increase in the environmental radiation was due only to star formation. Radiation and cosmic rays could be introduced in our simulations (similar to Clark & Glover 2014; Booth et al. 2013) helping to explore the evolution of clouds in the Galactic Centre (or other) environment.

Many galaxies have active galactic nuclei (AGN). In recent work, Bieri et al. (2015) investigate the effect of AGN feedback as a trigger for star formation. The ejecta from the AGN fall on the galactic plane increasing the pressure over the molecular gas and enhancing star formation. This could be another addition to the galactic models from where we extract the molecular clouds.

Galaxies are not isolated entities. The tidal interaction and mergers between galaxies are relatively frequent (Schneider 2006). The effect of these interactions on the star formation process could be investigated by performing zoom-in high resolution simulations with higher detail than Renaud et al. (2014); Hopkins et al. (2013).

6.2.6 Including Additional Physics

In this thesis we have only considered winds and SNe as feedback mechanisms. However, it would be desirable to simulate the effect of other sources such as momentum driven winds and especially ionising radiation, and their combined effect. Using an approach similar to Agertz et al. (2012) we could model feedback in our clouds introducing momentum, energy and mass loss form stellar winds, SNe, radiation pressure and winds from AGB stars.

Magnetic fields are difficult to implement numerically, particularly in SPH codes. For instance, one problem in SPH algorithms is maintaining $\nabla \cdot \vec{B} = 0$ in the calculations (as due to numerical errors the divergence of the magnetic field grows). There have been some developments to solve this issue (Tricco & Price 2013), and magnetic fields could potentially be included in future SPH simulations, or with a grid code (Masson et al. 2012).

Dust is involved in many processes in the ISM, and in star formation. H_2 is formed on the surface of the dust grains (Gould & Salpeter 1963), it is responsible of the photoelectric heating of the ISM (Draine 1978), and used to calculate the column densities of H_2 by studying the opacity of the clouds. Some authors (like Loren-Aguilar & Bate (2014)) are including the interaction of gas and dust in SPH formulation to model protoplanetary disks. Recently Hopkins & Lee (2015) studied the effect of dust grains in turbulent molecular clouds. The precision of the chemical network can be increased by including the concentration of dust in the ISM cooling and heating, as well as in the models for H_2 and CO shielding (instead of estimating the concentration of dust via H_2 column densities).

Bibliography

Agertz, O. & Kravtsov, A. V. 2015, The Astrophysical Journal, 804, 18

Agertz, O., Kravtsov, A. V., Leitner, S. N., & Gnedin, N. Y. 2012, The Astrophysical Journal, 770, 26

Agertz, O., Lake, G., Moore, B., et al. 2009, in IAU Symposium, Vol. 254, IAU Symposium, ed. J. Andersen, Nordströara, B. M, & J. Bland-Hawthorn, 1P

Agertz, O., Teyssier, R., & Moore, B. 2011, Monthly Notices of the Royal Astronomical Society, 410, 1391

Allen, A. & Shu, F. 2000, The Astrophysical Journal, 536, 368

André, P., Di Francesco, J., Ward-Thompson, D., et al. 2014, in Protostars and Planets VI (University of Arizona Press), 24

Arce, H. G., Borkin, M. A., Goodman, A. A., Pineda, J. E., & Halle, M. W. 2010, The Astrophysical Journal, 715, 1170

Balbus, S. & Hawley, J. 1991, The Astrophysical Journal, 376, 214

Ballesteros-Paredes, J., Hartmann, L., & Vazquez-Semadeni, E. 1999, The Astrophysical Journal, 527, 285

Balsara, D. 1995, Journal of Computational Physics, 121, 357

Banerjee, R., Vázquez-Semadeni, E., Hennebelle, P., & Klessen, R. S. 2009, Monthly Notices of the Royal Astronomical Society, 398, 1082

Barnes, J. & Hut, P. 1986, Nature, 324, 446

Bate, M. R. 2009, Monthly Notices of the Royal Astronomical Society, 392, 590

Bate, M. R., Bonnell, I. A., & Bromm, V. 2002, Monthly Notices of the Royal Astronomical Society, 336, 705

Bate, M. R., Bonnell, I. A., & Bromm, V. 2003, Monthly Notices of the Royal Astronomical Society, 339, 577

Bate, M. R., Bonnell, I. A., & Price, N. M. 1995, Monthly Notices of the Royal Astronomical Society, 277, 362

Bate, M. R. & Burkert, A. 1997, Monthly Notices of the Royal Astronomical Society, 288, 1060

Baudry, A., Perault, M., de La Noe, J., Despois, D., & Cernicharo, J. 1981, Astronomy and Astrophysics, 104, 101

Bergin, E. A., Hartmann, L. W., Raymond, J. C., & Ballesteros - Paredes, J. 2004, The Astrophysical Journal, 612, 921

Bertram, E., Glover, S. C. O., Clark, P. C., & Klessen, R. S. 2015, Monthly Notices of the Royal Astronomical Society, 451, 3679

Bieri, R., Dubois, Y., Silk, J., Mamon, G., & Gaibler, V. 2015, Arxiv 1507.00730

Bigiel, F., Leroy, A., Walter, F., et al. 2008, The Astronomical Journal, 136, 2846

Binney, J. & Tremaine, S. 1987, Galactic dynamics

Black, J. & Dalgarno, A. 1977, The Astrophysical Journal Supplement Series, 34, 405

Bolatto, A., Leroy, A., Rosolowsky, E., Walter, F., & Blitz, L. 2008, The Astrophysical Journal, 686, 948

Bonazzola, S., Perault, M., Puget, J., et al. 1992, Journal of Fluid Mechanics, 245, 1

Bonet, J. & Kulasegaram, S. 2000, International Journal for Numerical Methods in Engineering, 47, 1189

Bonnell, I. A., Dobbs, C. L., & Smith, R. J. 2013, Monthly Notices of the Royal Astronomical Society, 460, 1790

Booth, C. M., Agertz, O., Kravtsov, A. V., & Gnedin, N. Y. 2013, The Astrophysical Journal, 777, L16

Bot, C., Boulanger, F., Rubio, M., & Rantakyro, F. 2007, Astronomy and Astrophysics, 471, 103

Brunt, C. & Federrath, C. 2014, Monthly Notices of the Royal Astronomical Society, 442, 1451

Burgh, E. B., France, K., & McCandliss, S. R. 2007, The Astrophysical Journal, 658, 446

Burstein, P., Borken, R. J., Kraushaar, W. L., & Sanders, W. T. 1977, The Astrophysical Journal, 213, 405

Cazaux, S. & Tielens, A. G. G. M. 2004, The Astrophysical Journal, 604, 222

Chandar, R., Whitmore, B. C., & Fall, S. M. 2010, The Astrophysical Journal, 713, 1343

Churchwell, E. 2008, in Asp Conference Series Vol 390, Vol. 390, 63–71

Churchwell, E., Povich, M. S., Allen, D., et al. 2006, The Astrophysical Journal, 649, 759

Clark, P. C. & Bonnell, I. A. 2004, Monthly Notices of the Royal Astronomical Society, 347, 36

Clark, P. C. & Bonnell, I. A. 2005, Monthly Notices of the Royal Astronomical Society, 361, 2

Clark, P. C. & Bonnell, I. A. 2006, Monthly Notices of the Royal Astronomical Society, 368, 1787

Clark, P. C. & Glover, S. C. O. 2014, Monthly Notices of the Royal Astronomical Society, 444, 2396

Clark, P. C., Glover, S. C. O., & Klessen, R. S. 2008, 79–81

Clark, P. C., Glover, S. C. O., & Klessen, R. S. 2012a, Monthly Notices of the Royal Astronomical Society, 420, 745

Clark, P. C., Glover, S. C. O., Klessen, R. S., & Bonnell, I. A. 2012b, Monthly Notices of the Royal Astronomical Society, 424, 2599

Clark, P. C., Glover, S. C. O., Klessen, R. S., & Bromm, V. 2011, The Astrophysical Journal, 727, 110

Colin, P., Vazquez-Semadeni, E., & Gomez, G. C. 2013, Monthly Notices of the Royal Astronomical Society, 435, 1701

Cox, D. P. & Gomez, G. C. 2002, The Astrophysical Journal Supplement Series, 142, 261

Dale, E. & Bonnell, I. A. 2008, Monthly Notices of the Royal Astronomical Society, 391, 2

Dale, E. & Bonnell, I. A. 2012, Monthly Notices of the Royal Astronomical Society, 422, 1352

Dale, J., Bonnell, I. A., Clarke, C., & Bate, M. R. 2005, Monthly Notices of the Royal Astronomical Society, 358, 291

Dale, J., Ercolano, B., & Bonnell, I. A. 2013a, Monthly Notices of the Royal Astronomical Society, 431, 1062

Dale, J. E., Ercolano, B., & Bonnell, I. 2012, in 'Labyrinth of Star Formation' meeting (18-22 June 2012, Chania, Greece), 2–5

Dale, J. E., Ercolano, B., & Bonnell, I. a. 2013b, Monthly Notices of the Royal Astronomical Society

Dale, J. E., Ngoumou, J., Ercolano, B., & Bonnell, I. A. 2014, Monthly Notices of the Royal Astronomical Society, 442, 21

Dame, T. M., Hartmann, D., & Thaddeus, P. 2001, The Astrophysical Journal, 547, 792

Dawson, J. R., Ntormousi, E., Fukui, Y., Hayakawa, T., & Fierlinger, K. 2015, The Astrophysical Journal, 799, 64

De Marchi, G., Paresce, F., Panagia, N., et al. 2011, The Astrophysical Journal, 739, 27

Dehnen, W. & Aly, H. 2012, Monthly Notices of the Royal Astronomical Society, 425, 1068

Dobbs, C. L. 2015, Monthly Notices of the Royal Astronomical Society, 447, 3390

Dobbs, C. L., Bonnell, I. A., & Clark, P. C. 2005, Monthly Notices of the Royal Astronomical Society, 360, 2

Dobbs, C. L., Bonnell, I. a., & Pringle, J. E. 2006, Monthly Notices of the Royal Astronomical Society, 371, 1663

Dobbs, C. L., Burkert, A., & Pringle, J. E. 2011a, Monthly Notices of the Royal Astronomical Society, 413, 2935

Dobbs, C. L., Burket, A., & Pringle, J. 2011b, Monthly Notices of the Royal Astronomical Society, 417, 1318

Dobbs, C. L., Glover, S. C. O., Clark, P. C., & Klessen, R. S. 2008, Monthly Notices of the Royal Astronomical Society, 389, 1097

Dobbs, C. L., Krumholz, M. R., Ballesteros-Paredes, J., et al. 2014a, Protostars and Planets VI, 25

Dobbs, C. L. & Pringle, J. E. 2013, Monthly Notices of the Royal Astronomical Society, 432, 653

Dobbs, C. L., Pringle, J. E., & Duarte-Cabral, A. 2014b, Monthly Notices of the Royal Astronomical Society, 446, 3608

Doran, E. I., Crowther, P. A., de Koter, A., et al. 2013, Astronomy & Astrophysics, 558, A134

Drabek, E., Hatchell, J., Friberg, P., et al. 2012, Monthly Notices of the Royal Astronomical Society, 426, 23

Draine, B. & Bertoldi, F. 1996, The Astrophysical Journal, 468, 269

Draine, B. T. 1978, The Astrophysical Journal Supplement Series, 36, 595

Draine, B. T. 2011, Physics of the Interstellar and Intergalactic Medium, 540

Duarte-Cabral, A., Acreman, D. M., Dobbs, C. L., et al. 2015, Monthly Notices of the Royal Astronomical Society, 447, 2144

Duarte-Cabral, A., Chrysostomou, A., Peretto, N., et al. 2012, Astronomy & Astrophysics, 543, A140

Dubinski, J., Narayan, R., & Phillips, T. G. 1995, The Astrophysical Journal, 448, 226

Duley, W. & Williams, D. 1993, Monthly Notices of the Royal Astronomical Society, 260, 37

Ehrenfreund, P. & Foing, B. H. 2010, Science, 329, 1159

Elmegreen, B. G. 2000, The Astrophysical Journal, 530, 277

Elmegreen, B. G. 2007, The Astrophysical Journal, 668, 1064

Evans, N. J., Dunham, M. M., Jørgensen, J. K., et al. 2009, The Astrophysical Journal Supplement Series, 181, 321

Everett, J. & Churchwell, E. 2010, in Asp Conference Series Vol 438

Federman, S. R., Glassgold, A. E., Jenkins, E. B., & Shaya, E. J. 1980, The Astrophysical Journal, 242, 545

Federrath, C. 2015, Monthly Notices of the Royal Astronomical Society, 450, 4035

Federrath, C. & Klessen, R. S. 2012, The Astrophysical Journal, 761, 34

Federrath, C. & Klessen, R. S. 2013, The Astrophysical Journal, 763, 51

Federrath, C., Schrön, M., Banerjee, R., & Klessen, R. S. 2014, The Astrophysical Journal, 790, 128

Federrath, C., Sur, S., Schleicher, D. R. G., Banerjee, R., & Klessen, R. S. 2011, The Astrophysical Journal, 731, 62

Field, G. B. 1965, The Astrophysical Journal, 142, 531

Field, G. B., Goldsmith, D. W., & Habing, H. J. 1969, The Astrophysical Journal, 155, L149

Fierlinger, K. M., Burkert, A., Ntormousi, E., et al. 2015, Monthly Notices of the Royal Astronomical Society

Gammie, C. F. & Ostriker, E. C. 1996, The Astrophysical Journal, 466, 814

Gatto, A., Walch, S., Low, M.-M. M., et al. 2015, Monthly Notices of the Royal Astronomical Society, 449, 1057

Geen, S., Rosdahl, J., Blaizot, J., Devriendt, J., & Slyz, A. 2015, Monthly Notices of the Royal Astronomical Society, 448, 3248

Gingold, R. a. & Monaghan, J. J. 1977, Monthly Notices of the Royal Astronomical Society, 181, 375

Girichidis, P., Federrath, C., Banerjee, R., & Klessen, R. S. 2011, Monthly Notices of the Royal Astronomical Society, 413, 20

Girichidis, P., Walch, S., Naab, T., et al. 2015, 26

Glover, S. C. O. & Clark, P. C. 2012, Monthly Notices of the Royal Astronomical Society, no

Glover, S. C. O. & Mac Low, M. M. 2006, The Astrophysical Journal, 659, 66

Glover, S. C. O. & Mac Low, M.-m. 2007a, The Astrophysical Journal, 169, 239

Glover, S. C. O. & Mac Low, M.-m. 2007b, The Astrophysical Journal, 659, 1317

Gnedin, N. Y. 2014, 191

Goldreich, P. & Lynden-Bell, D. 1965, Monthly Notices of the Royal Astronomical Society, 130, 125

Goldsmith, P. F. & Langer, W. D. 1978, The Astrophysical Journal, 222, 881

Gorski, K. M., Hivon, E., Banday, A. J., et al. 2005, The Astrophysical Journal, 622, 759

Gould, R. J. & Salpeter, E. E. 1963, The Astrophysical Journal, 138, 393

Gouliermis, D. a., Schmeja, S., Dolphin, A. E., et al. 2012, The Astrophysical Journal, 748, 64

Grassi, T., Bovino, S., Schleicher, D. R. G., et al. 2014, Monthly Notices of the Royal Astronomical Society, 439, 2386

Gritschneder, M., Naab, T., Walch, S., Burkert, A., & Heitsch, F. 2009, The Astrophysical Journal, 694, L26

Güdel, M., Briggs, K. R., Montmerle, T., et al. 2008, Science (New York, N.Y.), 319, 309

Habing, H. 1968, Bulletin of the Astronomical Institutes of the Netherlands, 19, 421

Hansen, Carl J.; Kawaler, S. D. 1994, Stellar Interiors: Physical Principles, Structure, and Evolution. (Birkhäuser)

Hartmann, L., Ballesteros-Paredes, J., & Bergin, E. 2001, Astrophysics Journal, 562, 852

Haworth, T. J., Harries, T. J., & Acreman, D. M. 2012, Monthly Notices of the Royal Astronomical Society, 426, 203

Haworth, T. J., Harries, T. J., Acreman, D. M., & Bisbas, T. G. 2015, Monthly Notices of the Royal Astronomical Society, 453, 2277

Haworth, T. J., Harries, T. J., Acreman, D. M., & Rundle, D. A. 2013, Monthly Notices of the Royal Astronomical Society, 431, 3470

Heiderman, A., Evans, N. J., Allen, L. E., Huard, T., & Heyer, M. 2010, The Astrophysical Journal, 723, 1019

Heiles, C. & Troland, T. H. 2003, The Astrophysical Journal, 586, 1067

Heitsch, F., Slyz, A. D., Devriendt, J. E. G., Hartmann, L. W., & Burkert, A. 2006, The Astrophysical Journal, 648, 1052

Hennebelle, P., Banerjee, R., Vázquez-Semadeni, E., Klessen, R. S., & Audit, E. 2008, Astronomy and Astrophysics, 486, 43

Hensler, G. 2010, in Proceedings IAU Symposium No. 270, No. 270, 119–127

Hernquist, L. & Katz, N. 1989, The Astrophysical Journal Supplement Series, June, 419

Heyer, M., Krawczyk, C., Duval, J., & Jackson, J. M. 2009, The Astrophysical Journal, 699, 1092

Hollenbach, D. & McKee, C. F. 1989, The Astrophysical Journal, 342, 306

Hollenbach, D. J., Werner, M. W., & Salpeter, E. E. 1971, The Astrophysical Journal, 163, 165

Hopkins, P. F. 2011, Monthly Notices of the Royal Astronomical Society, 423, 2016

Hopkins, P. F. 2012, Monthly Notices of the Royal Astronomical Society, 430, 1653

Hopkins, P. F., Cox, T. J., Hernquist, L., et al. 2013, Monthly Notices of the Royal Astronomical Society, 430, 1901

Hopkins, P. F. & Lee, H. 2015, Arxiv 1510.02477, 14

Hopkins, P. F., Quataert, E., & Murray, N. 2011, Monthly Notices of the Royal Astronomical Society, 417, 950

Hopkins, P. F., Quataert, E., & Murray, N. 2012, Monthly Notices of the Royal Astronomical Society, 421, 3522

Hubber, D. A., Batty, C. P., McLeod, A., & Whitworth, A. P. 2011, Astronomy & Astrophysics, 529, A27

Ibáñez-Mejía, J. C., Mac Low, M.-M., Klessen, R. S., & Baczynski, C. 2015, 13

Jappsen, A.-K., Klessen, R. S., Larson, R. B., Li, Y., & Mac Low, M.-M. 2005, Astronomy and Astrophysics, 435, 611

Jeans, J. H. 1902, Philosophical Transactions of the Royal Society A: Mathematical, Physical and Engineering Sciences, 199, 1

Jenkins, E. B. & Meloy, D. A. 1974, The Astrophysical Journal, 193, L121

Julian, W. H. & Toomre, A. 1966, The Astrophysical Journal, 146, 810

Kavanagh, P., Norci, L., & Meurs, E. 2011, New Astronomy, 16, 461

Kennicutt, R. C. 1998, The Astronomical Journal, 498, 541

Kim, J.-H., Krumholz, M. R., Turk, M. J., Goldbaum, N. J., & Abel, T. 2012, The Astrophysical Journal, 779, 17

Kim, W. & Ostriker, E. C. 2002, The Astrophysical Journal, 570, 132

Kim, W. & Ostriker, E. C. 2006, The Astrophysical Journal, 646, 213

Kimm, T., Cen, R., Devriendt, J., Dubois, Y., & Slyz, A. 2015, 22

Klessen, R. S. 2003, Arxiv 301.381, 33

Kolmogorov, A. 1941, Akademiia Nauk SSSR Doklady, 30, 301

Konstandin, L., Shetty, R., Girichidis, P., & Klessen, R. S. 2015, Monthly Notices of the Royal Astronomical Society, 446, 1775

Kroupa, P. 2001, Monthly Notices of the Royal Astronomical Society, 322, 231

Kruijssen, J. M. D., Dale, J. E., & Longmore, S. N. 2014, Monthly Notices of the Royal Astronomical Society, 447, 1059

Krumholz, M. R., Bate, M. R., Arce, H. G., et al. 2014, Protostars and Planets VI, Vol. 1401 (University of Arizona Press), 24

Krumholz, M. R. & Mckee, C. F. 2005, The Astrophysical Journal, 630, 250

Krumholz, M. R., McKee, C. F., & Klein, R. I. 2005, Nature, 438, 332

Krumholz, M. R. & Tan, J. C. 2007, The Astrophysical Journal, 654, 304

Laibe, G. & Price, D. J. 2014, Monthly Notices of the Royal Astronomical Society, 444, 1940

Larson, R. 1981, Monthly Notices of the Royal Astronomical Society, 194, 809

Le Bourlot, J., Pineau des Forets, G., & Flower, D. R. 1999, Monthly Notices of the Royal Astronomical Society, 305, 802

Le Teuff, Y. H., Millar, T. J., & Markwick, A. J. 2000, Astronomy and Astrophysics Supplement Series, 146, 157

Lewis, B. T., Bate, M. R., & Price, D. J. 2015, Monthly Notices of the Royal Astronomical Society, 451, 288

Lopez, L. A., Krumholz, M. R., Bolatto, A. D., Prochaska, J. X., & Ramirez-Ruiz, E. 2010, 14

Lopez, L. A., Krumholz, M. R., Bolatto, A. D., et al. 2014, The Astrophysical Journal, 795, 121

Loren-Aguilar, P. & Bate, M. R. 2014, Monthly Notices of the Royal Astronomical Society, 443, 927

Lucy, L. B. 1977, The Astronomical Journal, 82, 1013

Mac Low, M. 1999, The Astrophysical Journal, 524, 169

Mac Low, M.-M. & Klessen, R. S. 2004, Reviews of Modern Physics, 76, 125

Masson, J., Teyssier, R., Mulet-Marquis, C., Hennebelle, P., & Chabrier, G. 2012, The Astrophysical Journal Supplement Series, 201, 24

McKee, C. F. & Ostriker, J. P. 1977, The Astrophysical Journal, 218, 148

Meidt, S. E., Hughes, A., Dobbs, C. L., et al. 2015, The Astrophysical Journal, 806, 72

Moeckel, N. & Burkert, A. 2015, The Astrophysical Journal, 807, 67

Momose, R., Koda, J., Kennicutt, R. C., et al. 2013, The Astrophysical Journal Letters, 772, 5

Monaghan, J. 1992, Annu. Rev. Astron. Astrophys., 543

Murray, N. 2011, The Astrophysical Journal, 729, 133

Myers, A. T., McKee, C. F., Cunningham, A. J., Klein, R. I., & Krumholz, M. R. 2013, The Astrophysical Journal, 766, 97

Myers, P. C. & Gammie, C. F. 1999, The Astronomical Journal, 522, 141

Narayanan, D., Krumholz, M. R., Ostriker, E. C., & Hernquist, L. 2012, Monthly Notices of the Royal Astronomical Society, 421, 3127

Nelson, R. P. & Langer, W. D. 1997, The Astrophysical Journal, 482, 796

Ntormousi, E., Burkert, A., Fierlinger, K., & Heitsch, F. 2011, The Astrophysical Journal, 731, 16

Offner, S. S. R., Hansen, C. E., & Krumholz, M. R. 2009, The Astrophysical Journal, 704, 124

Okabe, A., Okabe, M., & Boots, B. 2000, Spatial Tessellations: Concepts and Applications of Voronoi Diagrams (John Wiley & Sons, Inc.), 700

Osterbrock, D. & Ferland, G. 2006, Astrophysics of gaseous nebulae and active galactic nuclei

Ostriker, E. C., Lee, C., Stone, J. M., & Mundy, L. G. 2001, The Astrophysical Journal, 557, 443

Padoan, P., Haugbølle, T., & Nordlund, Å. 2012, The Astrophysical Journal, 759, L27

Padoan, P. & Nordlund, Å. 2011, The Astrophysical Journal, 730, 40

Padoan, P., Pan, L., Haugboelle, T., & Nordlund, A. 2015

Palmeirim, P., André, P., Kirk, J., et al. 2013, Astronomy & Astrophysics, 550, A38

Peretto, N., André, P., Könyves, V., et al. 2012, Astronomy & Astrophysics, 541, A63

Pettitt, A. R. 2014, PhD thesis, University of Exeter

Pettitt, A. R., Dobbs, C. L., Acreman, D. M., & Price, D. J. 2014, Monthly Notices of the Royal Astronomical Society, 444, 919

Pineda, J. E., Caselli, P., & Goodman, A. A. 2008, The Astrophysical Journal, 679, 481

Planck Collaboration, Ade, P. A. R., Aghanim, N., et al. 2015, 28

Price, D. J. 2007, Publications of the Astronomical Society of Australia, 24, 159

Price, D. J. 2012, Journal of Computational Physics, 231, 759

Price, D. J. & Bate, M. R. 2009, Monthly Notices of the Royal Astronomical Society, 398, 33

Price, D. J. & Federrath, C. 2010, Monthly Notices of the Royal Astronomical Society, 406, 16

Price, D. J., Federrath, C., & Brunt, C. M. 2011, The Astrophysical Journal, 727, L21

Quinn, T., Katz, N., Stadel, J., & Lake, G. 1997, The Astrophysical Journal, 10/1997, 16

Renaud, F., Bournaud, F., Emsellem, E., et al. 2013, Monthly Notices of the Royal Astronomical Society, 436, 1836

Renaud, F., Bournaud, F., Kraljic, K., & Duc, P.-A. 2014, Monthly Notices of the Royal Astronomical Society: Letters, 442, L33

Renaud, F. & Gieles, M. 2015, Monthly Notices of the Royal Astronomical Society, 449, 2734

Rey-Raposo, R., Dobbs, C., & Duarte-Cabral, A. 2015, Monthly Notices of the Royal Astronomical Society Letters, 446, 46

Ripple, F., Heyer, M. H., Gutermuth, R., Snell, R. L., & Brunt, C. M. 2013, Monthly Notices of the Royal Astronomical Society, 431, 1296

Rogers, H. & Pittard, J. M. 2013, Monthly Notices of the Royal Astronomical Society, 431, 1337

Rogers, H. & Pittard, J. M. 2014, Monthly Notices of the Royal Astronomical Society, 441, 964

Roman-Duval, J., Federrath, C., Brunt, C., et al. 2011, The Astrophysical Journal, 740, 120

Rosdahl, J. & Blaizot, J. 2012, Monthly Notices of the Royal Astronomical Society, 423, 344

Rosen, A. L., Lopez, L. A., Krumholz, M. R., & Ramirez-Ruiz, E. 2014, Monthly Notices of the Royal Astronomical Society, 442, 2701

Rosolowsky, E. & Blitz, L. 2005, The Astrophysical Journal, 623, 826

Salpeter, E. 1955, The Astrophysical Journal, 121, 161

Santander-García, M., Bujarrabal, V., & Alcolea, J. 2012, Astronomy & Astrophysics, 545, A114

Schinnerer, E., Meidt, S. E., Pety, J., et al. 2013, The Astrophysical Journal, 779, 42

Schmidt, M. 1959, The Astrophysical Journal, 129, 243

Schneider, P. 2006, Extragalactic Astronomy and Cosmology: An Introduction (Springer)

Sheffer, Y., Rogers, M., Federman, S. R., et al. 2008, The Astrophysical Journal, 687, 1075

Shetty, R., Kelly, B. C., & Bigiel, F. 2013, Monthly Notices of the Royal Astronomical Society, 430, 288

Shu, F., Adams, F., & Lizano, S. 1987, Annu. Rev. Astron. Astrophys., 25, 23

Silva, A. & Viegas, S. 2002, Monthly Notices of the Royal Astronomical Society, 329, 135

Smith, R. J., Glover, S. C. O., Clark, P. C., Klessen, R. S., & Springel, V. 2014, Monthly Notices of the Royal Astronomical Society, 441, 1628

Solenthaler, B. & Pajarola, R. 2009, ACM Trans. Graph., 28, 40:1

Solomon, P. M., Rivolo, A. R., Barrett, J., & Yahil, A. 1987, The Astrophysical Journal, 319, 730

Sousbie, T. 2011, Monthly Notices of the Royal Astronomical Society, 414, 350

Sousbie, T., Pichon, C., & Kawahara, H. 2011, Monthly Notices of the Royal Astronomical Society, 414, 384

Springel, V. 2005, Monthly Notices of the Royal Astronomical Society, 364, 1105

Springel, V. 2009, Monthly Notices of the Royal Astronomical Society, 401, 791

Springel, V. & Hernquist, L. 2002, Monthly Notices of the Royal Astronomical Society, 333, 649

Stahler, S. W. & Palla, F. 2008, The Formation of Stars

Steinmetz, M. 1996, Monthly Notices of the Royal Astronomical Society, 278, 1005

Sternberg, A., McKee, C. F., & Wolfire, M. G. 2002, The Astrophysical Journal Supplement Series, 143, 419

Strömgren, B. 1939, The Astrophysical Journal, 89, 526

Sutherland, R. S. & Dopita, M. A. 1993, The Astrophysical Journal Supplement Series, 88, 253

Teyssier, R. 2002, Astronomy and Astrophysics, 385, 337

Townsley, L. K., Feigelson, E. D., Montmerle, T., et al. 2003, The Astrophysical Journal, 593, 874

Tricco, T. S. & Price, D. J. 2013, Monthly Notices of the Royal Astronomical Society, 436, 2810

Ungerer, V., Nguyen-Quang-Rieu, Mauron, N., & Brillet, J. 1985, Astronomy and Astrophysics, 146, 123

Vázquez-Semadeni, E. 1994, The Astrophysical Journal, 423, 681

Vázquez-Semadeni, E., Banerjee, R., Gomez, G., et al. 2011, Monthly Notices of the Royal Astronomical Society, 414, 2511

Vázquez-Semadeni, E., Colín, P., Gómez, G. C., Ballesteros-Paredes, J., & Watson, A. W. 2010, The Astrophysical Journal, 715, 1302

Vázquez-Semadeni, E., Gomez, G. C., Jappsen, A. K., et al. 2007, The Astrophysical Journal, 657, 870

Vázquez-Semadeni, E., Ryu, D., Passot, T., Gonza, R. F., & Gazol, A. 2006, The Astrophysical Journal, 1, 245

Walch, S. & Naab, T. 2015, Monthly Notices of the Royal Astronomical Society, 451, 2757

Walch, S., Whitworth, A. P., Bisbas, T., & Hubber, D. 2012, Monthly Notices of the Royal Astronomical Society, 427, 625

Wang, Q. D., Dong, H., & Lang, C. 2006, Monthly Notices of the Royal Astronomical Society, 371, 38

Wendland, H. 1995, Advances in computational Mathematics, 4, 389

Wolfire, M. G., McKee, C. F., Hollenbach, D., & Tielens, A. G. G. M. 2003, The Astrophysical Journal, 587, 278

Zuckerman, B. & Evans, N. J. 1974, The Astrophysical Journal, 192, L149

A
Appendix

A.1 A Conservative Formulation of SPH

In some SPH formulations energy is not totally conserved because of trunkation errors due to the differences in the smoothing lengths for different particles. To solve this Springel & Hernquist (2002) minimize the Lagrangian equation of motions using Lagrange multipliers and realizing that they have N constraints to simplify the problem (N being the total number of SPH particles). They start with the Lagrange equations

$$\frac{d}{dt}\frac{\partial \mathcal{L}}{\partial \dot{q}_i^j} - \frac{\partial \mathcal{L}}{\partial q_i^j} = 0 \quad for\ j = 1 \rightarrow 3, \tag{A.1.1}$$

where the Lagrangian $\mathcal{L}$ of a SPH particle is

$$\mathcal{L} = \frac{1}{2}\sum_{i=1}^{N} m_i \dot{\vec{r}}_i^{\,2} - \frac{1}{\gamma - 1}\sum_{i=1}^{N} m_i A_i \rho_i^{\gamma-1}. \tag{A.1.2}$$

In a 3D simulation Eq.A.1.1 and A.1.2 represent a set of $3N$ coupled differential equations that needed to be solved. However we have N extra constrains coming from the neighbour-density equation

$$\frac{4\pi}{3} h_i^3 \rho_i = N_{neigh}\, m_p. \tag{A.1.3}$$

These constraints are defined as

$$\psi_i(\vec{r}) \equiv \frac{4\pi}{3} h_i^3 \rho_i - N_{neigh}\, m_p = 0. \tag{A.1.4}$$

The Lagrange equation with the Lagrange multipliers is then

$$\frac{d}{dt}\frac{\partial \mathcal{L}}{\partial \dot{q}_i^j} - \frac{\partial \mathcal{L}}{\partial q_i^j} = \sum_{k=1}^{N} \lambda_k \frac{\partial \psi_k}{\partial q_i^j} \quad for\ j = 1 \rightarrow 3. \tag{A.1.5}$$

If we minimize this equation and solve for λ

$$\lambda_i = \frac{3}{4\pi}\frac{m_i}{h_i^3}\frac{P_i}{\rho_i^2}\left[1 + \frac{3\rho_i}{h_i}\left(\frac{\partial \rho_i}{\partial h_i}\right)^{-1}\right]^{-1}. \tag{A.1.6}$$

where the f_i are defined as

$$f_i = \left[1 + \frac{h_i}{3\rho_i}\left(\frac{\partial \rho_i}{\partial h_i}\right)\right]^{-1}. \tag{A.1.7}$$

Therefore, the equations of motion now are

$$m_i \frac{d\vec{u}_i}{dt} = \sum_{j=1}^{N} m_j \frac{P_j}{\rho_j^2} f_j \nabla_i \rho_j. \tag{A.1.8}$$

To calculate the gradient of the density we use

$$\nabla_i \rho_i = m_i \nabla_i W_{ij}(h_j) + \delta_{ij} \sum_{k=1}^{N} m_k \nabla_i W_{ki}(h_i). \tag{A.1.9}$$

We find the equation of movement used by GADGET2

$$\frac{d\vec{u}_i}{dt} = -\sum_{j=1}^{N} m_j \left(f_i \frac{P_i}{\rho_i^2}\, \nabla_i W_{ij}(h_i) + f_j \frac{P_j}{\rho_j^2}\, \nabla_j W_{ij}(h_j) \right). \tag{A.1.10}$$

A.2 Conservation of Invariants when Increasing Resolution

In any of the methods described in Chapter 2, for an initial particle with position $\vec{R_j}$ we will generate F new particles with positions $\vec{R_j} + \vec{\delta_k}$, and masses $\mu = m_o/F$, where m_o is the mass of the particle in the original simulation and F the factor to increase resolution. As the particles newly generated are scattered around the initial one, then it follows

$$\sum_{k=1}^{F} \delta_k \simeq 0. \tag{A.2.1}$$

This is strictly true for the cubic case, and approximate for the scattering of particles using both random distributions.

A.2.1 Mass and Linear Momentum

The method conserves the mass by construction. In the original simulation the momentum of the jth-particle is

$$\vec{p}_j = m_o \cdot \vec{u}_j. \tag{A.2.2}$$

When we increase the resolution the original particle splits into F new particles, with mass μ and the same velocity as the original

$$\vec{p}_j = m_o \cdot \vec{u}_j = \sum_{k=1}^{F} \mu \cdot \vec{u}_j = F\mu \cdot \vec{u}_j = m_o \cdot \vec{u}_j. \tag{A.2.3}$$

A.2.2 Angular Momentum

The angular momentum of the original jth-particle is

$$\vec{L}_j = \vec{R}_j \times \vec{p}_j. \tag{A.2.4}$$

For the F new particles the total angular momentum is

$$\vec{L}_j = \vec{R}_j \times \vec{p}_j = \sum_{k=1}^{F} [(\vec{R}_j + \vec{\delta}_k) \times \mu \cdot \vec{u}_j]. \tag{A.2.5}$$

And as the vectorial product is additive and using Eq. A.2.1

$$\vec{L}_j = \left(\vec{R}_j + \sum_{k=1}^{F} \vec{\delta}_k \right) \times m_o \cdot \vec{u}_j \approx \vec{R}_j \times m_o \cdot \vec{u}_j = \vec{R}_j \times \vec{p}_j. \tag{A.2.6}$$

A.2.3 Kinetic Energy

The Kinetic Energy of the jth-particle in the original cloud is

$$K_j = \frac{1}{2} m_o \cdot |\vec{u}_j|^2. \tag{A.2.7}$$

Using the same argument as for the linear momentum (Eq. A.2.3)

$$K_j = \frac{1}{2} m_o \cdot |\vec{u}_j|^2 = \sum_{k=1}^{F} \frac{1}{2} \mu \cdot |\vec{u}_j|^2 = \frac{1}{2} N\mu \cdot |\vec{u}_j|^2 = \frac{1}{2} m_o \cdot |\vec{u}_j|^2. \tag{A.2.8}$$

A.2.4 Gravitational Energy

Gravitational Energy requires the summation over the total number of particles. For simplicity we calculate the gravitational energy of only the new particles generated by the j-th particle in the original simulation. For this particle the gravitational energy is

$$V_j = \sum_{i=1}^{N_{tot}} G \frac{m_i m_j}{r_{ij}} \quad i \neq j, \tag{A.2.9}$$

where N_{tot} is the number of particles in the original simulation and $r_{ij} = |r_i - R_j|$. If we compute the energy of the F new particles corresponding to the j-th original particle and considering that all new particles have the same mass $m_o = F \cdot \mu$

$$V_j = \sum_{i=1}^{N_{tot}} G \frac{m_o^2}{r_{ij}} \Rightarrow \sum_{i=1}^{N_{tot}} \sum_{k=1}^{F} \frac{G m_o \mu}{|r_i - (R_j + \delta_k)|}. \tag{A.2.10}$$

In a typical SPH simulation the smoothing length is smaller than R_j, so we can consider $\delta_k \ll R_j$ for most cases and $r_{ij} = |r_i - R_j|$, we can rearrange the factors

$$V_j = \sum_{i=1}^{N_{tot}} \sum_{k=1}^{F} \frac{G m_i \mu}{|r_{ij} + \delta_k|} = \sum_{i=1}^{N_{tot}} \frac{G m_o^2}{r_{ij}} \sum_{k=1}^{F} \frac{1}{|1 + \frac{\delta_k}{r_{ij}}|}, \tag{A.2.11}$$

where $\frac{\delta_k}{r_{ij}} \ll 1$. So, if we do a Taylor expansion of the last term

$$V_j = \sum_{i=1}^{N_{tot}} \frac{G m_o^2}{r_{ij}} \sum_{k=1}^{F} \left(1 + \frac{\delta_k}{r_{ij}}\right)^{-1} \approx \sum_{i=1}^{N_{tot}} \frac{G m_o^2}{r_{ij}} \left(1 - \sum_{k=1}^{F} \delta_k\right), \tag{A.2.12}$$

as the particles were evenly scattered (Eq. A.2.1) we have the initial result:

$$V_j = \sum_{i=1}^{N_{tot}} \frac{G m_o^2}{r_{ij}} \left(1 - \sum_{k=1}^{F} \delta_k\right) \approx \sum_{i=1}^{N_{tot}} \frac{G m_o^2}{r_{ij}}. \tag{A.2.13}$$